University of Alberta

SEISMIC MONITORING OF HEAVY OIL RESERVOIRS: ROCK PHYSICS AND FINITE ELEMENT
MODELLING

by

Ulrich Theune ©

A thesis submitted to the Faculty of Graduate Studies and Research in partial fulfillment
of the requirements for the degree of **Doctor of Philosophy.**

in

Geophysics

Department of Physics

Edmonton, Alberta
Fall 2004

Canadä

To my best friend ever: *Schnuffi*

Acknowledgements

Now that's it! This is my PhD-thesis. That I could finish it has very much to do with the support I received from many people. First of all, I must thank my supervision committee for letting me finish my work and recommending it as sufficient for a doctoral thesis: Dr. Douglas Schmitt, who, being my supervisor, deserves a special mention for supporting me finacially and equipment-wise during the past five years, Dr. Moritz Heimpel, Dr. Richard Marchand, Dr. Marcel Polikar, Dr. Mauricio Sacchi, and Dr. Gerhard Pratt as the external reviewer. I do not want to forget Richard Sydora, an early member of the committee, who is currently on sabbatical leave. Their suggestions have been proven to be valuable for improving this thesis.

To Mauricio Sacchi I owe much respect and gratitude for many educational and entertaining discussions throughout these years. His interest in my work and problems as well as his apparently bottomless pool of time helped me a lot to go forward on the rocky road towards this thesis (and my sincere apologies to the SAIG-students for taking so much of your supervisor's time - he is all yours now). Muchas Gracias! Many of the simulations would not have been possible without the patience of the Global Dynamics group. I thank Moritz Heimpel for letting me use his powerful computers; and to his students ... well, I hope you had some nice coffee breaks while I slowed down your work - sorry and thanks for that.

James McKinnon and Jay Haverstock were always there when I had soft- or hardware problems, very often their help was very unbureaucratic. Dean Rokosh's help with interpretating well logs and the geology of the Western Canadian Sedimentary basin is much appreciated. The same goes for Yajun Zhang for providing the processed data in Figure 3.2.

I appreciated and enjoyed the discussions I had with Ron Sawatzky about various topics related to heavy oil - thanks, Ron.

Life would be much harder and working much more challenging if there wouldn't have been some people to go out with for a beer or to see a movie. For their time and some distracting (and amusing) emails I like to thank James Brown, Pavlo Cholach, Mahmadou Diallo, Olga Kostenko, Henning Kühl, Michael Lazorek (please forgive my German accent!), Verónica Martínez, Cristina Moldoveanu-Constantinescu, Lara de Nardo, Jillian and Wendell Pardasie (without his questions I wouldn't have thought so deeply about some fundamental geophysical problems ...), Ismael Rumzan, Mauricio Sacchi, Shah Shareef, Wolfgang Soyer, Martyn Unsworth, and Carrie and Oliver Youzwishen! No, I did not forget Nathalie Lara and Brent Frey: I am glad that I have met you and hope things are going well in la manzana grande! Pavlo deserves a special mentioning for patiently explaining for the ten-thousands time how to draw a straight line in CorelDraw (among many other things ... but sorry, my world is still isotropic)! I enjoyed sharing the office

with you and Henning a lot.

I like to thank Verónica for the nicest time I had in Edmonton, and I hope that you will find the home you are looking for.

Now at the end of my PhD my thoughts also travel back to where everything began. I send my thankful greetings to Martin Brudy for the fun I had working with him, and also for the great experience of team-working. The same is true for Matthias Gölke. I am glad that the contact to the two of you never ended; your emails certainly helped to keep my spirits up. It is important for me to include Klaus Huber (†), who unfortunately died too early (but didn't Billy Joel (1977) say that *"only the good die young"*?); yet, I think he help me very much in developing a methodological, scientific way of thinking in his very special way. A thank you also goes to Jürgen Dornstädter, Hans Bässler, Thomas "Thomson" Hertweck, Stefan Hettel, Birgit Müller, Blanka Sperner, Uwe Beyer, Olaf Eisen, and many others at the Universität Karlsruhe for some nice coffee breaks and discussions about "God and the world".

Two industrial summer internships will remain to be a very good experience: greetings to the people at the Statoil R&D-centre in Trondheim/Norway and the Schlumberger Research Center in Cambridge, UK. I am especially thankful to Martin Brudy (formerly Statoil R&D, Trondheim) and Björn E. Rommel (SCR) for enabling and managing my visits at these places.

At the very beginning of my "academic career" I met Nina Döhr and Susanne Kober at the Technische Universität München. That the contact has survived during all these years and despite the distance means very much to me. I am thankful for your friendship and hope that there will be more time in the future for some Weizenbiere in a nice (and real) Biergarten!

Finally, I am very much in debt for the moral support I received from my family back home in Germany. Especially my mother had to suffer from much frustration, yet she was always there when I was short of money or just needed someone to talk to, even in the middle of the night. I just can hope that one day I will be able to pay back for everything.

And as this is very important to me I am going to repeat this in German: Ein ganz, ganz besonderer Dank geht an meine Mutter, die so unter mancher Frustration meinerseits leiden mußte, dennoch war sie immer da, wenn ich jemanden zum reden brauchte, und sei es mitten in der Nacht. Ich kann nur hoffen, daß ich eines Tages in der Lage sein werde, ihr in angemessener Weise von ihrer Unterstützung wieder etwas zurück geben kann. (Considering the current anarchy regarding grammar rules in Germany, the above text will surely be correct ... according to one or another spelling!)

Contents

List of Tables

List of Figures

List of symbols and abbreviations

Numerics

$\mathcal{L}$ generalized PDE operator

$\mathbf{u}$ displacement field

$\mathcal{R}$ Residual after FEM approximation

σ_{ij} stress tensor

ϵ_{kl} strain tensor

c_{ijkl} elastic stiffness tensor

λ first Lamé parameter

μ second Lamé parameter or shear modulus

ρ bulk density

$\hat{\mathbf{u}}$ approximation of the displacement field $\mathbf{u}$ by a finite series

ϕ basis function

$\mathbf{w}$ weighting function

$\mathbf{M}$ mass matrix

$\mathbf{K}$ stiffness matrix

$\mathbf{C}$ damping matrix (for Rayleigh attenuation)

$\mathbf{S}$ seismic source tensor

f_c centre frequency of a Ricker wavelet

λ_{min} minimum wavelength supported by a numerical grid/mesh

$\ell_{\alpha}^{n_\ell}$ Lagrangian polynomial

n_ℓ degree of the Lagrangian polynomial

$[\mathbf{x}, \mathbf{y}]$ physical co-ordinates

$[\xi, \eta]$ natural co-ordinates

ω_i Gauss-Lobatto quadrature weights

α, β, γ parameters for the Rayleigh attenuation technique

Δx grid spacing of a discrete numerical grid

h typical size of a finite element

p used here to denote the degree of an interpolation polynomial in the standard finite element and global spectrum methods

Δt time sampling interval of time series or discrete time step

c_{max} maximum velocity occurring in a numerical model

n_d dimensionality of a computational model

Rock physics

$\mathcal{AI}$ Acoustic impedance [kg/m^2/s]

K bulk modulus [Pa]

K_S bulk modulus of the solid material [Pa]

K_O bulk modulus of oil [Pa]

K_W bulk modulus of water or brine [Pa]

K_{St} bulk modulus of steam [Pa]

K_f bulk modulus of a composite fluid [Pa]

K_d bulk frame modulus [Pa]

K_{eff} effective bulk modulus of a composite material (solid and fluid) [Pa]

μ shear modulus [Pa]

μ_d shear frame modulus [Pa]

η (shear) viscosity of a fluid [Pa·s]

ϕ porosity [-]

S_{St} steam saturation [-]

S_W water or brine saturation [-]

S_O oil saturation [-]

ρ_{eff} effective density [kg/m^3]

ρ_S density of the solid material [kg/m^3]

ρ_O oil density [kg/m^3]

ρ_{St} steam density [kg/m^3]

ρ_W water or brine density [kg/m^3]

ρ_f effective density of a composite fluid [kg/m^3]

V_P P-velocity [m/s]

$V_{P_{Gass}}$ P-velocity according to the Gassmann model [m/s]

$V_{P_{patchy}}$ P-velocity after the patchy saturation model [m/s]

V_S S-velocity [m/s]

P_{pore} pore pressure [Pa]

P_c lithostatic or confining pressure [Pa]

P_{eff} effective pressure [Pa]

M P-wave modulus [Pa]

M_{frame} frame modulus [Pa]

M_{pore} pore space modulus [Pa]

$\mathcal{R}$ reflection coefficient [-]

α absorption coefficient [1/m]

Q quality factor [-]

k permeability [m^2, darcy]

Abbreviations

GSLS Generalised Standard Linear Solid

SAGD Steam Assisted Gravity Drainage

SFEM Spectral Finite Element Method

A note on mathematical notation

Vectors and matrices

Mathematical symbols for vectors and matrices as well as mathematical operations are handled quite flexibly later on. Therefore, a description of the various notations is provided first. A vector will be either written as a bold lower case letter, e.g., the displacement vector will be

$$\mathbf{s} = [s_1, s_2, s_3]^T \text{ or just } s_i.$$

Here, $s_i, i = 1, 2, 3$ are the three cartesian components of the vector. The superscript T denotes the transposed of a vector or a matrix.

In case of a column vector the index is written as a subscript whereas a superscript indicates a row vector.

Similarly, a matrix A is either written as a bold upper-case letter or in indicial notation as

$$\mathbf{A} = \begin{pmatrix} A_{11} & A_{12} & A_{13} \\ A_{21} & A_{22} & A_{23} \\ A_{31} & A_{32} & A_{33} \end{pmatrix} \text{ or just } A_{ij}.$$

Again, $i, j = 1, 2, 3$ is implicitly assumed for the indicial notation. There are some exeptions from this convention: for example, the elastic stiffness tensor will be a lower-case letter c, the stress tensor will be σ, and the strain tensor will be greek lower case epsilon ϵ.

Two different vector products will be used when deriving the finite element algorithm. The first product is the inner-product, which is written as

$$a = \mathbf{b}^T \cdot \mathbf{c} \text{ or } a = b^i c_i.$$

For the symbolic notation the inner product is indicated by the dot '·' between the two vectors. For the indicial notation the well-known Einstein summation convention applies, i.e. a summation for repeated indices must be performed. Then

$$a = b^i c_i = b_1 c_1 + b_2 c_2 + b_3 c_3.$$

The second vector product is the outer product, which in symbolic and indicial notation is

$$\mathbf{A} = \mathbf{a} \mathbf{b}^T \text{ or } A_{ij} = a_i b^j.$$

The product of a matrix and a vector in symbolic notation is

$$\mathbf{a} = \mathbf{A} \cdot \mathbf{b} \text{ or } a_i = A_{ij} b_j.$$

Again, the Einstein summation convention applies for the repeated index j.

In some equations a special tensor product will be employed, the *doubly contracted product* of two tensors. This product is written as $a = \mathbf{A} : \mathbf{B}$ in the symbolic notation or in indicial notation as $a = A_{ij} B_{ji}$. This product reduces the rank of the tensors by two. For example, the product of two tensors of rank two is a scalar.

Derivatives

Often, a comma notation will be used for derivatives. If an index appears in subscript after a comma then it indicates the derivative of the variable. For example, the divergence of a vector $\mathbf{u}$ can be written as $\partial_i u_i = u_{i,i}$. Derivative operators are written in the standard way using the Nabla (∇) operator, which is defined in cartesian coordinates as

$$\nabla = \left(\frac{\partial}{\partial x}, \frac{\partial}{\partial y}, \frac{\partial}{\partial z} \right)^T.$$

A gradient of a scalar is denoted by

$$\mathbf{a} = \nabla u \quad \text{or} \quad a_i = \partial_i u \quad \text{or} \quad a_i = u_{,i},$$

the gradient of a vector by

$$\mathbf{A} = \nabla \mathbf{u} \quad \text{or} \quad A_{ij} = \partial_j u_i \quad \text{or} \quad A_{ij} = u_{i,j},$$

and the divergence of a vector by

$$a = \nabla \cdot \mathbf{u} \quad \text{or} \quad a = \partial_i u_i \quad \text{or} \quad a = u_{i,i}.$$

Time derivatives are written in two different ways. First the traditional 'dot'-notation is employed. A dot above a variable indicates the first derivative with respect to time, two dots the second derivative. Alternatively, the comma notation applies as well, where the index t is reserved for the time derivative:

$$\frac{\partial u}{\partial t} = \dot{u} = u_{,t} \quad \text{and} \quad \frac{\partial^2 u}{\partial t^2} = \ddot{u} = u_{,tt}.$$

Preface

Within the discipline of geophysics, remotely probing the earth is a large area of study. Much of geophysical science deals with describing, interpreting, and understanding the subsurface structure of the earth that is not directly accessible. With exploration geophysics one attempts to image the earth's geological structure in order to especially discover potential natural hydrocarbon containing reservoirs.

During the last decade the potential of monitoring changes in the subsurface with geophysical methods has attracted increasing interest (e.g. *Greaves and Fulp*, 1987; *Nur*, 1989; *Lumley et al.*, 1997; *Lumley*, 2001). The essential concept is that changes in the earth can be detected with data sets repeatedly acquired from the same location. Possible applications are, among others, monitoring the changes in a oil or gas reservoir due to engineering actions (e.g. *Greaves and Fulp*, 1987; *Hare et al.*, 1999; *Watson et al.*, 2002), changes in magma chambers of volcanos or geysers (*Kieffer*, 1977; *Ito et al.*, 1979; *Gunasekera et al.*, 2003), and monitoring of fluid movements in hot-dry-rock (HDR) power plants (e.g. *Shapiro et al.*, 1999). All these applications are based on the idea that the fundamental physical properties of the earth change with time. For example, variations in the elastic parameters of the material will change the seismic response after the changes took place. Similarly, changes of the electric properties will be detectable by repeated resistivity measurements (e.g. recently *Ziolkowski et al.*, 2002) or density variations by gravity surveys.

The utilization of repeated seismic surveys for geophysical monitoring is often called *time-lapse* seismology or *4D seismic* in the context of 3D seismic imaging that is repeated with calender date.

Traditionally, seismic methods have been used in exploration geophysics to mostly provide structural images of the subsurface that may be interpreted to look for hydrocarbon resources. To a lesser degree they have also supplied information on the properties of

1

the earth via inversion of the seismic data. Such information could then be used to build geological models for various uses. In this traditional work flow, seismic information did not play an active role in reservoir management decision processes. A different situation exists today with the application of expensive and technically challenging enhanced oil recovery processes (EOR). Repeated seismic surveys can assist in observing production related changes in the reservoir and hence influencing reservoir management decisions.

This thesis considers such an application of seismic monitoring for heavy oil reservoirs, particularly the feasibility of seismic monitoring of heavy oil reservoirs produced with the help of the *steam-assisted gravity drainage* (SAGD, *Butler*, 1994) enhanced oil recovery method. This thesis has two complementary parts. First, the physical properties of a steam zone are estimated and the effects on the seismic response are modelled. Second, an advanced numerical scheme to calculate the propagation of seismic waves through complex geometries using a finite element based method is developed.

The following sections will briefly introduce the issues related to seismic monitoring of heavy oil reservoirs. This will include a more detailed description of the SAGD method. A discussion of various aspects regarding seismic monitoring and its role in reservoir management follows. As the numerical simulation of seismic waves is a second main focus in this work; a brief overview of numerical modelling is included in this chapter, with a more detailed description to follow subsequently.

Heavy oil reservoirs in Western Canada

The world's heavy oil and oil sand (bituminous) accumulations, that is, those containing hydrocarbons with densities larger than 900 kg/m^3 (equivalent to API specific gravity $\leq 21^{\circ 1}$), are becoming increasingly important. Global reserves are estimated to be approximately 2.5 trillion barrels (397 $\times 10^9$ m^3) of oil, an amount comparable to that for the remaining medium and light oils. The largest deposits are found in Canada and Venezuela, reservoirs in Russia and China also contain significant amounts of heavy oil.

---

[1]The American Petroleum Institute (API) defines the fluid density in terms of the *API gravity*, which is related to the *the specific gravity* of a fluid by

$$\text{API gravity} = \frac{141.5}{\text{specific gravity at } 60°F} - 131.5.$$
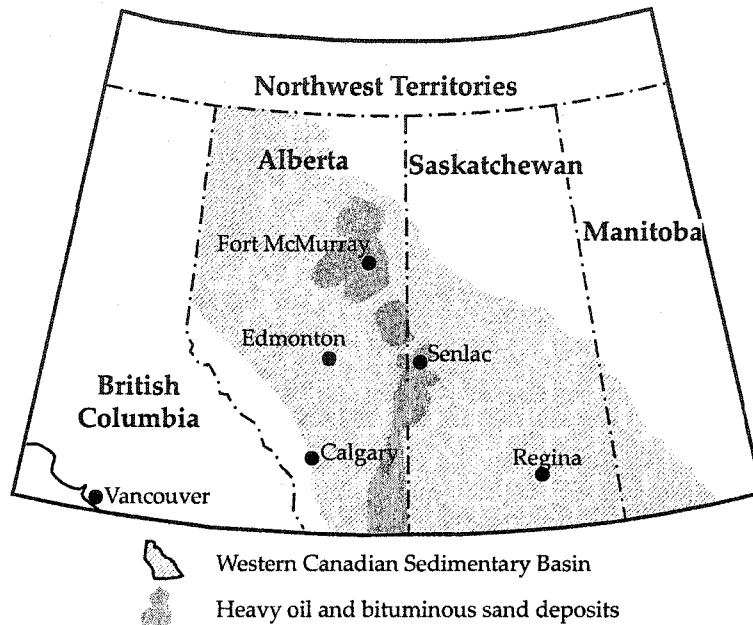
Figure 1: Map of the Western Canadian Sedimentary Basin with the areas containing the major heavy oil or bituminous sand reservoirs.

The heavy oil and bituminous reservoirs in Western Canada contain a significant fraction of these hydrocarbons. The largest known deposit is in the Athabasca oilsands of Alberta, which is believed to contain over 800 billion barrels (127×10^6 m^3) of oil in form of bitumen. There is little doubt that heavy oil reservoirs will play an increasing role in providing needed hydrocarbons in the future.

The heavy oil reservoirs in the Western Canadian Sedimentary Basin are large and shallow and are therefore relatively easily found. As such, seismic methods have not been widely applied in exploration, which has relied on shallow drilling and, more recently, electrical methods. The major reservoirs considered in this thesis are the Athabasca reservoir in North-Eastern Alberta, the Lloydminster reservoir complex extending from central to southern Alberta along the border between Alberta and Saskatchewan, and the Cold Lake reservoir located roughly between the two other (Figure 1). However, there are other reservoirs in Alberta and Saskatchewan storing a significant amount of heavy oil and bitumen (e.g. *National Energy Board*, 2001). The Peace River area also holds heavy

oil, some of which lie in carbonate zones.

Thermal enhanced oil recovery - the SAGD method

At typical in-situ temperatures ($T \lesssim 30°C$) and pressures ($P_{pore} \lesssim 5\,MPa$) for the Western Canadian Basin reservoirs heavy oils are essentially immobile due to their high viscosities, which are as great as 500 Pa·s. Therefore, heavy oils typically have not been a major target for conventional production; indeed, a large fraction of Canada's current bituminous oil is produced instead from active surface mining and processing of these deposits. However, the viscosity of these hydro-carbons decreases significantly when heated (Figure 2) and the heavy oils become mobile on timescales that make their production economic. New technical developments such as modern thermal recovery tech-
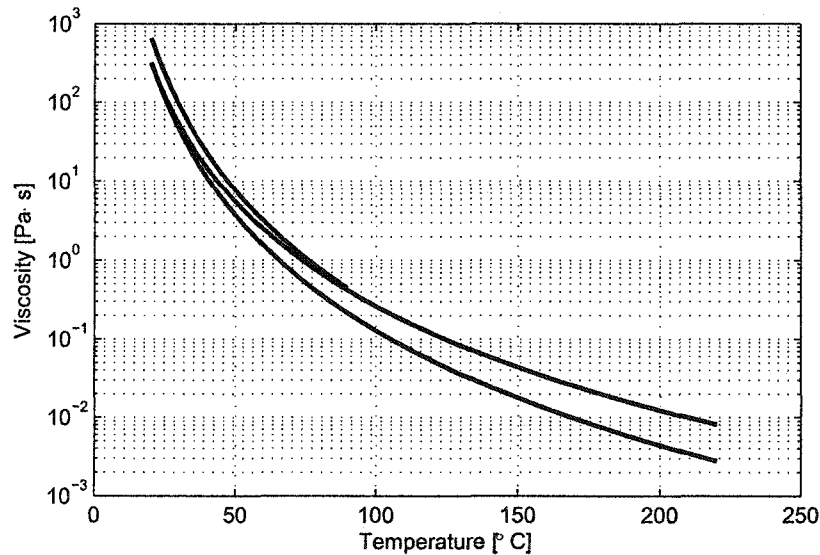
Figure 2: Dependence of heavy oil's viscosity on temperature based on data by *Ward and Clark* (1950), *Seyer and Gyte* (1989), and *Eastwood* (1993). The viscosity of some bituminous hydrocarbons found in the Athabasca reservoirs can be as high as $\eta = 10^3$ Pa· s at in situ temperature. For comparison: the viscosity of water under room condition is about $10^{-3}\,Pa \cdot s$.

4
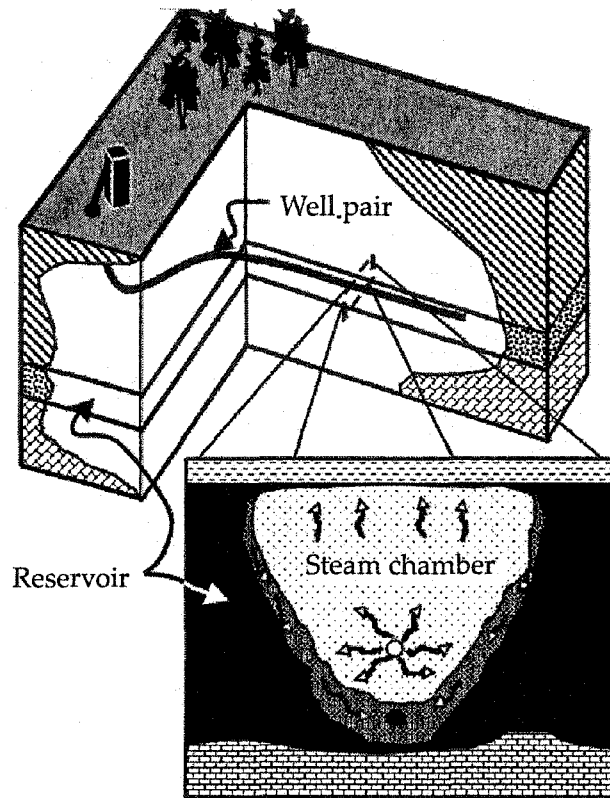
Figure 3: Schematic sketch of a SAGD process.

niques, particularly steam assisted gravity drainage (*Butler*, 1994)[2], now allow for the economic exploition of heavy oil reservoirs. During a SAGD program hot steam, typically in the temperature range between 120°C and 300°C, is injected into the reservoir from an upper horizontal wellbore (Figure 3). The principal idea of a SAGD-process is to establish a chamber of hot steam within the reservoir. Conduction of heat will then increase the temperature in the material immediately adjacent to the steam chamber, thereby melting and mobilising the bitumen. The difference in the densities of the steam and the heavy oil allows the latter to gravitationally drain to the bottom of the chamber. The hot steam replaces the displaced oil and comes in proximity to the cold formation

---

[2]Detailed information on the technique and mechanics of the SAGD process can be found in the literature (e.g., *Butler*, 1991, 1994; *Chalaturnyk*, 1996).

again. By progressively melting and displacing the oil the steam chamber grows upward and outward, as long as enough steam is available and the drained heavy oil is removed from the chamber through a lower horizontal well. Ideally, the pore space within the steam chamber is saturated by steam with just a small fraction of residual oil remaining.

Clearly, such processes are complicated and expensive. Many operational problems are likely to occur, particularly if portions of the reservoir are by-passed or steam is lost outside the reservoir. As such, remote monitoring of the changes within the reservoir is an increasingly important tool to assist in engineering decision processes. For example, by-passed sections within the reservoir are a production problem that can result from complexities in the geology or completion problems with horizontal well bores.

Numerical simulation of seismic surveys

Given the complexity of real world scenarios, the underlying physical principles of wave propagation can seldomly be analysed analytically. Instead, numerical techniques are employed when the geometry or heterogeneity of the problem do not allow for a determination of an analytical solution of fundamental partial differential equations.
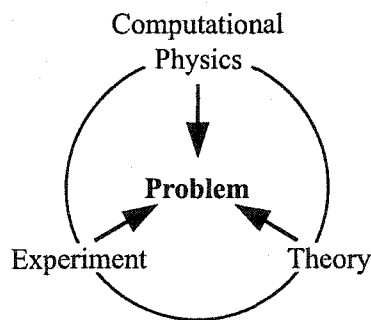
Figure 4: The three 'modern' approaches in physics to a problem.

Traditionally, problems in physics were only considered by either an experimental or an theoretical approach. Experimentalists describe the physical phenomena by empirical laws and large data sets. Theoreticians aim to express these empirical relationships in an analytical framework that in many cases require the use of partial differential equations. The exact mathematical solution of these equations is, however, restricted to only rather simple cases (e.g. homogeneous and isotropic situations and simple geometries). Therefore, a comprehensive description of real phenomena in complex situations is difficult to obtain. On the other hand, experimental methods are limited by the impossibility of measuring the quantities of interest at all locations for all times and circumstances. Therefore, a conceptual gap

exists in the traditional way of describing natural events. During the last decades with increasing computer resources a new branch of physics called *computational physics* has developed. Computational physics seeks to bridge the conceptual gap between experiment and theory. With a well-organised approach using all three branches, it is possible to narrow the ambiguities that arise from the complexity of a particular problem. However, numerical simulations can never fully represent real physical processes, as some simplifications need always to be assumed in the derivation of a numerical scheme. Nevertheless, such simulations can provide valuable insight into a physical problem.

In computational physics, the differential equations or their solutions are approximated in various ways. A key feature of these approximations is that the heterogeneity and anisotropy of the fundamental physical properties (e.g. the seismic velocities, density) may be incorporated within a model and realistically considered. Of course, the approximate solution is only close to the exact solution of the differential equation; and one has to take care that the numerical errors are minimized.

To ensure reliable results, a modelling technique must be developed with an eye towards various aspects such as accuracy, the proper implementation of boundary conditions, and, especially in simulations for seismic exploration, the ability to model complex surface topography and irregular subsurface interfaces. During the last three decades finite difference methods have been intensively used in geophysics to simulate wave propagation in heterogeneous and anisotropic media (e.g. *Alford et al.*, 1974; *Dablain*, 1986; *Kelly et al.*, 1976). In the eighties, this simulation technique was improved by the introduction of Fourier methods for the calculation of the derivatives (e.g. *Gazdag*, 1981; *Kosloff and Baysal*, 1982). Further improvements led to Pseudo-Spectral methods which use Chebychev polynomials to approximate a function and its partial derivatives (*Kosloff et al.*, 1990). All these algorithms can simulate the propagation of acoustic or elastic waves within the model more or less accurately. Unfortunately, finite difference and pseudo-spectral methods exhibit problems with the accurate implementation of appropriate boundary conditions and particularly with the free surface. In the case of high-order finite difference operators such problems are due to the operator length. The failure of the Fourier method to simulate the free surface can be explained by its periodic character (e.g. *Canuto et al.*, 1988; *Press et al.*, 1997). Pseudo-spectral methods allow a one-

dimensional approximation of the free-surface condition but it is still difficult to model all of the surface effects properly. Another common shortcoming of all these methods is that they require a uniform grid with a mesh of rectangular cells. This makes it almost impossible to properly incorporate surface topography or other complex features such as arbitrarily-shaped bodies embedded in the model.

Geometrically complex models can be modelled more easily with the finite element method because it offers greater flexibility in designing a computational model. Although *Bolt and Smith* (1976) used the finite element method to simulate wave propagation phenomena. Since then, this method has been seldom used for such purposes in the geophysical community. One reason for this may lie in the computational difficulty of implementing this technique. Another may be in its poor performance with regards to numerical dispersion performance as reported by *Marfurt* (1984). A significant improvement of the standard Finite Element Method was achieved with the introduction of the Spectral Element Method by *Patera* (1984). This technique allows for a very efficient suppression of numerical dispersion that is comparable to that of global spectral methods, while preserving the geometrical flexibility of the Finite Element Method.

In chapter 2 the standard numerical techniques and their practicability for simulating seismic surveys in geometrical complex environments are discussed in more detail.

Seismic monitoring

In seismic monitoring one tries to supply additional information to the reservoir management decision process. Before the rise of geophysical monitoring, seismic data were only used to assist in constructing the reservoir model, that is, in defining the size and shape of a potential reservoir and only seldomly its petro-physical properties (step A in Figure 5). This is commonly referred to as *development* geophysics. Once the reservoir model has been established, seismic data did not play any further active role. Reservoir management decisions were then made based on flow simulation and history matching techniques with measured mass balance and pressure data. However, such information is based on punctual and accurate well information and no information were available about the distribution of, for example, the saturation of oil or the pore pressure between
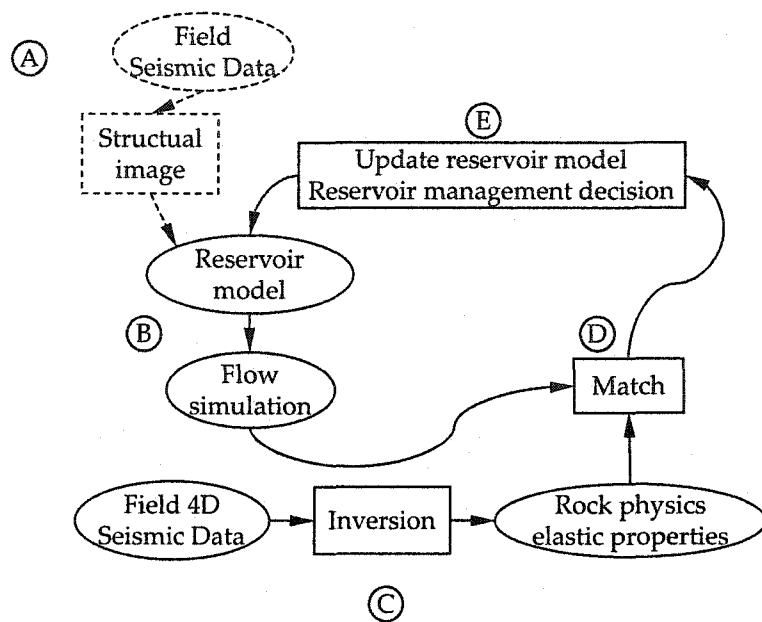
Figure 5: Possible workflow for seismic monitoring.

the wells. As well, production history matching usually relies on highly simplified assumptions and is generally not unique.

A different situation exists today. Seismic data are acquired not only at the initial stages of a reservoir's life, but repeatedly with time in order to supply additional constraints on what part of the reservoir is being produced and to provide data for the reservoir simulator. As before, an initial seismic survey assists in creating a preliminary reservoir model (step A in Figure 5). After the following flow simulation (step B) the lateral distribution of some effective elastic parameters of the reservoir or attributes are predicted for a later stage in the life of the reservoir. However, these results can often at best only be validated at the well locations. Seismic data, on the other hand, provide lateral information between wells. In such a case, the flow simulation can then be tested against a much larger amount of measured information. To incorporate such time-lapse data, the workflow shown in Figure 5 includes the inversion of seismic data for some elastic parameters in step C. The inverted data are then compared to a second data set calculated on the basis of the results of the reservoir simulation in step D. Depending

on the match the reservoir model needs either be updated (in case of a bad match) or reservoir management decisions can be drawn to further improve the production of the reservoir (step E). Note, that different workflows are possible (see for example *Lumley and Behrens,* 1998).

However, no guarantee exists that such a seismic monitoring program will be successful. Given the costs of repeated acquisition of seismic data the feasibility of time-lapse monitoring must be assessed before embarking an expensive field program. Issues that come to mind in the above workflow are:

- Are the expected changes in the reservoir large enough to be detected in seismic data?

- Given the possible survey parameters (e.g., frequency content of the seismic source): is the vertical and lateral resolution fine enough to be able to separate the changes from the background?

- Can the data be accurately inverted such that potential but subtle changes are preserved?

- Will the *signal-to-noise*-ratio be sufficiently small enough to ensure reliable inversion results?

- How accurately can elastic parameters be inferred from the field data? What are the uncertainties of the parameters inverted for?

As time-lapse seismology is a young field most of these issues have not yet been resolved. This thesis reports work done to address the first two questions. The feasibility of seismic monitoring is investigated by a rock-physical study that simulates the steam-assisted gravity drainage process. The resolution question is addressed by two-dimensional Finite element simulations of elastic waves for simplified geological models representing reservoirs subjected to SAGD programs.

Scope of the thesis

Chapter 1 - Introduction to rock-physics

The purpose of this chapter to introduce fundamental concepts of rock-physics and the propagation of waves within the earth. Various rock-physical and mathematical models are discussed and evaluated for their later use in the research for this thesis. In particular, the variation of seismic parameters such as density, wave-velocities, and dispersion as a tool for reservoir characterization are discussed in detail. The second aspect covered in this chapter is a review of the standard mathematical models commonly used, which are the acoustic, elastic, poro-elastic, and visco-elastic wave equations.

Chapter 2 - Application of the high-order Finite Element Method to the elastic wave equation

In this chapter the formulation of the spectral finite element solution to the two-dimensional elastic wave equation is derived. The potential, advantages, and short-comings of this method are compared to other numerical techniques. Furthermore, current problems are addressed and possible directions for future work are outlined at the end of this chapter.

Chapter 3 - A rock-physical feasibility study for seismic monitoring of steam floods

An extensive rock-physical study has been carried out to assess the feasibility of seismic monitoring of SAGD-processes for two particular heavy oil reservoirs in the Western Canadian sedimentary basin. The feasibility itself is estimated by analysing the change in three seismic attributes that are often used in the analysis or interpretation of seismic data. Although these reservoirs are geologically similar, the time-lapse seismic response of these reservoirs differs significantly. Based on fluid-substitution modelling the different behaviour of these reservoirs can be explained in terms of rock physics. The investigated work-flow for estimating the feasibility of seismic monitoring can be an important tool in planning seismic monitoring programs.

Chapter 4 - Spectral finite element simulation of time-lapse seismic surveys for SAGD programs

The results of the two previous chapters are combined in simulations of elastic waves for different simple reservoir models to extend the feasibility study of the previous chapter and to investigate the resolution problem. At the moment these simulations are rather preliminary; however, useful insight is gained.

Chapter 1

Introduction

Seismology deals with the propagation of waves through the body and along the surface of the earth. These waves can originate from natural sources (for example earthquakes) or artificial sources such as accelerated weight drops, seismic vibrators, or controlled detonations ranging from some tons of dynamite to nuclear explosions. The aim of applied seismology is to learn more about the local structure of the earth. While earthquake and teleseismic seismology is more applicable to the global structure of the earth, applied seismology rather deals with imaging and characterising of a small part of the earth (usually of a volume in the range of a few km^3). The work presented here deals with the latter application of seismic methods.

In the past, seismic surveys have dominantly been used to obtain two and three-dimensional images of the structure of the earth. During the last decade there has been an increasing interest in using seismic data to monitor changes with time in the subsurface. These so-called time-lapse or 4D surveys have been proven to be especially useful in remotely monitoring of oil production and enhanced oil recovery processes.

The propagation of seismic waves through the earth depends on the distribution of the seismic velocities in the medium. These velocities are directly related to the elastic constants and densities of the medium. Basically, there are two different types of waves propagating through the earth, the *primary P*-wave (a compressional or longitudinal wave) and the *secondary S*-wave (a transverse wave), which are distinguished on the basis of their propagation velocity and polarisation.

The earth is a composite of solids and fluids. The densities and seismic velocities

13

within the earth depend on many factors, the most important of which is the overall composition. If for example the pore space of a rock is initially filled with oil, and in the course of production this oil is replaced by water, both the density and the effective elastic parameters will change, and the seismic velocities must also change accordingly. Repeated seismic surveys can be used to infer the production-state of a reservoir from data recorded at the surface or within the earth via the evolution of the overall seismic response.

Other characteristics of wave propagation through the earth also have the potential of providing additional information about the *in-situ* conditions. Seismic attenuation for example is one of such aspects of wave propagation. In real rocks, seismic energy is irreversibly converted into heat due to a variety of inelastic processes. This absorption of energy results in both attenuation of the wave energy and dispersion of the waves. From model calculations it is known that amplitude attenuation and wave dispersion are greatly affected by enhanced oil recovery processes (e.g. *Dilay and Eastwood*, 1995; *Boadu*, 2000). This is especially true for processes when heat in form of hot steam is injected into the reservoir. The variation in attenuation and wave dispersion with time can be mainly attributed to the changes of the pore fluid, so that the analysis of attenuation and dispersion can be used to infer the properties and the distribution of the fluids filling the pores.

1.1 The rock physical basis for seismic monitoring

The heavy oils in the Western Canadian Sedimentary basin are characterised by both high density and viscosity, because they are composed of many long hydrocarbon molecule chains. The density of the heavy oils is about 10° to 13° API (equivalent to density range of 975 to 1000 kg/m^3). Its viscosity at reservoir temperature of approximately 20°C is in the range of 10,000 to 60,000 mPa·s (cP) (*Ward and Clark*, 1950; *Becki and McIntosh*, 1988; *Seyer and Gyte*, 1989; *Eastwood*, 1993). The high viscosity makes the oil essentially immobile in such low temperature environments. For successful production, heavy oil requires a high grade reservoir in which the porosity of the rock exceeds thirty percent and the permeability k is larger than 4 Darcies ($4 \times 10^{-12}\,m^2$) for the oil to flow naturally.

Even at such high porosities, heavy oil does not flow easily enough through the reservoir for conventional oil extraction methods (such as creating a negative pressure gradient towards the producing well) to be economical. Consequently, enhanced methods like steam or solvent injection have to be used. The purpose of these methods is to either decrease the viscosity of the oil (steam injection) or to displace the oil in the pore space with the injected fluid and push the oil towards a producing well. A special form of steam flooding is the steam assisted gravity drainage (SAGD, *Butler*, 1994), which allows a higher oil recovery than conventional steam flooding processes (*Chalaturnyk*, 1996).

By injecting steam into the reservoir the physical properties of the porous rock and the pore fluids are changed in various ways due to the new extrinsic temperature and pressure conditions, and varied pore fluid compositions. For the propagation of seismic waves and their interpretation with respect to changes in a reservoir the important parameters are the elastic and viscous moduli as well as the density of the porous medium and the saturating pore fluid. These parameters determine the velocities of the seismic waves and the amount of absorbed mechanical energy that is irreversibly transformed into heat. In the following sections, the effects of temperature, pressure, and pore fluid variations on the seismic velocities and wave attenuation are discussed. The important changes of the physical properties with time will take place in isotropic sand reservoirs only; elastic isotropy is therefore assumed throughout this thesis for the clarity and simplicity. Additionally, there are no information available about possible anisotropy in the reservoirs rock matrices of interest. Each section also explains how these effects can help to detect changes in the earth.

Seismic velocities basically depend on the elastic moduli and the density of the medium. There are two different wave modes propagating through solid material. The first mode is a compressional wave, which is referred to as the P-wave. The second wave type describes a propagating shearing of an elastic solid. This wave type is called the S-wave. In an isotropic and homogeneous material the P-wave velocity depends on the bulk (K) and shear (μ) modulus of the material and on its density (ρ). The P-wave is related to these properties by (e.g. *Lay and Wallace*, 1995)

$$V_P = \sqrt{\frac{K + 4/3\mu}{\rho}}. \tag{1.1}$$

15

The velocity of the second wave type is defined by

$$V_S = \sqrt{\frac{\mu}{\rho}}. \tag{1.2}$$

For a composite material such as a saturated porous medium the elastic moduli and the density depend on numerous factors. Effective media models are used to account for these factors in the calculation of the velocities. *Gassmann* (1951) developed a widely employed theory to calculate the effective bulk modulus K_{eff}. This theory assumes that the porous media consists of one solid material, has a uniform porosity ϕ, and is saturated by a single component pore fluid that does not resist shear motion.

The effective bulk modulus K_{eff} depends on the bulk modulus of the solid material, K_S, the bulk modulus of the fluid, K_f, the bulk modulus of the rock matrix frame, K_d, and the porosity ϕ. To derive an expression for the effective bulk modulus Gassmann assumed a quasi-static (or zero/low frequency) case. The effective bulk modulus K_{eff} is then given by

$$K_{eff} = K_d + \frac{(1 - K_d/K_s)^2}{(1 - K_d/K_s - \phi)/K_s + \phi/K_f}. \tag{1.3}$$

The advantage of Gassmann's equation is that it attempts to approach the porous structure not only by volumetric proportions as, for example, the Voigt and Reuss averages do (e.g. *Watt et al.*, 1976), but also by the stiffness of the frame. Therefore, the degree of elastic consolidation of the material, that is the compressibility of the frame, can be taken into consideration. Another assumption in Gassmann's work is that the effective shear modulus is independent of the saturating pore fluid. This implies that changes in the pore fluid affect the shear wave velocity only by the bulk density. The effective shear modulus, μ_{eff}, is equal to the shear modulus of the frame, μ_d,

$$\mu_{eff} = \mu_d. \tag{1.4}$$

In real situations the pore space is filled not only with a single fluid but with a mixture of gas, water, and oil. Wood's formula (e.g. *Batzle and Wang*, 1992) provides a possibility to calculate an effective bulk modulus from the individual properties of the fluid's component:

$$\frac{1}{K_f} = \sum_i \frac{S_i}{K_{f_i}}. \tag{1.5}$$

The fractional weighting factor S_i is the saturation of the fluid component i, and K_i is its bulk modulus.

To determine the effective or bulk density a volume averaging approach is employed:

$$\rho = (1 - \phi)\rho_f + \phi\rho_s. \tag{1.6}$$

The densities of the fluid and the solid are denoted by ρ_f and ρ_s, respectively. However, if the pore fluid is a mixture of several fluids its density can be calculated by the weighted sum

$$\rho_{fluid} = \sum_i S_i\rho_i, \tag{1.7}$$

in which the weighting factor S_i is the saturation of the ith component and ρ_i is its density.

When using Gassmann's model some care must be taken as it does not account for heterogeneous distribution of the fluids. The theory developed by *Mavko and Mukerji* (1998) and *Dvorkin et al.* (1999) considers a *patchy saturation* within the pore space and reveals that there can be significant differences in the P-velocity. These differences are discussed in chapter 3; for the sake of simplicity only Gassmann's model will be used in the following illustrative discussions.

1.1.1 Velocity variations as a result of different pore fluids

The Gassmann equation can be used to predict the saturating pore fluid dependent changes of the compressional and shear wave velocities. By replacing the fluid bulk modulus and density with the values of oil, water, or an weighted mixture, the velocity of the composite material can be calculated. Figure 1.1 shows the P-wave velocity as a function of porosity ϕ and water saturation S_W. The following bulk moduli were used: the bulk modulus of the solid material $K_S = 36.0$ GPa, the frame bulk modulus $K_d = 8.2$ GPa, the shear frame modulus $\mu_d = 4.2$ GPa, and the moduli of the liquids were $K_{Oil} = 2.0$ GPa and $K_{Water} = 2.2$ GPa; and the density of the solid material, the oil, and the water were $\rho_S = 2650$ kg/m^3, $\rho_{Oil} = 800$ kg/m^3, and $\rho_{Water} = 1000$ kg/m^3, respectively.

As the porosity increases from 0.1 to 0.35 the velocity decreases by about 300 m/s. For seismic monitoring of enhanced oil recovery purposes the change of the seismic velocity with variation in the oil saturation is more important in the 'water-flooding' example

17
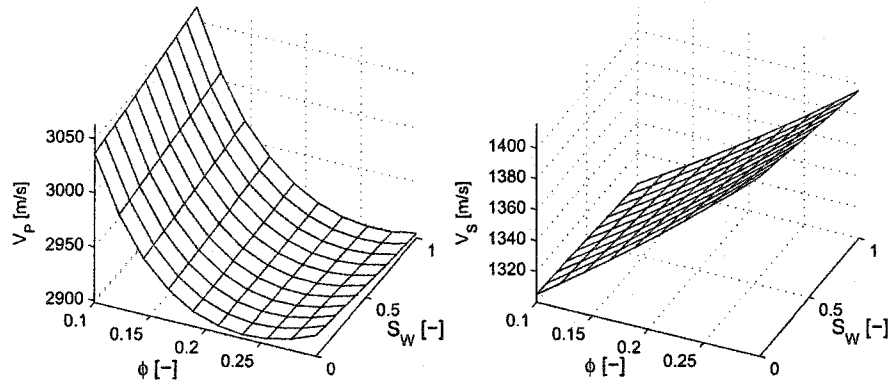
Figure 1.1: Velocity variations of the compressional and shear waves as a function of porosity ϕ and water saturation S_W according to Gassmann's equation.

considered here. If all oil in the pore space is replaced by water the velocity decreases. For highly porous environments, as for example an unconsolidated sand with porosities exceeding thirty percent, the change in the P-wave velocity can easily be inferred from seismic data (*Batzle and Wang*, 1992). Similar calculations show that the S-wave velocity depends only weakly on the pore fluid (Figure 1.1). The changes in the velocity are solely due to variation of the effective density, as the Gassmann model assumes that the S-velocity does not depend on the elastic parameters of the pore fluid (e.g., equation 1.4).

1.1.2 Temperature effects on seismic velocities

Temperature dependent variations in seismic velocities are mainly due to changes of the elastic bulk modulus and density of the pore fluid. The experimental results of *Eastwood* (1993) suggest that the effects of temperature on the elastic moduli of the unsaturated rock matrix can be neglected relative to the much larger effects on the pore fluids. The dominance of the temperature dependent pore fluid properties is also evident from the similar behaviour of the pore fluid velocity with temperature and that of the saturated porous medium. For example, the compressional velocity of an oil sand saturated with bitumen of the Cold Lake area decreases by about 15 percent when it is heated from $T= 22°C$ to $T= 127°C$ (*Eastwood*, 1993). Separate measurements of the seismic velocities

of the bitumen and the dry (air saturated) sand show that the former velocity decreases by approximately 30 percent when the temperature increases. The velocity of the dry sand sample, however, decreases only by two percent. Studies by *Wang and Nur* (1988), *Wang and Nur* (1990), *Wang et al.* (1991), and *Batzle and Wang* (1992) on the temperature dependence of seismic velocities show a similar decrease of the velocities of oil and reservoir rock matrix, respectively.

Increasing temperature causes the compressional velocity to decrease significantly; this is due to the decreasing bulk modulus of the pore fluid. On the other hand, the shear wave velocity decreases only slightly with increasing temperature (*Timur*, 1977; *Eastwood*, 1993). This is not in agreement with Gassmann's theory, which predicts an increase of the S-wave velocity. This is because the density decreases as temperature increases, and theoretically, the effective shear modulus neither depends on the pore fluid nor on temperature. However, it is not clearly stated in *Timur* (1977) nor *Eastwood* (1993) whether the effective pressure during the measurements remained constant. A possible explanation of the observed decrease in the S-wave velocity could be that while heating an oil saturated sample the pore pressure will change due to the relatively large thermal expansion of such fluids and, to a lesser extent, the solid material. An increasing pore pressure can reduce the shear frame modulus of a rock and consequently the S-wave velocity. The pressure effects on seismic velocities are discussed in more detail in the following section and especially in section 3.5.4.

The published data of temperature dependent velocities of reservoir rocks and sands, respectively, suggest that the temperature effect on the rock matrix can be neglected in the calculation of the saturated seismic velocity. Due to the lack of experimental data of the temperature dependence of the oil's properties for the Lloydminster reservoir the results published by *Eastwood* (1993) will be used to calculate the temperature dependent bulk modulus and density of the oil. These data can be approximated by the following linear relationships (the effective pressure during these measurements was $P_{eff} = 0.1$ MPa):

- the oil's acoustic velocity by
  $$V_P \, [m/s] = 1673.3 - 4.19 \cdot T \, [^\circ C],$$
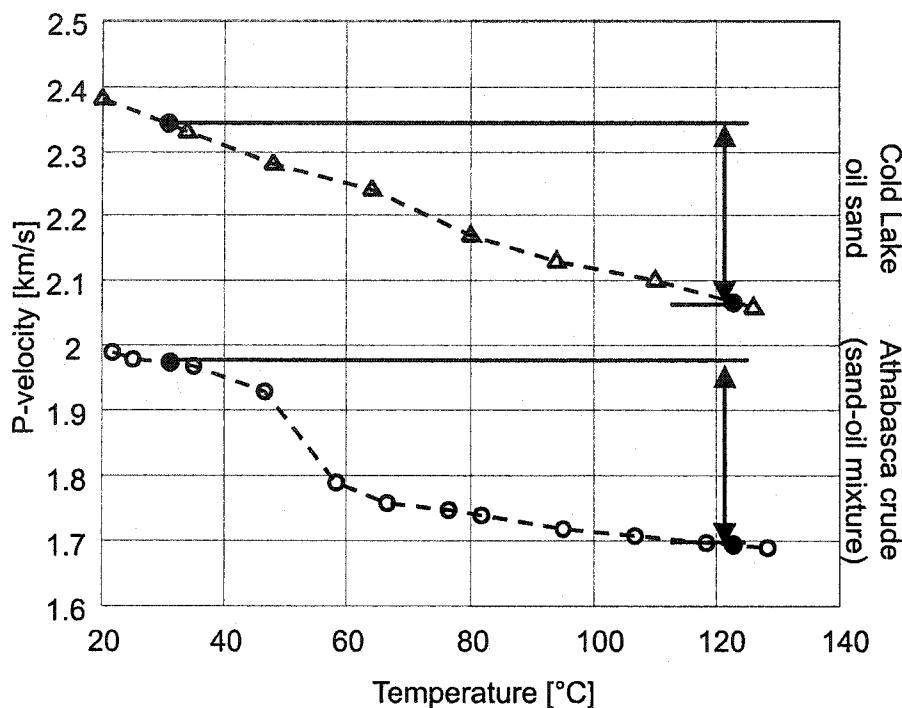
Figure 1.2: The P-velocity of a sand sample saturated with heavy oil decreases significantly when heated. The top curve has been measured by *Eastwood* (1993) for a Cold Lake reservoir sample (P_{eff}=5 MPa), the second data set was taken from *Wang and Nur* (1988), who analysed a sample from the Athabasca reservoir (P_{eff}=4 MPa).

- the density as a function of temperature

$$\rho\,[kg/m^3] = 1007.2 - 0.6111 \cdot T\,[^\circ C],$$

- the bulk modulus of the fluid

$$K\,[GPa] = 2.1667 - 0.0083 \cdot T\,[^\circ C].$$

The linear relationships are based on temperature data that cover the range from 20°C to 127°C. However, as long as the state of the fluid is removed from any phase boundaries, these linear approximations of the dependence of the velocities, densities, and moduli on pressure and temperature appears to work well (*Batzle and Wang*, 1992).

Figure 1.2 shows the decrease of the seismic velocity of two different samples saturated with hydro-carbons when heated. The first sample is from a Cold Lake, Alberta,

reservoir. The velocity decreases nearly linearly over the temperature range. The second sample from an Athabasca reservoir, however, shows a significant drop in the velocity at approximately 50°C. This sudden decrease is possibly due to a bitumen having a finite shear modulus at sufficient low temperature (*Hornby and Murphy*, 1987; *Wang and Nur*, 1988). At this particular temperature the oil 'melts' losing its rigidity, resulting in this substantial decrease of the effective *P*-velocity in the sample. In either case the velocity decreases by approximately 300 m/s over the temperature interval from 20°C to 120°C.

The temperature effect on the effective seismic velocities is mainly due to variations of the fluid properties. When using Gassmann's equation (1.3) and the volume averaging method for the density (equation 1.6) to determine the effective properties required in equation (1.1), one assumes that the temperature induced variations of the solid properties are negligible. However, temperature has certainly an effect on the density and elasticity of the solid material due to, for example, thermal expansion and elastic weakening. Additionally, the porosity may decrease with increasing temperature (*Chalaturnyk*, 1996). On the other hand, it is generally assumed that these effects influence the bulk properties only marginally when compared to the changes of the liquid phase (*Eastwood*, 1993).

1.1.3 Effective pressure effects on the seismic velocities

Pressure affects seismic velocities through different mechanisms. Temperature effects are dominantly caused by thermally induced variations of the fluid properties, whereas the pressure dependence of the velocities is mostly to changes in the compressibility of the rock frame (e.g. *Eastwood*, 1993; *Batzle and Wang*, 1992).

Generally, there are two different pressures that need to be taken into consideration when investigating pressure effects on seismic velocities. The first pressure is called the *confining* pressure P_c, a term that is commonly used when dealing with laboratory measurements, or *lithostatic* pressure P_l, which describes the pressure imposed on a 'buried rock sample' by the overburden. The lithostatic pressure at depth z is usually found by integrating density well log data,

$$P_c(z) = \int_0^z \rho(\xi) g \, d\xi.$$

21

However, it would be more accurately to describe the rock as subjected to the full state of 3D stress, which requires the knowledge of the three principal stress magnitudes and directions. These parameters are difficult to determine *in-situ* (*Brudy*, 1995; *Huber et al.*, 1997), and a 'hydrostatic stress state' (described by the above integral) is assumed to be adequate for the present discussion.

The second pressure is that of the pore fluid enclosed in the rock. This pressure is called the *pore* pressure P_{pore}. It is the difference of these two pressures called the *effective* or *differential* pressure that determines the pressure dependance of the seismic velocities:

$$P_{eff} = P_c - P_{pore}.$$

Published data of the velocity variations show that the velocities of porous media increase at higher effective pressures (e.g. *King*, 1966; *Christensen*, 1985; *Christensen and Wang*, 1985; *Han et al.*, 1986; *Eberhart-Phillips et al.*, 1989). The standard explanation for this behaviour is that pores, particular large aspect ratio micro-cracks, close at higher pressures. This compaction increases the effective stiffness of the rock and subsequently the velocity. Once all the cracks and pores are closed, the velocity increases only slightly with increasing pressure due to the much slower increase of the bulk modulus of the minerals.

Within the framework of Gassmann's equation (1.3) the pressure effects on the seismic velocities can be described through pressure dependent variations of the frame bulk modulus K_d. The frame bulk modulus describes the stiffness of a porous material, which in many cases depends on the nature of the grain contacts. In well-consolidated sedimentary rocks the individual grains are cemented to each other resulting in a relative high resistance against external stresses; the material is stiff. On the other hand, in unconsolidated sands the grains can more easily move along and past each other. Therefore, the rock frame is more compressible and the deformation due to an external stress is larger than in consolidated rocks. This can also result in a change in the porosity ϕ of the rock and consequently in the seismic velocities.

There is not much available data published on the elastic frame properties for unconsolidated sands and on their variation with pressure. Such measurements are complicated particularly in unconsolidated sands by non-linear elasticity, strong hysteresis, and

time dependent effects (e.g. *Gardner et al.*, 1965; *Christensen and Wang*, 1985). Several theoretical and semi-empirical models have been proposed to relate the elastic frame properties to other marcoscopic parameters that are more easily determined. For example, *Murphy et al.* (1993) and *Nolen-Hoeksma* (1993) suggested linear relationships between the frame bulk (K_d) and shear (μ_d) moduli to the corresponding moduli of the solid material (K_s and μ_s, respectively) with dependance on porosity ϕ according to

$$K_d \approx K_s(1 - 2.5\phi), \tag{1.8a}$$

$$\mu_d \approx \mu_s(1 - 2.5\phi). \tag{1.8b}$$

Murphy et al. (1993) derived these equations by fitting a straight line to numerous measurements of the bulk frame modulus on gas saturated rock samples at different porosities. *Nolen-Hoeksma* (1993) derived basically the same relationships from considering consolidation of mineral grains. His work results in

$$K_d \approx K_s(1 - \phi/\phi_0), \tag{1.9a}$$

$$\mu_d \approx \mu_s(1 - \phi/\phi_0), \tag{1.9b}$$

where ϕ_0 is the *precompaction* (*Nolen-Hoeksma*, 1993) or *critical* porosity (*Nur*, 1992; *Nur et al.*, 1998), which marks the transition from a loose arrangement of grains to a strong stress-bearing framework of the rock matrix. This porosity is in the range of $0.36 \leq \phi_0 \leq 0.40$ (*Nolen-Hoeksma*, 1993) for sands and sandstones. Using the upper limit of ϕ_0 in equations (1.9) one obtains the relationships experimentally determined by *Murphy et al.* (1993).

The relationships by *Murphy et al.* (1993, equation 1.8) predict a constant ratio of the bulk to shear frame modulus, which for a rock consisting of quartz minerals is equal to 0.9. On the other hand, the substantial scatter in the values of elastic frame properties observed by *Spencer et al.* (1994) suggest that there is no unique relationship between the elastic frame properties and other macroscopic parameters such as the mineral moduli and porosity; this contradicts the observations by *Murphy et al.* (1993) and *Wang* (2000b). In the analysis presented in chapter 3 the elastic frame properties will be inferred from well log data under the assumption that Gassmann's equation holds. Unfortunately, this technique can not supply information on the pressure dependence of this frame moduli.

Instead, general trends for the velocity variation with effective pressure will be employed to *estimate* the impact of changes in the effective pressure in the reservoirs studied (section 3.5.4).

1.1.4 Attenuation and dispersion variation related to temperature and pore fluid composition

When a seismic wave propagates through real media, wave energy is irreversibly converted into heat. This energy absorption can be caused by different effects such as inelasticity of the rock matrix, induced fluid flow within the porous medium, and scattering of seismic energy at cracks and fractures in the solid material. The latter mechanism is sometimes referred to as elastic attenuation to distinguish it from intrinsic attenuation, which includes the first two classes of absorption.

To introduce the effects of absorption of seismic wave energy consider the propagation of a compressive plane wave $\mathcal{P}(x,t)$ propagating in an absorptive medium. The amplitude of this wave at distance x and time t is given by

$$\mathcal{P}(x,t) = \mathcal{P}_o e^{-\alpha x} \cdot e^{i(\omega t - k \cdot x)}, \tag{1.10}$$

where $\mathcal{P}_o$ is a reference amplitude (say at $x = 0$ and $t = 0$), ω is the angular frequency, and k is the wave number. The factor α occurring in the first exponential term is called the *absorption coefficient*. Its value is a measure of the attenuation, it is defined as the inverse of the distance d at which the amplitude of the wave has decreased to a fraction $1/e$. Other common quantities describe the attenuation as well: the quality factor Q and its inverse, the dissipation factor Q^{-1}. The quality factor Q gives the number of wavelengths a wave must propagate in an absorptive medium until its energy decreases by a factor of $e^{-\pi}$. It is also the ratio of the energy stored to that dissipated during one cycle. In the case of low losses (e.g. $Q \gg 1$) the quality factor is related to the absorption coefficient α, the phase velocity $v(\omega)$, and the frequency ω by (*Johnston and Toksöz*, 1981)

$$Q(\omega) = \frac{\omega}{2\alpha v(\omega)}. \tag{1.11}$$

As the quality factor depends on the frequency according to the above equation the absorption coefficient is also dependent on the frequency.
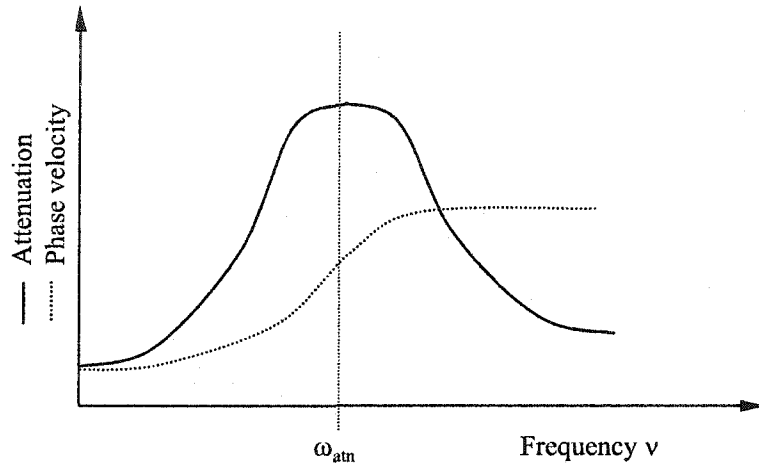
Figure 1.3: Qualitative dispersion relationship $V(\omega)$ and attenuation $Q(\omega)$ as a function of frequency ν.

Furthermore, if the medium is absorptive it must also be dispersive; i.e. the propagation velocity of a phase depends on the frequency. Velocity dispersion and attenuation are not independent from one another but related through the Kramers-Krönig relationship (*Futtermann*, 1962). This implies that the knowledge of the quality factor describes the attenuation and velocity dispersion characteristics of a given medium completely. Figure 1.3 shows qualitatively the typical dependence of the inverse quality factor (i.e. the attenuation) and the phase velocity as functions of frequency. The attenuation first increases with frequency until it reaches its maximum at the peak frequency ω_{atn}. Then the attenuation decreases again with increasing frequency. The phase velocity increases over the entire frequency range with the largest change occurring over the width of the attenuation peak.

Numerous processes can cause the attenuation of wave amplitude. The total attenuation acting on the passing seismic wave can be considered as a superposition of all those processes. In saturated porous materials, experimental observations indicate that attenuation is related to (*Johnston et al.*, 1979):

1. **Solid frictional losses** - The propagating seismic wave induces displacements between grains and cracks. The friction involved in this relative motion dissipates

25

some of the wave's energy. The absorption depends linearly on frequency and the Q-factor is therefore frequency independent. A constant Q is commonly observed in dry sandstones within the seismic frequency bandwidth (e.g. *Kjartansson*, 1979; *Toksöz et al.*, 1979; *Johnston et al.*, 1979). The quality factor for shear waves is slightly larger than for compressional waves in dry, air saturated, rocks. The opposite is true if the rock is saturated with a liquid. As this absorption process is caused by the relative motion of grains it depends substantially on the effective pressure (*Toksöz et al.*, 1979; *Fjær et al.*, 1992): if the pressure increases the grains are pressed together and their relative motion is reduced. The attenuation due to grain friction decreases with increasing pressure.

There are, however, two problems with this attenuation mechanism. The strain amplitudes of seismic waves are too small to cause sufficient grain motion to produce reasonable attenuation (*Savage*, 1969). Additionally, solid friction should also result in nonlinear wave propagation (*Winkler and Nur*, 1982). This has only been observed at high strain amplitudes, for the low strains of seismic waves available data indicate that the attenuation is for practical purposes a linear process. Frictional sliding cannot explain the theoretical prediction of constant Q attenuation, particular in wet rocks.

2. **Biot fluid losses** - Pore fluids are accelerated within the pore space by a passing seismic wave. The motion of the fluid relative to the solid material causes friction and converts energy irreversibly into heat. A theoretical description of this phenomenon has been developed by *Biot* (1956a,b, 1962). This absorption mechanism depends strongly on the viscosity of the pore fluid η, its density ρ_f and the average pore size d'. As will be shown in a subsequent section the peak of the attenuation occurs at a frequency ω_{atn}, which is defined as (*Johnson*, 1984)

$$\omega_{atn} = \frac{2\eta}{\rho_f d'^2}$$

The peak frequency of the attenuation depends strongly on temperature via the viscosity of the pore fluid. However, calculations demonstrate that the attenuation peaks according to this theory will occur at high frequencies ($10^7 - 10^9$ Hz) and

26

as such are not an important attenuation mechanism for seismic waves (10 Hz$\leq$ $f_{seismic} \leq$ 500 Hz) and sonic logs (1000 Hz$\leq$ $f_{sonic} \leq 10^4$ Hz).

3. **Losses due to local fluid flow** - The previous absorption mechanism assumes that the fluid is only accelerated globally in the direction parallel to the propagation direction of the wave. In partially saturated rocks (but also in fully saturated rocks, although less pronounced) the passing seismic wave may also induce a 'radial' fluid flow. This fluid flow is due the to compression and dilatation of cracks. Fluid contained in such pores will be forced to flow out of the crack into rounder and hence stiffer pores. This local flow leads to a relaxation attenuation that also peaks at a certain frequency, which in this case depends inversely on the fluid's viscosity (e.g. *Dvorkin and Nur*, 1993). This peak frequency is normally close to the seismic frequency range. The inelastic effects due to local fluid flow are therefore more likely to affect seismic waves than losses due to Biot flow. Thus, this absorption mechanism potentially provides more information about the inelastic properties of the earth that can be inferred from seismic data.

   If the pressure increases this contribution to the overall attenuation decreases. This is because at higher pressures small cracks close and cannot any longer contribute to the local flow.

   Phenomenological and theoretical investigations of this attenuation mechanism has been published by *O'Connell and Budiansky* (1977); *Palmer and Traviolia* (1980); *Jones* (1986); *Dvorkin et al.* (1995, 1994); *Dvorkin and Nur* (1993); *Parra* (1997, 2000); *Parra and Xu* (1994);*Diallo* (2000); and *Diallo and Appel* (2000).

4. **Rayleigh scattering.** - When a seismic wave passes a crack or a fracture, scattering of the wave energy is caused due to the contrast in the seismic properties of the solid material and the fluid-filled crack. The effect is stronger in dry than in saturated rocks, decreases with increasing pressure and is proportional to the 4th power of frequency. However, this effect is only important for higher frequencies (*Fjær et al.*, 1992).

   Strictly speaking this effect is not due to the inelasticity of the rock matrix but an elastic effect. This differs from the other cases discussed in that the mechanical en-

ergy is globally preserved during a scattering process but the forward propagating pulse will have diminished energy.

5. **Reflections from thin (cyclic) layers.** - Lastly, the shape of the reflected wavelet is also influenced by *partial* reflections at thin layers. Dependent on the wavelength component the shorter wavelength 'see' the layer and loose some of their energy due to reflection, whereas longer wavelength are not affected by the thin layers. The amplitude spectrum of the recorded wavelet will therefore exhibit a 'notch'. Like Rayleigh scattering, this effect is not caused by intrinsic inelasticity. Globally, the original energy carried by the wavelet is conserved.

An example of this process can be found in *Martínez* (2002), who analyzed this problem of partial reflection at a thin coal seam in the Western Canadian Sedimentary Basin.

Other processes causing attenuation such as the motion of defects in mineral grains are ignored here, as they are expected to be important only at high temperatures.

The frequency dependence of these absorption mechanism is illustrated in Figure 1.4 (after *Johnston et al.*, 1979). The graph shows an example for a sandstone at two different pressures, thereby showing that the attenuation due to friction and squirt flow depend on the pressure. Biot flow and scattering are not visibly affected by the change in pressure.

For seismic monitoring of thermally enhanced oil recovery programs (such as SAGD) the attenuation mechanism due to fluid flow are the most interesting. The losses due to local fluid flow depend strongly on the viscosity of the pore fluid, which is greatly affected by the pore fluid composition and the temperature.

Experimental result show that the viscosity of heavy oil decreases by several orders of magnitude if the temperature is increased to about 200°C (*Ward and Clark*, 1950; *Seyer and Gyte*, 1989; *Eastwood*, 1993). The data shown in Figure 2 (page 4) shows an average of the viscosity values measured at various temperatures. An average viscosity-temperature relationship for heavy oils in Alberta has been published by *Seyer and Gyte* (1989). *Eastwood* (1993) specifically analysed the properties of bitumen from the Cold Lake area. Fitting the experimental values from these references by a double logarithmic function results in the following relationship for the dependence of the viscosity on temperature (measured
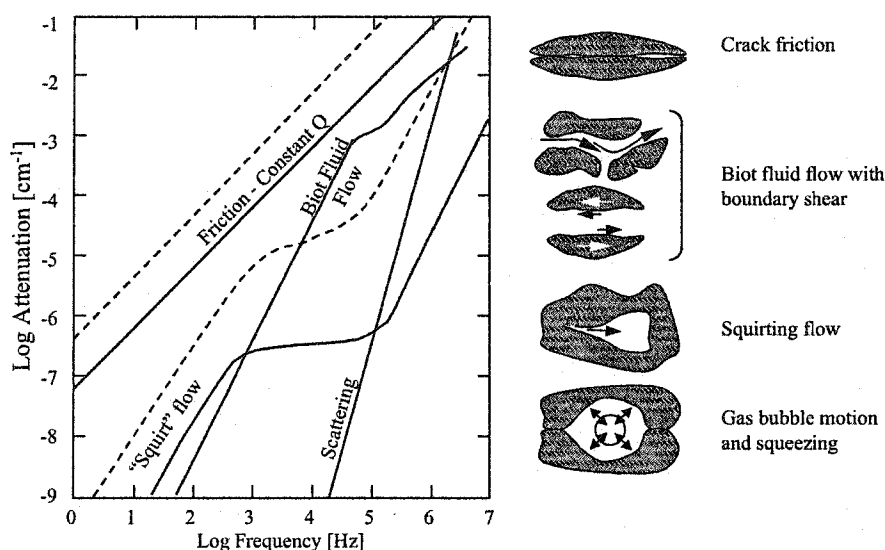
Figure 1.4: The various mechanisms causing P-wave attenuation as a function of frequency modelled for a saturated Berea sandstone at two different pressures . The solid line represents the attenuation at a pressure equivalent to a depth of 3000 m, the dashed lines are for surface conditions (redrawn after *Johnston et al.*, 1979).

in °C)

$$\eta(T) = 1.37 \cdot 10^9 \cdot 0.00778^{ln(T)}, \qquad (1.12a)$$

$$\eta(T) = 1.64 \cdot 10^8 \cdot 0.0123^{ln(T)}, \qquad (1.12b)$$

$$\eta(T) = 6.76 \cdot 10^8 \cdot 0.00775^{ln(T)}. \qquad (1.12c)$$

Ward and Clark (1950) measured the viscosity only for a limited temperature range up to 100°C (equation 1.12a). As the temperature can increase to 270°C - 300°C in a steam chamber these data are shown only for comparison. *Seyer and Gyte* (1989, 1.12b) and *Eastwood* (1993, 1.12c) provide data in the important temperature range. Note that all curves show qualitatively the same temperature dependence.

1.1.5 Seismic attributes based on variations in velocity and absorption

Changes in subsurface condition change the seismic data recorded at the surface and are manifested as traveltime shifts, waveform tuning, frequency variations, and amplitude

changes. The changes in velocity primarily affect the traveltime of a signal. For example if the velocity decreases in the steam chamber relative to the virgin reservoir, the traveltime for the reflection of the bottom of the reservoir increases by a certain amount. The amplitude of the reflected signal is affected by changes in the density and velocity. The reflected amplitude depends also on the angle of incidence. The full description of the amplitudes of all reflected phases (including all converted phases) are given by the Zoeppritz equations (e.g. *Lay and Wallace*, 1995; *Aki and Richards*, 2002). The angle dependent reflected amplitude (or amplitude variation with offset, AVO) is another technique to infer information in the subsurface (e.g. *Castagna*, 1993). However, the solution of the full Zoeppritz equations are considered to be rather difficult to handle in an inverse process, instead approximations as the one by *Aki and Richards* (2002) are commonly used:

$$\mathcal{R}(\theta) = \frac{1}{2}\left(1 - 4V_S^2 p^2\right)\frac{\Delta\rho}{\overline{\rho}} + \frac{1}{2\cos^2\theta}\frac{\Delta V_P}{\overline{V}_P} - 4V_S^2 p^2\frac{\Delta V_S}{\overline{V}_S}, \tag{1.13}$$

where p is the ray parameter defined as $p = \sin(\theta_s)/V_P$ and θ_s is the *take-off angle* at the source (*Aki and Richards*, 2002). $\Delta\rho$, ΔV_P, ΔV_S, and $\overline{\rho}$, $\overline{V}_P$, $\overline{V}_S$ are the jumps and the mean values of the properties across the interface, respectively. For normal incidence, the reflected relative amplitude is given by

$$\mathcal{R}(\theta = 0) = \frac{\rho_2 V_{P_2} - \rho_1 V_{P_1}}{\rho_2 V_{P_2} + \rho_1 V_{P_1}}, \tag{1.14}$$

with ρ_i and V_{P_i} being the density and P-wave velocity in the top and bottom medium separated by the interface.

The two attributes described so far provide information about the interface between two layers. For the seismic history match (see step D in Figure 5, page 9) seismic attributes defined in the reservoir layer are preferable. The seismic attribute of the *acoustic impedance* $\mathcal{AI}$, which is defined as

$$\mathcal{AI} = \rho V_P, \tag{1.15}$$

is closely related to the reflection coefficient. The acoustic impedance can be considered as a measure of the stiffness of a geological formation.

As the effective velocity in the reservoir changes during an enhanced oil recovery process, the variation in the travel time to the bottom of the reservoir, Δt, can also be

employed to characterise the reservoir. In most oil recovery processes it can be assumed that the thickness h of the reservoir layer remains constant. If V_{t_1} and V_{t_2} are the seismic velocities at two different times then the change in the recorded travel time is equal to

$$\Delta t = t_2 - t_1 = 2h \left(\frac{1}{V_{t_2}} - \frac{1}{V_{t_1}} \right). \tag{1.16}$$

The velocity at time t_2 can be expressed as $V_{t_2} = V_{t_1} + \Delta V$, where ΔV is the change in velocity due reservoir production. Assuming only small velocity changes ΔV equation (1.16) can be rewritten as

$$\begin{aligned} \Delta t &= 2h \left(\frac{1}{V_{t_2}} - \frac{1}{V_{t_1}} \right) \\ &= 2h \left(\frac{1}{V_{t_1}(1 + \Delta V/V_{t_1})} - \frac{1}{V_{t_1}} \right) \\ &\approx -2h \frac{\Delta V}{V_{t_1}^2}. \end{aligned} \tag{1.17}$$

If the thickness of the reservoir and the velocity V_1 are known from well logs then the measurable change in travel time Δt can be used to determine the change of the velocity ΔV in the reservoir. From this value, changes of the saturation or pore pressure can be derived using rock physical models such as Gassmann's theory.

1.2 Mathematical models for wave propagation

The propagation of waves is mathematically described by a hyperbolic partial differential equation, which is called the wave equation. There are several approximations to the real wave propagation phenomenon including more or less of the physical phenomena (i.e. two different wave velocities and energy absorption). The three standard mathematical models will be briefly introduced in the following sections. These models can be derived from physical laws. The last mathematical model, the viscoelastic wave equation, is a phenomenological description of wave propagation in an absorbing medium and cannot be derived directly from physical processes. However, as it describes the absorption of wave energy, and hence amplitude attenuation and wave dispersion, in a compact and relatively straight forward way it has become the standard wave equation for numerical finite difference simulation of seismic wave propagation.

1.2.1 The acoustic wave equation

The acoustic wave equation is the simplest approximation describing wave propagation phenomenon in fluid-like environments. It can be derived from Newton's law and the constitutive equations, respectively (e.g. *Lay and Wallace*, 1995):

$$\rho \frac{\partial^2 u_i}{\partial t^2} = \frac{\partial P}{\partial x_i}, \tag{1.18a}$$

$$P = K \frac{\partial u_i}{\partial x_i}. \tag{1.18b}$$

In these equations u_i are the components of the displacement vector, P is a pressure, x_i are the components of the cartesian co-ordinates, ρ denotes the mass density, and K represents the material's bulk modulus. Taking the second derivative with respect to time, and also assuming time and space invariance of the density and the bulk modulus, respectively, the following equation is obtained after some algebraic operations:

$$\frac{\partial^2 P}{\partial t^2} = \frac{K}{\rho} \frac{\partial^2 P}{\partial x_i^2} \hat{x}_i. \tag{1.19}$$

This equation describes the propagation of a disturbance in a pressure field $P(x, t)$, which propagates with the velocity $V_{acoust} = \sqrt{K/\rho}$. As only a single elastic modulus is included in the derivation there is only one wave type. The acoustic wave equation describes only the propagation of a compressional wave through a medium. A further simplification is that absorption effects are not included in this model. Another shortcoming of this approximation is that the reflected amplitude at a subsurface horizon in the earth is not determined correctly. During the reflection of a P-wave amplitude part of the incident energy is reflected as a P-wave, another part as a S-wave, and some energy is transmitted across the interface. As the acoustic wave equation does not allow shear waves, the reflected P-wave amplitude has to be larger than in a more realistic case.

The acoustic wave equation is still often used in seismic imaging and simple forward modelling application. However, it has been replaced by more sophisticated mathematical models for numerical simulation of seismic waves.

1.2.2 The elastic wave equation

A better approximation is the elastic wave equation. It can be derived similarly to the acoustic wave equation. Instead of using the gradient of the pressure in Newton's law

(1.18a) the divergence of the elastic stress tensor σ_{ij} is included in the derivation (*Lay and Wallace*, 1995):

$$\rho \frac{\partial^2 u_i}{\partial t^2} = \sigma_{ij,j}, \tag{1.20a}$$

$$\sigma_{ij} = c_{ijkl} u_{k,l}. \tag{1.20b}$$

As in the acoustic wave equation $u_i, i = 1, 2, 3$, are the three components of the particle displacement vector and ρ is the density of the material. The elastic parameters of the material are represented by the fourth-order elastic stiffness tensor c_{ijkl}. Theoretically, this tensor contains 81 components. By assuming a homogeneous isotropic material and making use of symmetry properties of the stress tensor σ_{ij} and the strain tensor ϵ_{ij}, the two Lamé parameters λ and μ are sufficient to express the elastic properties of the material. For isotropic and homogeneous material, the constitutive equation can be written as

$$\sigma_{ij} = \lambda \epsilon_{kk} \delta_{ij} + 2\mu \epsilon_{ij}. \tag{1.21}$$

Using this relationship for the stress tensor in equation (1.20) results in

$$\rho u_{i,tt} = (\lambda + \mu) u_{k,ki} + \mu u_{i,kk}. \tag{1.22}$$

The elastic wave equation describes the propagation of two elastic waves with wave velocities $V_P = \sqrt{(\lambda + 2\mu)/\rho}$ for the fast compressional wave and $V_S = \sqrt{\mu/\rho}$ for the shear wave. In including shear and compressional motion in the conceptual framework, the elastic wave equation enables a more accurate approximation of the true wave propagation phenomenon. Absorption effects, however, are still not included in this formalism.

1.2.3 The poro-elastic wave propagation theories

To include absorption effects into a mathematical description of wave propagation in saturated porous media several theories have been developed (*Biot*, 1956b,a, 1962; *Dvorkin et al.*, 1995, 1994; *Dvorkin and Nur*, 1993; *Parra*, 1997, 2000; *Parra and Xu*, 1994). The initial work of Biot assumes only energy dissipation due to fluid flow relatively to the motion of the solid frame. Based on this assumption, Biot was able to derive expressions for the dispersion and attenuation of the compressional and shear waves, respectively. The most spectacular aspect of Biot's theory is the prediction of a second compressional wave in

addition to the other two ordinary waves (P and S). As the speed of the second P-wave is slower than the P-wave and the S-wave this wave is usually referred to as the 'slow wave'. Experimental observations of these wave modes have recently been provided by *Batzle et al.* (2001) and *Bouzidi* (2003).

The initial theory by Biot

In the initial work *Biot* (1956a,b) considered a homogeneous isotropic medium with a single fluid in the pore space. By assuming that the fluid is interconnected throughout the sample and the attenuation is only due to viscous damping created by the relative motion of the fluid against the solid *Biot* (1962) derived a dissipation function. Together with a Lagrangian function he was able to derive the equation of motion for the wave propagation through a porous sample (see also *Johnson* (1984)):

$$\nabla^2[(P + S)e + Q\epsilon] \;=\; \partial_{tt}(\rho_{11}e + \rho_{12}\epsilon) + \frac{\eta\phi^2}{k}F(\omega)\partial_t(e - \epsilon), \qquad (1.23a)$$

$$\nabla^2[Qe + R\epsilon] \;=\; \partial_{tt}(\rho_{12}e + \rho_{22}\epsilon) - \frac{\eta\phi^2}{k}F(\omega)\partial_t(e - \epsilon). \qquad (1.23b)$$

In these equations P, Q, R, and S are generalised elastic constants, and ρ_{11}, ρ_{12}, and ρ_{22} are generalised densities. These generalised parameters are related to the elastic constants and densities of the solid rock matrix and pore fluid (see *Geertsma and Smit*, 1961; *Biot*, 1962; *Johnson*, 1984). The symbols e and ϵ represent the absolute dilatations of the bulk material and the pore fluid, respectively. Other symbols denote the shear viscosity of the fluid (η), the permeability (k), and the porosity (ϕ). Finally, $F(\omega)$ is a frequency correction factor introduced by *Biot* (1956a,b). The significance of the latter parameter will be discussed in a coming section.

The dilatation of the solid and the fluid component are coupled in two ways. First, there is an inertial coupling between both components by the two terms $\partial_{tt}(\rho_{11}e + \rho_{12}\epsilon)$ and $\partial_{tt}(\rho_{12}e + \rho_{22}\epsilon)$, respectively. The physical explanation for this coupling phenomenon is a inertial drag that the fluid exerts on the solid as the latter is accelerated relative to the former and vice versa (*Johnson*, 1984). This coupling process gives rise to the existence of the second compressional wave in a fluid saturated porous medium (*Bourbi et al.*, 1987; *Rasolofosaon*, 1991). The second coupling process is included by the relative particle velocity terms $\partial_t(e - \epsilon)$. These terms describe the viscous drag that the fluid and solid

impose on each other. It is this term that leads to the absorption of energy in porous media. The quantity $F(\omega)$ allows for the fact that the absorption of energy changes with the frequency of the seismic waves. At low frequencies the fluid oscillates in phase with the solid frame. Hence, there is little relative motion between the fluid and the frame and the attenuation is low. Indeed, at 'zero' frequency the theories of Biot and Gassmann converge (*Geertsma and Smit*, 1961; *Bourbi et al.*, 1987). Conversely, with increasing frequency the motion of both phases are out of phase. This increases the relative motion, and the resulting frictional force causes an irreversible change of mechanical energy into heat. The major part of energy dissipation occurs in a thin layer close to the walls of the pores. Its thickness is assumed to be given by the viscous skin depth $d_s = \sqrt{2\eta/\rho_f\omega}$ (*Johnson*, 1984; *Bourbi et al.*, 1987). The maximum energy dissipation occurs when the skin depth becomes approximately equal to the size of the pores. If d' is a measure of the average size of the pores, the peak frequency ω_{atn} for attenuation is given by

$$\omega_{atn} = \frac{2\eta}{\rho_f d'^2},\tag{1.24}$$

as noted earlier. With further increases of the frequency the viscous skin depth d_s decreases and the effect of viscous dissipation weakens. Therefore, for frequencies $\omega > \omega_{atn}$, the attenuation decreases again (Figure 1.3).

At low frequencies, viscous effects in the fluid dominate the inertial effects and the shear and 'fast' compressional wave become propagatory. The viscosity of the fluid has locked the fluid motion to the solid's with the result that there is no relative motion between the frame and the fluid. In this case, dissipative effects can be neglected for such low frequencies and the wave velocities are given by:

$$V_S = \sqrt{\frac{\mu}{(1-\phi)\rho_s + \phi\rho_f}},\tag{1.25a}$$

$$V_P = \sqrt{\frac{K + 4/3\mu}{(1-\phi)\rho_s + \phi\rho_f}},\tag{1.25b}$$

where the effective bulk modulus K can be determined by Gassmann's equation (1.3) for $\omega \ll \omega_{atn}$ (*Geertsma and Smit*, 1961). Therefore, the Gassmann model can be considered as the low or *zero* frequency limit of Biot's theory.

After the frequency exceeds the peak frequency of the attenuation the flow becomes turbulent. Then, the effects of viscosity are only felt in a thin boundary layer (*Johnston*

35
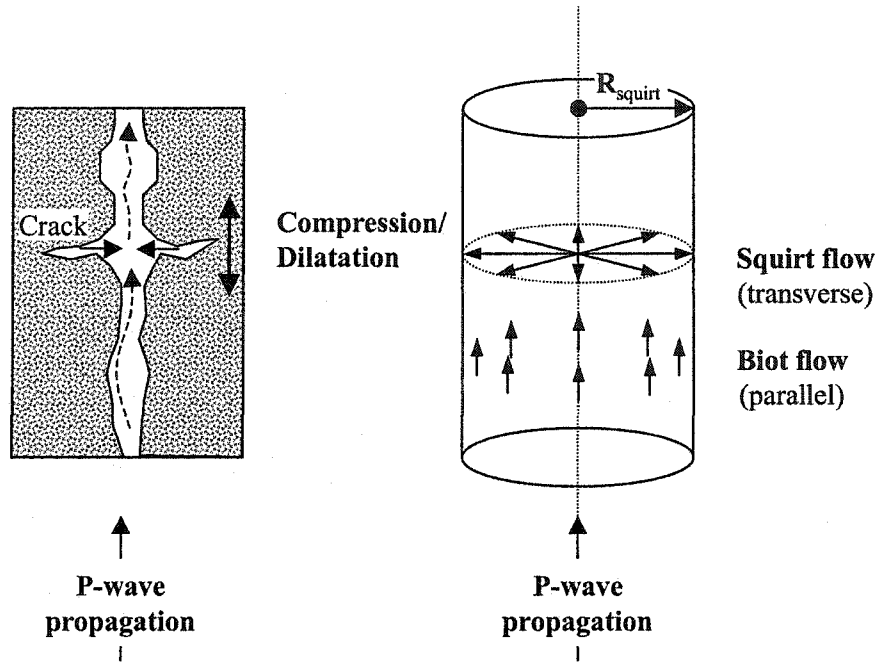
Figure 1.5: Schematic sketch of the poro-elastic effects. The figure on the left shows two possible flow modes that can be induced by a seismic wave. The dashed arrows indicate Biot fluid motion, solid lines the Squirt flow. The figure to the right shows the idealized pore volume that is assumed to derive the Squirt-flow equations. R_{Squirt} is the Squirt flow length. (Redrawn after *Dvorkin et al.*, 1994).

et al., 1979) and the attenuation decreases at high frequencies. In the high frequency range the fluid oscillates in phase with the solid frame. It therefore contributes to the stiffness of the effective medium. This implies that at these high frequencies, the wave speeds are higher than at low frequencies and energy absorption is low.

In deriving these equations, Biot assumed a uniform pore space in which the pore fluid only oscillates parallel to the direction of the exciting P-wave (see Figure 1.5). Based on these assumption he derived an attenuation-frequency relationship that is proportional to ω^2 for low frequency and to $\sqrt{\omega}$ for high frequencies (*Biot*, 1956a,b, 1962; *Fjær et al.*, 1992, among others). However, experimental data of the attenuation as a function of frequency suggest a linear proportionality between both (i.e. $\alpha \sim \alpha(\omega)$). Furthermore, the Biot theory predicts a shift of the attenuation peak frequency towards higher frequen-

cies if the viscosity of the pore fluid increases. This prediction is opposite to observations in several experimental studies (e.g. *Toksöz et al.*, 1979; *Winkler*, 1985; *Jones*, 1986; *Batzle et al.*, 2001)). This does not mean that the Biot theory is false but that there are additional and different absorption mechanisms contributing to the energy dissipation in real rocks that were not included in the original Biot theory. Particularly, radial flow in and out of highly compressible micro cracks may be an important contribution to the overall dissipation (e.g. *O'Connell and Budiansky*, 1977; *Johnston et al.*, 1979; *Jones*, 1986).

To facilitate the discussion of the improvements to the Biot theory in the following section the poro-elastic wave equation will be rearranged in a form similar to the elastic wave equation. Following *Rice and Cleary* (1976) and *Dvorkin and Nur* (1993) the constitutive equation has to be modified to include stresses that are caused by pressures in the fluid P that acts on the solid material. Considering only uniaxial deformation the total stress is given by

$$\sigma^t = Me - (\alpha_p - \phi)P \tag{1.26}$$

In this equation α_p is the so-called Biot or poro-elastic constant, M is a generalised elastic parameter, and $e = du/dx$ represents the deformation of the skeleton. Then, the equations of motion become

$$\rho_{11}u_{,tt} + \rho_{12}w_{,tt} + \frac{\eta\phi^2}{k}(u_{,t} - w_{,t}) = \sigma_{,x}, \tag{1.27a}$$

$$\rho_{12}u_{,tt} + \rho_{22}w_{,tt} - \frac{\eta\phi^2}{k}(u_{,t} - w_{,t}) = -\phi P_{,x}. \tag{1.27b}$$

To determine the pressure in the fluid an auxiliary equation is required:

$$P_{,t} = -F\left(w_{,xt} + \frac{\alpha_p - \phi}{\phi}u_{,xt}\right). \tag{1.28}$$

The various symbols represent the following parameters:

u is the displacement of the solid rock matrix,

w is the displacement in the pore fluid,

F $= (1/K_f + 1/(\phi Q)^{-1}$,

Q $= (1/K_S(1 - \phi - K_d/K_S))^{-1}$,

$\alpha_p = 1 - K_d/K_S$.

A compact form of the solution of the poro-elastic wave equation has been derived by *Geertsma and Smit* (1961). By defining V_{P0} and $V_{P\infty}$ as the low and high frequency limits of the fast compressional wave, the frequency dependent relationship for the P-wave, V_P, and the inverse of the quality factor Q_P are given as

$$V_P^2 = \frac{V_{P\infty}^4 + V_{P0}^4 \left(\frac{\omega_c}{A\omega}\right)^2}{V_{P\infty}^2 + V_{P0}^2 \left(\frac{\omega_c}{A\omega}\right)^2},$$ (1.29a)

$$Q_P^{-1} = \frac{\frac{V_{P\infty}}{V_{P0}} - 1}{\frac{\omega_c}{A\omega} + \frac{\omega A}{\omega_c}\frac{V_{P\infty}^2}{V_{P0}}},$$ (1.29b)

with

$$A = \frac{(\rho_{11} + 2\rho_{12} + \rho_{22})\rho_{22} - (\rho_{12} + \rho_{22})}{(\rho_{11} + 2\rho_{12} + \rho_{22})\phi^2}, \quad \text{and} \quad \omega_c = \frac{\eta}{k\rho}.$$

Improvements of the Biot-theory

A compressional wave will compress and dilate the porous media it is passing through. The compression of a microcrack induces a radial pressure gradient in the fluid between the crack and the pore (Figure 1.5). The relative motion of the fluid to the solid material causes frictional energy dissipation and therefore attenuation and wave dispersion.

At low frequencies there is sufficient time for the pressure in the fluid saturated sample to reach an equilibrium state. The relative motion between fluid and rock is negligible and the attenuation is low. For these frequencies it is said that the rock sample is at a relaxed state. Alternatively, if the frequency is sufficiently large then there is not enough time for the pressure to relax and a pressure gradient within the crack will remain causing relative motion between the fluid and solid phase. In this case the viscous dissipation due to relative motion can be neglected. This implies that the attenuation decreases with increasing frequencies. The lack of a pressure gradient also 'locks' the fluid in the cracks. This results in an increased effective stiffness of the rock sample and the velocities increase with frequency (*Johnston et al.*, 1979; *Dvorkin et al.*, 1995, 1994; *Dvorkin and Nur*, 1993). For intermediate frequencies, however, the absorption of energy reaches its maximum at a frequency ω_{squirt}, which depends on the effective bulk modulus of the

rock, K_{eff}, the viscosity of the fluid and the aspect ratio of the microcracks, δ (*Palmer and Traviolia*, 1980; *Jones*, 1986):

$$\omega_{squirt} = K_{eff}\frac{\delta^3}{\eta}. \tag{1.30}$$

From this equation it can be seen that this absorption depends strongly on the microstructure of the porous media as represented in part by the aspect ratio δ. Based on experimental data of the peak frequency w_{squirt} as function of pore fluid viscosity and bulk modulus of the rock *Murphy et al.* (1986) and *Jones* (1986) concluded that crack aspect ratios in the range of 10^{-3} to 10^{-4} causes most of the attenuation. If the aspect ratio is less (i.e. rounder stiffer pores) the pores will not deform sufficiently under the stress perturbation of a passing wave. Although there is probably no explanation for the reduction of attenuation for smaller aspect ratios (e.g. $\delta < 10^{-4}$) it is assumed that there is not enough free fluid in such small and thin cracks (*Jones*, 1986), the fluid is *bound* to the crack wall by van der Waals forces.

This local flow (as opposite to Biot's global flow) is probably the dominant absorption mechanism (*Johnston et al.*, 1979; *Jones*, 1986). However, this flow mechanism is not included in the original Biot theory. In a series of papers *Dvorkin et al.* (1995, 1994); *Dvorkin and Nur* (1993) extended the original Biot-equations to include the squirt flow into the poro-elastic wave equation. Their work will be briefly reviewed in the following paragraphs.

Dvorkin et al. (1995, 1994); *Dvorkin and Nur* (1993) assumed that there is an additional fluid flow component that is purely radial (i.e. perpendicular to the propagation direction of the seismic wave, see Figure 1.5). This leads to a modified differential equation for the pressure in the porous medium. The changes of the average pressure in the pore space with respect to time is given by

$$\frac{\partial P_{ave}}{\partial t} = -F\left[1 - \frac{2J_1(\lambda R)}{\lambda R J_0(\lambda R)}\right]\left(w_{,xt} + \frac{\alpha_p - \phi}{\phi}u_{x,t}\right),$$

$$\lambda R = \sqrt{R^2\frac{\rho_f\omega^2}{F}\left(\frac{\phi + \rho_a/\rho_f}{\phi} + i\frac{\eta\phi}{k\rho_f\omega}\right)}, \text{ and} \tag{1.31}$$

$$\lambda = \sqrt{\frac{\rho_f\omega^2}{F}\left(\frac{\phi + \rho_{12}/\rho_f}{\phi} + i\frac{\omega_c}{\omega}\right)}.$$

39

In these equation R is the squirt-flow length that has been introduced by *Dvorkin and Nur* (1993) to derive the differential equation (1.31). They consider the squirt-flow length to be a fundamental rock physical parameter that depends only on the pore space but not on the properties of the pore fluid. The physical explanation of the squirt-flow length is the radius of the cylinder where the pressure does not change with time. If the squirt flow length increases the squirt flow theory approaches the Biot model. This observation is justified by the fact that if R increases local heterogeneities become less significant and fluid flow in the radial direction can be neglected. Then, the propagation of elastic waves in porous media can be described by Biot's theory alone (*Dvorkin and Nur*, 1993).
Further symbols denote

- J_1 and J_0 are Bessel functions,

- ρ_a is the additional density according to *Biot* (1956a,b),

- $1/F = 1/(\rho_f V_{P_f}^2) + 1/(\phi\Gamma)$ and $1/\Gamma = (1 - \phi - \alpha_p)/K_S$

Finally, the dispersion relationships for the P-wave are given by (*Dvorkin et al.*, 1994)

$$V_P(\omega) = \frac{1}{Re\left(\sqrt{-\frac{B}{2A} - \sqrt{\left(\frac{B}{2A}\right)^2 - \frac{C}{A}}}\right)}, \tag{1.32a}$$

$$Q_P^{-1}(\omega) = 2\frac{Im\left(\sqrt{-\frac{B}{2A} - \sqrt{\left(\frac{B}{2A}\right)^2 - \frac{C}{A}}}\right)}{Re\left(\sqrt{-\frac{B}{2A} - \sqrt{\left(\frac{B}{2A}\right)^2 - \frac{C}{A}}}\right)}, \tag{1.32b}$$

where

$$A = \frac{\phi F_{SQ} M}{(\phi\rho_f)^2},$$

$$B = \frac{F_{SQ}\left(2\alpha_p - \phi - \phi\frac{(1-\phi)\rho_S}{\phi\rho_f}\right) - \left(M + F_{SQ}\frac{\alpha_p^2}{\phi}\right)\left(1 + \frac{\rho_a}{\phi\rho_f} + i\frac{\omega_c}{\omega}\right)}{\phi\rho_f},$$

$$C = \frac{(1-\phi)\rho_S}{\phi\rho_f} + \left(1 + \frac{(1-\phi)\rho_S}{\phi\rho_f}\right)\left(\frac{\rho_a}{\phi\rho_f} + i\frac{\omega_c}{\omega}\right),$$

$$F_{SQ} = F\left[1 - \frac{2J_1(\lambda R)}{\lambda R J_0(\lambda R)}\right].$$

40
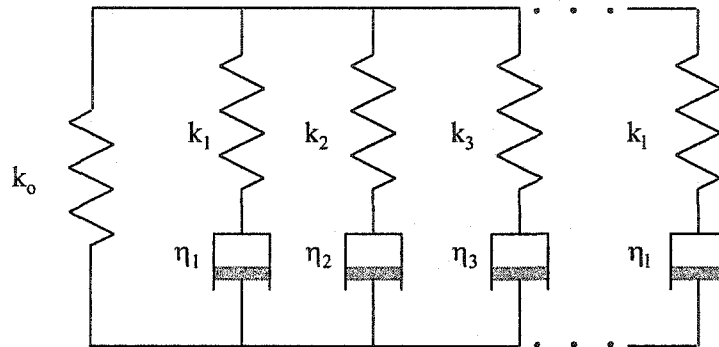
Figure 1.6: The Generalised Standard Linear Solid (GSLS) can be used to approximate dissipative rheology.

The combined work of Biot and Dvorkin et al., referred to as the BISQ-theory, provides a theoretical framework that is consistent with the experimental data over a wide frequency range. The squirt-flow length, however, is still a difficult to determine and somewhat ambiguous parameter.

1.2.4 The viscoelastic wave equation

The poro-elastic wave equations include many parameters, which are difficult to determine experimentally. Additionally, the system of equations describing the propagation of waves in a poro-elastic medium is quite complex and difficulties can be expected if these equations are to be solved numerically (*Carcione and Quiroga-Goode*, 1995). To circumvent this problem *Borcherdt* (1973), *O'Connell and Budiansky* (1977), *Liu et al.* (1976), *Kjartansson* (1979), *Emmerich and Korn* (1987), *Carcione* (1988); *Carcione et al.* (1988), and *Blanch et al.* (1995), among others, investigated the potential of employing a viscoelastic rheology to simulate the absorption of wave energy in the earth. *Biot* (1962) already discussed the possibility to describe the absorption phenomena by a viscoelastic rheology. In contrast to the poro elastic wave equation above, the viscoelastic wave equation cannot be derived from physical laws for problems in saturated porous media, but it is a phenomenological description of amplitude attenuation and waveform dispersion.

The basic hypothesis is that the current value of the stress tensor $\sigma(t)$ is related to the entire history of the strain tensor $\epsilon(t)$. The viscoelastic rheology is approximated by

41

parallel connections of a *Hooke* and *Maxwell* bodies with each Maxwell body consisting of one Hooke and a *Newton* element (Figure 1.6). The Hooke body, a spring with an elastic constant k, simulates the elastic (i.e. reversible) part of the medium. The Newtonian element, which approximates the visco-elasticity, is an absorbing 'dashpot' with a viscosity η. Each Maxwell body forms a *relaxation mechanism*, which can differ through their values for k_l and η_l, respectively.

The viscoelastic wave equation is similar to the elastic wave equation, but to include viscoelastic behaviour the constitutive law is modified using a convolutional relationship (*Bland*, 1960; *Christensen*, 1971)

$$\sigma(t) = R(t) * \dot{\epsilon}(t) = \dot{R}(t) * \epsilon(t), \tag{1.33}$$

where $R(t)$ is the *relaxation function*. The $'*'$ in this equation denotes time convolution. Equation (1.33) is based on the principle of superposition that has been proposed by *Boltzmann* in 1876. He described this phenomenon as:

> "... the forces acting on a parallelepiped at a certain time do not depend only on its strain at this time but also on the preceding strains."

Because of this characteristic viscoelastic media are also said to have a 'memory'.

The solution of a dissipative wave propagation can be written in the form of equation (1.10). Rewriting this equation as

$$\mathcal{P}(x,t) = \mathcal{P}e^{i(\omega t - \tilde{k}x)}$$

leads to the introduction of the complex wavenumber $\tilde{k} = k - i\alpha$. Using $\tilde{k}$ the dispersion relationship becomes

$$V(\omega) = \frac{\omega}{\tilde{k}} = \Re\sqrt{\frac{M(\omega)}{\rho}},$$

where $M(\omega)$ is a frequency dependent, complex modulus, which is related to the Fourier transform of $R(t)$ (*Emmerich and Korn*, 1987)

$$M(\omega) = i\omega\tilde{R}(\omega). \tag{1.34}$$

The quality factor $Q(\omega)$ can be calculated from the complex modulus according to (*Emmerich and Korn*, 1987)

$$Q(\omega) = \frac{Re(M(\omega))}{Im(M(\omega))} \tag{1.35}$$

42

and the velocity dispersion function is given by (*Emmerich and Korn*, 1987)

$$\frac{c(\omega_r)}{V(\omega)} = \sqrt{\frac{|M(\omega_r)|}{M(\omega)}}, \tag{1.36}$$

where ω_r is a reference frequency, $c(\omega_r)$ is the phase velocity at the reference frequency, and $V(\omega)$ is the complex phase velocity.

The relaxation function $R(t)$ can be described in terms of the properties of a generalised standard linear solid (GSLS), which consist of L relaxation mechanisms (Figure 1.6). The absorption properties of such GSLS are described through the relaxation function according to (e.g. *Carcione et al.*, 1988; *Robertson et al.*, 1994)

$$R(t) = M_R \left[1 + \sum_{l=1}^{L} \left(\frac{\tau_{\epsilon l}}{\tau_{\sigma l}} - 1 \right) e^{-t/\tau_{\sigma l}} \right] H(t), \tag{1.37}$$

where M_R is the unrelaxed modulus (i.e., the modulus for $\omega \rightarrow \infty$) and the relaxation times of the strain, $\tau_{\epsilon l}$, and the stress, $\tau_{\sigma l}$, are related to the properties of the lth Hooke and Newton body by

$$\tau_{\epsilon l} = \frac{\eta_l}{k_o} + \frac{\eta_l}{k_l}, \tag{1.38a}$$

$$\tau_{\sigma l} = \frac{\eta_l}{k_l}. \tag{1.38b}$$

Finally, $H(t)$ is the *Heaviside function*.Then, the complex modulus $M(\omega)$ to calculate the attenuation and dispersion relationships (equations 1.35 and 1.36) is results as

$$M(\omega) = i\omega \tilde{R}(\omega) = M_R \left[1 - L + \sum_{l=1}^{L} \frac{1 + i\omega\tau_{\epsilon l}}{1 + i\omega\tau_{\sigma l}} \right]. \tag{1.39}$$

By a proper choice of the number of Maxwell bodies, L, and the relaxation times $\tau_{\epsilon l}$ and $\tau_{\sigma l}$, respectively, the GSLS body can be adjusted to a given attenuation relationship $Q(\omega)$.

The viscoelastic wave equation can now be derived my modifying the constitutive equation (1.21), which becomes (e.g. *Blanch et al.*, 1995; *Bohlen*, 1998)

$$\sigma_{ij}(t) = \left(\dot{R}_P - 2\dot{R}_S \right) * \epsilon_{ll}\delta_{ij} + 2\dot{R}_S * \epsilon_{ij}. \tag{1.40}$$

43

The relaxation functions R_P and R_S are determined by

$$R_P(t) = \pi \left[1 + \sum_{l=1}^{L} \left(\frac{\tau_{\epsilon l}^P}{\tau_{\sigma l}} - 1 \right) e^{-t/\tau_{\sigma l}} \right] H(t), \qquad (1.41a)$$

$$R_S(t) = \mu \left[1 + \sum_{l=1}^{L} \left(\frac{\tau_{\epsilon l}^S}{\tau_{\sigma l}} - 1 \right) e^{-t/\tau_{\sigma l}} \right] H(t), \qquad (1.41b)$$

where $\pi = \lambda + 2\mu$ is the unrelaxed modulus for compressional waves. *Blanch et al.* (1995) showed that the same stress relaxation times can be used for both P- and S-waves.

1.3 Discussion

This chapter started with a review of the effects that variations of temperature, pressure, and pore fluid have on the seismic velocities, attenuation, and density. Basically it was shown that temperature dominantly influences these seismic parameters through the properties of the pore fluid. In case of the seismic velocities, the pressure effects on the bulk properties are mainly related to the influence on the rock frame, whereas the pressure dependence of the pore fluid are small and can often be neglected. However, it is particularly difficult to measure or describe the pressure dependent elastic frame properties for unconsolidated sands. In order to estimate the possible effects of effective pressure variations on unconsolidated sands generalized curves describing the changes of the P-velocity with effective pressure can be employed (as will be done in chapter 3.5.4).

Mathematics is the language of physics. To describe the phenomena related to wave propagation several mathematical models have been developed. In particular, these are the acoustic, elastic, poro-elastic, and viscoelastic wave equations that have been discussed in section 1.2. Each model incorporates more or less of the characteristics of real wave propagation in its description, that is, different wave motions (i.e., both compressional and shear motion or just one) and also energy dissipation in case of the poro- and viscoelastic wave equation.

Numerical simulation of seismic surveys will be an important part in this work. To include all characteristics of wave propagation in the modelling process a poro-elastic wave equation that incorporates aspects of local and global fluid flow would be the best

choice. However, for reasons to be discussed in the following chapter, poro-elasticity gives rise to numerical difficulties, which can lead to computationally expensive schemes (e.g. *Carcione and Quiroga-Goode*, 1995). Also, this theory includes several parameters that are difficult to determine experimentally. as well, there remains considerable discussions of the applicability of such theories to complex earth materials. The second choice could be the viscoelastic theory as it mimics the dissipation processes described in the poro-elastic wave equation fairly accurately and efficiently. This approach has been often used in numerical simulations using the finite difference technique (e.g. *Carcione et al.*, 1988; *Robertson et al.*, 1994; *Blanch et al.*, 1995). The drawback of the viscoelastic wave equation for numerical modelling compared to the elastic or acoustic wave equation is that it requires significantly more hardware memory to store the additional variables and system parameters. As such, the elastic wave equation will be used in the numerical simulations performed in the framework of this current research project. In fact, seismic modelling using the spectral finite element method, which has been employed in this work, has only used the elastic constitutive equations to describe the rheology of the model.

Chapter 2

Application of the spectral finite element method to the elastic wave equation

To assist in the preparation, analysis, interpretation, and verification of geophysical field surveys numerical simulations have become increasingly important in the past decades. For example, the interpretation of seismic data is often difficult and results in an model of the subsurface that is not necessarily unique. To verify the model, simulated seismic surveys based on the results of the interpretation are often employed. If such synthetic data agree sufficiently well with the observations the model can be considered as a valid image of the earth. Another example application of numerical forward modelling is the optimization of a survey design, especially if the structure is already understood, as it is often the case in repeated (or time-lapse) experiments.

The challenges in numerical modelling are to include all the features of the real earth, thus making the solution of the physical problem difficult. In particular, the requirements for an adequate simulation algorithm are:

- First, the program must enable all important physical features of seismic wave propagation such as variations of the seismic velocities. In the case of seismic monitoring of oil reservoirs the features of interest, as considered here, are velocity dependent wave propagation in two dimensions, and the reflection and transmission at interfaces.

- The simulated seismic surveys must be as free as possible of numerical artifacts

46

which can be caused by insufficient representation of the partial differential equations within the model and an inaccurate incorporation of the boundary conditions. For seismic simulation, for which the main interest is in detecting small changes, an accurate result at the free surface (where the seismic data are 'recorded') is of considerable significance.

- Steam chambers in heavy oil reservoirs might assume a nontrivial geometry. The numerical method should therefore allow for an accurate handling of complex-shaped bodies within the computational model.

- Finally, the method should be computationally efficient. Reasonable sized models should be calculated within a reasonable time. The size of the computational model is limited by the amount of hardware memory of a computer. However, with improving technology this limitation becomes less important. In order to be able to run many simulations with different parameters for a sensitivity analysis the computation time is a more important limiting factor. The program has to be especially efficient in this point. Therefore, it would be of advantage if the program can be easily executed on parallel computers.

During the past decades several numerical simulations techniques have been developed and applied in seismic modelling, with each meeting more or less of the above criteria. In the following section the different approaches to solving the wave equation numerically, notably the *Finite Difference Method*, the *Pseudo-Spectral Method*, and the *Method of Finite Elements*, are described in more detail and the potential of each method for simulating wave propagation in complex geological model is discussed.

2.1 Methods for solving the wave equation numerically

As discussed in section 1.2 the mathematical models describing the propagation of waves are based on different rheological laws. An analytical solution of these differential equations is, however, only possible if the computational domain is very simple and regular as in homogeneous spheres, cylinders, or parallelepipeds. For real case simulations of complex geological structures, it is only possible to derive an approximate solution

---

47

with numerical techniques. Various methods are used today to solve the wave equations numerically depending on criteria such as the complexity of the model, the computation time required, and computer hardware resources. In the following sections these techniques are introduced and discussed briefly with respect to their practicability for modelling the seismic signature of small heterogeneities embedded in a larger model.

Common to all these techniques is a discrete grid or mesh of points that approximates the continuous real model. The material parameters (e.g. elastic constants, densities) and values of the solution are defined only at these points. The continuous partial differential equations have to be converted into a discrete approximation to solve the problem over the grid. This is done in different ways for the finite difference and spectral methods techniques, whereas the finite element methods and their modern improvements, such as the spectral finite element method, approximate the solution of the differential equation on the grid and subsequently minimize the approximation error.

To ensure reliable results a modelling algorithm must meet several conditions (*Karrenbach*, 1996):

- Convergence ensures that the numerical approximation of the differential equation becomes equal to the continuous equation if the grid spacing h is chosen sufficiently small. If u is the continuous solution and the discrete solution is denoted by v_h then convergence requires that

$$\lim_{h \to 0} v_h \to u.$$

- If the differential operator $\mathcal{L}$ is applied onto the function u, then consistency of the continuous differential equation

$$\mathcal{L}u = 0$$

with the discrete equation

$$\mathcal{L}v_h = 0$$

is defined as the pointwise convergence at each grid point for any smooth function v_h as long as the discretisation interval is sufficiently small.

- Finally, the stability criterion requires that the energy of the solution does not grow without limits during the simulation. This criterion is connected to an energy limit

and to the well-posedness of the partial differential equation. In practical terms, the energy in the model can not grow without limits. Therefore the numerical solution should not grow limitlessly as well.

Usually stability is the critical factor in designing a numerical scheme. According to *Karrenbach* (1996) *'a consistent numerical scheme is convergent if and only if it is stable'*.

Numerical dispersion is another numerical artifact that must be considered if hyperbolic differential equations (such as the wave equation) are solved numerically. It is a well-known fact that discrete solutions of such partial differential equations are intrinsically dispersive (*Press et al.*, 1997). Dispersion of a numerical scheme is defined as the mismatch between the true and the approximate propagation velocities. The wavelets, which are used in seismic modelling to describe the time evolution of the source, are a superposition of modes with different wavenumbers. It can be shown (*Press et al.*, 1997) that for each time step evaluated, the different modes of the wavelet are modified slightly differently. This modification is considerable if the wavenumber is comparable to the grid spacing h or smaller. To avoid this numerical dispersion band limited wavelets and a grid spacing sufficiently small compared to the smallest wave number must be chosen.

The first numerical technique that has been widely used in computational seismic modelling is the finite difference method. In the 1960's, *Alterman and Karal* (1968) started to use finite difference methods to numerically solve the elastic wave equation in homogeneous media. This work was extended by *Kelly et al.* (1976) to enable the solution for heterogeneous models. Finite difference methods became very popular in the following years, although they suffer from difficulties in meeting the stability criterion and numerical dispersion. To overcome this problem *Gazdag* (1981) introduced spectral methods to model the propagation of acoustic waves. This approach has been extended by *Kosloff and Baysal* (1982) and *Kosloff et al.* (1990) to the elastic wave equation. The advantage of these spectral methods is a considerable reduction in the numerical dispersion due to a significantly better approximation of the derivatives on the discrete grid. During the last five years finite element methods have been increasingly used in seismic modelling (e.g. *Padovani et al.*, 1994; *Faccioli et al.*, 1996, 1997; *Komatitsch and Tromp*, 1999; *Chaljub et al.*, 2003). The main interest in the development of this method, despite its higher computational cost, is in part due to its improved flexibility in the design of the model geometry

Continuous model
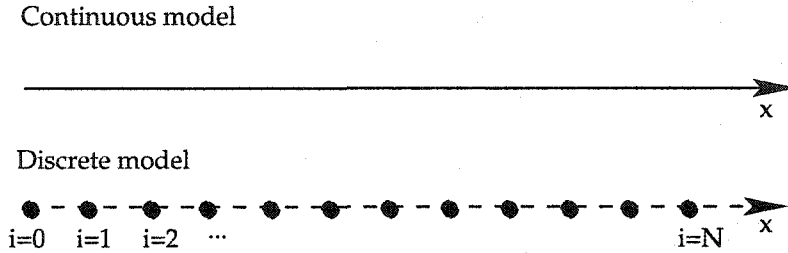
Discrete model

Figure 2.1: Approximation of a *continuous* 1D model (top) on a *discrete grid* (bottom) consisting of $N + 1$ points.

and a better handling of the free surface boundary condition, where the results of a simulation are typically collected.

2.1.1 Finite Difference Methods

In the finite difference method the continuous geophysical model is projected on an uniform discrete grid. To obtain the discrete differential operators the solution of the partial differential equation is approximated by a truncated Taylor series. This is illustrated for the one dimensional acoustic wave equation, which describes the propagation of a pressure perturbation in a fluid-like medium. The pressures P are sampled on N grid points each separated by a distance Δx (Figure 2.1). In a close neighborhood of a point i the derivative of the pressure with respect to space can be approximated by (e.g. *Press et al.*, 1997)

$$\frac{\partial P}{\partial x} \approx \frac{\Delta P_i}{\Delta x} = \frac{P_{i+1} - P_{i-1}}{2\Delta x}.$$

Similarly, the continuous time is broken into a series discrete time points $t_k = k\Delta t$, $k = 0, 1, \ldots, K$, with Δt being the time sampling interval. The second derivative with respect to time can is approximated by a central finite difference operator:

$$\frac{\partial^2 P}{\partial t^2} \approx \frac{\Delta^2 P_i^k}{\Delta t^2} = \frac{P_i^{k+1} - 2P_i^k + P_i^{k-1}}{\Delta t^2}.$$

50

On the discrete grid the acoustic wave equation in one dimension now becomes the discrete finite difference equation

$$\frac{\partial^2 P}{\partial t^2} - c^2 \frac{\partial^2 P}{\partial x^2} \approx$$
$$\frac{P_i^{k+1} - 2P_i^k + P_i^{k-1}}{\Delta t^2} - c_i^2 \frac{P_{i+1}^k - 2P_i^k + P_{i-1}^k}{\Delta x^2} = 0.$$

To solve this equation numerically for the time t^{k+1} the pressures P_i must be known at times t^k and t^{k-1}. Rearranging the above equation to isolate the term for the pressure at time t^{k+1} yields

$$P_i^{k+1} = 2P_i^k - P_i^{k-1} + \frac{c_i^2 \Delta t^2}{\Delta x^2} \left(P_{i+1}^k - 2P_i^k + P_{i-1}^k \right).$$

The main criteria to a finite algorithm is stability (*Karrenbach*, 1996). Stability of a finite difference scheme requires that the amplitude of the approximate solution can not grow without limits, i.e., it is bounded. To ensure stability the time step Δt has to be chosen sufficiently small relative to the Courant number (*Press et al.*, 1997). The Courant number relates the time sampling interval Δt to the highest velocity c_{max} and the spatial sampling interval Δx such that (e.g. *Carcione and Quiroga-Goode*, 1995)

$$c_{max} \frac{\Delta t}{\Delta x} < \frac{1}{\sqrt{n_d}},$$

with n_d being the dimensionality of the model.

Another problem must be considered in finite difference modelling of the wave equation. Finite difference methods for hyperbolic partial differential equations are intrinsically dispersive, which means they exhibit numerical dispersion or phase errors if the spatial sampling interval is too large relative to the smallest wavelength λ_{min} in the model (*Dablain*, 1986). *Alford et al.* (1974) suggested that λ_{min} should be supported by at least ten grid points, indicating that a very fine spatial sampling is required in order to avoid numerical dispersion. Hence, finite difference methods can be computationally very expensive.

Despite these difficulties, the finite difference method is essentially a simple numerical technique to solve a partial differential equation on a numerical grid. It has been widely used in computational seismic modelling since the late 1960's. The initial work of

Alterman and Karal (1968) has been improved by *Alford et al.* (1974), and extended to fully elastic heterogeneous media by *Kelly et al.* (1976). *Dablain* (1986) introduced high-order finite difference method to reduce numerical dispersion , and *Madariaga* (1976), *Virieux* (1984), *Virieux* (1986), and *Levander* (1988) developed the so-called staggered grid operators, which reduce numerical dispersion significantly. Finally, *Robertson et al.* (1994) and *Blanch et al.* (1995) extended the work by *Levander* (1988) to include viscoelastic rheology in the algorithm. Their scheme has become the standard method for seismic finite difference modelling.

Another drawback of finite difference schemes is that this method is constrained by a rather rigid grid, in which the grid points must be strictly perpendicular to each other. This makes including arbitrary shaped bodies into the model problematic. Surface topography is also difficult to incorporate into the model. *Carcione* (1994), *Robertson* (1996), and *Hestholm and Ruud* (1998) used mapping techniques to fit the numerical grid to a model with some irregular but smooth bodies and surface topography. Their approach is, however, limited to shapes that can be described by some analytical function like sines or cosines. Thus, the embedded geometry is not truly arbitrary.

2.1.2 Pseudo-Spectral Methods

Numerical or grid dispersion often requires the grid spacing to be small in the finite difference method. The number of grid points, which are needed in the model to reduce this artifact, can become very large making the numerical simulation uneconomical. A more accurate and economical scheme can be obtained if the Fourier transformation is applied instead of approximating the spatial derivatives by a local finite difference operator. This technique, used by *Gazdag* (1981) for the first time in seismic forward modelling and later on extended and improved by *Kosloff and Baysal* (1982), *Reshelf et al.* (1988), *Kosloff et al.* (1990), and *Kosloff and Tal-Ezer* (1993), among others, results in a significant reduction of the numerical dispersion error. When using the Fourier spectral method to compute the spatial derivatives, the wave numbers supported by the computational grid range from $k = 0$ to the Nyquist wave number $k_{Ny} = \pm\pi/\Delta x$. Instead of ten grid points per minimum wavelength as required above the Fourier based methods require only two grid points to simulate the propagation of waves (*Kosloff and Baysal*, 1982). If the source

function is band limited with the smallest wave number less than the Nyquist wave number of the grid then the approximation is infinitely accurate (*Carcione and Quiroga-Goode*, 1995).

For this technique a truncated Fourier series approximate the solution of the wave equation. If u_j denotes the discrete solution at the grid point j then the discrete transform pair is given by

$$u_j = \sum_{l=-[N/2]}^{[N/2]-1} \tilde{u}_l \, exp\left(i\frac{2\pi l}{N\Delta x}j\Delta x\right),$$

$$\tilde{u}_l = \frac{1}{N}\sum_{j=0}^{N-1} u_j \, exp\left(-i\frac{2\pi l}{N\Delta x}j\Delta x\right).$$

In these equations, N is the number of grid points and Δx stands for the spatial sampling interval. The operator $[\cdot]$ depicts the integer part of the argument (*Canuto et al.*, 1988). By introducing the discrete spatial wave number $k_l = 2\pi l/N\Delta x$ and replacing $j\Delta x$ by x_j the above transform pair becomes

$$u_j = \sum_{l=-[N/2]}^{[N/2]-1} \tilde{u}_l \, exp(ik_l x_j),$$

$$\tilde{u}_l = \frac{1}{N}\sum_{j=0}^{N-1} u_j exp(-ik_l x_j).$$

Making use of the fact that the derivative in the space domain is equivalent to a multiplication by ik in the Fourier domain (e.g. *Canuto et al.*, 1988) the spatial derivatives may be calculated by the following scheme:

$$u \xrightarrow{FFT} \tilde{u} \rightarrow ik\tilde{u} = \frac{\partial \tilde{u}}{\partial x} \xrightarrow{iFFT} \frac{\partial u}{\partial x}.$$

Therefore, two Fourier transformations are required for the calculation of each spatial derivative in each dimension, and hence, the computational efficiency gained by the reduction of the grid size is partially lost by the higher cost for the Fourier transformations. Another shortcoming of this method is that the implementation of both the free surface and absorbing boundary conditions is difficult. For Fourier methods only cyclic boundary conditions have been effectively applied at the edges of the model (*Fornberg*, 1987).

To implement a free surface condition the model must be padded with zeros above the free surface. This enables a fairly good approximation for waves propagating at small angle of incidence towards the surface, but for larger incident angles significant 'ringing' at interfaces or free surface has been observed (*Kosloff et al.*, 1990). Thus, this method is not suitable when recording of the computed wave amplitudes at the free surface is crucial for the analysis. This is a severe limitation when one hopes to model a typical seismic exploration program.

Fourier series, despite their simplicity, are not always a good choice for the approximation functions. In fact, for reasons discussed above, Fourier series are only advisable for problems with periodic boundary conditions (*Canuto et al.*, 1988). The introduction of Chebychev polynomials for the calculation of the spatial derivatives by *Kosloff et al.* (1990) improved the pseudo spectral technique in the sense that the free surface and boundary condition can be better implemented.

Chebychev polynomials are only defined on the interval $[-1, 1]$ so that the model must be mapped onto this interval. The values of the discrete polynomial are given by

$$T_k(x_j) = \cos(k\Theta_j),$$

with $\Theta_j = \arccos(x_j)$, $k = 0, 1, 2, ...N$, and $N + 1$ being the number of grid points in the x-direction. A convenient choice for the grid points in a Chebychev algorithm are

$$x_j = \cos(j\pi/N), \ j = 1, ..., N,$$

because, despite being economical, this choice results in a very accurate approximation of the solution (*Canuto et al.*, 1988). With this choice for the grid points the Chebychev polynomials become

$$T_k(x_j) = \cos\left(\frac{j\pi}{N}k\right), \ k = 0, ..., N.$$

A continuous function $u(x)$ can be expressed in terms of Chebychev polynomials by

$$u(x_j) = \sum_{k=0}^{N} \alpha_k T_k(x_j).$$

More details of the modelling algorithm are included in Appendix A.3.2.
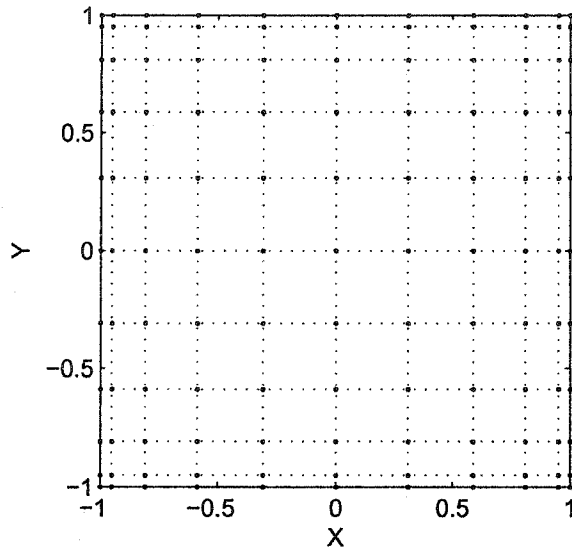
Figure 2.2: A discrete Chebychev grid with 11 grid points in each direction. Note the denser distribution of the grid points towards the edges of the model.

Global pseudo-spectral methods exhibit spectral accuracy in the sense that the error of the approximation decreases exponentially to zero with increasing the degree of the interpolation polynomial. However, as this technique requires a non-uniform distribution of the grid points with a very dense number of nodes at the boundaries of the computational domain and a rather sparse concentration of grid points in the middle (Figure 2.2). It is therefore difficult, if not impossible, to resolve a complex geological structure within the model. To circumvent this problem *Faccioli et al.* (1996) decomposed the computational model into subdomains and solved the wave equation locally on each domain separately[1].

Global pseudo-spectral techniques provide a very accurate simulation of the waves within a model, but the model geometry must be very regular. Additionally, they do not work well for models containing discontinuities such as a layered structure with different parameters (*Press et al.*, 1997). Modelling the seismic response of a small reservoir requires the simulation technique to be able to handle irregular numerical grids contain-

---

[1]Note: This approach is similar to the spectral element method by *Patera* (1984), which will be discussed in section 2.1.4.

55

ing discontinuities. Therefore, this numerical technique is not suitable for the purpose of this work.

2.1.3 Multigrid method

Although multigrid techniques have been used in resistivity modelling (e.g. *Moucha and Bailey*, 2001) and migration/inversion (e.g. *Gray and Epton*, 1989, 1990; *Saleck et al.*, 1993) application to seismic modelling are rare. Apparently, only *Kim* (2001) employed this technique to forward modelling of seismic waves.

The principle of multigrid techniques is that the solution of a partial differential equation is calculated on a fine grid only if there are significant variations of the variables. Otherwise, it is projected onto a coarser grid, or in several steps onto a much coarser grid (*Press et al.*, 1997). On the coarser grid the solution can be calculated with much less computational effort. Afterwards, the solution of the coarser grid is interpolated on the original fine grid.

If this technique is applied to seismic modelling one has to ensure that numerical dispersion does not affect the solution on the coarse grid. As discussed previously the shortest wavelength in the simulation must be supported by a minimum number of grid points. If the wave equation is solved on a too coarse grid the stability and accuracy of the solution is jeopardized by numerical dispersion. On the other hand, starting with a very dense grid to ensure a sufficient support of the wavelet on the coarse grid does not make sense either as it is computational inefficient. Generally, there is one number of grid points that is both sufficient to suppress numerical dispersion and provides the maximum computational efficiency of the model.

Additionally, the computational grid must be designed such that the important geometrical features of the model are sufficiently represented. This criterion is together with numerical stability the main factor that defines the discrete grid spacing. However, after the solution has been projected on a coarser grid the geometrical resolution of the model may be lost. Therefore, similar arguments as previously discussed with respect to numerical accuracy applies: generally, there is an optimum grid spacing for resolving the geometry of the model and computational efficiency.

To which extent multigrid methods can be used in computational seismic modelling

needs to be investigated in more detail. *Kim* (2001) presented an application of multigrid techniques to seismic modelling and experienced convergence problems, which eventually led to a failure of the simulation. He suggested that a lack of physical characteristics in the coarse grid solution as an explanation, which led to instabilities and subsequently caused convergence problems.

2.1.4 The Finite Element Method

The propagation of waves through a finite (or bounded) earth model Ω will be described in terms of displacements, e.g. small perturbation of particles in an elastic medium. The earth model may contain any number of internal interfaces separating regions with different physical properties such as density or elastic constants. A typical problem in seismic modelling is shown Figure 2.3. The model Ω enclosed within the bold line is bounded at the top by a free surface boundary $\partial\Omega$ and an artificial boundary Γ elsewhere. In reality, the seismic waves originating from some point within the earth propagate through the entire earth. In a computer simulation of this phenomenon it is generally not possible, or of interest, to include the entire earth in a model, thus the model must be truncated and artificial boundaries introduced. Seismic waves are reflected at the free surface boundary $\partial\Omega$ and, ideally, they are completely absorbed at the artificial boundaries Γ to mimic the real unbounded propagation.

The equations of motion governing the propagation of waves in elastic solids can be solved numerically based on either the so-called *strong* or the *weak* formulation of the partial differential equations. The strong formulation is the basis for the numerical solution of the problem by finite difference and global pseudo-spectral methods. These techniques deal directly with the equation of motion and associated boundary conditions written in differential form. The weak formulation, which forms the solution basis for the finite element methods, instead transforms the partial differential equation into an integral form which is subsequently solved numerically.

Consider a partial differential operator $\mathcal{L}$ applied to a function $\mathbf{u}$, which is the unknown solution of the differential equation $\mathcal{L}\mathbf{u} = \mathcal{F}$, where $\mathcal{F}$ denotes external forces applied to the problem. Finite element methods solve the weak or variational form of the partial differential equation, which leads to the method of weighted residuals. Instead of
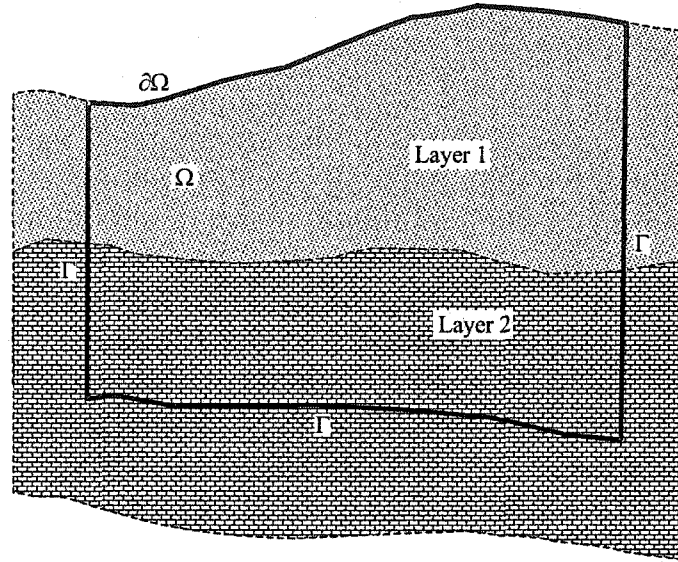
Figure 2.3: A sketch of finite multi-layer earth model Ω with surface topography $\partial\Omega$ and the artificial boundary denoted by Γ.

approximating the derivatives by finite differences, the solution of the differential equation, $u(x, t)$, is approximated by a finite series $\hat{u}(x, t)$ on the N discrete points in the model (e.g. *Lapidus and Pinder*, 1982; *Bathe*, 1990),

$$u(x, t) \approx \hat{u}(x, t) = \sum_{j=1}^{N} U_j(t)\, \phi_j(x) \tag{2.3}$$

In this equation $U_j, j = 1, 2, ..., N$ are the yet undetermined displacements at the grid points. The interpolation functions $\phi_j(x)$ are continuous functions, usually polynomials, that satisfy the boundary condition imposed on the problem. These functions are often called the *basis functions*. While the basis functions are chosen to satisfy the boundary conditions, they will not necessarily perfectly satisfy the partial differential equation. Consequently, upon substituting $\hat{u}(x, t)$ into the partial differential equation, a residual $\mathcal{R}$ will remain:

$$\mathcal{L}\hat{u} - \mathcal{F} = \mathcal{R}. \tag{2.4}$$

For the exact solution u this residual vanishes, and a good approximation must ensure

58

that the residual is small at all points in the model. In line with this concept, the finite element method attempts to determine the unknown coefficients U_j such that the residual $\mathcal{R}$ in the model is minimized at each discrete point. For example, one could require that the integral over the model Ω must be zero

$$\iint_{\Omega} \mathcal{R}(\mathbf{x}, t) \, d\Omega = 0. \tag{2.5}$$

For the unique determination of the N unknowns U_j in equation (2.3) N independent equations of the form (2.5) are necessary. In order to obtain N equations, the above integral can be suitably modified by multiplying equation (2.5) with N *weighting functions* w_i. Setting the integral of each weighted residual to zero yields N independent equations of the form

$$\iint_{\Omega} \mathcal{R}(\mathbf{x}, t) \cdot w_i \, d\Omega = 0, \ i = 1, 2, ..., N \tag{2.6}$$

that are used to determine the unknowns U_j. Upon convergence the residual $\mathcal{R}$ approaches zero since the approximation $\hat{u}(\mathbf{x}, t)$ becomes equal to the exact solution as $N \to \infty$.

The nature of the scheme is determined by the particular choice of the expansion or basis function $\phi_j(x)$ and the weighting functions w_i. Different functions for the interpolation and weighting functions have been used. The collocation method that uses Dirac-delta functions, Chebychev polynomials, leading to the spectral element method, and Lagrangian polynomials are the most commonly used. The Galerkin method that is usually applied in finite element methods assumes that the weighting functions are the same function base as the basis function, that is, $w_i = \phi_i$. The advantage of the Galerkin method over other techniques as, for example, the collocation method is that it produces symmetric and positive system matrices for a certain class of problems, which are preferred in numerical solution algorithms (*Bathe*, 1990).When using Galerkin's method equation 2.6 becomes

$$\iint_{\Omega} \mathcal{R}(\mathbf{x}, t) \cdot \phi_i(\mathbf{x}) \, d\Omega = 0, \ i = 1, 2, ..., N. \tag{2.7}$$

In the finite element method the model of interest is subdivided into several elements of finite size with the function values defined at the corners of the elements (Figure 2.4). The

---

59
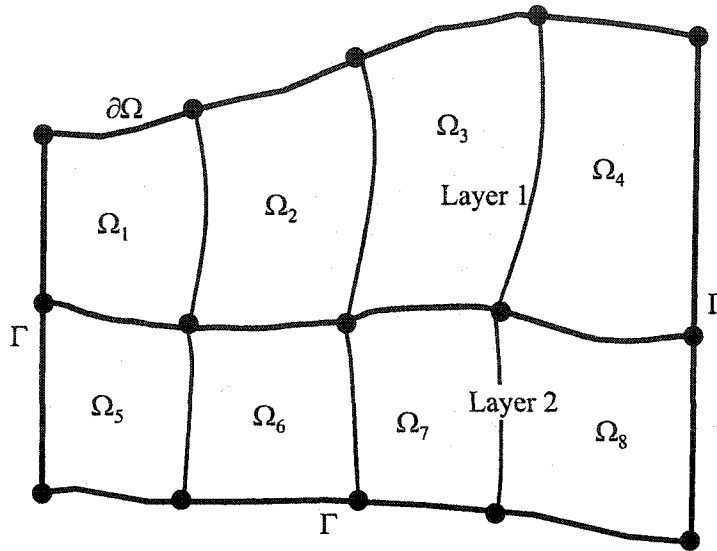
Figure 2.4: The model shown in Figure 2.3 is subdivided into curved elements whose shape are adapted to the boundaries and interfaces of the model.

continuous function is obtained by polynomial interpolation over the elements according to equation (2.3). These polynomials and their derivatives are continuous to a specified order within the element. The interpolating polynomials, which build the function base for the basis and weight functions are chosen such that they assume the value one at the assigned node and zero at all other nodes.

2.1.5 Discussion

The numerical schemes discussed above solve partial differential equations in different ways. Each technique has its advantages and shortcomings in terms of simplicity, numerical accuracy, and geometrical flexibility. Of all these techniques the finite difference method offers the most simplistic modelling approach. However, the potential of the technique to solve partial differential equations numerically is limited in two ways. First, it is not very efficient in suppressing numerical artifacts such as numerical dispersion. Secondly, the requirement of a strictly regular grid significantly reduces the geometrical flexibility of adapting the model to a complex geological model. The pseudo-spectral method reduces numerical artifacts much more efficiently than the finite difference tech-

nique. However, the particular choice of the grid points for the Chebychev polynomials (Figure 2.2) does not easily allow the simulation of wave propagation for geological models containing embedded bodies of arbitrary shape. The best tool for numerical simulation on complicated shaped models is the finite element method. The practicability of the standard finite element method for seismic modelling was always reduced by the poor reduction of numerical artifacts in the simulation (*Marfurt*, 1984). However, the modern improvement of this algorithm called the *spectral element method* (*Patera*, 1984) suppresses numerical dispersion much more efficiently while preserving the geometrical flexibility of the finite element technique. Therefore, the spectral finite element method is the most suitable numerical technique for the purpose of this research.

2.2 The weak form of the elastic wave equation

The elastic wave equation describes the propagation of seismic waves in terms of the particle displacements u of the solid material. The partial differential equation describing this phenomenon is derived by equating Newton's law with the divergence of the generalized Hooke's law, as shown in the following momentum equation (e.g. *Lay and Wallace*, 1995; *Aki and Richards*, 2002):

$$\rho(\mathbf{x})\ddot{u}_i(\mathbf{x},t) = \partial_j\sigma_{ij}(\mathbf{x},t) + f_i^s(\mathbf{x},t), \; i = 1, 2. \tag{2.8}$$

As will become evident, equation (2.8) implicitly describes the propagation of elastic waves by a set of 2nd-order hyperbolic partial differential equations. In this equation, u is the particle displacement vector, and $\rho(\mathbf{x})$ represents the bulk density of the medium. The two dots denote the second derivative of the displacements with respect to time. On the right side of equation (2.8) the first term represents the divergence of the stress tensor σ_{ij}. This stress tensor is linearly related to the strain tensor ϵ_{ij} by Hooke's law, which reads (e.g. *Aki and Richards*, 2002)

$$\sigma_{ij} = c_{ijkl}(\mathbf{x})\,\epsilon_{kl}, \tag{2.9}$$

here the elastic stiffness tensor of rank four is denoted by $c_{ijkl}(\mathbf{x})$. The last term in equation (2.8) is the seismic source vector $\mathbf{f}^s$.

61

For the isotropic case, exclusively considered here, the stress-strain relationship is given by

$$\sigma_{ij} = \lambda \epsilon_{kk} \delta_{ij} + 2\mu \epsilon_{ij}, \tag{2.10}$$

and the strain tensor in indicial notation is defined as

$$\epsilon_{ij} = \frac{1}{2} \left(\frac{\partial u_i}{\partial x_j} + \frac{\partial u_j}{\partial x_i} \right). \tag{2.11}$$

However, anisotropy can be included in the formulation by choosing a different stress-strain relationship.

This formulation of the partial differential equations as in equation (2.8) is called the *strong* form. Finite difference and global pseudospectral methods have been used to solve the partial differential equations in this form numerically by *Kelly et al.* (1976), *Dablain* (1986), *Virieux* (1986), *Levander* (1988), *Kosloff and Baysal* (1982), and *Kosloff et al.* (1990), among others.

2.2.1 Derivation of the Finite Element matrices

As outlined in the previous section the terms in the differential equation are modified in two steps. First, the solution is replaced by a separation ansatz (equation 2.3). Then, the remaining residual is multiplied by a weighting function w to obtain the weak formulation that leads to the integral equations for the finite element method. Upon replacing the displacements u by their polynomial representation û (equation 2.3) and multiplying by the weighting function the first part of equation (2.8) containing the acceleration term ü becomes

$$\iint_{\Omega} \rho(\mathbf{x}) \ddot{\mathbf{u}}(\mathbf{x}, t) \cdot \mathbf{w}_i \, d\Omega \approx \iint_{\Omega} \rho(\mathbf{x}) \ddot{\hat{\mathbf{u}}}(\mathbf{x}, t) \cdot \phi_i \, d\Omega =$$
$$\sum_j \iint_{\Omega} \rho(\mathbf{x}) \ddot{\mathbf{U}}_j(t) \phi_j(\mathbf{x}) \cdot \phi_i(\mathbf{x}) \, d\Omega, \quad i = 1, 2, ..., N. \tag{2.12}$$

As the integration is with respect to the volume Ω and $\ddot{\mathbf{U}}_j$ does not depend on the spatial variables equation (2.12) can be rewritten as

$$\iint_{\Omega} \rho(\mathbf{x}) \ddot{\mathbf{u}}(\mathbf{x}, t) \cdot \mathbf{w}_i \, d\Omega \approx \sum_j \ddot{\mathbf{U}}_j(t) \cdot \iint_{\Omega} \rho(\mathbf{x}) \phi_j(\mathbf{x}) \phi_i(\mathbf{x}) \, d\Omega, \quad i = 1, 2, ..., N, \tag{2.13}$$

After introducing the matrix M

$$M_{ij} = \iint_{\Omega} \rho(\mathbf{x})\phi_j(\mathbf{x})\phi_i(\mathbf{x})\, d\Omega, \tag{2.14}$$

equation (2.12) can now be formally written as a product of a matrix times a vector:

$$\iint_{\Omega} \rho\ddot{\mathbf{u}} \cdot \mathbf{w}_i\, d\Omega \approx M_{ij}\ddot{U}_j = \mathbf{M} \cdot \ddot{\mathbf{U}}. \tag{2.15}$$

The matrix M is traditionally called the *mass* matrix in the finite element literature.

The next term to be evaluated contains the divergence of the stress tensor. After multiplying by the weighting function vector and subsequently integrating by parts, one obtains (*Valette*, 1986)

$$\iint_{\Omega} \mathbf{w} \cdot (\nabla \cdot \sigma)\, d\Omega = -\iint_{\Omega} \nabla\mathbf{w} : \sigma\, d\Omega + \int_{\Gamma} (\sigma \cdot \hat{n}) \cdot \mathbf{w}\, d\Gamma. \tag{2.16}$$

For the sake of simplicity a Dirichlet boundary condition is assumed in the subsequent derivation such that $\sigma = 0$ on the boundary Γ. In this case the boundary integral in equation (2.16) vanishes. The : - operator appearing in the volume integral denotes doubly contracted tensor multiplication (e.g. $\sigma : \nabla\mathbf{w} = \sigma_{ij}\,w_{j,i}$). Using also $\sigma_{ij} = c_{ijkl}\,u_{k,l}$, the first term of this tensor product becomes

$$\sigma : \nabla\mathbf{w} = \pi\frac{\partial u_1}{\partial x_1}\frac{\partial w_1}{\partial x_1} + \dots .$$

Here, $\pi = \lambda + 2\mu$ has been used for the sake of brevity. Upon using this expression together with the polynomial representation of the solution u and the weight function w, the integral in equation (2.16) becomes

$$\iint_{\Omega} \mathbf{w}_i \cdot (\nabla \cdot \sigma)\, d\Omega \approx \sum_j \left(U_j \cdot \iint_{\Omega} \pi\omega_1\frac{\partial \phi_i}{\partial x_1}\frac{\partial \phi_j}{\partial x_1}\, d\Omega + \dots \right). \tag{2.17}$$

The last integral can again be formally regarded as an element of a matrix K such that

$$K_{ij} = \iint_{\Omega} \pi\omega_1\frac{\partial \phi_i}{\partial x_1}\frac{\partial \phi_j}{\partial x_1}\, d\Omega + \dots . \tag{2.18}$$

This matrix K is often called the *stiffness* matrix in the finite element literature. The right hand side of equation (2.16) can now be written as

$$\iint_{\Omega} \mathbf{w} \cdot (\nabla \cdot \sigma)\, d\Omega \approx K_{ij}U_j = \mathbf{K} \cdot \mathbf{U}. \tag{2.19}$$

The last term to be evaluated in equation (2.8) is the source term. In the seismological literature it is usual to describe the source by a 2nd-order moment tensor S_{ij} (e.g. *Lay and Wallace*, 1995) according to

$$f_i^s = -\partial_j S_{ij}. \tag{2.20}$$

If the spatially distributed source tensor is actually point source the source moment tensor becomes $S_{ij}(\mathbf{x}) = S_{ij}\,\delta(\mathbf{x})$. After applying the weak formulation to (2.20) and making use of the properties of the delta function, we find that

$$\mathbf{F}_s = \mathbf{S} : \nabla \mathbf{w}. \tag{2.21}$$

After applying the finite element algorithm to the elastic wave equation (2.8) it finally becomes a linear matrix equation

$$\mathbf{M} \cdot \ddot{\mathbf{U}} + \mathbf{K} \cdot \mathbf{U} = \mathbf{F}_s. \tag{2.22}$$

Thus, the finite element method has transformed the partial differential equation into an algebraic system of ordinary differential equations that may now be solved using linear algebraic techniques. For example, if the second time derivative of $\mathbf{U}$ in equation (2.22) is approximated by a central difference operator

$$\ddot{\mathbf{U}}^k \approx \frac{\mathbf{U}^{k+1} - 2\mathbf{U}^k + \mathbf{U}^{k-1}}{\Delta t^2}, \tag{2.23}$$

then the displacements in the model at time step t^{n+1} can be calculated from the known values of $\mathbf{U}$ at the times t^n and t^{n-1}, respectively according to

$$\mathbf{U}^{k+1} = 2\mathbf{U}^k - \mathbf{U}^{k-1} + \Delta t^2 \mathbf{M}^{-1} \cdot (\mathbf{F}_s - \mathbf{K} \cdot \mathbf{U}^k). \tag{2.24}$$

Although finite difference schemes are readily implemented, they must be used carefully as discussed above. It is well-known that finite-difference algorithm become unstable if the time step Δt is too large (e.g. *Press et al.*, 1997, among others). To ensure stability of the numerical solution the Courant condition often requires such a small time step that finite-difference methods can be computationally uneconomical. However, as these matrices $\mathbf{M}$ and $\mathbf{K}$ are sparse, the resulting calculations can be performed fast and the requirement of a small time step for finite difference is not a severe limitation for the computational performance.

2.2.2 The finite element mesh

The accurate incorporation of the surface topography and the interfaces as exemplified in Figure 2.3 is not trivial for most of the methods discussed in the preceding sections. Using domain decomposition, the finite element method subdivides the model Ω into N_{el} elements Ω_e of finite size such that

$$\Omega = \bigcup_{e=1}^{N_{el}} \Omega_e.$$

Upon this approach a very accurate match to the geological structure is possible, as the shape of the elements can be adapted to both boundary edges $\partial\Omega$ and Γ and the interior interfaces bounding geological layers of contrasting physical properties of the model (Figure 2.4). Continuity of the numerical grid within the model is ensured by the finite element nodes, i.e., the vertices shared by adjacent elements. Generally, the elements can have triangular and quadrilateral shapes; however, to my knowledge, an efficient and accurate implementation of the spectral finite element method is at the current state restricted to the use of quadrilateral elements alone. This restriction arises from the construction of the interpolation functions in 2D and 3D, as will be shown in the following section.

After the model has been subdivided into several elements the integrals introduced in the previous section do not need to be evaluated over the entire model but are separately calculated locally for each element. This procedure results in *local* matrices $\mathbf{M}_e$ and $\mathbf{K}_e$, which are combined into the global matrices by an *assembling* process

$$\iint_{\Omega} f \, d\Omega = \bigcup_{e=1}^{N_{el}} \iint_{\Omega_e} f \, d\Omega.$$

The basis and weighting function for corner or edge nodes span over neighbouring elements (see Figure 2.5). After determining the local matrices the contribution from all elements to a node are combined to form the *global* matrices by summation of each element's contribution.

Each quadrilateral element is isomorphous to the unit reference square Λ defined by $[\xi, \eta]$, $-1 \le \xi \le 1$, $-1 \le \eta \le 1$. As such, there always exists a unique mapping from the reference square to the element of the mesh. Each element is geometrically defined by a

65
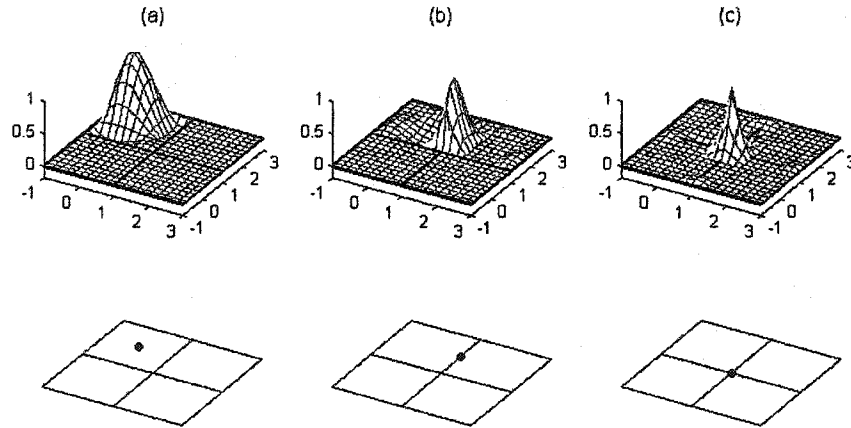
Figure 2.5: 2D interpolation functions for (a) a internal point, (b) a point on an edge, and (c) a corner point of a quadrilateral element.

set of n_a control or anchor points x_a and a set of n_a shape functions $N_a(\xi, \eta)$. Figure 2.6 shows two types of quadrilateral elements, which are defined by nine and four anchor points, respectively. Elements with four anchor points are sufficient when the model consists of straight boundaries and interfaces. If nine anchor points are used then the shape of the element can be better approximated to curved edges of the model. The relation between a point x within an element Ω_e and a point $\xi = (\xi, \eta)$ in the reference square Λ is given by the transformation

$$x(\xi, \eta) = \sum_{a=1}^{N_a} N_a(\xi, \eta) x_a. \tag{2.25}$$

The shape functions are products of Lagrangian polynomials of degree one for elements with four anchor points and two, if nine anchor points define the element (Bathe, 1990).

As Lagrangian polynomials are important for the numerical procedure they will be discussed in more detail in the following section.

66
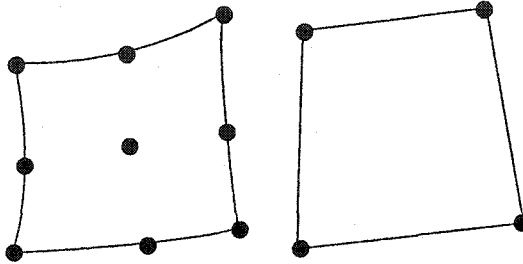
Figure 2.6: Two quadrilateral elements defined by nine (left) and four (right) anchor points.

2.2.3 Polynomial representation on elements

In the traditional finite element method the model is broken into many small quadrilateral or triangular elements and the function values are expanded over the elements by low-order polynomials. This approach is often called the h-method (*Canuto et al.*, 1988), where h is a measure of the size of the elements. Global pseudo-spectral methods do not divide the model into subdomains but approximate the solution function by high-order polynomials. This technique is often referred to as the p-method with p being the order of the polynomial used. While the h-finite element method allows for excellent flexibility in designing a model, it suffers significantly from numerical artifacts such as dispersion. The p-approach, on the other hand, allows an efficient reduction of numerical dispersion. However, the drawback of this technique is the difficulty of incorporating complex-shaped models or even multi-layer models. A modern variant of the classical finite element method, the spectral element method (*Patera*, 1984) or hp-method (*Karniadakis and Sherwin*, 1999), combines the advantages of both the h and p-method. The computational model Ω is subdivided into finite elements Ω_e. Within each element the functions are approximated by higher-order polynomials. To ensure continuity across the model Ω these polynomials must be continuous at the edges $\partial\Omega_e$ of the elements.

In the classical pseudo-spectral methods trigonometric functions or Chebyshev polynomials have been employed for the interpolation polynomials ϕ (e.g. *Canuto et al.*, 1988; *Gazdag*, 1981; *Kosloff and Baysal*, 1982; and *Kosloff et al.*, 1990), whereas the classical finite element method uses low-order Lagrangian polynomials. The advantage of the spectral

polynomials (i.e. trigonometrical or Chebyshev) is that for a sufficiently smooth solution, the convergence of the method is faster than $1/N$ (*Canuto et al.*, 1988). However, using spectral polynomials for the expansion of the functions over the elements is problematic as they do not provide C^0 continuity across the boundaries of the elements (*Blackburn and Schmidt*, 2003). To overcome this problem modern spectral element methods use high-order Lagrangian polynomials to approximate the solution on the elements, this still preserves the accuracy and fast convergence of spectral methods provided the solution is sufficiently smooth (e.g., *Henderson and Karniadakis*, 1995; *Giraldo*, 1998 and *Blackburn and Schmidt*, 2003).

The spectral finite element method is an *h-p* finite element that approximates the functions within each element by a high-order polynomial such as Lagrangian polynomials of degree n_l, which are defined on the interval $[-1\ 1]$ as

$$\ell_\alpha^{n_l}(\xi) = \frac{(\xi - \xi_0)\cdots(\xi - \xi_{\alpha-1})(\xi - \xi_{\alpha+1})\cdots(\xi - \xi_{n_l})}{(\xi_\alpha - \xi_0)\cdots(\xi_\alpha - \xi_{\alpha-1})(\xi_\alpha - \xi_{\alpha+1})\cdots(\xi_\alpha - \xi_{n_l})}. \tag{2.26}$$

For a given degree n_l of the polynomials there are $n_l + 1$ functions distinguished by the order α with $0 \le \alpha \le n_l$ and defined by $n_l + 1$ *collocation points* $\xi_\alpha \in [-1\ 1]$. A property of the Lagrangian polynomial is that the αth polynomial assumes the value of one at only the collocation point ξ_α but is equal to zero at all other collocation points:

$$\ell_\alpha^{n_l}(\xi_\beta) = \delta_{\alpha\beta}. \tag{2.27}$$

This property, often called the *discrete orthogonality* of the Lagrangian polynomials (*Blackburn and Schmidt*, 2003), is important as it ensures a reduction of numerical dispersion similar to spectral methods. Another advantage of this property is that the use of Lagrangian polynomials will result in diagonal mass matrices, as will be shown in the next section. This matrix structure is preferable for a computational efficient program.

Interpolation polynomials in higher dimensions are obtained by tensor multiplication. For example, in two dimensions the interpolant is defined as (Figure 2.7)

$$\ell_{\alpha\beta}^{n_l}(\xi, \eta) = \ell_\alpha^{n_l}(\xi)\ell_\beta^{n_l}(\eta). \tag{2.28}$$

If the values of a function f defined at the collocation points are denoted by f_α then an
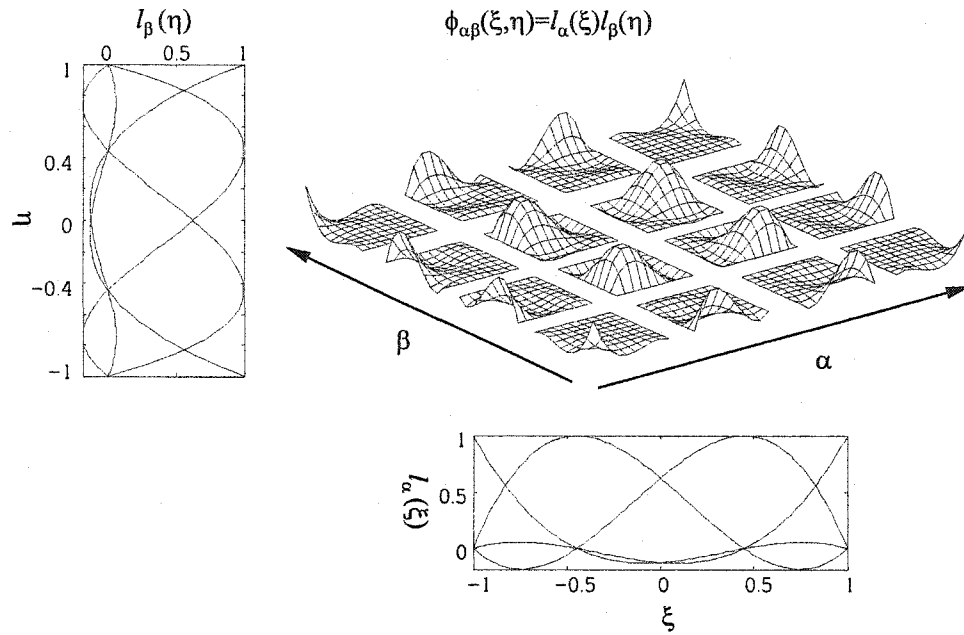
Figure 2.7: Construction of a 2D interpolating function from two Lagrangian polynomial of degree 3

approximation to the continuous function $f(\xi)$ can be calculated by

$$f(\xi) = \sum_{\alpha=0}^{n_l} f_\alpha \, \ell_\alpha^{n_l}(\xi).$$ (2.29)

in one dimension and similarly in two dimensions by

$$f(\xi, \eta) = \sum_{\alpha,\beta=0}^{n_l} f_{\alpha\beta}\ell_{\alpha\beta}^{n_l}(\xi, \eta).$$ (2.30)

The Jacobian of the mapping (2.25), which will be necessary for the numerical integration, is defined by

$$J = \left\| \frac{\partial \mathbf{x}}{\partial \xi} \times \frac{\partial \mathbf{x}}{\partial \eta} \right\|.$$ (2.31)

69

The requirement of the unique existence of the Jacobian and its inverse imposes certain constrains on the shape of the elements (e.g. *Bathe*, 1990). That the relation between the local and the natural coordinates must be definite is required, that is, a value (ξ, η) in Λ corresponds exactly to only one value in the (x, y)-domain. This essential requirement can be violated if the mesh contains self-overlapping or extremely distorted elements (*Bathe*, 1990).

The partial differentials occurring in equation (2.31) are calculated by differentiating the mapping (2.25):

$$\partial_\xi \mathbf{x}(\xi, \eta) = \sum_{a=1}^{n_a} \partial_\xi N_a(\xi, \eta) \, \mathbf{x}_a, \tag{2.32a}$$

$$\partial_\eta \mathbf{x}(\xi, \eta) = \sum_{a=1}^{n_a} \partial_\eta N_a(\xi, \eta) \, \mathbf{x}_a. \tag{2.32b}$$

The general derivative of a Lagrangian polynomial (2.26) is calculated according to

$$\frac{d\ell_\alpha^{n_l}}{d\xi} = \left(\sum_{k=0}^{n_l} \prod_{\substack{i=0 \\ i \neq k}}^{n_l} (\xi - \xi_i) \right) \bigg/ \left(\prod_{\substack{i=0 \\ i \neq \alpha}}^{n_l} (\xi_\alpha - \xi_i) \right) \tag{2.33}$$

Using equations 2.26 and 2.33 the partial derivatives of the shape functions can be calculated analytically.

2.2.4 Numerical integration

Up till now it has been assumed that all integrals are determined analytically. After an element has been mapped onto the reference square Λ the integrals in the Finite Element equations are of the form

$$\int_{-1}^{1} f(\xi) d\xi.$$

As the mapping depends on the shape of the elements it will therefore be different for every element. The integrals cannot be evaluated analytically; numerical integration, also called quadrature, must be used.

Assuming that the function f can be approximated by a polynomial representation

70

such as in equation (2.3) the above integral becomes

$$\int_{-1}^{1} f(\xi)d\xi \approx \int_{-1}^{1} \hat{f}(\xi)d\xi =$$
$$\int_{-1}^{1} \sum_{i=0}^{n} F^i \phi_i(\xi)d\xi. \tag{2.34}$$

Upon interchanging summation and integration by making use of the fact that values of F^i do not depend on ξ the last expression in equation (2.34) then becomes

$$\sum_{i=0}^{n} \left(\int_{-1}^{1} \phi_i(\xi)d\xi \right) F^i = \sum_{i=0}^{n} \omega_i F^i,$$
$$\text{with } \omega_i = \int_{-1}^{1} \phi_i(\xi)d\xi. \tag{2.35}$$

Therefore, numerical integration algorithms approximate the integral of a function by a sum of its value at a set of collocation points multiplied by aptly chosen weighting factors, which depend on the interpolation function being used and the number of discrete sections the interval $[-1\ 1]$ is subdivided into.

Several numerical integration techniques are available, which differ in the choice of interpolation polynomials and the collocation points. Most commonly used are Gaussian quadrature as they evaluate the integrals accurately (*Press et al.*, 1997). Among the Gaussian quadratures there are several different versions. In the classical finite element method a *Gauss-Legendre* quadrature is used. The modern spectral finite element method, however, prefers the *Gauss-Lobatto-Legendre* quadrature.

The Gauss-Lobatto-Legendre quadrature assumes the use of Lagrangian polynomials (2.26), where the collocation points ξ_α, in the following referred to as the *Gauss-Lobatto-points*, are the roots of

$$(1 - \xi)^2 L'_m(\xi) = 0, \tag{2.36}$$

where $L'_m(\xi)$ is the derivative of the Legendre polynomial of degree m, which are recursively defined by (*Canuto et al.*, 1988)

$$L_m(\xi) = \frac{2m - 1}{m} \xi L_{m-1}(\xi) - \frac{m - 1}{m} L_{m-2}$$

71

and its derivative follows as

$$L'_m(\xi) = \frac{m}{1 - \xi^2}(L_{m-1} - \xi L_m).$$

The quadrature weights ω_i are calculated according to (*Canuto et al.*, 1988)

$$\omega_i(\xi_i) = \frac{2}{m(m+1)L_m(\xi_i)^2} \qquad i = 0, \ldots, m, \tag{2.37}$$

where ξ_i are the m collocation points previously determined as the roots of equation (2.36).

Integration in two dimension is accomplished in a similar way:

$$\int\int\limits_{-1}^{1} f(\xi, \eta) d\xi \approx \sum_{\alpha=0}^{n} \sum_{\beta=0}^{n} \omega_\alpha \omega_\beta F^{\alpha\beta}. \tag{2.38}$$

In this equation $F^{\alpha\beta}$ are the values of the function f evaluated at the Gauss-Lobatto points.

Using the algorithms discussed so far the mass matrix $\mathbf{M}$ (equation 2.14) and the stiffness matrix $\mathbf{K}$ (equation 2.18) can be determined numerically. For the mass matrix we find after mapping the element Ω_e onto the reference square Λ that

$$
\begin{aligned}
M_{ij} &= \int\int\limits_{\Omega_e} \rho \phi_j \phi_i \, d(x, y) \\
&= \int\int\limits_{-1}^{1} \rho \phi_j \phi_i J(\xi, \eta) \, d(\xi, \eta) \\
&\approx \sum_{\alpha=0}^{N} \sum_{\beta=0}^{N} \omega_\alpha \omega_\beta \rho^{\alpha\beta} \phi_j^{\alpha\beta} \phi_i^{\alpha\beta} J^{\alpha\beta}.
\end{aligned}
\tag{2.39}
$$

Remembering that on Λ $\phi_i(\xi, \eta)$ and $\phi_j(\xi, \eta)$ are defined in terms of Lagrangian polynomials as

$$\phi_i(\xi, \eta) \rightarrow \ell_{\sigma\tau}^{n_l}(\xi, \eta) = \ell_\sigma^{n_l}(\xi)\ell_\tau^{n_l}(\eta)$$

$$\phi_j(\xi, \eta) \rightarrow \ell_{\mu\nu}^{n_l}(\xi, \eta) = \ell_\mu^{n_l}(\xi)\ell_\nu^{n_l}(\eta)$$

and making use of the discrete orthogonality of the Lagrangian polynomials (equation 2.27) it can be shown that the product of the four Lagrangian polynomials in the Gauss-Lobatto-Legendre quadrature is equivalent to (Appendix A.1):

$$\ell_\sigma^{n_l}(\xi^\alpha)\ell_\tau^{n_l}(\eta^\beta)\ell_\mu^{n_l}(\xi^\alpha)\ell_\nu^{n_l}(\eta^\beta) \Leftrightarrow \delta_{ij}.$$

72

This implies that the mass matrix has only entries in the main diagonal with

$$M_{ii} = \sum_{\alpha=0}^{n_l} \sum_{\beta=0}^{n_l} \omega_\alpha \omega_\beta \rho^{\alpha\beta} J^{\alpha\beta}$$

$$M_{ij} = 0 \text{ for } i \neq j.$$

(2.41)

This is one of the chief advantages of the Gauss-Lobatto-Legendre quadrature compared to, for example, the Gauss-Legendre method. The diagonality of the mass matrix is important from a computational point of view in such that it first means a considerable reduction in the memory required (as only the diagonal elements have to be stored) and that the inversion of the matrix **M** needed in equation (2.24) is equal to $M_{ii}^{-1} = 1/M_{ii}$; the off-diagonal elements of the inverted matrix, M_{ij}^{-1}, $i \neq j$, are zero.

2.3 Boundary conditions

In reality wave propagation occurs in an infinite, unbounded medium, but in numerical simulations the model must be constrained to a size suitable to the available computer memory and simulation time. For these reasons the model must be truncated and boundaries must be introduced at the bottom and sides of the model. As these are not present in reality they are often called artificial boundaries. The introduction of such boundaries in the models causes waves to be reflected from the boundaries whereas, in the actual physical process, waves pass through these locations with no reflection. *Reynolds* (1978) demonstrated that the standard boundary conditions, i.e. Dirichlet and von-Neumann conditions, result in the total reflection of the wave energy at the boundaries; therefore, different boundary conditions must be formulated.

The introduction of these artificial boundaries causes waves to be reflected from the boundaries if no special conditions are imposed on them. These reflection are not consistent with the physical process being simulated, as waves in the real situation pass through these boundaries. In order to avoid reflections of the waves at these artificial boundaries some numerical conditions must be applied to reduce, or eliminate, the wave energy travelling back into the interior of the model. This requirement led to the term 'non-reflecting boundary' conditions, which is widely used in the literature. The development of efficient boundary conditions has been a research topic since numerical mod-

73

elling has been introduced in the geophysical community and is still a subject of ongoing research.

In a review article on non-reflecting boundary conditions *Givoloi* (1991) formulated several requirements that a successful artificial boundary condition must fulfill:

- First, the interior of the model with the artificial boundary condition should be a good approximation of the real situation in the infinite domain, which implies that the interior of the model must include all the interesting, or important, features of the geology being simulated. This is because the use of non-reflecting boundary conditions will not allow any energy scattered or reflected at a reflector outside the model to propagate back into the model.

- Secondly, the boundary condition must be compatible with the numerical scheme, it must not involve enormous computational effort, and it must not reduce the computational performance of the modelling method.

- And third, the energy of the spurious reflections generated at the artificial boundaries should be insignificant, if it cannot be eliminated.

Two different approaches have been developed to eliminate the spurious reflections from the artificial boundaries.

1. The first type of boundary conditions attempt to decrease the wave amplitude gradually as the wave approaches the boundaries in a damping layer that surrounds the model. In this case, only a small amount of wave energy reaches the edge of the model to be reflected back. Hence, the artificial boundary condition seems to be transparent to outgoing waves. Several techniques have been developed to attenuate the wave energy towards the boundary of the model. *Lysmer and Kuhlemeyer* (1969) applied a viscoelastic layer around the central part of the model in which the wave energy is forced to dissipate. This technique is particularly useful if viscoelastic mechanisms are employed in the simulation. An increasing damping coefficient can be used to achieve the decay of the wave amplitude towards the boundaries. If, however, the propagation of waves in an purely elastic medium is the goal of the simulation, then this boundary condition is rather incompatible.

Generally, including viscoelastic rheology in the simulation algorithm requires significantly more memory to store additional imaginary moduli and this also makes the computational work considerably greater (*Carcione*, 1988, *Carcione et al.*, 1988, and *Carcione*, 1993). An additional drawback of this approach is the difficulty in choosing appropriate damping parameters. It is well known that reflections occur not only at interfaces between two layers with different elastic impedances, but also at changes in the Q-value (*Kjartansson*, 1979). Therefore, the transition from the interior to the boundary zone of the model must be chosen carefully to avoid new artificial reflections. Often a gradual damping profile is applied that increases the energy reduction with distance from the boundary of the central part of the model.

To overcome the conceptual difficulties of the viscoelastic damping technique *Cerjan et al.* (1985) and *Kosloff and Kosloff* (1986) developed instead a method in which the amplitudes of waves travelling towards a boundary of the model gradually decreases. A layer surrounds the model in which the wave amplitude is forced to decrease exponentially. Their implementation of this boundary condition into a pseudo-spectral modelling method proved to be efficient and numerically feasible. However, the slow decay of the amplitude in the boundary layer requires the absorbing zone to be rather wide. A significant amount of memory must be used, making this method computationally inefficient. Additionally, the reduction of the wave amplitude by multiplying it by an exponential function is actually mathematically the same as introducing an inelastic damping in the boundary layer, as suggested by *Furumura and Takenaka* (1995). Therefore, additional spurious reflections will occur as for the viscoelastic damping technique.

2. The second method imposes a local condition on the boundary to reduce reflection. The principle concept of these absorbing boundary conditions, which are based on paraxial approximation of the acoustic and elastic wave equations (*Clayton and Enquist*, 1977), is to separate the wave field propagating out of the model from the wave field being reflected at the artificial boundary Γ and propagating back into the model. Consider the acoustic wave equation:

$$\left(\frac{\partial^2 u}{\partial t^2} - c^2 \frac{\partial^2 u}{\partial x^2} \right) = \left(\frac{\partial u}{\partial t} - c \frac{\partial u}{\partial x} \right) \left(\frac{\partial u}{\partial t} + c \frac{\partial u}{\partial x} \right).$$

The second-order wave equation is decomposed into two components propagating in the positive and negative x-direction, respectively. At an artificial boundary a new operator can now be defined to eliminate the component that represents the wave travelling back into the model. This technique, first used by *Clayton and Enquist* (1977) works particularly well for simulations of acoustic waves in one-dimensional models. As this boundary condition can only be optimized for one wave velocity at a time, it will not be efficient for elastic waves where two waves (i.e. P and S) are present with different propagation speeds. The second shortcoming of this technique is that it does not work satisfactorily well for waves travelling at inclined angles towards the boundary. Especially to improve the absorption of incident waves *Higdon* (1991) suggested a modified paraxial approximation scheme that uses higher-order operators. However, the use of high-order operators make this boundary condition difficult to implement in an existing finite element program.

Clearly, there is no perfect boundary condition that reduces spurious reflection efficiently and is also computational effective. In an attempt to improve the efficiency of each technique, the two schemes will be combined here. The model will be surrounded by an additional layer where the wave field amplitudes are reduced. Theoretically, the remaining wave energy will then be reduced furthermore by a simple paraxial boundary condition.

2.3.1 Rayleigh attenuation

Attenuation can be included in the algorithm by adding a damping matrix C in equation (2.22), which then becomes

$$M \cdot \ddot{U} + C \cdot \dot{U} + K \cdot U = F_s. \tag{2.42}$$

The structure of the damping matrix depends on the attenuation method employed. Here, a Rayleigh damping technique is employed to achieve the attenuation in the boundary layer. This algorithm is suitable to finite element modelling of the wave equation as the damping matrix C is defined as a linear combination of the mass M and stiffness K matrices (*Bathe*, 1990)

$$C = \alpha M + \beta K. \tag{2.43}$$

76

The absorption coefficients α and β can be expressed in terms of the material properties and the frequency of the wave using a set of equations of the form (*Caughey*, 1960)

$$\alpha + \beta\omega_i^2 = 2\omega_i\gamma, \ i = 1, \ 2, \tag{2.44}$$

where ω_i are two frequencies within the bandwidth of the source wavelet and γ are material -dependent damping parameters. *Sarma et al.* (1998) report values of γ ranging from about 0.05 (hard crystalline rocks) to 0.30 (loose soil) for geological matter. With numerical tests these authors narrowed the efficient range for damping to $0.2 \le \gamma \le 0.3$. If γ is less than 0.2 a damping effect was not observed. On the other hand, these authors could not recognize further improvement of the attenuation of the waves if γ excesses 0.3.

Upon solving equation (2.44) the absorption coefficients can be determined. For example the peak frequency and the lower or upper half width frequency of the wavelet can be employed to determine α and β.

To test the boundary condition a simple homogeneous model similar to that used by *Sarma et al.* (1998) was constructed with the material properties provided in Table 2.3 (Figure 2.8). To dissipate wave energy at the edges of the model, it is surrounded by an absorbing layer on the left, right, and the bottom. The finite element mesh, consisting of 400 elements, is uniform to avoid potential numerical artifacts from a distorted mesh. The choice of the degree for the interpolation polynomial was rather conservative in that a relatively high degree was chosen to safely suppress numerical dispersion. The source was represented by a vertical point force applied in the center of the model and its time evolution was described by a Ricker wavelet with a central frequency of $f_c = 25$ Hz. In order to meet the stability criterion according to the Courant number the time step Δt was selected with respect to the maximum wave speed and a 'typical length scale' h of the model after

$$\Delta t < \frac{h}{\sqrt{2}V_P}.$$

An estimate for the length scale is the average size of the elements divided by the degree of the interpolating polynomial (*Komatitsch and Vilotte*, 1998).
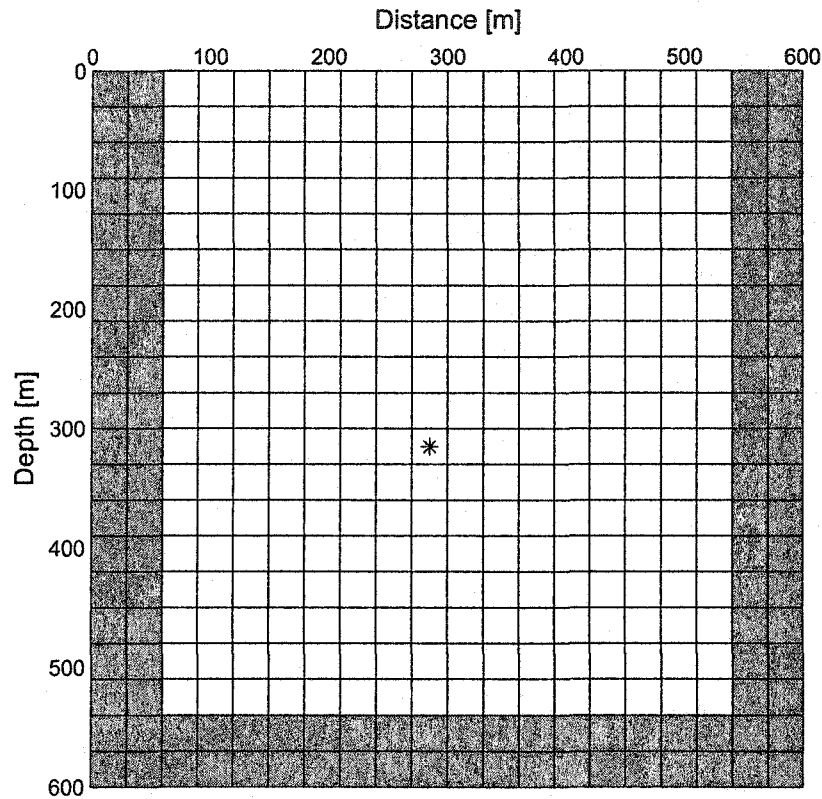
Figure 2.8: Sketch of the boundary test model. The source position is marked by a '*', and the elements within the absorbing boundary layer are plotted in gray.

2.3.2 Results

The numerical solution of equation (2.42) is accomplished by first approximating the time derivatives using the central finite difference operators. The resulting difference equation is then solved using a Newmark integration scheme (e.g. *Bathe*, 1990). The details of this algorithm are described in more details in Appendix A.2.1. The displacement field calculated at progressive times is shown in Figure 2.9. The snapshots shown in the left column result from a simulation without an absorbing boundary condition applied to the model, that is, a free surface condition was applied at all boundaries of the model. The waves propagate radially from the source towards the edges of the model where they are reflected back into the model. These results are in accordance with the expected wave

78

Table 2.1: Properties of the absorbing boundary test model.

(a) Seismic parameters

ρ [kg/m^3]	V_P [m/s]	V_S [m/s]
2000.0	4000.0	2000.0

(b) Mesh data

$N_{elements}$	n_ℓ	N_{nodes}	Model size	
400	6	14641	x: 600 m	z: 600 m

(c) Absorption parameters

γ	f_1 / f_2	α	β
0.25	25.0 Hz / 41.2 Hz	48.89 1/s	0.0012 s

propagation behavior; this figure shows that the numerical algorithm works properly on a simple model. In the simulation data presented in the right column of Figure 2.9 the two outermost elements of the model included damping parameters. The inclusion of attenuation in the boundary layer, however, causes strong numerical instabilities in the center of the model. That is, the waves do not propagate uniformly from the source, and compared to the images in the left column the propagation speed of the waves is reduced. This effect occurred regardless of the value chosen for the damping parameter γ or the width of the boundary layer. It seems that the contrast between the damping parameter within the center of the model ($\gamma = 0$) and the boundary layer ($\gamma > 0$) causes the instabilities of the simulation.

The Rayleigh damping technique, a standard method to include inelasticity in engineering finite element simulation, has been employed by *Sarma et al.* (1998) in seismic modelling to attenuate plane waves at the boundaries of their model. The simulation performed for this work caused severe numerical instabilities, which made the modelling impossible.

It seems that the numerical approach, that is the Newmark scheme along with the Conjugate Gradient matrix solver, of solving equation (2.42) is not the cause of the problem as the simulation without damping in Figure 2.9, left column, shows. One of the major differences between this work and the one by *Sarma et al.* (1998) is that they used a *plane wave* excitation at the surface as the source (that is, an array of sources along the surface of the model), whereas point sources were used here. The existing program is
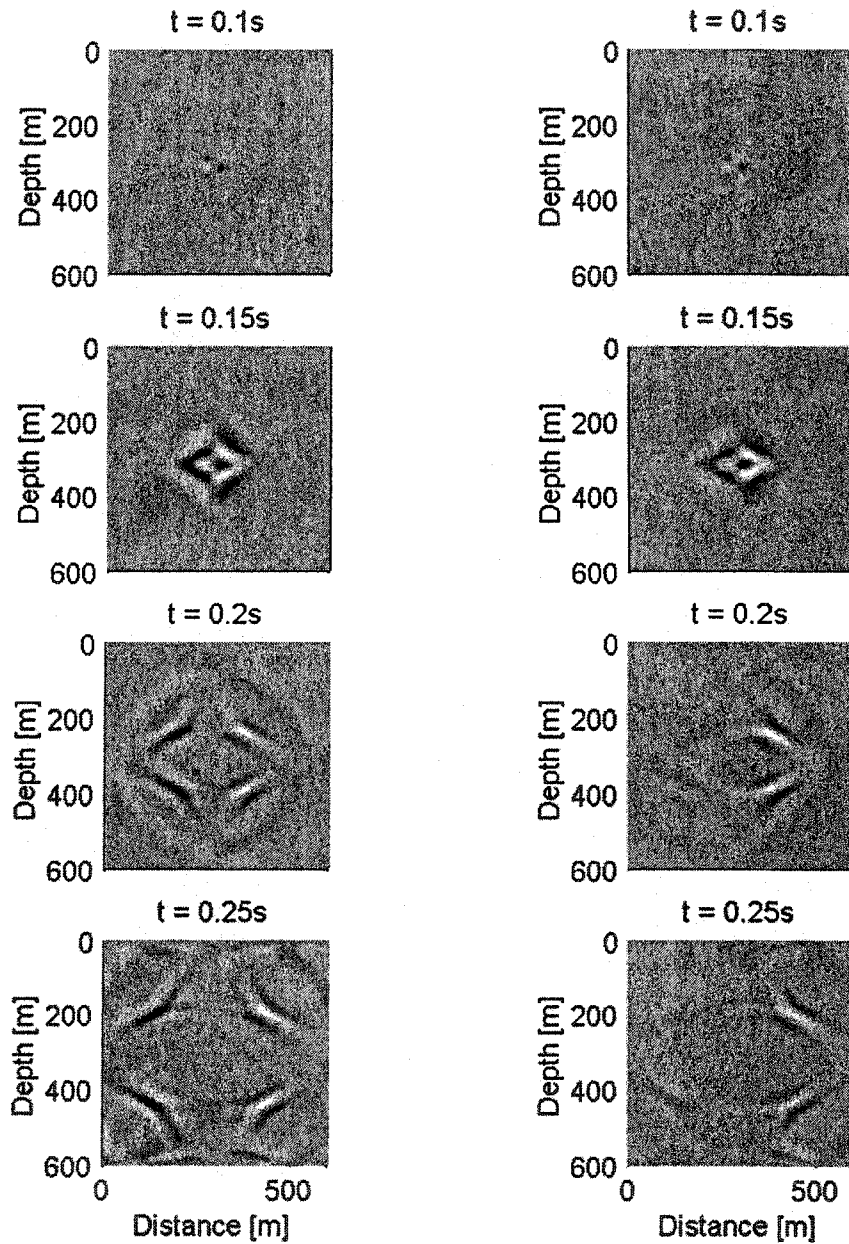
Figure 2.9: Results of the absorbing boundary layer test (vertical displacements). Left: without wavefield attenuation, right: including Rayleigh attenuation.

incapable of exciting plane waves. The present program was not modified because the plane wave simulation does not properly model the wavefield response needed for the simulated seismic required for the current study. Therefore, a direct comparison between the performance this finite element program and the results published by *Sarma et al.* (1998) was not possible.

2.4 Numerical experiment

The efficiency and accuracy of the spectral finite element method is chiefly controlled by the size of the elements, the length of the time step, and the degree of the Lagrangian polynomials. All these parameters are connected to each other by requirements that ensure reduction of numerical dispersion, stability, and adaptability of the mesh to the geometrical model. The purpose of this section is threefold. First, the conditions ensuring stability and reduction of numerical dispersion are discussed. Then, the accuracy of the algorithm is tested against a reflectivity method that provides accurate synthetic data for horizontal interfaces. Finally the potential of this method for seismic modelling is illustrated for a simple but realistic example.

2.4.1 Performance parameters

The spatial accuracy of the algorithm, mainly determined by the reduction of numerical dispersion, is controlled by the typical size of the elements, h, and the degree of the Lagrangian interpolant, n_ℓ. The spectral finite element method mainly differs from traditional finite element techniques in that n_ℓ is significantly larger. In practice, if the polynomial degree is too small the spectral finite element method becomes essentially equivalent to the standard finite element method and as such suffers in the same way from numerical dispersion (*Marfurt*, 1984). To efficiently suppress numerical dispersion the smallest wavelength in the simulation must be supported by a certain minimum number of grid points (e.g. *Press et al.*, 1997). This critical number can be determined by a von-Neumann analysis for finite difference and global pseudo-spectral methods (e.g. *Karrenbach*, 1996, see Appendix A.4). However, such an analysis is rather cumbersome and instead, one must rely on numerical experiments to determine an optimum combination

of the element size and the polynomial degree. *Faccioli et al.* (1997), *Komatitsch and Vilotte* (1998), and *Komatitsch and Tromp* (1999) report that numerical dispersion is sufficiently suppressed if the minimum wavelength λ_{min} meets the following criterion:

$$\frac{\lambda_{min} \; (n_\ell + 1)}{h} \approx 5.$$

This means that the average size of the elements must be chosen such that the minimum wavelength is supported by roughly five points in order to obtain accurate results.

The upper limit for the frequency bandwidth of the seismic signal is also closely related to the shortest possible wavelength. Ricker wavelets (*Ricker*, 1953) are often employed in seismic modelling to describe the characteristics of the source time series. Ricker wavelets are defined by the central frequency f_c; its upper limit that can be supported by the mesh without being degraded by numerical dispersion is related to the maximum velocity, V_{max}, and the minimum wavelength by

$$f_c \leq \frac{V_{max}}{2\lambda_{min}}.$$

The second parameter to be considered is the time step Δt used in the discrete approximation of the time derivatives. When using an explicit finite difference scheme to approximate the time derivative as in equation (2.24), this parameter must be aptly chosen depending on the maximum wave velocity in the model, V_{max}, and the minimum spacing between two grid points within the elements, h_{min}, according to a modified Courant condition such that

$$\sqrt{2} \, V_{max} \, \frac{\Delta t}{h_{min}} < 1.$$

If the time step Δt is too large the simulation is unstable and the solution grows without limits.

An efficient suppression of numerical dispersion can basically be achieved in two ways. In the first, the size of the elements h can be reduced while maintaining the degree of the polynomial constant. Alternatively, larger elements and values of n_ℓ can be chosen. Aside from issues related to numerical dispersion, the size of the elements is also controlled by the geometrical complexity one wants to resolve in the model. If smaller elements are used the geometry of the model can be better approximated. However, to

82

achieve efficient reduction of numerical dispersion, the degree of the Lagrangian polynomial should be at least four or larger (*Komatitsch and Tromp*, 1999). Therefore, combining small elements and a relatively high polynomial degree results in large number of nodes in the model, making the simulation computational lengthy. As a rule of thumb *Komatitsch and Tromp* (1999) suggest to design the mesh such that Lagrangian polynomials of degree $4 \leq n_\ell \leq 10$ are sufficient to suppress numerical dispersion. The sufficiency of this range for n_ℓ was confirmed in the present simulations.

While using higher polynomial degrees to efficiently suppress numerical dispersion one has also to keep in mind that the smallest spacing between two points in the mesh decreases as well (as a rough estimate h_{min} scales like $h/2n_\ell$). Therefore, increasing n_ℓ also reduces the maximum possible time step Δt according to the Courant condition.

The limitation imposed on the simulation by the stability condition could be circumvented by using an implicit forward stepping scheme in time like the Newmark algorithm (Appendix A.2.1), for which it is possible to use a much larger time step. However, this method requires the inversion of an effective stiffness matrix. As the matrices must be stored in a sparse format due to their size, only iterative methods such as the Conjugate Gradient algorithm can be applied to solve the resulting matrix equation. However, such iterative algorithms are also computationally time consuming and as such any advantages of using a larger time step can be offset by the increased computational work.

2.4.2 Accuracy of the method

The accuracy of a numerical technique is usually assessed by comparing numerical results to an analytical solution. In seismic modelling the propagation of seismic waves in a homogeneous half-space is often simulated and compared to Garvin's problem (*Garvin*, 1956), as done, for example, by *Komatitsch and Tromp* (1999). However, for the purpose of the simulations in chapter 4, it is more important to know the accuracy of a reflection of waves at interfaces within the model. Therefore, the spectral finite element program is tested here against another numerical tool that calculates very accurately the reflection of elastic waves at internal interfaces.

Several techniques have been developed to calculate synthetic seismograms for horizontally stratified earth models. The reflectivity method (e.g., *Fuchs and Müller*, 1971;

83

Table 2.2: a) Parameters of test model A used for comparison with a reflectivity program. b) Theoretical zero-offset travel times for test model A.

(a)

Layer	Top depth	ρ	V_P	V_S	λ	μ
I	$0.00\ m$	$2000\ kg/m^3$	$2400\ m/s$	$1386\ m/s$	$3.84\ GPa$	$3.84\ GPa$
II	$405.40\ m$	$2300\ kg/m^3$	$2700\ m/s$	$1559\ m/s$	$5.59\ GPa$	$5.59\ GPa$
III	$810.81\ m$	$2700\ kg/m^3$	$3000\ m/s$	$1732\ m/s$	$8.10\ GPa$	$8.10\ GPa$

(b)

Interface	$\overset{\frown}{PP}$	$\overset{\frown}{PS}_V$
I	0.33 s	0.45 s
II	0.63 s	—

Chapman and Orcutt, 1985) provides an accurate and fast computation of theoretical seismic data for an elastic $1 - D$ earth model. It determines the exact seismic response of a layered earth model that includes reflected and converted waves at the interfaces.

To access the accuracy of the spectral finite element program the seismic wavefield was calculated for a three-layer model described in Table 2.2(a). The same model was used for the computation of synthetic seismic data using a reflectivity program.

Figure 2.10 shows the synthetic seismograms calculated by the reflectivity program (written by *Gallop*, 1999). The first panel shows P-reflections only, the second panel only reflected S_V-events, and the third graph includes both phases (i.e. P- and S_V-reflections). The calculation of the direct wave has been omitted for the sake of clarity. In these calculations the source has been placed $20\ m$ beneath the surface. The theoretical zero-offset two-way travel times to the first and second interface for this model are included in Table 2.2(b). Only those times of an incoming P-wave ($\overset{\frown}{P}$) that is reflected as P- and S_V-waves ($\overset{\frown}{P}$ and $\overset{\frown}{S}_V$), respectively, are included. The zero-offset travel times agree very well with the calculations in table 2.2(b) indicating that the reflectivity program determines the travel times accurately.

The result of the finite element simulation is shown in Figure 2.11. Usually the direct surface waves dominate the seismograms and the weaker reflected waves are barely visible. To remove the direct waves and artifacts related to the source (which are to be discussed in section 2.5.1) two simulations were carried out. First, a homogeneous model with the properties of layer I (Table 2.2(a)) was calculated. The second model then con-
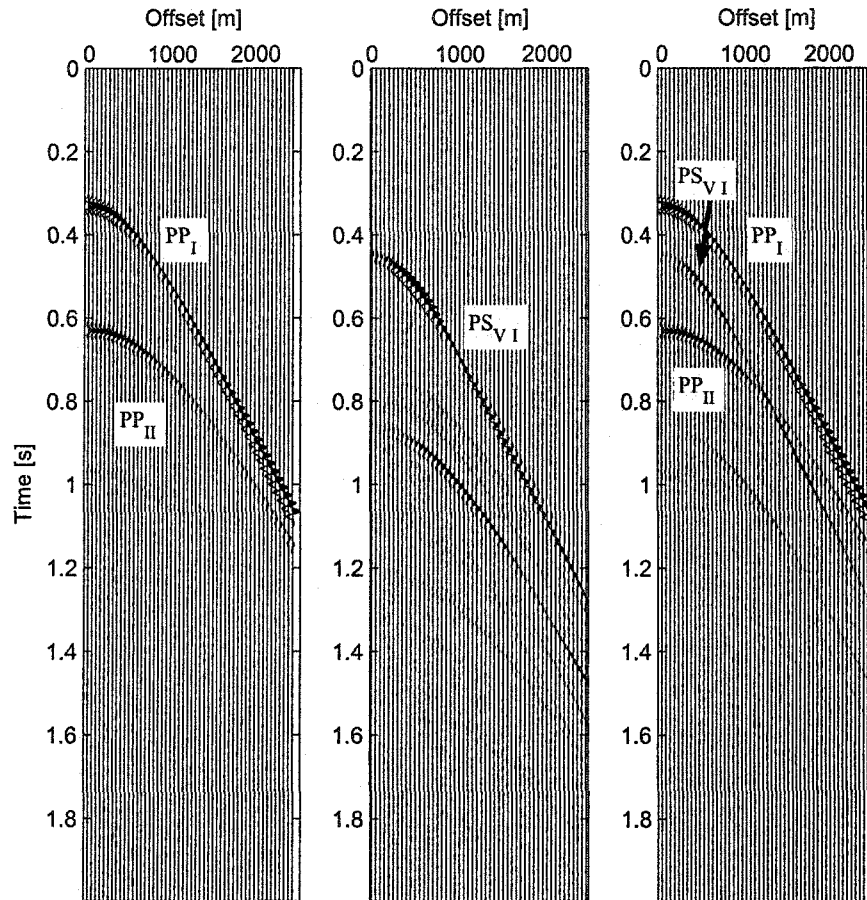
Figure 2.10: Vertical displacement synthetic seismograms calculated by a reflectivity program. Left: P-wave seismogram. Middle: S_V- seismogram. Right: combined seismogram.

tained all three layers. After subtracting the seismogram of the first model from the results of the second simulation the direct waves and source artifacts are eliminated in the resulting data set (Figure 2.11).

Comparing both data sets directly is not possible because both programs simulate the source differently. The spectral finite element program implements the source through a tensor product of the seismic moment tensor and the derivative of the interpolation function (equation 2.21) distributed over a small region within the model. This implies

85
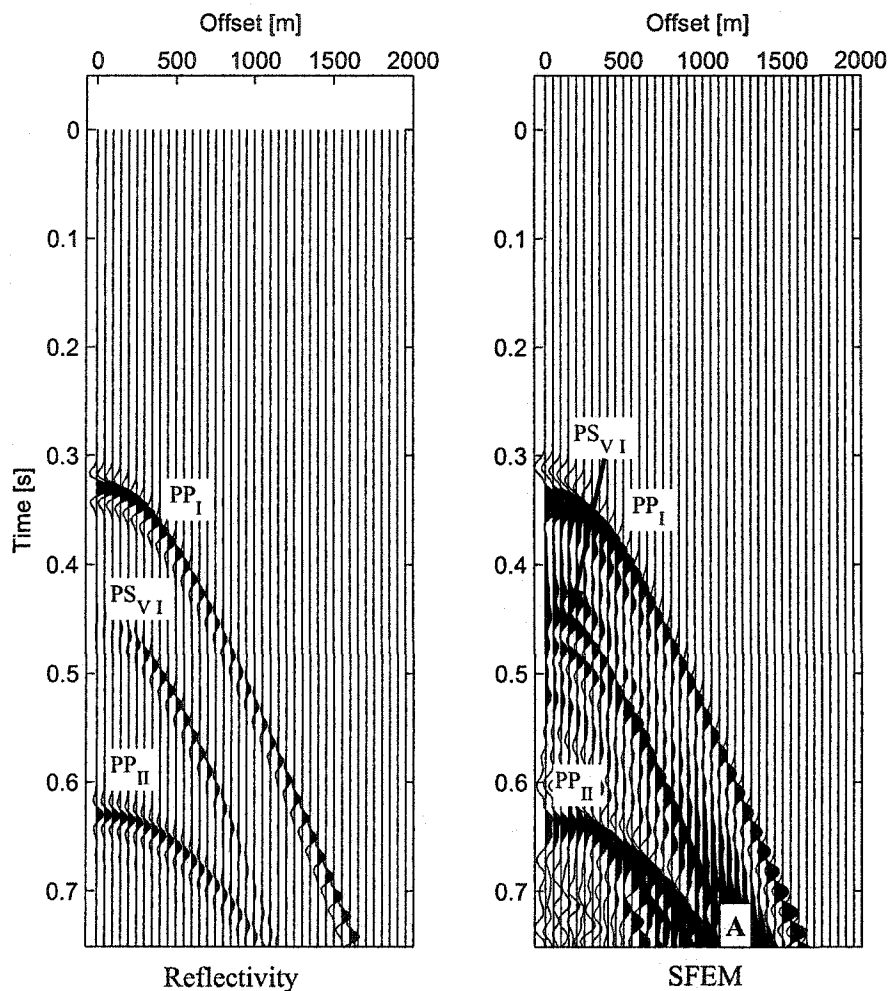
Figure 2.11: Comparison of synthetic seismograms. Left: reflectivity method, right: spectral finite element method (SFEM).

that the actual propagating wavelet is the derivative of the Ricker wavelet. From Figure 2.11 it becomes apparent that the reflectivity program simulates the propagation of a Ricker wavelet. Hence, the different shapes of the wavelets for the two numerical tools in the seismograms.

Generally, the reflection of the P-wave at the first interface (labelled PP_I) shows qualitatively the same behaviour in both data sets. At near offsets the amplitude of the re-

flected wave is strong. With increasing offset the amplitude decreases first until approximately 1200 m offset. After that, the amplitude increases again but the phase of the wavelet has changed in both cases. However, the data calculated by the spectral finite element program exhibit a significant 'ringing' that follows the main reflection. The same ringing is present for the arrival of the converted wave from the first interface (labelled $PS_{V\ I}$). This event is additionally contaminated by the erroneous amplitudes labelled A. These amplitudes probably result from an incorrect handling of the reflection at long offsets or large angles of incidence. For the last reflection of the P-wave at the second interface it can be said that the near offset travel times agree with the expected times (Table 2.2(b)). However, the amplitudes are difficult to evaluate due to significant contamination of spurious amplitudes from previous reflections.

The spectral finite element technique determines the travel times of the main events accurately. However, presently, the accuracy of the amplitude variation with offset seems to be problematic. Future work could concentrate on whether the amplitudes with offset improve for different material properties (e.g., different ratios of the seismic velocities V_S/V_P) or for different frequencies of the source. The last thought is based on the consideration that the spurious reflection amplitudes may be due to numerical dispersion.

2.4.3 A generic example

A generic example will illustrate the potential of the spectral finite element method for seismic modelling. The model does not represent an actual case but nevertheless does show typical features one is often confronted with in land seismic surveys. Consider the model in Figure 2.12(a), which consists of five layers including significant variations in surface topography and layer interfaces. The interfaces separate regions of different seismic properties listed in Table 2.3, where the labels I to V refer to the layers from the top to the bottom.

To match the shape of the surface and the interfaces the geometry of the model was approximated by a finite element mesh consisting 1250 elements (Figure 2.12(b)), with the average size of the elements being approximately 40×40 meters. Lagrangian polynomials of degree 6 were used to interpolate the displacements on the elements. Then, the critical parameters for the simulation were determined based on the criteria discussed in section
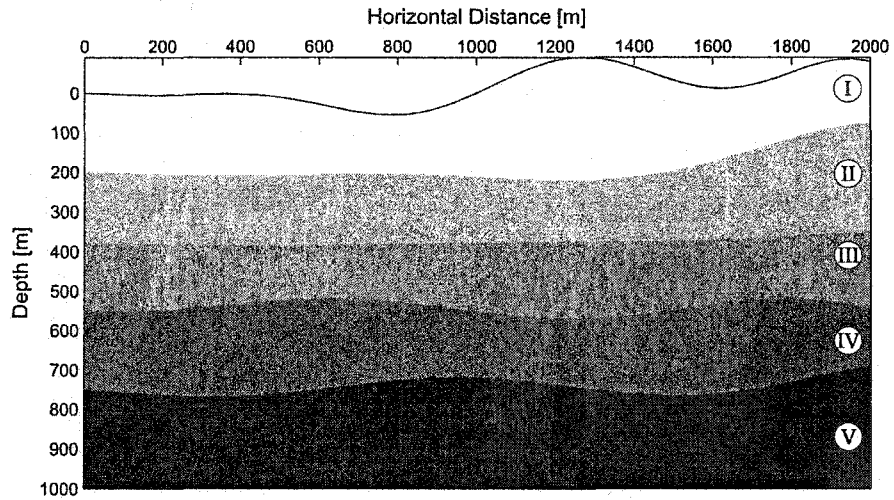
(a)
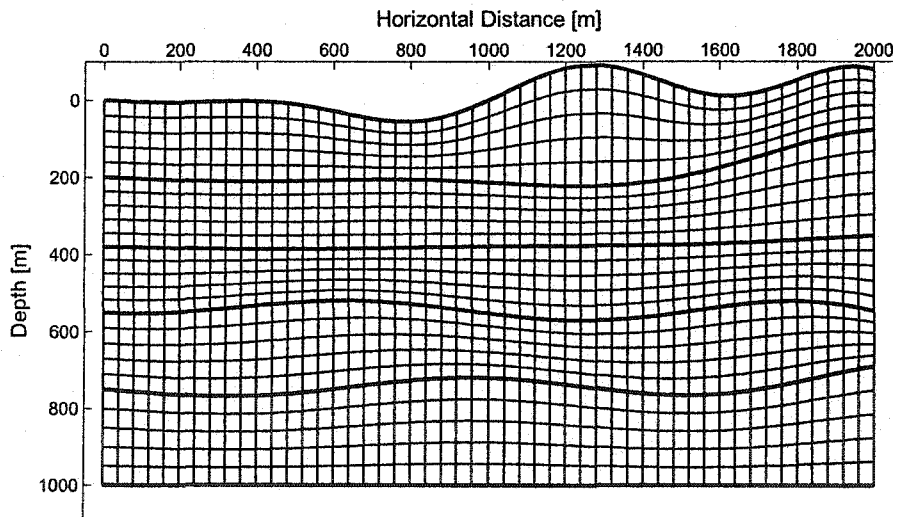
(b)

Figure 2.12: Top: sketch of the five-layer generic model. Bottom: Approximation of the model by a finite element mesh.

2.4.1. These are that the shortest wavelength supported by the mesh is $\lambda_{min} \approx 29\ m$ and the maximum possible time step is limited by $\Delta t \leq 0.9\ ms$. Finally, the upper limit for the center frequency of the source wavelet is $f_c = 23\ Hz$.

With $Deltat = 0.1\ ms$ the time step in the simulations was shorter than the maximum possible because the average element size h used to calculate the upper limit of Δt does not represent the minimum length of the elements; therefore, a shorter time step must be chosen to ensure a stable numerical solution. A typical time sampling interval in an exploration seismic survey is $\Delta t_{sample} = 1.0\ ms$, which one would consider as an upper limit for a reasonable discrete time step when simulating such surveys. The time step employed was chosen to be only one-tenth of this sampling interval in order to ensure a stable solution. The computational penalty of such a small time sampling interval is a significant longer computation time when using an explicit finite difference time stepping technique. However, the use of a computationally expensive, but unconditionally stable implicit time marching scheme (i.e., the Newmark method) does not seem to be justified. Simple numerical experiments suggest that the time step Δt must increase by more than a factor of 10 in order to outperform an explicit time stepping method. Hence, for an efficient simulation employing the Newmark scheme the time step must be chosen larger than the selected upper limit of $1.0\ ms$. Therefore, the explicit time stepping using the finite difference approximation (as in equation 2.24) is the appropriate choice for the simulations to come.

The limit for the frequency bandwidth of the seismic signal was calculated using the average element size. For the same reasons as discussed for the choice of the time step a slightly lower value for the center frequency was chosen in order to safely suppress numerical dispersion.

Table 2.3: Seismic properties of the generic model (Figure 2.12(a))

	$\rho\ [kg/m^3]$	$V_P\ [m/s]$	$V_S\ [m/s]$	$\lambda\ [GPa]$	$\mu\ [GPa]$
I	2200	2200	1270	3.55	3.54
II	2300	2300	1328	4.05	4.06
III	2400	2500	1443	5.01	5.00
IV	2500	2400	1386	4.79	4.80
V	3000	2700	1559	7.29	7.29

Figures 2.13 and 2.14 show the evolution of the seismic wavefield at different time steps for two different source locations. These snapshots demonstrate the potential of the spectral finite element method to simulate the propagation of waves along curved interfaces and, particularly, at the free surface. Unfortunately, the lack of functioning boundary conditions requires the simulations to cease as the waves approach the artificial boundaries Γ of the model in order that the reflected waves do not contaminate the desired arrivals.

An interesting feature develops in the seismic wavefield shown in Figure 2.13 when the direct waves reach the closed peak to the right of the source location. These waves are trapped in the body of the peak; almost no energy is carried as the direct waves passes this hill. Only those seismic waves reflected from deeper interfaces will carry energy to the right-hand portion of the model. Although this model does not represent any particular geology it illustrates quite well how seismic modelling can, in advance, help to indicate possible problems in seismic land surveys.

2.4.4 Numerical problems due to improper mesh design

Besides numerical dispersion simulations of seismic wave propagation can also suffers apparent mesh anisotropy, which is another grid or mesh-related artifact.

The motivation for developing the model shown in Figure 2.15(a) was initiated by the problems occurring in seismic surveys in rough terrain that are discussed in *Li* (2004). In areas with significant surface variations in topography a dedicated field survey layout is required that suits the complicated geological structure. Pre-survey testing of the survey design using numerical simulation will be a valuable contribution to the success of the field experiment.

To investigate the potential of the spectral finite element technique to simulate surveys in rough terrains, the generic model shown in Figure 2.15 was constructed. Whereas the first generic model in Figure 2.12 contains a smooth surface variation, the second generic model contains a much 'rougher' surface topography (Figure 2.15(a)). The velocities and density are constant throughout the model with $V_P = 3200.0\,m/s$, $V_S = 1270.0\,m/s$, and $\rho = 2200.0\,kg/m^3$. The geological model was approximated by a finite element mesh consisting of 2500 elements. The degree of the Lagrangian polynomial
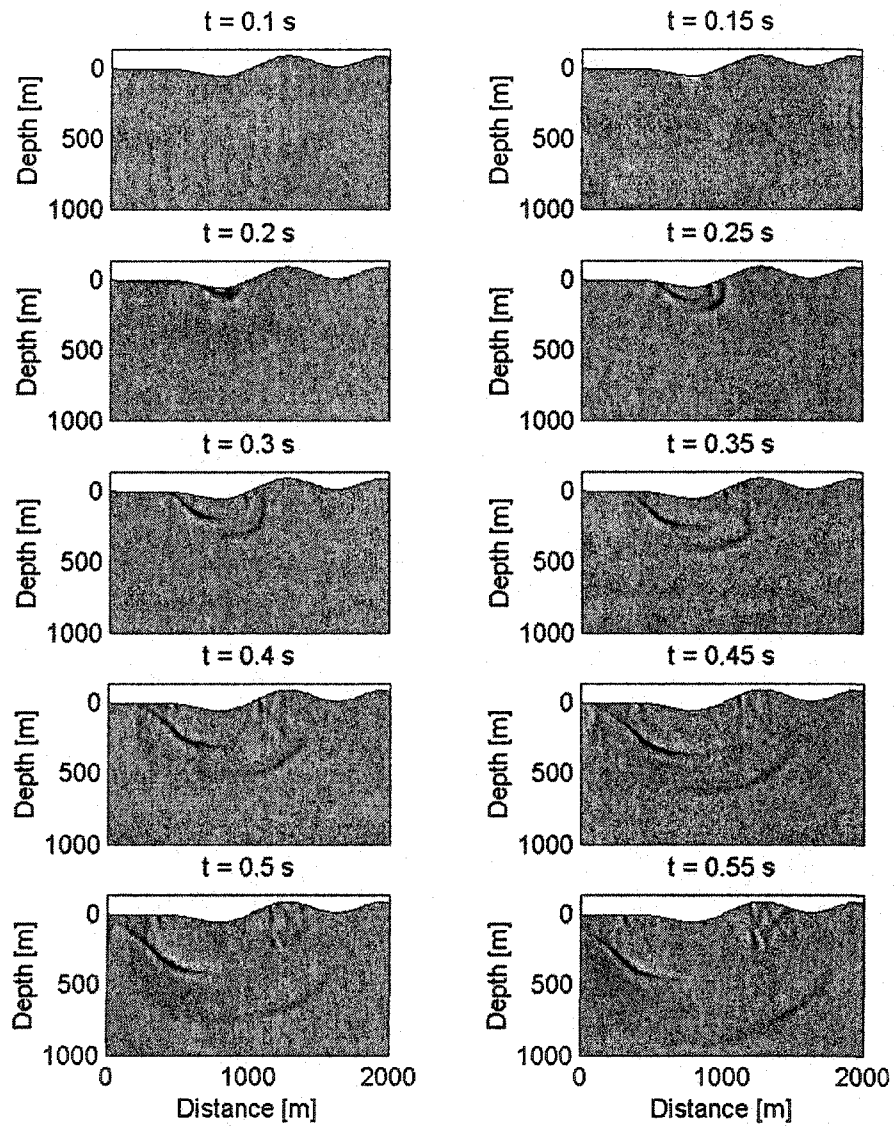
Figure 2.13: Simulated seismic wavefield at different times for the model shown in Figure 2.12.
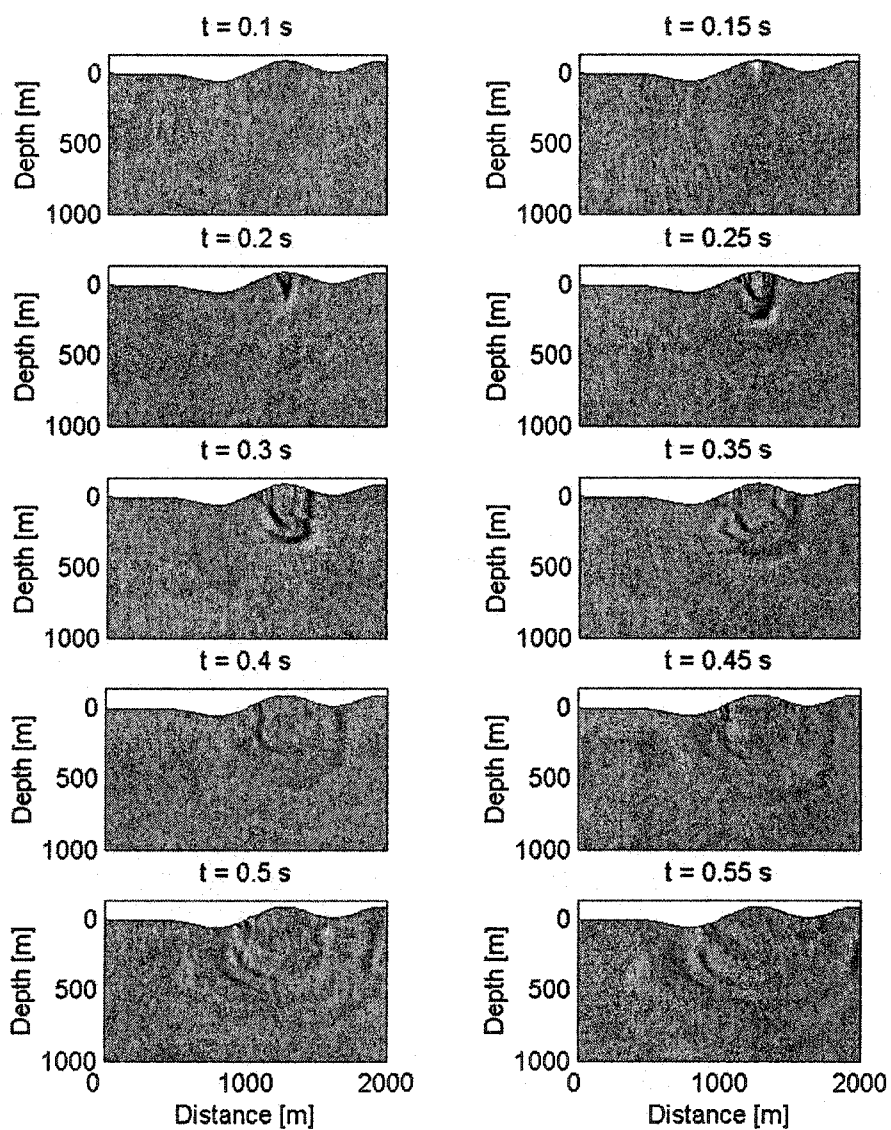
Figure 2.14: The simulated seismic wavefield for the generic model with the source located at top of the hill.

was chosen to be 7, resulting in 90751 nodes in the finite element model. The source was an explosive force close to the surface in the center of the model with a time history described by a Ricker wavelet with a center frequency of $f_c = 20\,Hz$.

Initially, the waves propagate as expected along the surface. However, it seems as if the wave propagation occurs in an anisotropic environment. In Figure 2.15(b), the P-wave front is not circular, as one would expect for an isotropic model, but is elongated in the vertical direction. Because the elasticity of the model is described by an isotropic constitutive equation, the apparent anisotropy must result from numerical artifacts. In the central part of the model, the elements are elongated in the vertical direction, and it seems that the spectral finite element method is not capable of adequately simulating the wave propagation in such a case.

The second numerical artifact occurring in this simulation is a strong numerical instability that develops at the surface (indicated by arrows in Figures 2.15(c) and (d)). When the surface wave reaches the 'deep valley' towards the right of the source it does not continue to propagate. Instead, an increasing and anomalous amplitude is observed in this region that is marked by the bright spot in the snap shots. With time, this amplitude continues to grow and becomes too large; the plotting program cannot resolve this artifact and the actual wave amplitudes after $t = 0.30\,s$.

At the moment, one can only speculate whether this numerical instability is related to the topographic variations that occur on a shorter length scale than, for example, in the first generic model (Figure 2.12). Perhaps, a limit exists for the *ratio of the shortest possible seismic wavelength and the length scale of the topographic variations* in the model? Further studies are required to answer this question.

2.5 Possible directions for future work

The simulations presented in the previous section clearly highlight the potential of the spectral finite element method for applied seismological studies. However, there remain several problems, which should be addressed in future work.
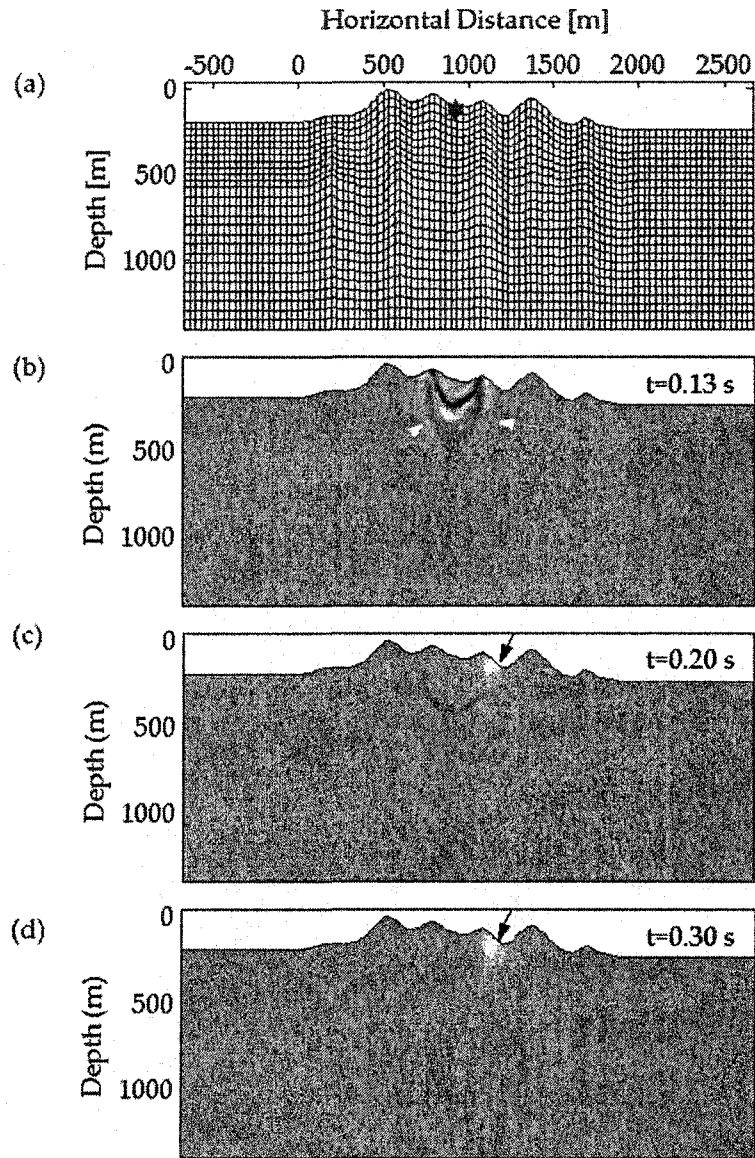
Figure 2.15: The 'rough surface' model. (a) the finite element mesh; snapshot of the horizontal wavefield after (b) $t = 0.13\,s$, (c) after $t = 0.20\,s$, and (d) after $t = 0.30\,s$. The source position is marked by a hexagram in (a). The white arrows in (b) are pointing to the P-wave front. In (c) and (d), the numerical instability at the surface condition is indicated by arrows.

94

2.5.1 Mesh generation

A problem appears in the simulation results in Figures 2.13 and 2.14, where erroneous small amplitude events originate from the source at later times. These are not related to the underlying physical model but most likely caused by the distorted elements in these particular regions of the model. It is worthwhile noting, that such events are not present in the simulations shown in Figure 2.9, in which a finite element mesh with regular quadrilateral elements was used. A possible explanation for these events could be numerical dispersion, which is caused by distorted elements. One can only speculate if a better mesh design would help do reduce such artifacts[2]. Professional mesh generation software usually reduces the distortion of the elements to obtain a 'smoother' mesh[3] but including such algorithms in the mesh generation software used is beyond the scope of this current work.

2.5.2 Improving the mesh adaptability

The reason only quadrilateral elements are employed in the current mesh generation process, as mentioned in section 2.2.2, arises from the requirement that two Lagrangian polynomials must undergo tensor multiplication to obtain the two-dimensional interpolation function (e.g., equation 2.30); this operation is presently only established for quadrilateral elements. On the other hand, quadrilateral elements are not as flexible as triangular elements in adapting complex model shapes; consequently, much work has been carried out in the recent years to provide routines to calculate high-order collocation points for triangular elements (e.g. *Bos et al.*, 2000; *Hesthaven and Teng*, 2000; *Taylor et al.*, 2000). *Sherwin and Karniadakis* (1996) and *Karniadakis and Sherwin* (1999) discuss extensively the combination of the *h-p* method with triangular meshes. At the moment, high-order finite element methods on triangular meshes require more computational effort in determining the optimum collocation points (the so-called *Fekete points*). A further problem is that numerical dispersion is not as efficiently suppressed as it would be the case for quadrilateral elements (*Komatitsch et al.*, 2001). However, the advantages of

---

[2]Note that the finite element meshes used in all simulations presented here were created using simple Matlab™ scripts.

[3]M. Goelke, Altair Engineering, personal communication.

---

using triangular meshes are significant where complicated geometry must be accurately incorporated into the model. This is particularly true for steam chambers or surface topography. Therefore, the existing program, currently limited to the use of quadrilateral elements only, should be extended to incorporate triangular elements.

2.5.3 Including dispersive effects

As discussed in chapter 1.1.4 seismic waves experience inelastic attenuation when propagating through the earth. In saturated porous rocks, this effect is perhaps best described by Biot's theory and its numerous extensions (e.g. *Biot*, 1956a,b; *Dvorkin and Nur*, 1993; *Dvorkin et al.*, 1994). However, a computationally efficient numerical solution of Biot's equation system is not easily obtained (*Carcione and Quiroga-Goode*, 1995). This is in particular due to the wide range of velocities occurring in this description as there is a third wave present beside the *P*- and *S*-wave, which propagates with much lower velocity through the medium (see section 1.2.3). To ensure a numerically stable solution, the two parameters Δt and λ_{min} must be significant smaller than, for example, in the case of a purely elastic constitutive relationship between stress and strain. A simulation incorporating this extra information can become computational impractical because the finer mesh requires substantially more memory and the smaller time step results in a much longer computation time.

As an alternative approach to simulate inelastic effects the phenomenological theory of viscoelasticity has been frequently used (*Emmerich and Korn*, 1987; *Carcione*, 1988; *Carcione et al.*, 1988; *Carcione*, 1993, *Robertson et al.*, 1994). The viscoelastic theory is well developed and its numerical implementation has proven to be efficient in finite difference schemes. Generally, the same approach can be implemented in a finite element algorithm, as done by *Kay and Krebes* (1999). However, the approximation of attenuation over an extended frequency range requires the use of several Maxwell bodies (see section 1.2.4). In a finite element scheme, each contribution of a Maxwell body requires additional matrices that are similar to the stiffness matrix K. This matrix requires the dominant part of the necessary computer memory; and therefore an algorithm using several matrices will be only feasible on computers with large memory resources. Apparently, the existing three-dimensional spectral finite element simulations do not employ a viscoelastic rheology

(e.g. *Faccioli et al.*, 1997; *Komatitsch and Tromp*, 2002a,b; *Chaljub et al.*, 2003), although these authors do not explicitly mention memory limitations for their choice of the rheological law.

Future work could concentrate on the feasibility of performing two- and three-dimensional finite element simulations on the existing parallel computer at the University of Alberta. Including inelastic effects into the simulation will certainly help to explore the physics being analysed in this study in more detail.

2.5.4 Absorbing boundary conditions

The simulations of the seismic wavefield propagation presented were aborted as soon as the wave fronts reached the boundaries of the model. Otherwise, reflections, and especially those of the surface waves at the edges of the model, produce numerical instabilities that diminish the utility of any further simulation in the interior of the model. Unfortunately, the implementation of an absorbing boundary condition using the Rayleigh technique failed here, as described in section 2.3.1. While this is something of a negative result, it is useful to know about this problem in order that other approaches might be taken.

An alternative promising approach is that of *Perfectly matched layers* (PML) first introduced by *Berenger* (1994) to absorb electromagnetic waves at the boundaries of a finite difference grid. *Chew and Liu* (1996) showed that these conditions can also be employed in elastic wavefield simulations. The PML condition was derived by *Berenger* (1994) for a system of first-order partial differential equation. After *Collino and Tsogka* (2001) reformulated the PML theory for the 2nd-order wave equation, *Komatitsch and Tromp* (2003) recently successfully applied this technique to finite element modelling of seismic waves for a simple model. Perfectly matched layers are perhaps the most efficient absorbing boundary condition as they require the least elements in the attenuation layer around the model and this approach should be pursued in future work.

2.6 Discussion

The chapter discussed the four standard numerical techniques, which are currently used to solve partial differential equations numerically. These are the finite difference method, the global pseudo-spectral method, the finite element technique, and finally the method of the spectral finite elements. From these techniques the spectral finite element method best meets the required criteria for the modelling algorithm, which are spectral accuracy (e.g., an efficient suppression of numerical dispersion) and geometrical flexibility (i.e., the adaptability of the numerical model to a complex geometry).

The numerical examples showed that the spectral finite element method is indeed capable of simulating seismic wave propagation accurately for geometrical models that include significant surface topography and variations of interior geological contacts. Such simulations are of interest in various fields of exploration geophysics. First, surface topography anomalies such as hills or valleys produce diffractions, which in turn will reduce the quality of the seismic survey. In order to test processing algorithms, including migration of such data, forward modelling is a very important tool. Secondly, seismic forward modelling is becoming a more and more essential step in preparing seismic surveys in order to access, for example, the feasibility of a time-lapse monitoring program.

The application of the spectral finite element method requires a carefully designed numerical mesh in order fully exploit its potential regarding spectral accuracy and geometrical adaptability. The examples shown in this chapter demonstrated that numerical instabilities as well as apparent anisotropy are introduced if the mesh includes substantially distorted elements.

An extension of the current program to three dimensions in principle does not require considerable modification of the existing finite element algorithm. The main difficulty probably lies in the mesh generation process. As mentioned before it is not trivial to match a given two-dimensional geological structure by a mesh consisting of quadrilateral elements; the use of triangular or tetrahedral elements would be a better approach. This problem is even more evident in three dimensions where tetrahedral elements will allow for a much better approximation to the geology than hexahedral elements. A mathematical theory, however, to determine the necessary Fekete points in three dimensions seems

98

not yet to be available. Aside from the mesh generation problem there seem to be no other obstacles for the extension of the modelling algorithm to three dimensions. Memory requirement and computation time will be considerably larger but with the steadily increasing computer power, three dimensional simulations are becoming more realistic (*Komatitsch et al.*, 2002).

Finally, it should be noted that aside from the application to forward modelling, the finite element method has recently been applied to migration of seismic data (e.g. *Zhang et al.*, 2004). The advantages of using the finite element method for this purpose are the same as for forward modelling: the technique enables one to handle complicated geological structures (for example surface topography) much better than other methods.

Chapter 3

A comparative rock physical study of the seismic response during steam-flooding of heavy oil reservoirs

[1]The suggestion that the seismic monitoring of thermal enhanced oil recovery processes is feasible was initially based on ultrasonic laboratory observations of the significant decrease in the compressional velocity with temperature in heavy oil saturated materials. For example, *Wang and Nur* (1988),*Wang and Nur* (1990), *Wang et al.* (1990), *Eastwood* (1993), and *Watson et al.* (2002) all report reductions in the ultrasonic P-wave velocity of approximately 11% after heating of a heavy oil saturated sample from 20°C to 120°C at constant effective pressure. While this change is certainly considerable, such measurements do not take into account the fact that steam replaces the heavy oil in much of the pore space during a SAGD-program. The engineering models suggest that only a thin zone of heated heavy oil saturated reservoir rock surrounds the steam chamber. If these engineering models are correct, it is likely that the heated oil-saturated regions will only minimally affect the overall seismic response.

Reservoirs in which SAGD is applied are typically from 10 m to 30 m thick; such thin reservoirs may make detection of changes with reflection seismic methods difficult, particularly if they are subtle. For example, a correlation of 'bright' seismic events with a triplet of SAGD well pairs was observed over the shallow (120 m to 160 m deep) bituminous Athabasca reservoir in Northern Alberta (Figure 3.1, *Schmitt*, 1999). In contrast, the

---

[1]Parts of this chapter have been submitted to GEOPHYSICS for publication.

100
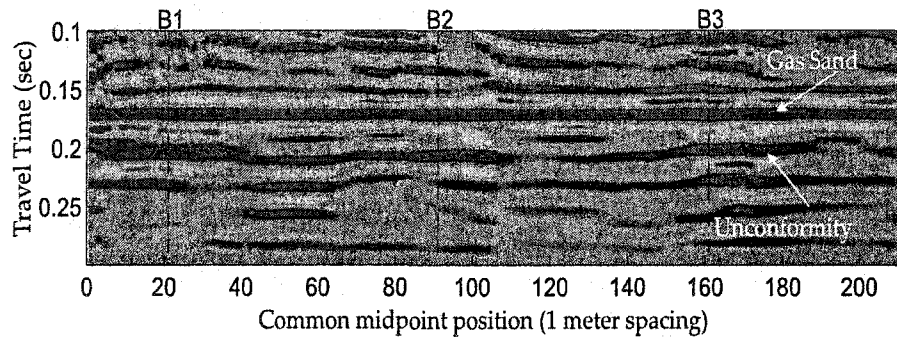
Figure 3.1: Seismic reflection data recorded over an Athabasca reservoir near Fort Mc-Murray, Alberta. Three SAGD well pairs intersect the seismic lines at the locations labelled B1, B2, and B3. (Redrawn after *Schmitt*, 1999)

time-lapse seismic reflectivity changed little over a three year period in a seismic monitoring program carried out over a the geologically similar but deeper (750m) Lloydminster style reservoir (Figure 3.2, *Zhang and Schmitt*, 2003). In order to better understand the differing behavior, an analysis of the physical properties of the rock units found in both reservoirs has here been carried out to simulate the effects of the fluid substitution believed to accompany the SAGD process. The change in the seismic response of two reservoirs, geologically similar but subjected to different effective stress conditions, is studied using Gassmann fluid substitution modelling (*Gassmann*, 1951). Relevant elastic moduli are extracted from well logs or from engineering tests. Appropriate fluid properties, under the pressure and the temperature regimes expected, are employed. Finally, the influence of effective pressure on the *in-situ* velocities is assessed. This chapter further discusses the aspects associated with attempts to carry out seismic monitoring of such reservoirs.

In chapter 1 the basic principles of geophysical remote monitoring and especially the physical basis for observing such changes in heavy oil reservoirs subjected to enhanced oil recovery processes were introduced. These ideas are applied in this chapter to assess the feasibility of seismic monitoring of thermal enhanced oil recovery for heavy oil reservoirs for two reservoirs in Western Canada. These reservoirs are geologically similar but are at different depths and show significant differences in their seismic time-lapse response. The first reservoir is a shallow bituminous deposit within the Athabasca forma-

101
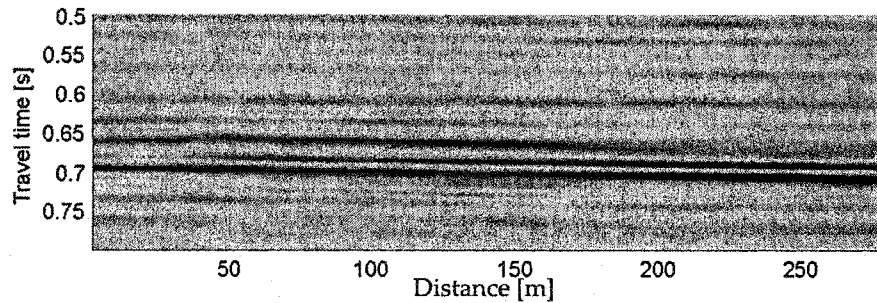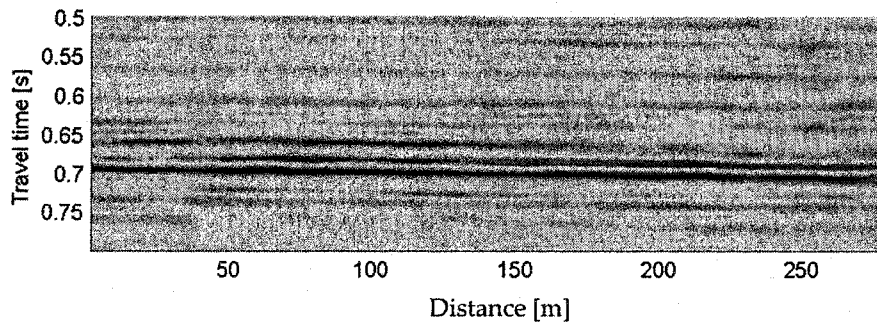
Figure 3.2: Two seismic data sets acquired over a SAGD well pair at a Lloydminster reservoir near Senlac, Sakatchewan at two different times. (After *Zhang and Schmitt*, 2003)

tion near Fort McMurray in Northern Alberta. The second reservoir is a Llyodminster-type reservoir located close to Senlac, Saskatchewan. Seismic monitoring programs have been carried out for both reservoirs by the University of Alberta with different results. The data recorded for the Athabasca reservoir at different times show significant changes in the seismic response whereas seismic surveys acquired over several years at the Senlac reservoir do not distinctly reveal any changes that might be related to the enhanced oil recovery process.

This chapter summarizes a comparative rock-physical study that tries to explain the different seismic responses of these two otherwise similar reservoirs. As mentioned above, feasibility studies for the monitoring of thermal oil recovery methods have so far only considered the temperature effect on the properties of the oil (i.e., velocity and

102

density). For modelling of SAGD processes this approach is insufficient as it does not consider the fluid replacement *steam-for-oil*. By including the temperature and pressure dependence into the fluid substitution to simulate the SAGD process as reported here an improved feasibility testing is achieved.

3.1 Methodology and theoretical considerations

3.1.1 Work flow

To investigate the seismic response of a thin heavy oil reservoir subjected to a SAGD process several well logs and a core analysis from the Senlac area are employed to determine the rock physical properties for this reservoir. For the Athabasca reservoir, the experimental data of various rock and fluid properties by *Chalaturnyk* (1996) provide the data basis. Based on such data representative values for the various elastic parameters occurring in Gassmann's equation 1.3 can be derived (section 3.4). If applicable, the elastic properties of the frame will be determined by inverting Gassmann's equation for the frame bulk modulus K_d. In a subsequent step a fluid replacement in the reservoir will take place to simulate the SAGD process (section 3.5). A simple but realistic model is assumed to represent the effective pore fluid in the steam chamber. Based on this simple model synthetic density and V_P-sonic well logs, assumed to be representative of the reservoir condition during a SAGD process, are calculated. To assess the feasibility of seismic monitoring synthetic seismic traces are calculated for the original and modified well log data, respectively (section 3.5.5). Seismic attributes are then used to quantitatively evaluate the potential of detecting changes in the seismic response between the two cases. The proposed process for testing the feasibility is summarized as a flow chart in Figure 3.3.

3.1.2 Theoretical fundamentals

The elastic properties of a composite material consisting of solid grains and an inviscid fluid is frequently described by *Gassmann's* (1951) equation. The bulk modulus of the effective fluid saturated medium, K_{eff}, is related to the bulk modulus of the solid grain material, K_s, the bulk modulus of the fluid, K_f, the (drained) bulk modulus of the solid
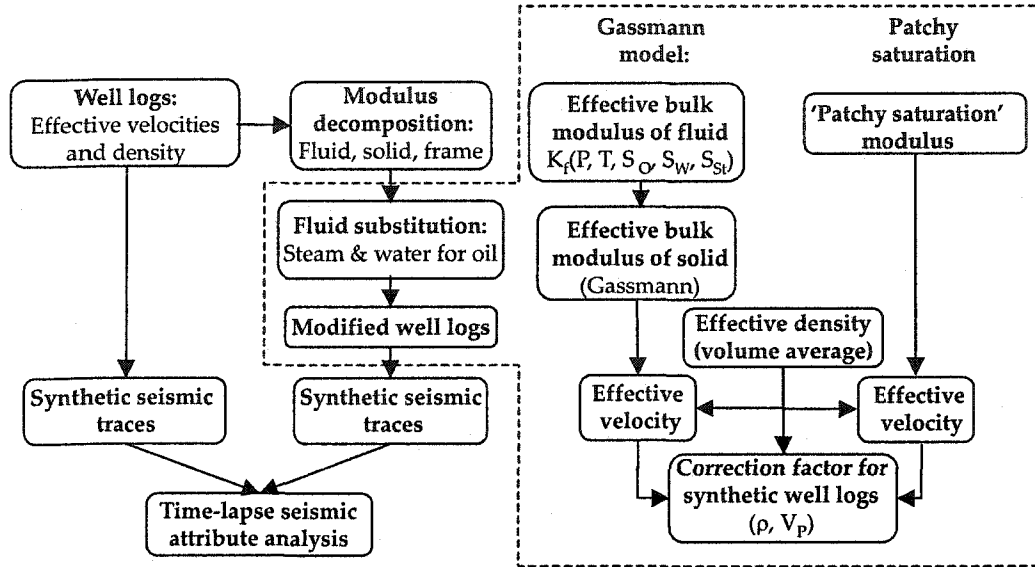
Figure 3.3: The flow-chart illustrates the process for the rock-physical feasibility study.

skeleton or frame, K_d, and the porosity ϕ via

$$K_{eff} = K_d + \frac{(1 - K_d/K_s)^2}{(1 - K_d/K_s - \phi)/K_s + \phi/K_f}. \tag{3.1}$$

The frame bulk modulus K_d describes the rigidity of the interconnected matrix of mineral grains. Its value is relatively large for well consolidated, compacted, and cemented sediments, making the rock solid and seismically fast. In contrast, K_d is lower in unconsolidated fragile sands and the seismic velocities are slow compared to more competent rocks.

A second assumption of Gassmann's theory is that the shear modulus of the effective medium, μ_{eff}, is solely determined by the shear properties of the frame, μ_d, i.e.

$$\mu_{eff} = \mu_d. \tag{3.2}$$

The elastic frame properties may be determined for well-consolidated sandstones using a dry sample or an unjacketed compression test (e.g. Fjær et al., 1992). For unconsolidated material, such measurements are more difficult because experiments are complicated by non-linear elasticity, strong hysteresis, and time dependent effects that are not as important for stiffer rocks (e.g. Gardner et al., 1965; Christensen and Wang, 1985).

Furthermore, the effective density measured in well logs can be separated into two contributions of the solid material, ρ_s, and the pore filling liquid, ρ_f. A volume averaging approach then allows the determination of the effective density:

$$\rho_{eff} = (1 - \phi) \rho_s + \phi \rho_f. \tag{3.3}$$

There have been only a few papers published regarding measurement on unconsolidated sands. *Hornby and Murphy* (1987) report some measurements of the ratio of the bulk to the shear frame modulus of unconsolidated sands. They observed a wide scattering of this ratio for different porosities. Conversely, *Murphy et al.* (1993) derived an empirical relationship for this ratio suggesting that both frame moduli depend linearly on each other. Additionally, these researchers suggest that above a certain porosity the elastic frame properties also depend linearly on the moduli of the grain material. In contrast, the analysis of unconsolidated materials by *Spencer et al.* (1994) reveals that the frame properties vary significantly. They did not measure the bulk and shear frame modulus directly but instead determined the Young's modulus and Poisson's ratio of the samples; these moduli depended only weakly on the properties of the solid mineral grains.

This initial literature survey shows that the experimental results of the frame properties are in a sense contradictory; at this time no simple rule can be applied to relate the frame properties to, for example, porosity or mineralogy. In unconsolidated materials the elastic frame properties most likely depend on the nature of the grain contacts (*Murphy et al.*, 1986, 1993). For example, the roughness of the grain surface and hence its friction against adjacent grains will certainly influence the stiffness of the frame. It is also important to note that, over the range of confining and fluid pressure encountered, the frame bulk modulus can be highly dependent on the differential stress. Since no clear basis for predicting the frame modulus exists, workers instead often rely on direct laboratory or well-log measurements to obtain representative values.

Here, it is assumed that Gassmann's equation applies in order to determine the elastic properties of the formation from V_P and V_S sonic and density logs. Aside from the frame bulk modulus, K_d, all the other moduli are either relatively easy to measure or are already available in the literature (e.g. *Mavko et al.*, 1998). A value for the frame bulk modulus K_d

can be determined from well log data by solving Gassmann's equation for K_d:

$$K_d = \frac{1 + K_{eff} \left((\phi - 1)/K_s - \phi/K_f\right)}{(1 - K_{eff}/K_s + \phi)/K_s - \phi/K_f}. \tag{3.4}$$

The effective bulk modulus K_{eff} is calculated directly using the sonic and density log data according to

$$K_{eff} = \rho \left(V_P^2 - 4/3\, V_S^2\right). \tag{3.5}$$

The shear modulus of the solid frame, μ_d, is similarly calculated from the shear sonic and density logs:

$$\mu_{eff} = \mu_d = \rho V_S^2. \tag{3.6}$$

To apply Gassmann's effective medium theory one has to ensure that the underlying assumptions are met. One important assumption is that the pore filling fluid does not possess a finite shear strength, i.e., the fluid must not resist shear motion. Secondly, no relative motion between the solid frame and the pore fluid is allowed when a seismic wave passes by. This condition is usually met for the frequency range used in exploration seismics.

Two different effective medium theories are assumed to simulate the effects of a SAGD process on the seismic properties on the reservoirs . One must consider how the fluids themselves may be distributed within the pore space; the end members of this are a homogeneous fluid distribution at one extreme and a patchy saturation at the other.

The first model considers a homogeneous fluid consisting of three phases: oil, liquid water, and steam. Then, the effective fluid density, ρ_f, and the bulk modulus, K_f, are given by:

$$\rho_f = S_O\,\rho_O + S_W\,\rho_W + S_{St}\,\rho_{St}, \tag{3.7a}$$

$$\frac{1}{K_f} = \frac{S_O}{K_O} + \frac{S_W}{K_W} + \frac{S_{St}}{K_{St}}, \tag{3.7b}$$

where S_O, S_W, and S_{St} are the oil, water, and steam saturations, respectively. Similarly, the temperature and pressure dependent densities and bulk moduli of the different components are labelled by the same subscripts as the saturations.

Upon substituting the effective fluid properties into equations (3.1) and (3.3), respectively, the density and bulk modulus of the effective medium are determined. This homogeneous model is also referred to as the *Gassmann* model in the following sections.

106

In the Gassmann model it is assumed that wave-induced pore pressure increases equilibrate in the phases during a seismic period. This assumption is satisfied if immiscible phases coexist in the pore space. However, this assumption breaks down if the saturation is not homogeneous over a characteristic diffusion length scale ℓ_C (*Mavko and Mukerji*, 1998), which is related to the permeability of the material, the frequency of the wave, and the dynamic viscosity and bulk modulus of the liquid phase (*Mavko and Mukerji*, 1998; *Dvorkin et al.*, 1999)

$$\ell_C = \sqrt{k\,K_L/(f\eta)},$$

where

- k: permeability,

- K_L: bulk modulus of the most viscous phase,

- f: seismic frequency,

- η: dynamic viscosity of the most viscous phase.

This characteristic length scale can be of the order of a few millimeters at ultrasonic frequencies to several meters in seismic frequency band. For *patchy* saturation distributions the Gassmann model can underestimate the effective elastic properties of a fluid filled porous medium. Table 3.1 shows some estimates of the critical diffusion length for the Lloydminster and Athabasca reservoir, respectively. In both cases, the permeability was assumed to be $k = 4$ Darcy (equivalent to $k = 3.95 \times 10^{-12}\,m^2$), the bulk modulus of the most viscous component (oil) was calculated according to equation (3.9b), and the viscosity after equation (1.12c). The differences in the length scales ℓ_C are due to different temperature conditions within the steam chamber, which effect the properties of the oil. For the Lloydminster reservoir, the assumed temperature is about 265°C, while for the Athabasca reservoir it is 165°C. As the distribution of the different phases in a steam chamber and hence the size of any fluid patches in the steam chamber is unknown, and indeed, is likely not very homogeneous especially in the early phases of the injection process, the second effective medium model employed in this work assumes a 'patchy' distribution of the components of the fluid in the pore space. Using both the Gassmann

107

Table 3.1: The characteristic diffusion length scale ℓ_C for the two reservoirs considered in this study.

f [Hz]	Lloydminster	Athabasca
25	0.23 m	0.11 m
50	0.17 m	0.08 m

and patchy saturation model provide approximate lower and upper boundaries for the seismic velocities of the effective material (*Mavko and Mukerji*, 1998) with

$$V_{P_{Gassmann}} \leq V_P \leq V_{P_{patchy}}.$$

For the case when the pore fluid phases are sufficiently separated (i.e., the sizes of the patches are much larger than the characteristic length scale) *Mavko and Mukerji* (1998) derived an expression of the effective elastic modulus by first calculating three parameters using Gassmann's equation (3.1) under assumption that the entire pore space is saturated by either phase. In a subsequent step they determined the final effective elastic modulus by averaging these three values assuming an iso-stress or Reuss method to obtain

$$\frac{1}{(K + \frac{4}{3}\mu)_{patchy}} = \frac{S_{St}}{(K_{S_{St}} + \frac{4}{3}\mu)} + \frac{S_O}{(K_{S_O} + \frac{4}{3}\mu)} + \frac{S_W}{(K_{S_W} + \frac{4}{3}\mu)}, \qquad (3.8)$$

where $K_{S_{St}}$, K_{S_O}, and K_{S_W} are the effective bulk moduli after Gassmann. Finally, equations (3.3) and (3.8) are combined to calculate the P-velocity of the effective medium to be

$$V_{P_{patchy}} = \sqrt{\frac{(K + \frac{4}{3}\mu)_{patchy}}{\rho_{eff}}}.$$

Again, it is assumed that the shear velocity V_S is not affected by the pore fluid, such that equation (3.6) applies to find the effective shear modulus.

3.2 Geology of the reservoirs

The heavy oils in the Western Canadian Sedimentary Basin (WCSB) are found in large and shallow oil sand deposits, predominantly in the Athabasca, Peace River, Cold Lake, and Lloydminster areas (see the map of the Western Canadian Sedimentary basin in Figure 1, page 3). There are generally two types of production methods: oil sands that are

Age	Alberta		Saskatchewan
	Alberta	Cold Lake	Senlac
Mesozoic Era — Lower Cretaceous Period	Lower Colorado Group		
	Mannville Group — Grand Rapids Fm. / Clear-water Fm. / Mc Murray Fm.	Mannville Group — Grand Rapids Fm. / Clear-water Fm. / Mc Murray Fm.	Mannville Group — Pense Fm. / Cantuar Fm. / Colony McLaren / Waseca Sparky GeneralPet. Rex Llodmin-ster Cummings / Dina Member
Paleozoic Era			

Legend:
Fm.   - Formation
～～ - unconformable contact
⌇ - diachronous contact

Figure 3.4: Stratigraphic chart of three major heavy oil deposits in Western Canada.

close to the surface are mined, and *in-situ* operations where wells are drilled and produced with the aid of technologies such as SAGD. According to the Energy and Utilities Board of Alberta (AEUB) the term oil sand does not refer to specific geological material. Rather, the term is loosely used to refer to mineable operations regardless of the lithology or age of the deposit that are sands or other rock materials, which contain a significant amount of heavy oil or bitumen.

Most of the heavy oil reservoirs in Western Canada, which are produced with the help of the SAGD technology are geologically similar in that they are fluvial and/or deltaic

deposits. The accepted stratigraphy in Figure 3.4 shows the general geological structure of the deposits in the Athabasca, Cold Lake, and Lloydminster areas. The reservoir at Athabasca of interest in this study is found in the McMurray formation of the lower Mannville group. The geological setting for the lower Mannville is similar in all areas. The lowest strata in this formation are strictly fluvial non-marine sediments and grade upward into marine deposits. The lowest strata in each area is comprised of homogeneous, non-marine sands. It grades up into estuarine point-bar type deposits whose upper beds show tidal influences as indicated by thin beds of shale.

The sands of the McMurray formation are essentially non-marine material of variable thickness deposited under fluvial conditions. For these reservoirs, the thickness of the oil bearing sands can vary between 6 m and 60 m . The formation is underlain by Paleozoic carbonates and overlain by the marine deposits of the Clearwater formation, which are mainly composed of layered thin silts and shales (*Rottenfusser et al.*, 1988).

The geological setting for the Lloydminster-styled reservoir at Senlac is geological similar. This reservoir is located within the Dina formation, which is a member of the Mannville group (*Christopher*, 1997). The Dina formation at Senlac, which is laterally equivalent to the McMurray formation in northern Alberta, is also a channel sand deposit overlying the Paleozoic carbonates. Deposition probably occurred either as fluvial or deltaic, estuary valley fill (*Chakrabarty et al.*, 1998). At the base the formation consists of massive sands, which then fines upwards and with increasing amount of shale interbeds merges with the overlying shales of Cummings formation.

3.2.1 Athabasca reservoir near Fort McMurray, Alberta

At Athabasca, the bituminous oil sands are found in shallow reservoirs and much of the bituminous crude is extracted by surface mining. The oils produced by upgrading this bitumen accounts for approximately 20% of Canada's total petroleum production. The representative well log for the Athabasca reservoir in Figure 3.5 shows the reservoir sand of interest between 135 m and 157 m depth.

The sands lie immediately above a sequence of high velocity carbonates and below a thin, low velocity gas saturated sand and a thin shale layer. The reservoir consists of unconsolidated sands with an average porosity of 32% (*Chalaturnyk*, 1996) and with a
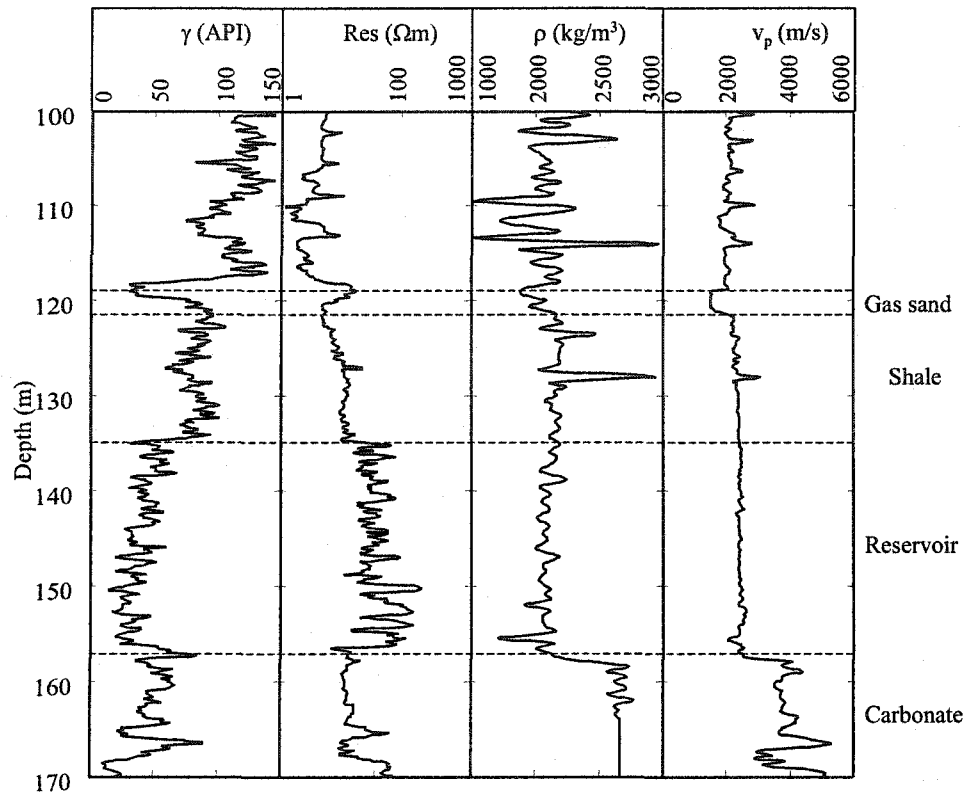
Figure 3.5: Typical well log from the Athabasca region.

bitumen saturation $S_O \approx 89\%$. The permeability of the oil sands averages to $k \approx 4D$, and this high value makes a SAGD program possible in sections of the reservoir too deep to mine. The viscosity of the heavy oil at reservoir condition is about 18 Pa·s (*Ward and Clark*, 1950). Therefore, the oil is basically immobile at reservoir temperature of approximately 8°C. The reservoir itself is discontinuous with siltstone and shale layers interbedded within the oil bearing sands (see the significant variations of the γ-log in Figure 3.5). There is evidence that viscous bitumen from the Athabasca oil sands has a finite shear strength (*Hornby and Murphy*, 1987). Therefore, at the in-situ reservoir conditions Gassmann's equation cannot be applied to determine the frame properties from zones saturated with heavy oil, as it assumes that the pore fluid does not exhibit resistance against shear forces. Furthermore, error would be added because the *in-situ* oil bulk

modulus and density are only approximately known. Instead, the quasi-static frame properties measured for geotechnical purposes on core samples by *Chalaturnyk* (1996) are employed in the calculations. From the same reference data for the porosity and saturations of oil and water were obtained. Table 3.4 summarizes the relevant data used in this work for this reservoir.

3.2.2 Lloydminster reservoir at Senlac

The Lloydminster type reservoir, located in central-eastern Saskatchewan, is at approximately 750 m depth one of the deepest reservoirs in Canada in which a SAGD-program has been applied. The representative well log shown in Figure 3.6 was recorded in a deviated well. Due to the lack of well deviation data the well could nor be corrected to (true) vertical depth. However, such a correction is not critical for the purpose of this study, which focuses on the rock properties and their influence on measurable seismic attributes. The reservoir lies between an overlying shale of the Cummings formation and the underlying high-velocity, Paleozoic carbonates. The shale layer is interrupted by a thin coal layer appearing at approximately 820 m log-depth, which is indicated by low density values. The overlaying shales of the Cummings formation are distinguished from other formations by the γ-ray log. Shales contain clay minerals with radioactive elements (such as potassium, uranium, and thorium, which attach to the clay lattice) and cause the typical signature of shales in well logs.

The water- and oil-saturated zones within the reservoir are distinguished in the resistivity log on the basis of high (oil) and low (water) resistivity, respectively. In contrast, all the other log curves are relatively uniform within the reservoir; and therefore we assume that the reservoir matrix is fairly homogeneous.

Core analysis further indicates that the reservoir consists of a clean and a unconsolidated to weakly consolidated sand with an average porosity of $\phi \approx 32$ %. Prior to steam injection, the oil and water saturations are $S_O \approx 85$ % and $S_W \approx 15$ %, respectively. The permeability of the reservoir is in the range of $k = 5 - 10\,D$.

Under reservoir condition the oil is basically immobile because of its high viscosity ($\eta \approx 5\,Pa \cdot s$). Furthermore, the oil is characterized by an API oil gravity of 13°, which corresponds to a density of $\rho = 980\,kg/m^3$ (*Chakrabarty et al.*, 1998).

112
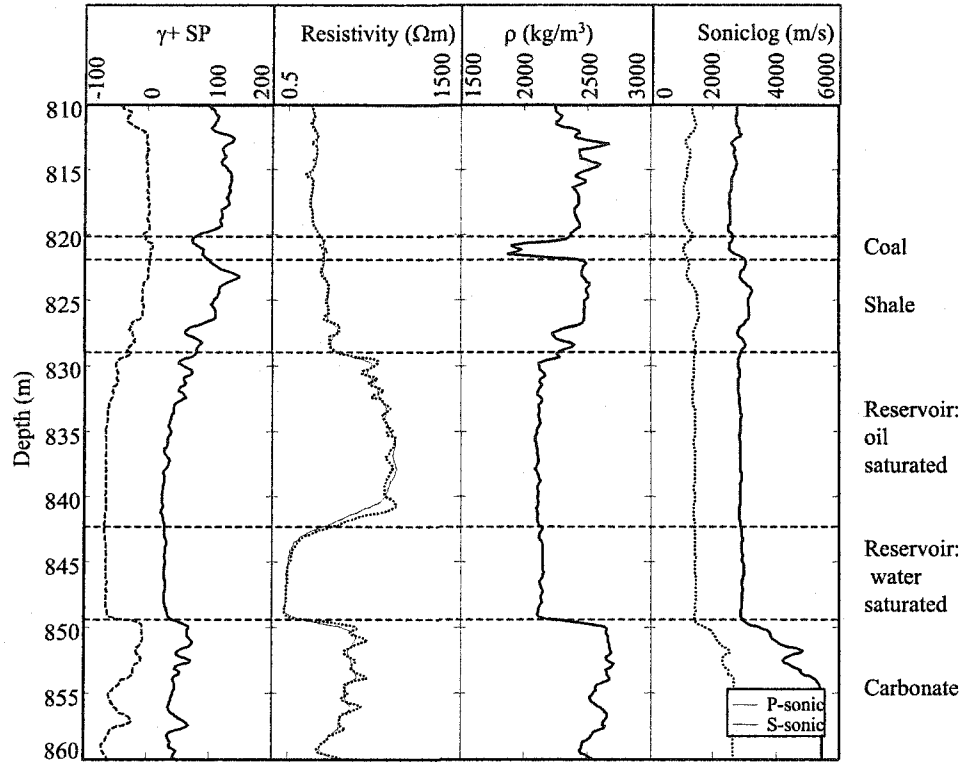
Figure 3.6: Typical well log from the Lloydminster reservoir.

3.3 Well log database

The reservoirs at Athabasca and Senlac are characterized petrophysically mainly by well log analysis. For the Athabasca reservoir only one well log was available in digital format, which is shown in Figure 3.5. However, comparison of these data with nearby well logs indicate that this well is representative of reservoirs in this area

Abundant well logs in digital form are available from the Lloydminster area. Figure 3.7 shows the layout of the plant, the horizontal SAGD wells (labelled B1 to B3), the two seismic lines, and the location of two wells, which have been employed to study the reservoir. Another nearby well was also included in the characterization process.
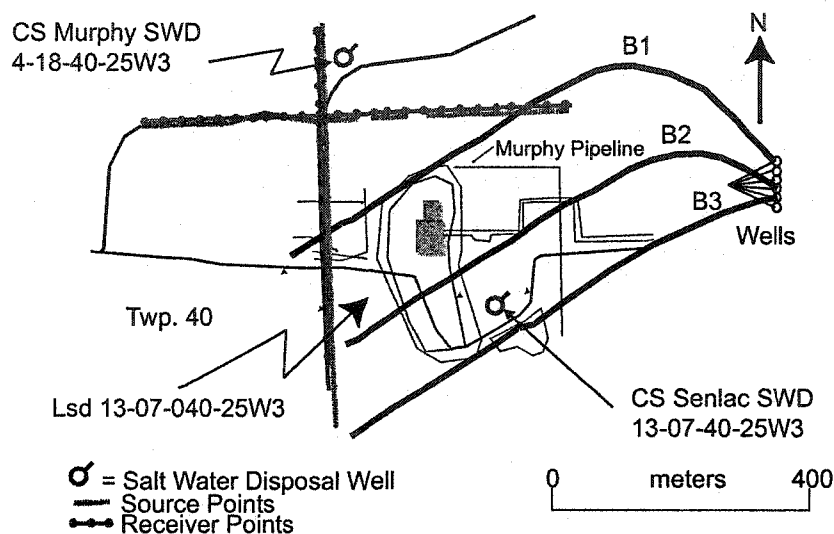
Figure 3.7: Map of the Senlac plant showing the relative location of the horizontal wells (thick solid lines), the two seismic profiles (blue and red lines), and the three wells, whose log data have been included in the analysis.

3.3.1 Lloydminster reservoir

Core analysis of well CS SENLAC A13-7-40-25 A core from the Murphy CS Senlac SWD A13-7-40-25 well has been analysed by Core Laboratory, Calgary (1993). This report summarises the geology and petrological information of the depth interval that contains the reservoir. The reservoir consists of fairly clean sandstone or sand with a negligible amount of clay. The thickness of the oil-saturated layer is about 8 m in this well. Overlying the reservoir is a sandy shale and thin sandstone layer, about 7 m thick, and a coal bed, 1-2 m thick. These two layers can be used as an indicator of the reservoir depth in the well logs as these layers have a distinguished signature in the γ-ray and density log, respectively. From the results of the core analysis values for various parameters for the reservoir are obtained by calculating the arithmetic average and the standard deviation (see also Figure 3.8 and Table 3.2). The high quartz content of about 95 % is reflected in the density of the solid grain material of $\rho_s = 2643$ kg/m^3, which is very close to the accepted value of 2650 kg/m^3 for quartz (e.g. *Mavko et al.*, 1998). With $\phi \approx 33$ % the core porosity in the reservoir layer is quite high (although it is not known if the porosity

114
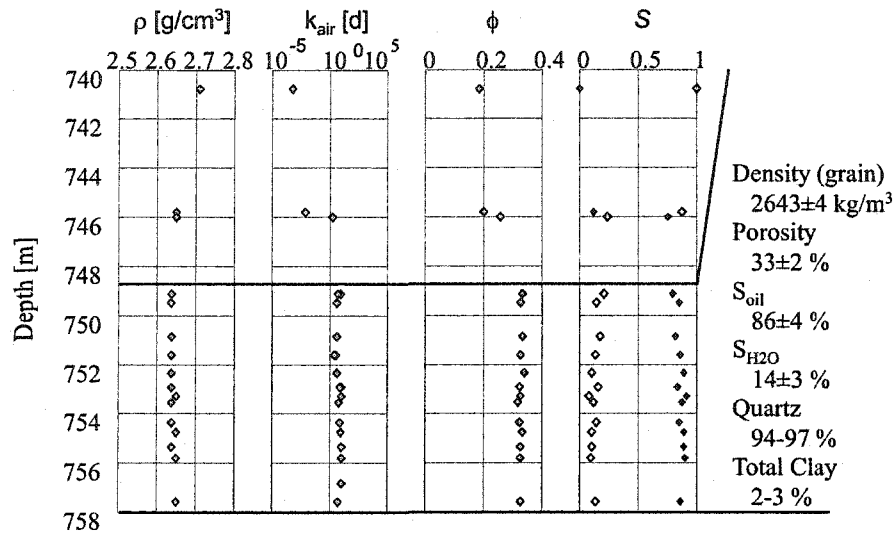
Figure 3.8: Results of the core analysis from Well A: CS SENLAC A13-7-40-25 (ρ: density of the solid material, k_{air}: permeability, ϕ: porosity, S: saturation, where open diamonds represent water and filled diamonds oil saturation).

has been measured under in-situ pressure conditions). Within the reservoir zone the oil saturation averages to 86 %, and water fills the remaining pore space.

The rock matrix is dominantly built of quartz grains with only a small amount of clay. However, the clay distribution within the rock matrix is not reported. If the clay minerals contribute to the rock frame, then the elastic moduli of the frame will be significantly affected (e.g. *Marion and Nur*, 1991 and *Han et al.*, 1986). If, on the other hand, the clay is located within the pore space, then the values for porosity and density of the effective medium will be affected by the clay, but not the stiff frame. However, to incorporate the effects of clay on the effective properties in the analysis, necessary information, most importantly the location of the clay minerals in the rock matrix, are presently not available. We therefore assume the clay content to be negligible.

Three well logs from the Lloydminster region have been analysed (see the detailed description in Appendix B). From these well logs average values of the density and the sonic velocities were determined, which are included in Table 3.3. The velocities and densities measured in the three wells are fairly consistent. This suggests that the

115

Table 3.2: Average rock and fluid properties measured for the core from the Lloydminster reservoir

ρ_s	$2643 \pm 4 \, \text{kg/m}^3$
ϕ	$33 \pm 2 \, \%$
P_{Quartz}	94-97 %
P_{Clay}	2-3 %
S_{Oil}	$86 \pm 4 \, \%$
S_{H_2O}	$14 \pm 3 \, \%$

properties of the reservoir layer are uniform at the study site. Although there is only one well log available that contains sufficient information to determine the elastic properties of the mineral frame according to the theory in section 3.1.2, these values are considered to be representative for this reservoir.

3.4 Determination of the elastic parameters

Before simulating the effects of steam injection on the seismic properties and thus accessing the magnitude of changes in the seismic attributes, the elastic properties required in Gassmann's equation (3.1) must be determined. While most of these parameters are easily measured from cores (e.g., the porosity ϕ) or are available in literature (e.g., the quartz grain bulk modulus, K_s, in e.g., *Mavko et al.*, 1998), the elastic moduli of the frame must be determined for each reservoir individually.

Table 3.3: Petrophysical properties of the Senlac reservoir

	Density [kg/m^3]	P-velocity [m/s]	S-velocity [m/s]
Well A: CS SENLAC A13-7-40-25			
Oil saturated layer	2123 ± 25	2968 ± 31	—
Well B: CS SENLAC SWD B4-18-40-25W3			
Oil saturated layer	2130 ± 21	2957 ± 27	—
Water saturated layer	2126 ± 15	2978 ± 25	—
Well C: PCP PCR SENLAC OBS DD 11C7-12-4C6-12-40			
Oil saturated layer	2120 ± 22	2864 ± 28	1403 ± 19
Water saturated layer	2144 ± 12	2930 ± 28	1448 ± 14

3.4.1 Athabasca reservoir

The Athabasca materials are relatively shallow and as such are much more compressible. Unfortunately, the lack of V_S-sonic log for the Athabasca reservoir does not allow the frame bulk modulus to be determined from well-logs. Also, as mentioned previously the bituminous crude from the Athabasca reservoir can possess a finite shear strength, therefore, the approach to determine K_d as outlined in section 3.1.2 can not be applied for this reservoir. Instead, the parameters determined by *Chalaturnyk* (1996) from quasi-static uni-axial bulk compressibility test are employed here (Table 3.4). The relative low value of $K_d = 0.667$ GPa reflects the weak consolidation of this material. It is interesting to note that this value is less than the liquid bulk moduli that are on the order of 2 GPa. It must also be noted that static and dynamic moduli are seldom the same due to the differences in strain accommodation (e.g. *Wang*, 2000a). As such, these static values must be taken as lower bound to the seismic (dynamic) values.

Table 3.4: Frame properties of the Athabasca reservoir.

K_d [GPa]	0.667
μ_d [GPa]	0.308

3.4.2 Lloydminster reservoir

The Lloydminster reservoir sand's frame bulk modulus was determined using the velocities of the lower water saturated sand primarily because the properties of brine with respect to salinity, pressure, and temperature are well known (e.g. *Batzle and Wang*, 1992). This information is then incorporated into equation (3.4) to determine the frame bulk modulus K_d. In contrast, the estimation of the *in-situ* frame modulus of the heavy oil saturated zone is substantially less certain because of incomplete knowledge of the pore scale distribution of the mixed fluids and because the heavy oil properties themselves are only poorly known. Furthermore, Gassmann's equation may not apply to the *in-situ* reservoir properties because of the possibility that the viscous heavy oil itself has a finite shear modulus.

As mentioned earlier, the sonic and the density log curves do not vary significantly within the reservoir sand unit; consequently, it is assumed that the frame bulk modulus

Table 3.5: Calculated brine properties for the Lloydminster reservoir

K_f	2.23 GPa
ρ_f	997 kg/m^3
K_S	36 GPa
ϕ	0.33 ± 0.02
ρ_{eff}	2119 ± 14 kg/m^3
V_P	2867 ± 27 m/s
V_S	1453 ± 13 m/s
K_{eff}	12.5 ± 0.4 GPa
K_d	8.7 ± 0.8 GPa
$\mu_{d_{Water}}$	4.5 ± 0.1 GPa
$\mu_{d_{Oil}}$	4.2 ± 0.2 GPa

is uniform in both the water and the oil saturated region. This assumption is further supported by the observation that the shear frame modulus μ_d calculated from the S-sonic log by equation (3.6) is nearly constant with values of 4.2 ± 0.2 GPa and 4.5 ± 0.1 GPa for the oil and water saturated zones, respectively.

Batzle and Wang (1992) compiled empirical equations for the density and P-velocity of water, which are derived on the basis of numerous measurements of the properties of water under various temperature, pressure, and salinity conditions. Particularly, their equations *27a* and *b* have been used to calculate the density of the water. The P-velocity of the pore fluid was obtained by applying their equations *28* and *29*. These empirical equations are included in Appendix C. The bulk modulus of the pore fluid could then be calculated according to

$$K_f = \rho_f V_{P_f}^2.$$

Using these values for the various bulk moduli in equation 3.4 yields the frame bulk modulus for the water saturated reservoir of $K_d = 8.7 \pm 0.8$ GPa (details of the uncertainty calculation are included in Appendix D).

It is useful to compare this value to those obtained for similar materials either experimentally (e.g. *Eastwood*, 1993) or theoretically (e.g. *Murphy et al.*, 1993). Such comparisons show that the Lloydminster reservoir's frame bulk modulus is relatively stiff, suggesting that the reservoir rock matrix consists of more consolidated material. This contrasts with *Eastwood* (1993) measurements on a dry, unconsolidated, possibly recon-

118

stituted sand from the Cold Lake heavy oil reservoir in Alberta. He derived empirical relationships for the frame bulk modulus in terms of the effective pressure and porosity. Applying this model using the Lloydminster reservoir conditions gives $K_d = 6.9$ GPa. *Murphy et al.* (1993)) compiled several measurements of the frame properties of consolidated and unconsolidated sands and also constructed an empirical dependence of the frame bulk modulus on the porosity; their formula yields $K_d = 4.9$ GPa for the Lloydminster reservoir porosity. Obviously, there is a wide scattering of the frame bulk modulus for the different assumptions with the value determined from well log data exceeding the other models substantially. Figure 3.9(a) shows an environmental scanning electron microscope (ESEM) image of a cleaned sample from the Lloydminster reservoir sands, which has been imaged under room temperature and pressure conditions, whereas Figure 3.10 shows an ESEM image of a sample containing residual oil.

The sand grains are highly rounded and almost no cementation or grain overgrowth is apparent, indicating that the reservoir consists of unconsolidated sands. ESEM images from other samples occasionally show the patches of quartz minerals that are connected to each other by clay minerals (Figure 3.9(b)). These patches, however, are localized and do not build a continuous network through the rock sample[2]. Under *in-situ* pressure conditions, which are approximately $P_{eff} = 15$ MPa at Senlac, the sand grains are most likely more pressed to each other and therefore more rigid against compression. This may explain the relative high values for the elastic frame moduli.

Of course, these values, based on information determined from well logs by parameter fitting, is affected by any erroneous sonic log data. However, these values are consistent with the well logs, and therefore the frame moduli probably accurately reflect the reservoir conditions of the Lloydminster reservoir.

3.5 Simulating the SAGD-process

Now that reasonable elastic parameters are established, the SAGD process can be simulated by substituting the original oil in the pore space by a mixture of oil, steam, and water at elevated temperatures and subjected to expected pore pressures. Initially, the

[2]Dean Rokosh, personal communication
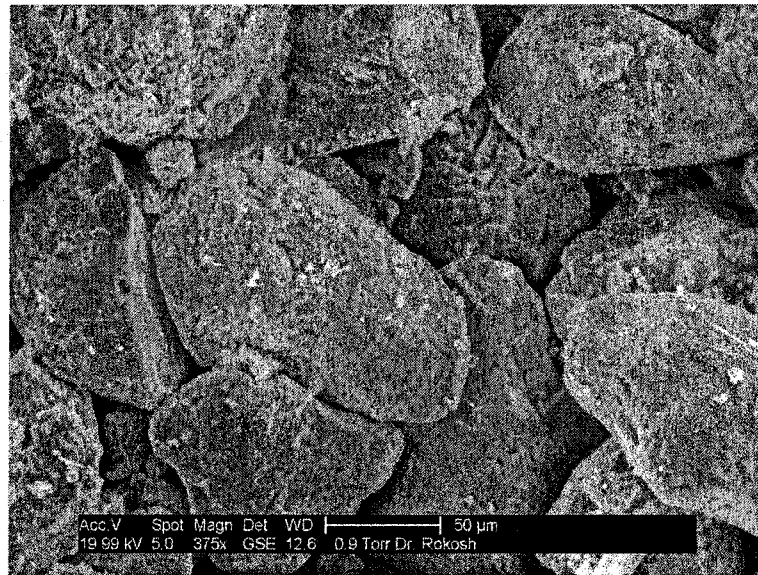
(a)
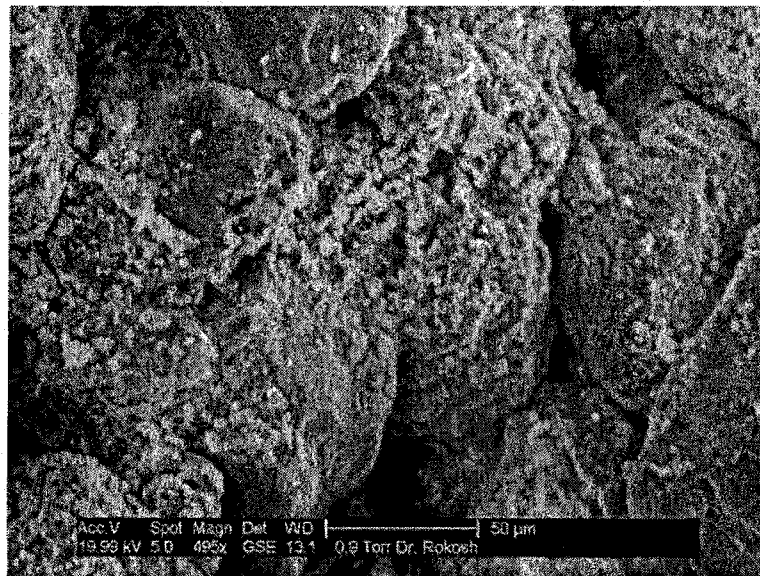
(b)

Figure 3.9: Top: ESEM image of a cleaned reservoir sand sample from the Lloydminster reservoir. The image shows a loose assemble of sand grains that are barely connected by cementation or overgrowth. Bottom: ESEM image of a cemented patch within the same sample.

120
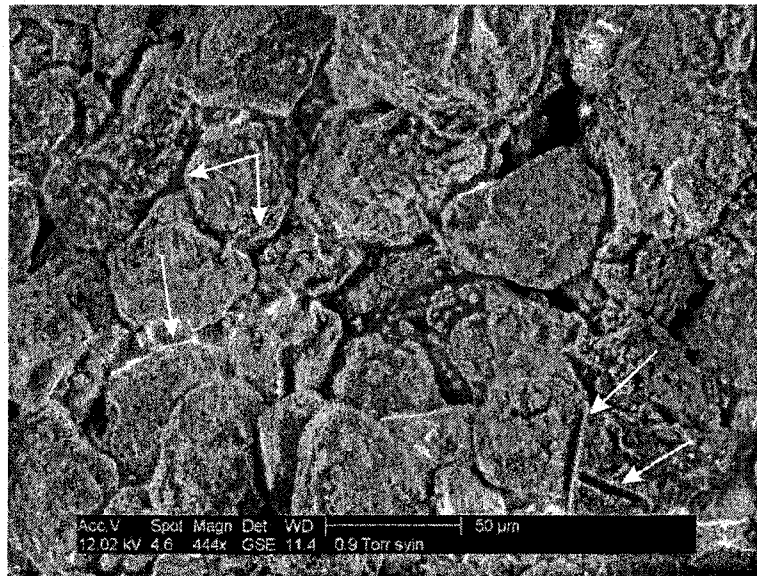
Figure 3.10: ESEM image of a oil saturated reservoir sand sample from the Lloydminster reservoir shown for comparison. Some oil patches are indicated by white arrows in the image.

pore pressure is assumed to remain unchanged by steam injection, which is consistent with standard models of SAGD processes (e.g. *Butler*, 1994). The potential effects of pore pressure variations on the seismic properties will be discussed in section 3.5.4.

3.5.1 Model for fluid substitution

Many studies have solely focussed on the decrease in velocity due to heating of oil saturated reservoirs. However, for the SAGD steam injection case considered here the situation is substantially more complicated. After steam injection, the 'effective' pore fluid will surely be an immiscible mixture of residual hydrocarbons and water in both liquid and gas phases, which are distributed in a complex fashion within the pore space of the rock. Other gases, most notably methane, may be present as well, as they exsolve if the pore pressure reaches the bubble point.

The effective acoustic velocity for a two-phase single component mixture such as water and steam involves complicated physical processes. In a theoretical analysis, *Kieffer* (1977) showed that the sound speed for water-steam (i.e. liquid-gas) mixture is signifi-

cantly lower than that of either phase alone (see also *Domenico, 1977*). Furthermore, for such a single-component, two-phase system the velocity depends on whether or not the compression by a passing seismic wave allows for thermodynamic equilibrium between the two phases. For very low frequencies of the seismic wave there can be sufficient time to establish thermal equilibrium between the two phases. In this case, the resulting isothermal velocity can be as low as 1 m/s (*Kieffer, 1977*). However, a criterion for the upper limit of the frequency for this process to occur is apparently not yet known. As the frequencies used in seismic exploration are relatively high, it will be assumed that the effective moduli of the porous medium are adiabatic. A similar discrepancy between adiabatic and isothermal compression also exists for the solid, but the velocity 'dispersion' is, however, much less for this case.

Ideally, injection creates a steam chamber filled with high quality steam (i.e. the injected water-steam fluid consists of more than 80 % of gas phase steam) at elevated temperature, but at nearly the original in-situ pore pressure. In reality, however, a residual amount of oil will remain in the depleted reservoir. The injection temperature of the steam is typically chosen such that it matches the temperature of the steam saturation condition for the in-situ pore pressure. Thermodynamically, the saturation conditions define the pressure and temperature at which liquid phase and steam phase water co-exists (see the phase diagram in Figure 3.11). Therefore, in an ideal SAGD process considered here, the in-situ pore pressure in the reservoir solely determines the temperature of the injected steam in the model.

For the Lloydminster reservoir the following reservoir model for the fluid substitution is assumed (Figure 3.12):

- Prior to steam injection, the oil saturation in the reservoir is $S_O = 85\%$, the water saturation is $S_W = 15\%$, the pore pressure is $P_{pore} = 5$ MPa, and the temperature is $T = 28°C$.

- In the steam chamber the temperature has been raised to $T = 265°C$ at the same pore pressure of 5 MPa. The oil saturation has decreased to 20% while steam and liquid water occupy 65% and 15% of the pore space, respectively. A solid diamond in the phase diagram (Figure 3.11) indicates the assumed pressure and temperature
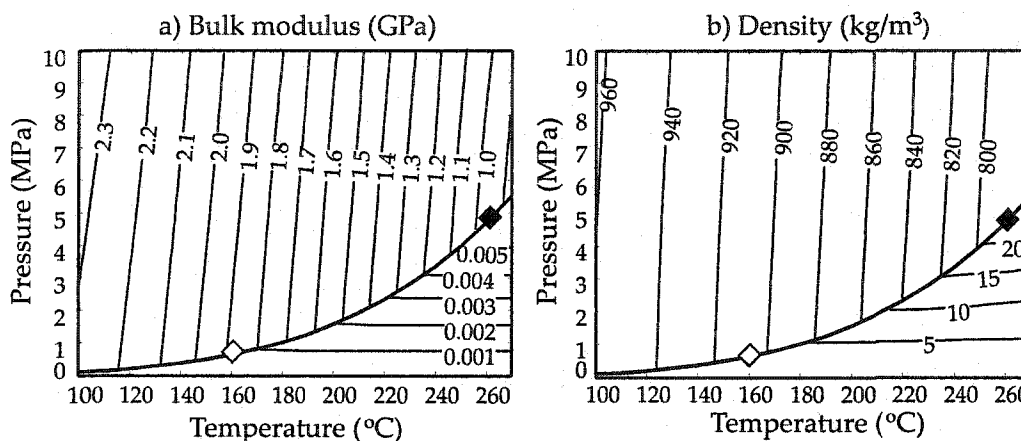
Figure 3.11: T-P-phase diagram for the bulk modulus and density of water and steam as a function of temperature and pressure. The thick line represents the steam saturation curve, which separates the liquid phase (above) from the steam (below). The diamonds represent the anticipated P-T conditions in the Lloydminster (black) and Athabasca reservoir (white), respectively. (Fluid properties taken from *Lemmon et al.*, 2003)

conditions within the steam chamber.

For the Athabasca reservoir the following temperature and saturation values are assumed:

- The initial oil saturation is 81% and the remaining 19% of the pore space are filled with water. The in-situ temperature and pore pressure of the reservoir are $T = 8°C$ and $P_{pore} = 0.5$ MPa (*Chalaturnyk*, 1996).

- After steam injection, a mixture of 19% water, 20% oil, and 61% steam fills the pore space in the steam chamber. The temperature within the steam chamber is 160°C, whereas the pore pressure remains at 0.5 MPa. The temperature and pressure condition in the steam chamber for this reservoir are marked by an open diamond in Figure 3.11.

The calculation of the effective properties of the fluid mixture in equations 3.7 and 3.8 requires the knowledge of these properties for the three fluid components at elevated pressures and temperatures. In this study, the data by *Lemmon et al.* (2003) are employed for the density and bulk modulus of steam and liquid water (Table 3.6).
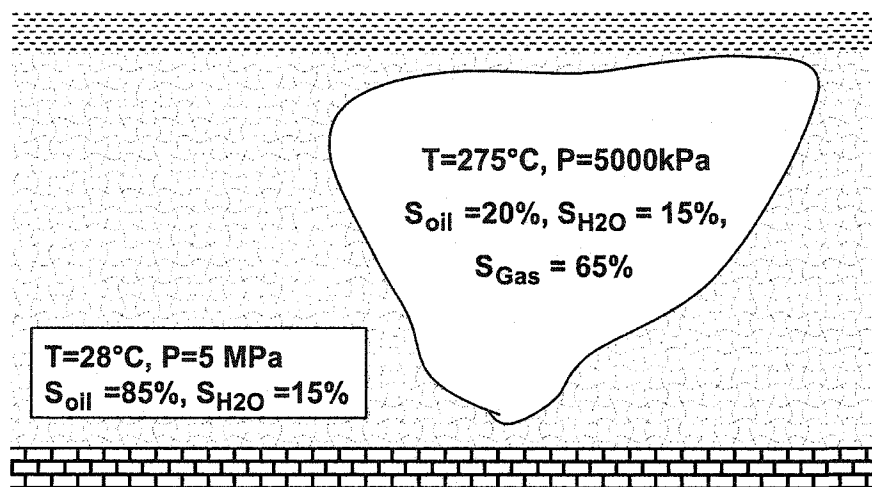
Figure 3.12: Schematic sketch of the steam chamber model for the Llyodminster reservoir.

Table 3.6: Saturation properties of steam and water

	Temperature [°C] / Pore Pressure [MPa]					
	120 / 0.2	179 / 1	212 / 2	234 / 3	250 / 4	263 / 5
ρ_{St} [kg/m^3]	1.12	5.15	10.04	15.00	20.10	25.35
ρ_W [kg/m^3]	942.0	887.0	849.0	821.0	798.0	777.0
K_{St} [GPa]	0.0003	0.0013	0.0026	0.0038	0.0051	0.0063
K_W [GPa]	2.17	1.72	1.42	1.21	1.05	0.92

Unfortunately, there are no data yet available for the properties of the oil from the Lloydminster reservoir. However, *Eastwood* (1993) measured the density and bulk modulus of oil from a nearby Cold Lake reservoir, which are employed in the present analysis under the assumption that these properties are also applicable to the Lloydminster reservoir. *Eastwood* (1993) measured the oil's density and bulk modulus only in the temperature range between 22°C and 127°C. His measurements of the density and bulk modulus at different temperatures can be approximated by the following linear relationships

$$\rho_o(T) = 1000.7 - 0.6111\,T\,[\text{kg/m}^3], \tag{3.9a}$$

$$K_o(T) = 2.0 - 0.0066\,(T - 20.8°C)\,[\text{GPa}], \tag{3.9b}$$

where the temperature is measured in °C.

Eastwood (1993) further reports that the properties of the oil sample does not change

significantly with pressure, an observation also supported by *Batzle and Wang* (1992). Given the small expected variations of the pore pressure during a SAGD-program, changes of the oil's properties with pressure may be neglected.

Steam at the Lloydminster reservoir is injected at a temperature of $T \approx 265°C$, this is above the temperature range covered by *Eastwood* (1993). The linear relationships (equations 3.9a and 3.9b) must therefore extrapolated. According to *Batzle and Wang* (1992), such an extrapolation is possible as long as one does not come close to the temperature of a phase transition.

As no measurements of the temperature dependent properties of the Athabasca oil are available, empirical equations compiled by *Batzle and Wang* (1992, equations 18, 19, and 20b, see Appendix C) serve in the analysis.

3.5.2 Application to the Athabasca reservoir

As mentioned earlier the temperature at which the steam is injected is typically chosen such that it meets the steam saturation conditions of the reservoir pore pressure. For the Athabasca reservoir, *Chalaturnyk* (1996) reports a pore pressure value of $P_{pore} = 0.5$ MPa; from Table 3.6 the corresponding temperature then is found by interpolation to be $T_{St} \approx 160°C$. The resulting properties for the steam, water, and oil, respectively, were then found in steam tables (e.g. *Lemmon et al.*, 2003) or determined by empirical equations.

Substituting these values into equations 3.7 gives the effective fluid properties for the Gassmann model. In the following step the equations 3.3 and 3.1 then allow for the calculation of bulk density and the bulk modulus of the effective medium, from which the seismic velocities are calculated.

To obtain the effective velocities after fluid substitution according to the patchy saturation model the properties of the different fluid components along with those of the solid material are used in equations 3.3 and 3.8. The results of these calculations are summarized in Table 3.7. Theoretically, the S-velocity could have been calculated for the reservoir after fluid replacement. However, as there are no S-sonic data included in the well log nor can such data be calculated due to the possibly finite shear strength of the bitumen, such a number would not provide any insight, and therefore, this value is not included in Table 3.7.

125

Table 3.7: Seismic properties before / after fluid substitution for the Athabasca reservoir.

	Before	After	Change
K_d [GPa]	0.667		—
μ_d [GPa]	0.443		—
K_f [GPa]	2.77	0.0015	−99.95%
ρ_f [kg/m^3]	1008.0	315.0	−68.75%
K_{eff} [GPa]	7.86	0.672	−91.45%
ρ_{eff} [kg/m^3]	2122.0	1898.0	−10.56%
$V_{P_{Gass}}$ [m/s]	1974.0	755.0	−61.75%
$V_{P_{patchy}}$ [m/s]	1974.0	877.0	−55.57%
V_S [m/s]	—	—	
$\mathcal{AI}$ [kg/m^2/s]	4.2×10^6	1.4×10^6	−66.67%

3.5.3 Results for the Lloydminster reservoir

Similar calculations give the results for the Lloydminster reservoir after fluid substitution, which are summarized in Table 3.8.

In both cases, the effective fluid bulk modulus of the steam-water-oil mixture is substantially lower than that of the original oil-water saturation and can be neglected when compared with all other elastic bulk moduli. As a consequence of such a low fluid bulk moduli, the effective bulk modulus of the effective medium approaches that of the undrained frame. Furthermore, upon substitution, the bulk density of the effective medium decreases by 11.8% while the P-wave velocity decreases by only 3.4% for the

Table 3.8: Seismic properties before / after fluid substitution for the Lloydminster reservoir.

	Before	After	Change
K_d [GPa]	8.7±0.8		—
μ_d [GPa]	4.2±0.2		—
K_f [GPa]	2.38	0.0096	−99.60%
ρ_f [kg/m^3]	998	301	−69.84%
K_{eff} [GPa]	11.8±0.5	8.7±0.7	−26.27%
ρ_{eff} [kg/m^3]	2120±14	1870±12	−11.79%
$V_{P_{Gass}}$ [m/s]	2864±27	2767±27	−3.38%
$V_{P_{patchy}}$ [m/s]	2864±27	2792±25	−2.51%
V_S [m/s]	1403±13	1498±14	+6.77%
$\mathcal{AI}_P$ [kg/m^2/s]	6.07×10^6	5.17×10^6	−17.34%
$\mathcal{AI}_S$ [kg/m^2/s]	2.97×10^6	2.80×10^6	−5.82%

Lloydminster reservoir. In contrast, the decrease of 62% of the P-wave velocity in the Athabasca reservoir are notably larger, whereas the effective density decreases by approximately 10%, a value similar to the one calculated for the Lloydminster reservoir. The patchy saturation model generally provides higher velocities. The 2.5% velocity decrease assuming patchy saturation for the Lloydminster reservoir does not differ significantly from the homogeneous distribution model. On the other hand, a much larger difference between the two saturation states is seen for the Athabasca reservoir, for which the velocity decrease assuming patchy saturation is 55.6%. The overall change due to fluid substitution in the Athabasca reservoir is large regardless of the model employed.

3.5.4 Modelling pressure effects

So far, only the effects of temperature and fluid substitution on the seismic parameters have been considered. However, pore pressure and effective confining stress effects are also important in all rocks but particularly in unconsolidated materials. Although engineers attempt to maintain the in-situ reservoir pore pressures during the SAGD processes, this is not always possible and consequently the effective stress on the reservoir will change.

Generally, seismic velocities increase with effective confining pressure P_{eff}, which is defined as the difference between confining (or total) P_c and pore pressures P_{pore}:

$$P_{eff} = P_c - P_{pore}. \tag{3.10}$$

The pressure effect is due to diminished porosity, closing of long aspect ratio crack-like porosity, and stiffening of grain contacts. Within the framework of Gassmann's theory this can be accounted for by assuming a dependence of the frame bulk modulus on the effective pressure. An intrinsic shortcoming of the method outlined in section 3.1.2 to estimate the frame bulk modulus K_d is that it yields a value valid only for the effective stress existing at the time the logs were recorded; as such the pore pressure effects for the reservoirs cannot be directly determined. However, such effects can be significant in weakly consolidated sands.

In order to estimate the influence of P_{eff} on the seismic velocity, the available literature data has been sampled. Figure 3.13a contains a compilation of several $V_P(P_{eff})$

127

relationships.

The curve after *Eberhart-Phillips et al.* (1989) represents an average dependence of the seismic velocity on effective pressure for a wide range of water saturated sandstones for porosities $\phi = 32\%$. The values used in this analysis were measurements on a large suite of sandstones and as such may be taken to represent the upper bound of that anticipated for weakly consolidated oil sands.

The second data set is derived from the measurements of *Eastwood* (1993) who measured the P-wave velocity of a saturated Cold Lake oil sand for various effective pressures. These measurements were taken at effective pressures significantly lower than those assumed for the deeper Lloydminster reservoir.

The measurements of *Domenico* (1977) on water-saturated glass beads and unconsolidated Ottawa sands provide further experimental values for clean and uncemented granular media. Also included in this figure is a theoretical curve representing a recent modification to the Hertz-Mindlin contact theory for a dry sand by *Makse et al.* (1999). This theoretical curve provides a lower bound for the experimentally determined acoustic velocities where there is no cementation between the quartz grains.

The curves of Figure 3.13a show a substantial variation in velocity that depends on the model used. However, what is more important for the present purpose is that all of the models give similar variations in the velocity dependence with P_{eff} (Figure 3.13b). The velocity gradients of the experimental data are consistent with the Hertz-Mindlin model. The scatter can possibly be attributed to experimental errors and to difficulties in picking the data from the curves in *Domenico* (1977) and *Eastwood* (1993). The curves from of the Eberhardt-Phillips and the Hertz-Mindlin models can be considered as providing the lower and upper bounds, respectively, for the velocity gradients.

In the Lloydminster reservoir, a typical pore pressure decline due to production can be of the order of 2 MPa. From the integration of the density log we estimated the lithostatic pressure to be 18 MPa; implying that the effective pressure increases from the original 13 MPa to 15 MPa during steam injection. At this pressure range the compressional wave speed will only increase by 10 to 20 m/s per every 1 MPa increase in effective pressure (Figure 3.13b). Consequently, a 2 MPa pore pressure decrease corresponds to a velocity increase in the range of 20 m/s to 40 m/s for the Lloydminster reservoir. This
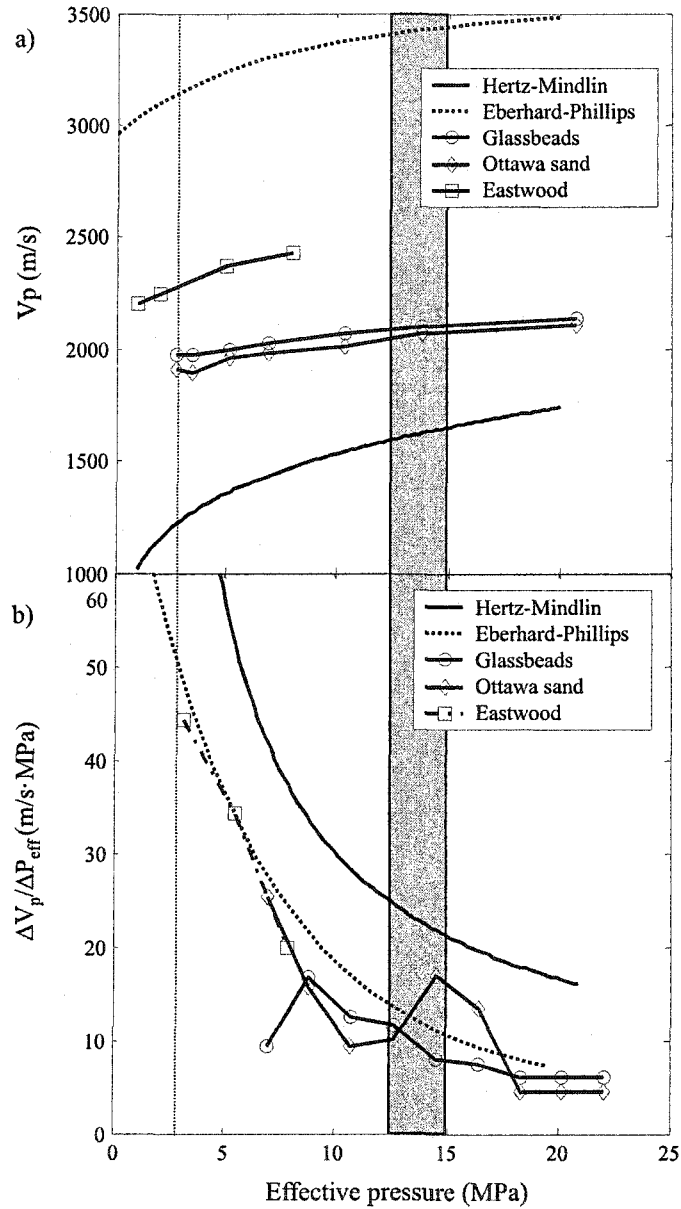
Figure 3.13: a) Variation of the *P*-velocity with effective pressure. b) Velocity-Pressure gradients against effective pressure. The gray-shaded area indicates the pressure range for the Lloydminster reservoir, the dotted line shows the assumed effective pressure for the Athabasca reservoir.

negates a substantial fraction of the $\sim$100 m/s decrease in velocity due to fluid substitution effects.

In the same way, the lithostatic pressure for the Athabasca reservoir is estimated to be approximately 3 MPa with an effective pressure near 2.5 MPa. For such low effective pressure the change in velocity with effective pressure is much more pronounced with velocity gradients of the order of 50 to 60 m/(s·MPa). However, the substantial reduction of the P-velocity due to fluid replacement more than compensates for any expected effects caused by increases in the effective pressure and should not jeopardize the feasibility of seismic monitoring in the shallow Athabasca reservoir. A possibly increased pore pressure, however, causes the P-wave velocity to decrease even further making seismic monitoring highly feasible for such cases.

3.5.5 Synthetic seismic analysis

The changes of the velocities and densities upon fluid substitution in the reservoir zone must influence the propagation of the seismic wavefield. The change in the normal incidence reflectivity at the top of the reservoir, $\Delta\mathcal{R}$, and the change in travel time to the bottom of the reservoir, Δt, before and after fluid replacement are two direct and physically meaningful seismic attributes that can provide information about the change in saturation within the reservoir. To examine the feasibility of seismic monitoring, the changes anticipated in the zero-offset seismic reflection response are examined in this section. The seismic response is predicted using standard 1-D convolution synthetic seismograms; the reflectivity time series for the original and the substitutional logs of velocity and density are calculated and then convolved with Ricker wavelets of different center frequencies.

Before applying fluid substitution the reservoir is carefully selected using the available suite of well logs. In a second step the density and P-velocity data are reduced according to the values given in Tables 3.7 and 3.8.

Generally, sonic well log measurements are averaged over a certain depth range, which is due to the distance between the source and the receiver on the tool. To mimic this effect in the well log modification the depth interval to be modified is smoothed at the upper and lower edge. Within the central part of the modification operator the well data are changed, for example, the density is reduced by 11.8% for the Lloydminster

130
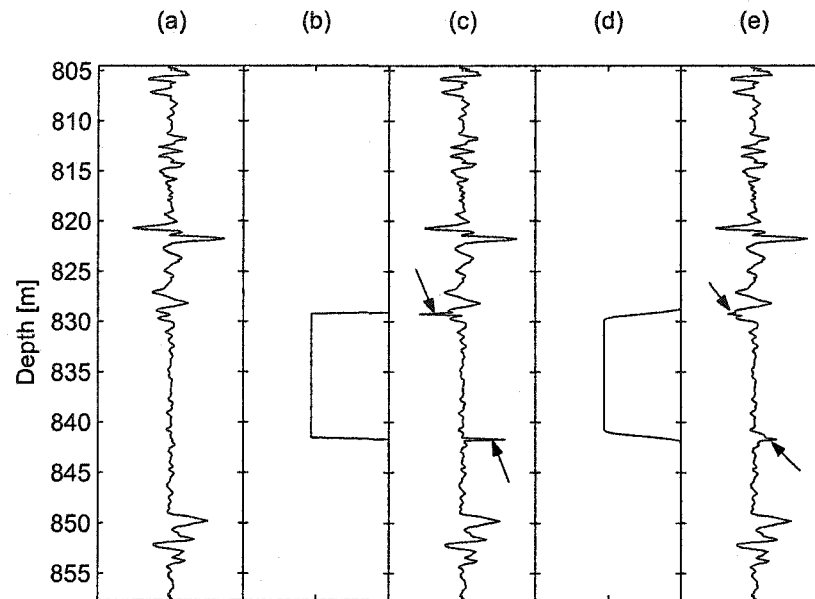
Figure 3.14: The smooth modification of the well log data to simulate the fluid substitution in a SAGD process. The arrows in the panels (c) and (e) are pointing to the new reflectivity peaks after fluid substitution.

reservoir according to Table 3.8. However, towards the edges of the reservoir the modification value becomes gradually less. This procedure and its effects are illustrated for the reflectivity data shown in Figure 3.14(a), which have been calculated for the Lloydminster reservoir. After fluid substitution the density and velocity data are decreased using the correction factor shown in Figure 3.14(b) with the resulting reflectivity data after modification in Figure 3.14(c). The new peaks in the reflectivity are unrealistically sharp, when compared to others in the data (for example the peaks at approximately 820 m depth, which are caused by the thin coal layer). If instead the edges of the correction factor are smoothed (Figure 3.14(e)) the resulting modified curve for the reflectivity shows more realistic peaks at the top and bottom of the reservoir. However, a clear rule for the choice of the width of the taper is not present, instead, an optimum parameter must be found experimentally by trial and error. If the taper is too wide the logs are not sufficiently modified at the edges. A very small width of the taper, on the other hand, will cause sharp peaks in the reflectivity time series, which are not likely to occur in well

131

log measurements for the reason mentioned above. A good value for the length of the window was found to be 10 samples of the log data.

After the well log data have been modified the reference base is changed from depth z to time t by the simple transformation

$$t(i+1) = t(i) + 2\frac{z(i)}{v(i)} \text{ for } i = 1, \ldots, N-1,$$

where N is the number of samples in the well log. Generally, it is not possible to determine the absolute time because the data recording in a log does not start at the surface. Therefore, this time base can not be compared directly to for example field seismic data. However, the absolute time is not important for the purposes of this study. More importantly is the relative time between events in the well log, which the depth-time conversion 3.11 accurately determines.

The next step is to calculate the reflectivity time series from the original and modified log data of the density and the P-sonic log according to

$$\mathcal{R}_{i+1} = \frac{\rho_{i+1} V_{P_{i+1}} - \rho_i V_{P_i}}{\rho_{i+1} V_{P_{i+1}} + \rho_i V_{P_i}} \text{ for } i = 1, \ldots, N-1.$$

The synthetic seismogram $\mathcal{S}$ can now be calculated by convolving the reflectivity time series $\mathcal{R}$ with a Ricker wavelet $\mathcal{W_R}$, which is usually characterized by its peak or center frequency f_c:

$$\mathcal{S} = \mathcal{R} * \mathcal{W_R}.$$

Synthetic traces have been calculated for center frequencies of 25 Hz, 50 Hz, 75 Hz, and 100 Hz to analyze the resolution required to detect the changes in the reservoir after steam injection. These traces are shown in Figure 3.16 along with the original and modified time series of the density (panel a), P-velocity (b), and reflectivity (c) for the Athabasca reservoir and in Figure 3.15 for the Lloydminster reservoir. In the panels d) the trace using a 25 Hz wavelet are shown, panels e) show the 50 Hz trace, panels f) the 75 Hz trace, and panels g) show the 100 Hz trace.
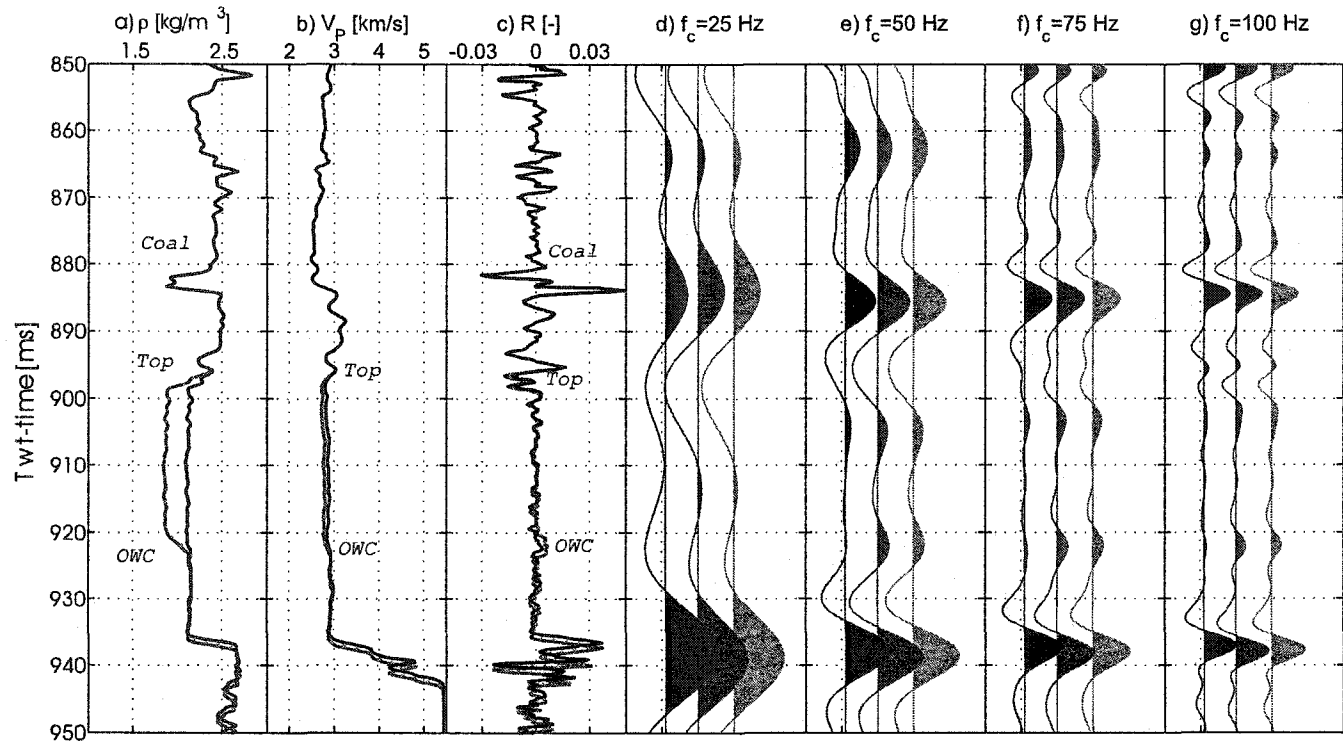
Figure 3.15: The original and modified well logs for the Senlac reservoir. a) density log, b) P-sonic log, c) P-reflectivity, d)-g) synthetic traces for different center frequencies of the Ricker wavelet. The blue curves represent the original well log data, in red are the data of the modified well log using the Gassmann model, and in green are the modified curves assuming a patchy saturation model. Indicated in the figures are the coal layer, the top of the reservoir (Top), and the oil-water contact (OWC).
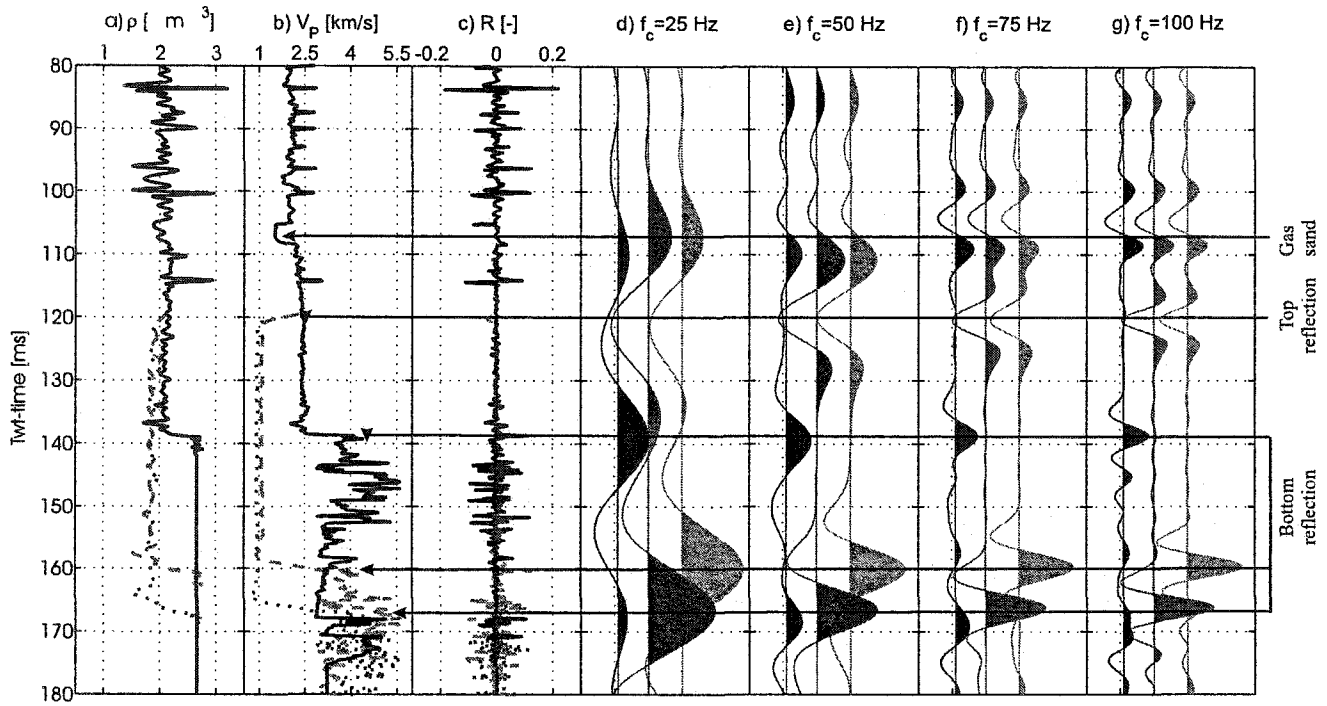
Figure 3.16: The original and modified well logs for the Athabasca reservoir. a) density log, b) P-sonic log, c) P-reflectivity, d)-g) synthetic traces for different center frequencies of the Ricker wavelet. The blue curves represent the original well log data, in red are the data of the modified well log using the Gassmann model, and in green are the modified curves assuming a patchy saturation model.

3.5.6 Attribute analysis

The well log time series for the Athabasca reservoir in Figure 3.16 a)-c) show a considerable change both in magnitude of the density and P-velocity and also in time-value of the bottom of the reservoir when compared to the original data (blue curves in Figures 3.15 and 3.16). The Gassmann model (red curves) results in lower velocities; therefore, the time to depth conversion (equation 3.11) gives higher values for the time than the patchy saturation model (green curves in both figures). However, both models predict changes in the reservoir that create significant differences in the traces calculated for the modified well logs to the original trace. For all frequencies the change in travel time to the bottom of the reservoir, and the changes in reflected amplitude at the top and bottom of the reservoir are easily detected.

A different situation is present for the Lloydminster reservoir in Figure 3.15. The P-velocity decreases only marginally after fluid substitution, which consequently reflects only in a small change of the travel-time to the bottom of the reservoir (see Figure 3.15 a)-c)). Although the density log shows considerable changes at the top of the reservoir and at the oil-water contact the reflectivity time series in panel c) changes little. Due to these subtle changes of the reflectivity the changes in the seismic traces, especially for low frequencies, are also small. A change in the travel-time to the bottom of the reservoir is hardly detectable at any frequency. The change at the oil-water contact, however, is a clear event for the higher frequencies, but with a very small amplitude. Also, only the high frequencies are able to detect the subtle changes at the top of the reservoir. As before, these amplitude changes are small. As real seismic data are always contaminated with noise it is likely that such small changes are not recognized in real seismic data sets. An additional complication arises from the presence of the strong reflection of the coal layer just above the reservoir. Particularly for the low frequencies this reflection dominates the events in the time window of the top of the reservoir (e.g. f_c=25 Hz). The resolution potential of such low-frequency waves is then insufficient to differentiate between the fine structures of the reflectivity series just below the coal layer.

The changes of the two attributes being analysed for both reservoirs after fluid substitution are summarized in Table 3.9 along with the calculated changes of the density and

Table 3.9: Changes of seismic attributes.

	Athabasca		Lloydminster	
	Before	After	Before	After
V_P [m/s]	2418	755	2864	2767
ΔV_P [m/s]	1219		93	
ρ [kg/m³]	2122	1898	2120	1870
$\Delta \rho$ [kg/m³]	250		224	
t [ms]	138	167	938	939
Δt [ms]	29		1	
$\mathcal{R}$ [-]	- 0.087	- 0.553	- 0.116	- 0.194
$\Delta \mathcal{R}$ [-]	0.466		0.078	

the P-velocity, respectively. These data underline the observations made in the seismic traces. For the calculations of the travel times and reflection coefficients and the changes thereof, the velocities of the Gassmann model have been employed; therefore, these values represent an upper limit of the possible range for these attributes.

For the Lloydminster reservoir the effects on the reflectivity are small, as might be anticipated from the small changes in the impedance. Only small variations in the traces before and after fluid substitution are seen. For example, the change in travel time of the reflection from the bottom of the reservoir is approximately 1 ms; a value less than typical sampling intervals and the amplitude of the reflection increases by only ~4%. Such a small change would be difficult to convincingly detect, given the relatively high noise levels near such sites. Also, changes in the reflected amplitude from the top of the reservoir are difficult to reveal. Lastly, note that there is no substantial difference between the synthetic traces obtained with the Gassmann or the patchy saturation models. These weak variations will in part explain the lack of an anomaly in the time-lapse seismic data described by *Zhang and Schmitt* (2003). However, it does not appear to shed light on the seismic observations of *Li et al.* (2001) who apparently found a substantial anomaly in an adjacent reservoir.

As mentioned earlier, a deviated well-log was taken as representative of the Lloydminster reservoir. In a deviated well-log, the apparent thickness of the reservoir is larger than the actual. This implies that the actual change in travel time is even less than previously calculated.

On the other hand, the synthetic seismic traces for the Athabasca reservoir show sig-

nificant changes. For the Gassmann model the two-way travel time to the bottom of the reservoir increases by 27 ms. A strong reflection from the top of the reservoir appears in the synthetic data after the fluid has been replaced. Although the increase in the travel time is less for the patchy saturation model due to its higher predicted velocity, a significant increase of this attribute with respect to the initial situation is still present ($\Delta T \approx 20$ ms). These substantial changes in the seismic signal suggest that seismic monitoring of SAGD at the Athabasca reservoir should be feasible. This result is in agreement with the strong signals observed by *Schmitt* (1999). In contrast, the small differences between the seismic traces for the Lloydminster reservoir as estimated by a standard Gassmann model suggest that seismic monitoring will be a challenging task, as mentioned earlier.

3.6 Discussion

The results from this analysis suggest that the feasibility of seismic monitoring does not only depend on the temperature induced change in the P-velocity of the oil but also on the frame properties of the rock matrix; a fact already noted by *Gardner et al.* (1965) on the basis of their measurements. The change in the seismic attributes for the deep and stiff Lloydminster reservoir is only marginal, while the steam injection in the shallow and compressible Athabasca reservoir results in significant changes. The reason for this is the much stiffer reservoir rock at Lloydminster. From Gassmann's equation it is clear that the influence of the fluid modulus for the Athabasca reservoir on the effective bulk modulus of the composite material is much stronger than for reservoirs with a relatively high frame bulk modulus. This effect is easily seen when considering the 'P-wave' modulus M

$$M = \rho V_P^2 = \underbrace{K_d + \frac{4}{3}\mu_d}_{M_{frame}} + \underbrace{\frac{(1 - K_d/K_s)^2}{(1 - \phi)/K_s - K_d/K_s^2 + \phi/K_f}}_{M_{pore}} . \tag{3.11}$$

The P-wave modulus can be decomposed into one part containing only the elastic frame moduli, M_{frame} and a second part subsequently referred to as the pore space modulus, M_{pore} (e.g. *Murphy*, 1984). It is only the pore space modulus that is affected by the fluid replacement, while the frame's contribution remains the same. To further illustrate this point, Table 3.10 provides the contribution of the two parts of the P-wave modulus for

137

Table 3.10: The P-wave modulus and its contribution from the frame and pore space (the numbers in the parenthesis indicate the relative contribution to the total P-modulus).

	Lloydminster	Athabasca
M [GPa]	17.2	8.27
M_{frame} [GPa]	14.3 (83%)	1.07 (13%)
M_{pore} [GPa]	2.9 (17%)	7.2 (87%)

both reservoirs. For the Lloydminster reservoir the contribution of the frame dominates, and only 17% of the P-wave modulus is affected by the fluid replacement. Therefore, the changes of the pore fluid have only a small effect on the seismic velocities. In contrast, these numbers show the dramatic effect that fluid replacement can have on the P-wave modulus of the Athabasca reservoir. Here, about 87% of the total value for M result from the pore space contribution. Therefore, changes in the properties have a stronger effect on the seismic velocities for the Athabasca reservoir than for the Lloydminster reservoir.

The observation that seismic monitoring of a SAGD process is feasible for weakly consolidated reservoirs like the Athabasca reservoir but difficult in stiff reservoirs (such as the Lloydminster reservoir) also reflects the work by *Lumley et al.* (1997) and *Lumley and Behrens* (1998), who state that for a *'successful seismic reservoir monitoring project the reservoir rock must be highly compressible and porous'*. Additionally, a large compressibility contrast between the initial pore fluid and the substitute fluid is another important parameter. Both reservoirs being analysed consist of very porous sands and the change in the bulk modulus of the pore fluid after fluid substitution is significant (the bulk modulus of the effective fluid reduces to approximately 0.1 % of its original value after fluid substitution). Therefore, two of the above criteria are certainly met. Although both reservoirs are described as unconsolidated or at least only weakly consolidated sands (*Chalaturnyk*, 1996; *Li et al.*, 2001), the difference in their compressibility is the only possible explanation for the different seismic response.

To further investigate the significance of the frame bulk modulus and the effective fluid properties on the feasibility of seismic monitoring, the two seismic attributes $\Delta \mathcal{R}$ and Δt have been calculated for a wide variety of values of K_d and pore fluid composition for a hypothetical reservoir similar to the two reservoirs analysed above. This hypothetical reservoir is 15 m thick, its porosity is $\phi = 32\%$, and it is bounded by a shale

layer at the top. Its frame bulk modulus varies within $0.5 \leq K_d \leq 10.0$ GPa, and the bulk modulus of the solid material is constant at $K_s = 36$ GPa. The pore fluid also varies in its composition. The water saturation remains constant at $S_W = 15\%$, but the steam saturation increases from $S_{St} = 0\%$ to 85%, where as the oil saturation reduces from initially $S_O = 85\%$ to 0%. Hence, the situation with $S_{St} = 0\%$ represents the case before the SAGD process takes place. For each value of K_d and pore fluid composition the seismic P-velocity has been calculated by equations (3.7, 3.3, 3.1) assuming the Gassmann model. The results of these calculations are provided in Figure 3.17.

Two different conditions for the pressure and temperature conditions were considered: for the first case the temperature of the fluids was $T = 120°C$ with the corresponding pore pressure of $P_{pore} = 0.2$ MPa (Figure 3.17a). Secondly, the temperature and pressure conditions were $T = 263°C$ and $P_{pore} = 5$ MPa, respectively (Figure 3.17b). The first row shows the change of the P-velocity relative to the velocity for zero steam saturation (i.e., the reservoir prior steam injection).

For both reservoirs the velocity first decreases significantly for low values of the steam saturation. However, with increasing steam saturation the velocity increases again, this is especially pronounced for the stiffer rocks (e.g., higher values of K_d). This velocity increase is due to the fact that even a small fraction of gaseous and compressible steam drastically reduces the bulk modulus of the pore fluid; and the effective bulk modulus basically reduces to the frame bulk modulus (see Tables 3.7 and 3.8). However, the effective bulk density decreases linearly with increasing steam saturation, and therefore the velocity increases with the steam saturation. For the situation in Figure 3.17b) the velocity even exceeds its initial value for very stiff reservoir rocks. Also note that the velocity decreases more for the low temperature case (left column). The explanation for the latter difference can be explained by examining the properties of the steam in Table 3.6. The bulk modulus of the steam as well as the density increases with temperature. However, the increase in the bulk modulus is more significant and the resulting velocities of the effective medium are generally higher.

The graphs in the second row show the change of the reflection coefficient $\mathcal{R}$ at the top of the reservoir. For these calculations it is assumed that a shale layer overlies the reservoir (acoustic imdedance $\mathcal{AI}_{shale} = 7.7 \times 10^6$ kg/m^2/s). As for the velocity the
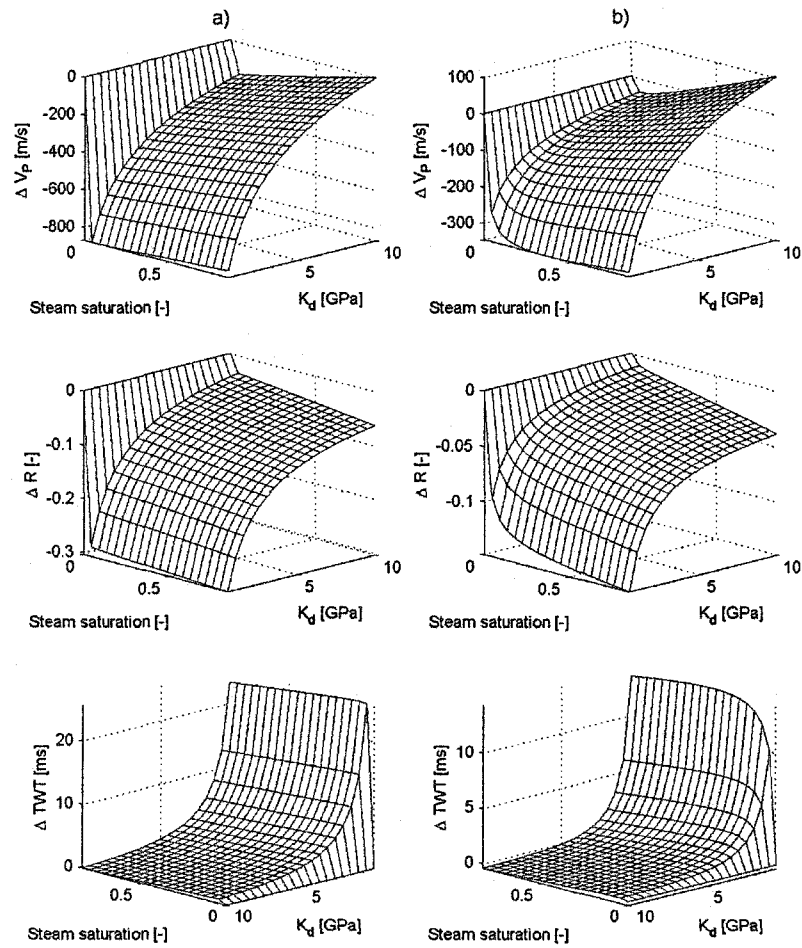
Figure 3.17: Variation of two seismic attributes with frame bulk modulus and steam saturation for two different temperature and pressure conditions: a) $T = 120°C$, $P_{pore} = 0.2$ MPa, b) $T = 263°C$, $P_{pore} = 5$ MPa.

reflection coefficient decreases substantially for a small volume of steam, but then decreases only slightly more with increasing steam saturation. As before the changes for the low temperature case are higher than for the high temperature case.

Finally, the two panels at the bottom of Figure 3.17 display the change in Two-way-travel time (TWT) to the bottom of the reservoir, whose thickness was assumed to be 15 m. (Note that the K_d- and S_{St}-axes are reversed to the axes in previous plots.) The increase in travel time is significantly larger for lower frame bulk moduli and lower temperatures.

Analysing the feasibility of seismic monitoring based on the data for the change of the reflection coefficient and the change in two-way travel time in Figure 3.17 the difference between the seismic response of the Athabasca and the Lloydminster reservoirs can now be explained by two effects. First, seismic monitoring is more likely to be feasible in highly compressible reservoirs. Additionally, the lower steam temperature for the Athabasca reservoir also facilitate the creation of significant changes of the seismic attributes being analysed. On the other hand, because high temperature steam is injected into the stiffer Lloydminster reservoir two effects merge that inhibit the development of detectable seismic anomalies in the reservoir, and hence, seismic monitoring for this reservoir is more difficult.

Chapter 4

Spectral finite element simulation of time-lapse seismic surveys for SAGD programs

The feasibility of time-lapse seismic monitoring for SAGD processes in heavy oil reservoirs has been tested through a rock physics study in the previous chapter 3 by the analysis of two seismic attributes that were determined from a simple synthetic zero-offset convolutional seismic modelling. In doing so it was assumed that the steam chamber extents infinitely in the horizontal direction.

The intention of this chapter is to extend these tests to more realistic 2-D simulations of the full seismic wave field using the spectral finite element technique discussed in chapter 2. Due to the lack of efficient absorbing boundary conditions only *differential* data sets will be considered, that is, the differences between two results simulated for different conditions in the reservoir. Then, aside from some small perturbations, contaminating reflections from the artificial boundaries will be removed from the synthetic data. In some sense, this procedure does not differ that from a field experiment in which one seeks only small changes.

The time-lapse process is investigated in two ways. First, the physical properties in a small region within the model representing a steam chamber of a SAGD-program are altered. With these simulations, the sensitivity of the seismic response to variations within the reservoir is analysed. Secondly, the size of the steam chamber is varied for different computations thus simulating the growth of the anomaly within the reservoir.

142
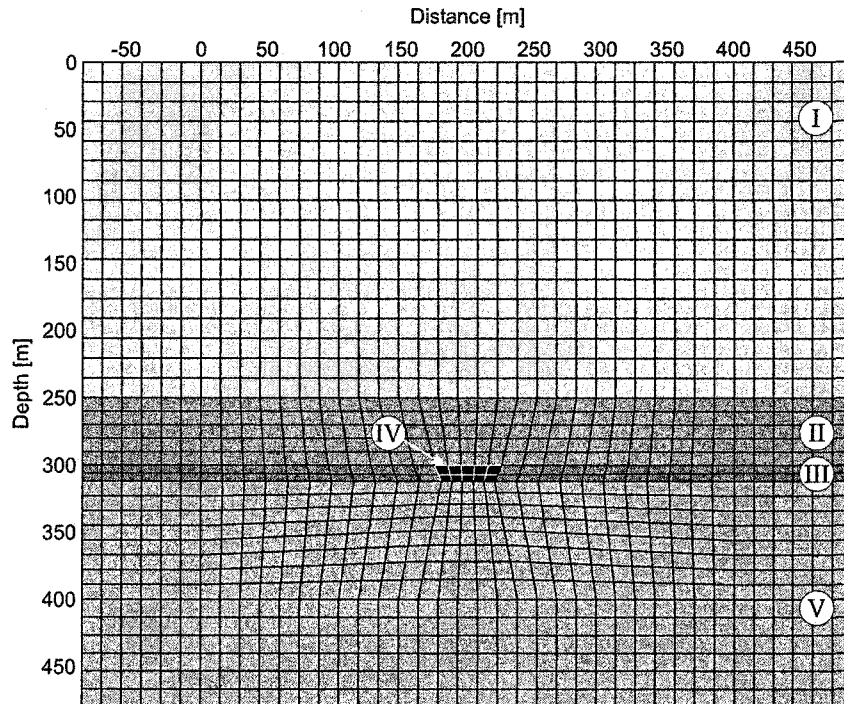
Figure 4.1: 1st finite element mesh of the SAGD model for the seismic modelling.

Such simulations are useful to determine how frequently the seismic surveys should be repeated in order to observe changes in the reservoir.

4.1 Model description

The exact shape of a steam chamber created during a SAGD-program within a reservoir is generally unknown and can be expected to be complicated. As there are currently no results from reservoir simulations or field observations publicly available, only geometrically simple and idealistic models are employed with respect to pressure and oil, water, and steam saturation distribution.

The simple model employed here is based on the assumption that the hot, low density steam rises to the top of the reservoir layer and then spreads out laterally. An approximation of such an early steam chamber would be a model of triangular cross section centered on the SAGD well-pair. With time the steam chamber extends horizontally only

to the sides such that the cross section becomes trapezoidal. Typically, several horizontal well pairs are installed to exploit a reservoir, which are about 50 to 70 metres apart (see Figures 3.1 (page 101) and 3.7 (page 114)). It can therefore be assumed that the steam chamber of a single well pair can be at the most 70 meters wide before it merges with the neighbouring steam chamber. The simulation domain and finite element mesh shown in Figure 4.1 is based on this idea. It consists of four horizontal layers with a zone included in the third layer that represents the steam chamber in some of the simulations. At the top the anomaly is approximately 80 meters; this width decreases to approximately 50 metres at the bottom.

4.1.1 Evolution of the finite element model

The mesh of the model in section 2.4.4 includes significantly distorted elements that caused numerical problems like mesh dispersion, mesh anisotropy, and numerical instability. Based on these experiences, the finite element model consists of elements with as little distortion as possible. The model consists of four layers with a zone enclosed in the third layer that represents a SAGD steam chamber in some simulations (zone IV in Figure 4.1). In order to match the shape of zone IV the elements in layer II, III, and V need to be deformed. However, care was taken that the elements are not too distorted to avoid numerical problems as described in section 2.4.4. Unfortunately, numerical instabilities still occurred in the simulation in the area of the deformed mesh. These instability express themselves as small amplitude events that suddenly appear in the centers of layers II to V, where the mesh is most deformed. The mechanism causing these erroneous events is not completely understood; the possible reason may be that the distortion of some of the elements is still too large for the current algorithm. It may be possible that such elements are not mapped accurately on the reference square Λ (section 2.2.2) because of an incorrect calculation of the Jacobian J (equation 2.31).

A new model was generated that does not contain any distorted elements (Figure 4.2). The model consists of four layers as before with a zone included in the third layer that represents the steam chamber. 1600 elements were used to build the mesh of this model. However, by using only strictly quadratic elements the mesh cannot be optimized anymore for the shape of the steam chamber (as for example in the first model); thereby

144

Horiz. Distance [m]
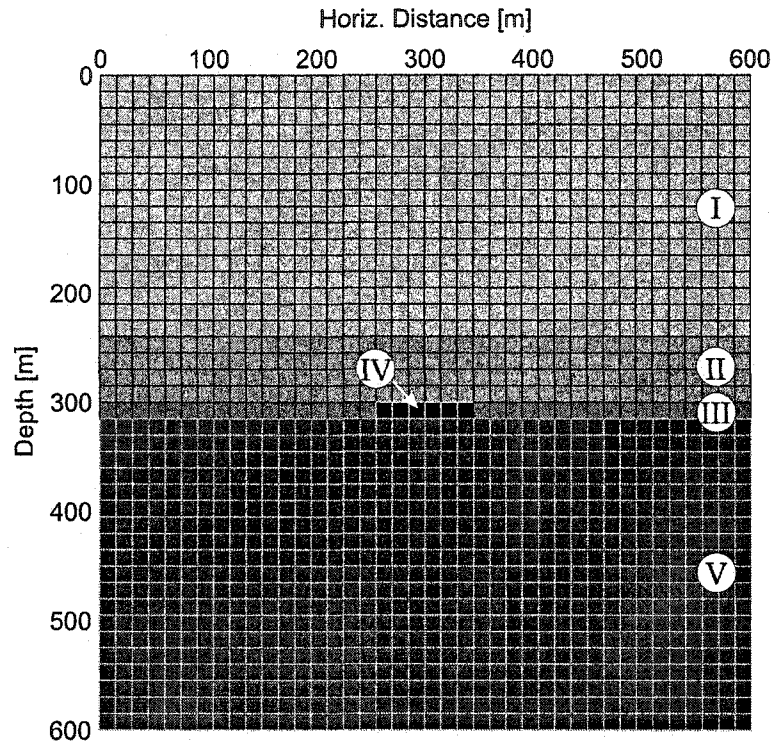
Figure 4.2: 2nd finite element model consisting only of regular elements.

loosing one of the main advantages of the finite element method. As it turned out, this model did not work either. This time, the simulation results became unrealistic when the wave reaches the thin layer representing the reservoir (layer III in Figure 4.2). Due to computational limitations, the size of the elements for this model needed to be chosen rather large, and the reservoir is only represented by one element layer. There should not be a problem in terms of numerical dispersion as the size of the elements, the degree of the Lagrangian polynomials, and the maximum frequency of the seismic wavelet are chosen according to the standard condition (equation 2.45). The test simulations in chapter 2 (section 2.4.2) showed that the present finite element program produces numerical artifacts in the presence of relatively thin layers. Whether the spectral finite element method requires a minimum size of a layer for a given wavelength of the seismic signal is a question that needs to be addressed in future studies.

For the last version of this model the fourth layer was omitted with the third layer

145
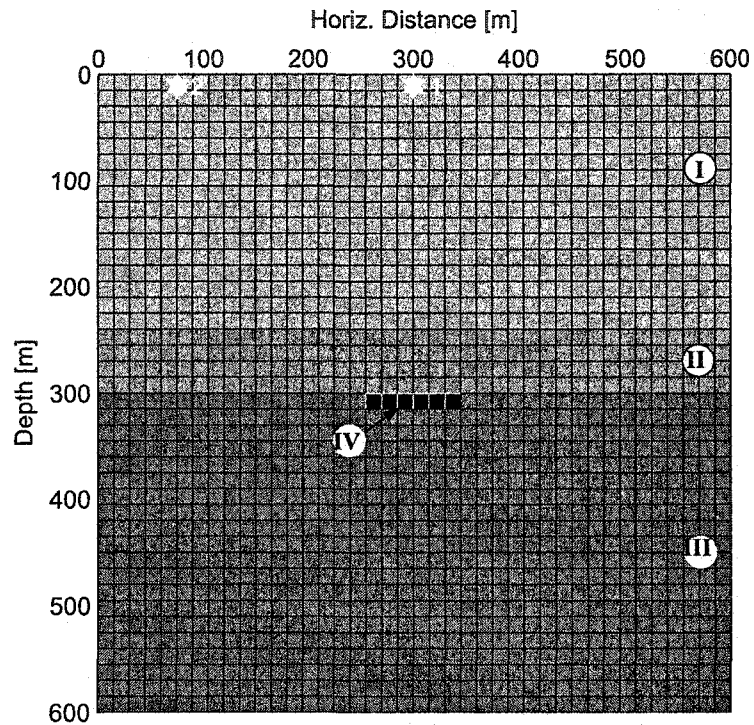
Figure 4.3: 3rd finite element model with the bottom layer replaced by the reservoir.

now extending to the bottom of the model (Figure 4.3). The problem causing thin layer is now removed; however, the internal shapes of the finite element model do no longer match the intended steam chamber described previously.

4.1.2 Summary

The problems occurring in the simulations using the first two finite element models need to be investigated in the future:

- Does a proper mesh design allow for an improved numerical stability? The use of unstructured meshes is probably required; however, with the currently available mesh generation programs, the design of such meshes was not possible.

- Is this numerical technique able to simulate the propagation of seismic waves for models including thin layers? Is a minimum number of elements or nodes in a layer

146

necessary to avoid numerical artifacts?

Unfortunately, it was not possible to improve the model or to solve the problems of the current program as described above due to time constraints. These problems in addition to the present lack of absorbing boundary conditions hinder the simulation of seismic surveys as intended in this thesis. Particularly the lack of the layer below the reservoir does not enable the testing of the seismic attribute 'time-delay of the bottom reflection' Δt, one of the parameters analysed in section 3.5.6. These constraints imply that the simulations presented here are for very simplified models; however, these initial calculations are useful for providing insight towards future research directions.

4.1.3 Physical properties

The physical properties of the different layers in the model, the density ρ and the two Lamé parameters λ and μ, respectively, are determined from the well log database and the fluid substitution modelling as described in chapter 3.

The properties of layer I, II, III, and V[1] remain constant in all simulations (Table 4.1(a)); only the properties within the reservoir (zone IV) change according to Table 4.1(b). The values for layer I and II have been loosely inferred from the well log data for the Lloydminster reservoir (Figure 3.6 and Table 3.3). The physical properties of layer III and V are taken from the reservoir zone and the carbonates below, respectively, whereas the properties of layer II are averages of the shale layer above the reservoir, and the data for layer I result from averaging the first 800 m of the well log data.

For the first set of simulations the rock physical parameters for zone IV vary, whereas the size of the steam chamber remains the same. For simulation A, the physical parameters of zone IV are the same as for the third layer. This simulation represents a base survey. In simulation B, the parameters for zone IV are as calculated for the Lloydminster reservoir assuming the Gassmann model (Table 3.8). The parameters in the last simulation of this set are not inferred from well log measurement or rock physical calculations but are assumed. This simulation was carried out to have a comparative data set for which the rock physical anomaly is larger than the calculated one for the Lloydminster

---

[1]For completeness, the fifth layer is included here; please note, that this layer is *not* present in the final simulations.

147

reservoir. For this simulation it is assumed that the P-velocity has decreased to 2577 m/s (-10.0%), but the density and S-velocity remain the same as in simulation B. These seismic properties could be representative for a reservoir with a less stiffer frame bulk modulus ($K_d \approx 1.18$ GPa compared to $K_d = 8.7$ GPa in simulation B, assuming that the shear frame modulus remains constant at $\mu_d = 4.2$ GPa).

In the second part the physical properties of zone IV remain constant but the size of the anomaly changes from initially 30.0 m width at the top (Simulation D, Figure 4.4(c)) to 60.0 m in simulation E (Figure 4.4(b)). For comparison, Figure 4.4(a) shows the size of the anomaly used for the simulations B and C, respectively. In these cases, the width at the top of the anomaly was 90.0 m. In all these simulations, the physical properties of zone IV are the same as for simulation C (Table 4.1(b)).

4.1.4 Simulation parameters

The criteria discussed in section 2.4.1 suggest that a time step of $\Delta t = 0.02 \times 10^{-3} s$ and a center frequency of $f_c = 30\,Hz$ ensure a numerically stable simulation. The total simulated time was set to $t_{total} = 0.5\,s$ (Table 4.2). For each rock physical parameter set and size of the steam chamber, two runs of simulations were performed with different positions of the source.

In a first step the finite element system matrices M and K were determined and written to the hard disk; a process that took, depending on the CPU of the computer used, up to ten hours. The second step the wave propagation was simulated; these simulations lasted for six hours at the most.

4.2 Modelling results

During the first simulation A the anomaly representing the steam chamber is not present (zone IV in Figure 4.3). This simulation is considered to be the base line survey against which all other simulations are compared.

The three panels in Figure 4.5 show the seismic wavefield for simulation A and the differential wavefield of simulation B with respect to A (that is, the wavefield calculated in simulation A is subtracted from the results of simulation B). In the first panel (Figure

Table 4.1: Properties of the model in the different simulations.

(a) Physical properties of the background geology.

Layer	ρ [kg/m^3]	V_P [m/s]	V_S [m/s]
I	2263	2306	1243
II	2307	2919	1473
III	2120	2864	1403
IV	— See Table 4.1(b) —		
V	2536	4983	2684

(b) Physical properties of the 'steam chamber'.

Simulation	A	B	C
ρ [kg/m^3]	2120	1870	1870
V_P [m/s]	2864	2767	2577
V_S [m/s]	1403	1498	1498

Table 4.2: Simulation parameters

Number of elements		1600
Number of points		58081
Degree of the Lagrangian interpolant		6
Time step Δt		$0.02 \times 10^{-3}\,s$
Simulated time t_{total}		$0.5\,s$
Wavelet center frequency f_c		$30\,Hz$
Source location 1	x	$300\,m$
	z	$11\,m$
Source location 2	x	$75\,m$
	z	$11\,m$

4.5(a)) another numerical artifact appears. In the differential wavefield, 'chaotic' amplitudes appear at early times. Theoretically, the differential amplitudes should be zero for these times and this part of the model, as the physical properties of both models are identical. Also, the seismic wavefield has not reached the anomalous zone in simulation B; therefore, no differences in the seismic wave amplitudes should be expected. An explanation of these artifacts is probably not directly related to the numerical scheme but is caused by computational inaccuracy of the numerous calculations involved in the algorithm. In general, no non-integer number can be stored accurately in the computer memory but will be truncated according to the floating point accuracy of the data type. For example, in the programming language C, a 'float' number is only accurate
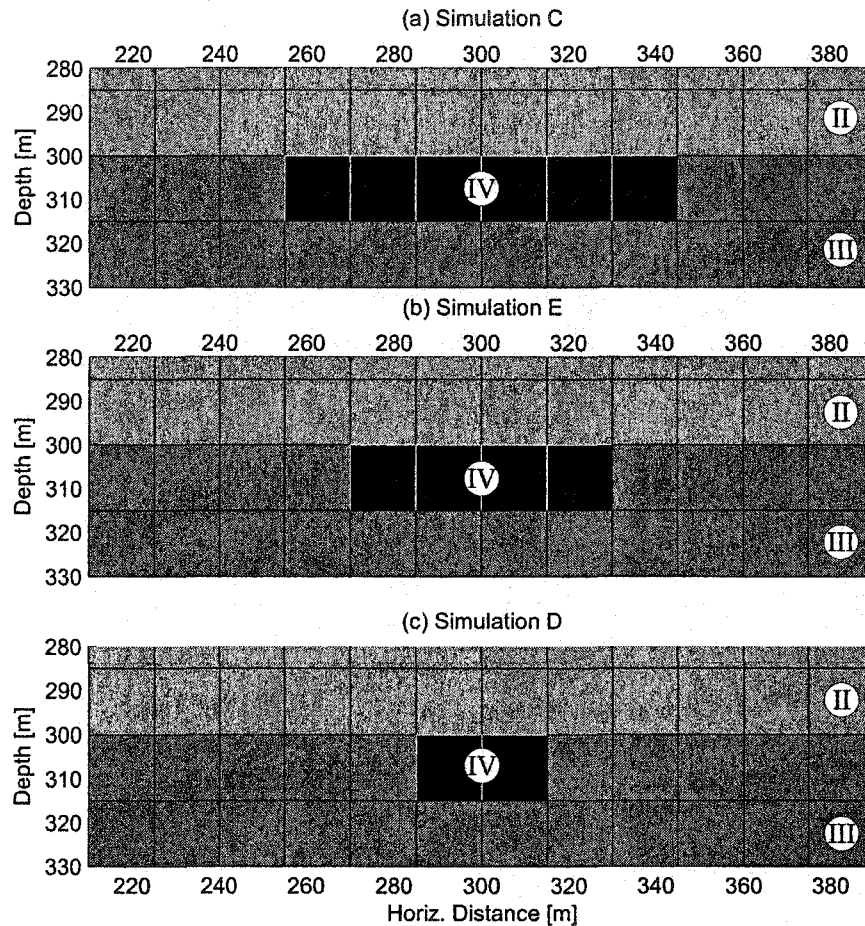
Figure 4.4: Different sizes of the 'steam chamber' in simulation D, E, and C. The width of the anomaly at the top is (a) 90.0 m, (b) 60.0 m, and (c) 30.0 (m).

to $\pm 10^{-6}$. Therefore, after every numerical operation (for example multiplication) the resulting number is rounded to the accuracy of the data type used and some information is lost. This rounding error grows with every iteration of the algorithm. The simulations were calculated on different computers running different versions of the operation system LINUX, and the programs were probably compiled with different compilers. Taking all these facts into consideration, it may be possible that this anomalous amplitudes in the differential wavefield result by computational 'noise' caused by different accuracy of the algorithm on the various computers. However, the magnitudes of these amplitudes

is approximately four order of magnitudes less than those of the main seismic waves; therefore, these artifacts do not contaminate the simulated data significantly.

After 0.2 s the P-wave has reached the reservoir in simulation B, and the reflected wave appears in the differential wavefield. At the same time the direct wave has reached the boundaries of the model and spurious reflections from these boundaries Γ as well as 'surface waves' along these boundaries begin to propagate. These waves, particular those propagating along the boundaries, cause numerical instabilities as soon as they approach the second layer (panel (c)). The reasons for this problem are possibly the same as discussed previously for the second version of the finite element model, where the thin layer caused instability in the numerical solution. However, the P-wave front is still visible, although when compared to the S-wave, its amplitude is very small and therefore barely visible.

Similar results are shown in Figure 4.6 for the simulation C that contains the lower P-velocity in zone IV (Table 4.1(b)). In general, the pattern of the differential wavefield is similar to the one in Figure 4.5; however, note that the amplitudes of the reflected wave are slightly larger for simulation C (compare the range of the amplitudes shown by the colourbars in both figures). This is expected as the velocity contrast of zone IV with respect to layer II, and consequently the impedance contrast, is larger for the simulation C. However, whether this difference is sufficient to be distinguished in seismic method cannot be answered with such preliminary simulation. For that, a simulation of a complete seismic survey would be necessary.

In the second series of simulations, the size of zone was varied (Figure 4.4) but the physical properties were kept constant. The results of these simulations are shown in Figures 4.7 and 4.8. The anomalous zone was of intermediate size in simulation E (width: 60 m) and the smallest in simulation D (width: 30 m). In either case, the size of the anomaly is too small to cause a clear reflection. The incident wave energy is rather scattered in all direction and the secondary P-wave fronts are of circular shape. It is worth noting that similar issues have been of interest in mining exploration where the dimensions of many massive sulphide ore bodies are of the order of the wavelength (e.g., *Eaton*, 1999; *Bohlen et al.*, 2003).

The differential wavefield for the simulations C, D, and E are plotted in Figure 4.9

151

at different times for comparison. The data in the left column, which are the results of simulation C, show a reflected wave that to a certain extend carries information of the shape of the reflecting body. In contrast, the secondary wavefield calculated for the simulations D (center column in Figure 4.9) and E (right column) are of circular shape. Therefore, these waves do not carry any information on the size of the reflecting body. However, there may be ways to interpret such results without perfectly imaging them.

A similar set of simulations was calculated with the seismic source placed towards the left border of the model (position 2, Table 4.2). Figure 4.10 shows the results of the differential wavefield and the 'base line' simulation for the parameter set B in Table 4.1(b). After 0.2 s a strange pattern of the seismic wavefield has developed for the simulation A, which is again shown in the right-side panels. Because the source is placed close to the border of the model a 'boundary multiple' follows the direct P-wave. The 'multiple' is the originally leftwards propagating wave, which, after reflection at the boundary, propagates back into the model. As in the first simulation set a 'surface wave' propagates along the left boundary and unfortunately causes numerical problems when it reaches the second and third layer. The differential wavefields show that the steam chamber in this simulation strongly reflects of the incoming P-wave. Similar results are obtained for simulation C (shown in Figure 4.11); as before, the wave propagation characteristics is similar with the wave amplitudes being larger for simulation C than B.

The results for the simulations D and E are included in Figures 4.12 and 4.13, respectively. In these simulations it becomes clear that the chosen size of the steam chamber is too small to cause a specular reflection. Instead, the secondary wave energy propagates almost uniformly in all directions; this is not at all unexpected.

Finally, Figure 4.14 compares the differential wavefield for simulations C, D, and E at different times. In these plots the effect of the size of the anomaly representing the steam chamber becomes apparent. Whereas the secondary wavefield for the simulations D and E is circular, the calculated wavefield for simulation C shows clear reflected amplitudes propagating to the right.

It is unfortunate that the numerical simulations became unstable before the secondary waves reached the surface and could be recorded in synthetic seismograms. Therefore, surface data could not be analysed with respect to seismic resolution or feasibility assess-

ment of seismic monitoring as intended in this thesis.

4.2.1 Discussion

Given the numerical problems the simulations needed to run for very simplified models. As such, the results of these simulations are rather preliminary. However, the results of this simple modelling approach suggest that seismic monitoring of steam chambers is not trivial. Only for the largest anomaly employed in simulations B and C, a reflection re-sampling the steam chamber can be expected. For the other models the steam chamber model is most likely too small to create a detectable seismic signal that can be considered as an image of the steam chamber. Most likely, only hyperbolas will be seen in seismograms, as are often seen for point like diffractors.

The resolution potential of seismic methods is usually determined by the half-width W of the first Fresnel zone (e.g. *Yilmaz*, 1987), which is defined as

$$W = \sqrt{\frac{1}{2}\lambda Z},$$
$$\text{or}$$
$$W = V/2\sqrt{\frac{t}{f_c}}, \tag{4.1}$$

with λ being the (dominant) wavelength and Z the depth of the reflector, V is the P-velocity in this case and f_c the centre frequency of the seismic wavelet. Using the data for the model the width becomes $W \approx 94m$, a value comparable to the size of the steam chamber model in simulation B and C. In simulations D and E, the width of the anomalous zone IV is much smaller than the first Fresnel zone and consequently, such small bodies cannot be resolved in the simulations. However, it should also be noted that migration can be applied to improve the seismic resolution in case of such small anomalies.

4.3 Summary

The simulations calculated for this chapter suffered from many numerical problems which were not anticipated nor have they been reported in the literature of this still recent technique. Particularly, the design of a proper finite element mesh to simulate the propagation of seismic waves is a question that must be addressed in more detail. Although it

---

153

(a)

(b)

(c)
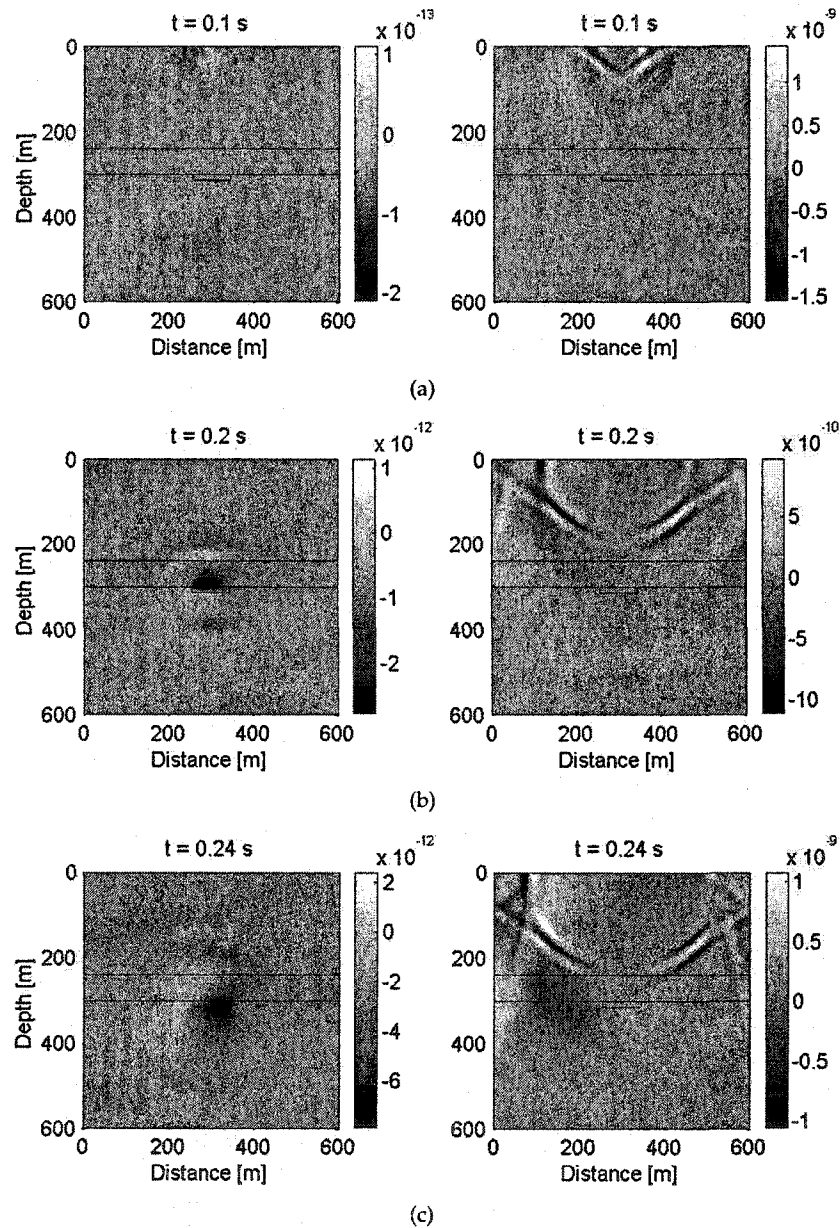
Figure 4.5: Left: Differential wavefields simulation B - simulation A. Right: Wavefield simulation A. The vertical displacements are shown here at three different times. The depths of the three interfaces and the shape of the anomalous zone IV are included by the black lines. Source location: 1.

154

(a)

(b)

(c)
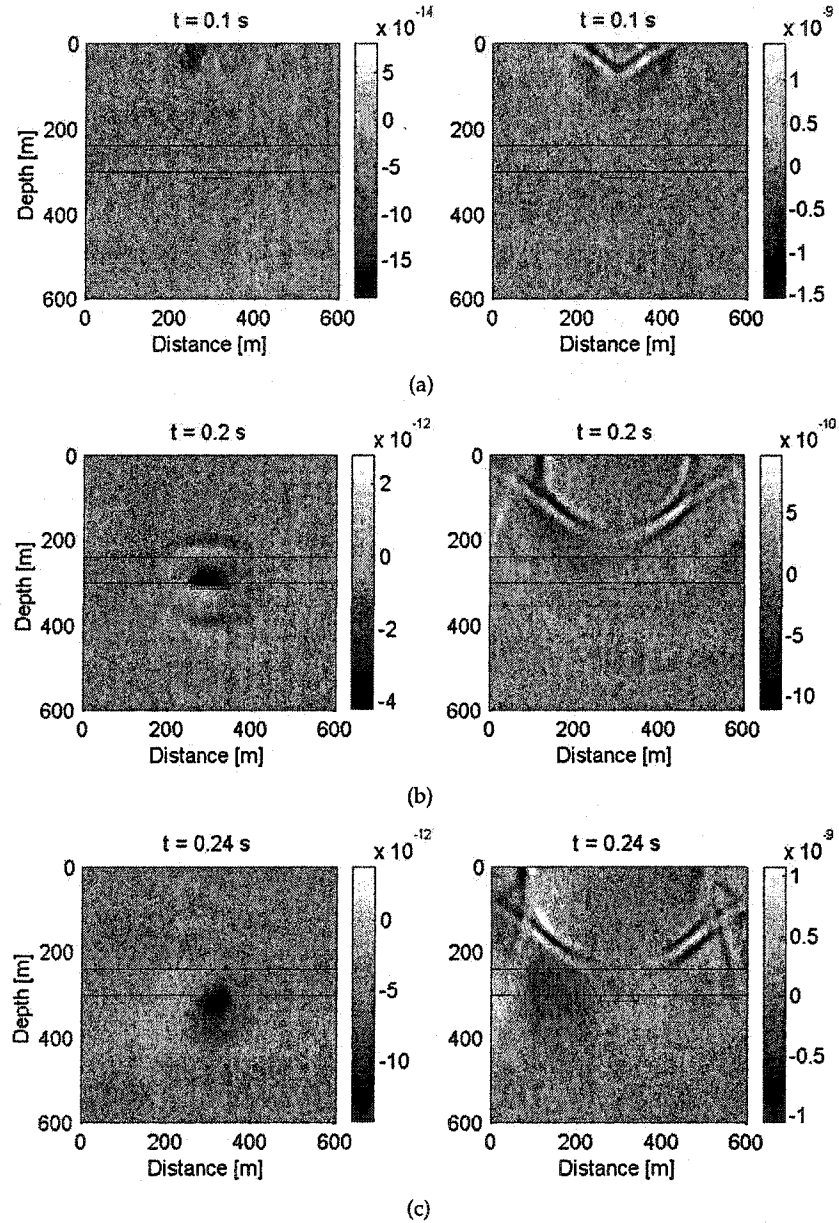
Figure 4.6: Left: Differential wavefields simulation C - simulation A. Right: Wavefield simulation A. The vertical displacements are shown here at three different times. Source location: 1.

155
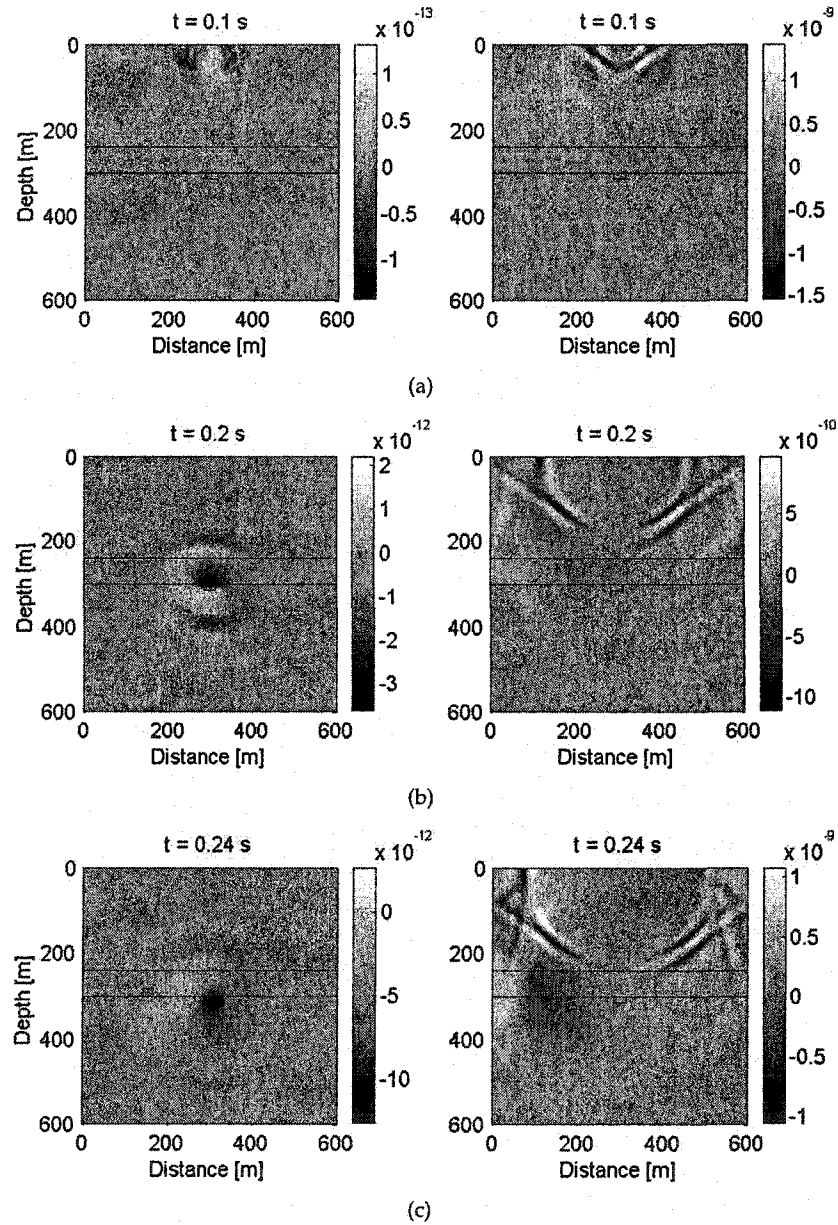
Figure 4.7: Left: Differential wavefields simulation D - simulation A. Right: Wavefield simulation A. The vertical displacements are shown here at three different times. Source location: 1.
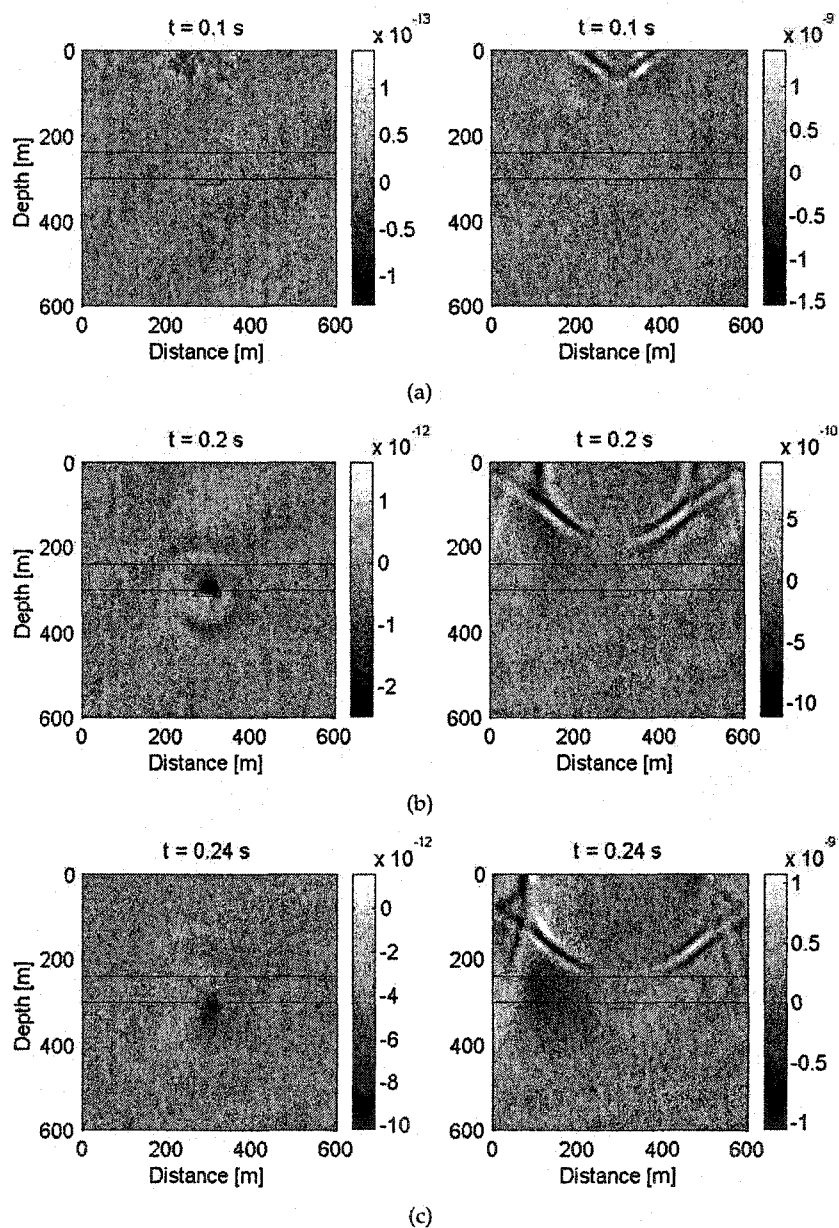
Figure 4.8: Left: Differential wavefields simulation E - simulation A. Right: Wavefield simulation A. The vertical displacements are shown here at three different times. Source location: 1.
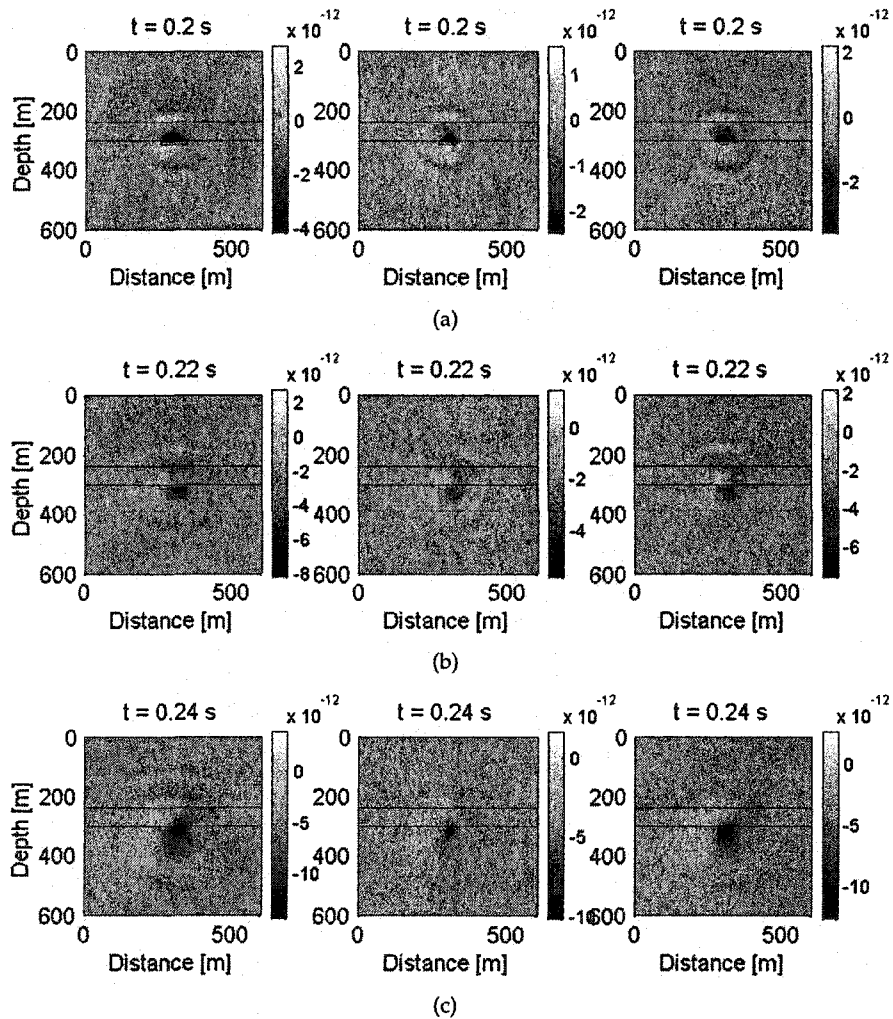
Figure 4.9: Comparison of the secondary wavefield for simulations C, D, and E at different times. Left panels: differential wavefield for simulation C; center: simulation E; right: simulation D. The vertical displacements are shown. Source location: 1.
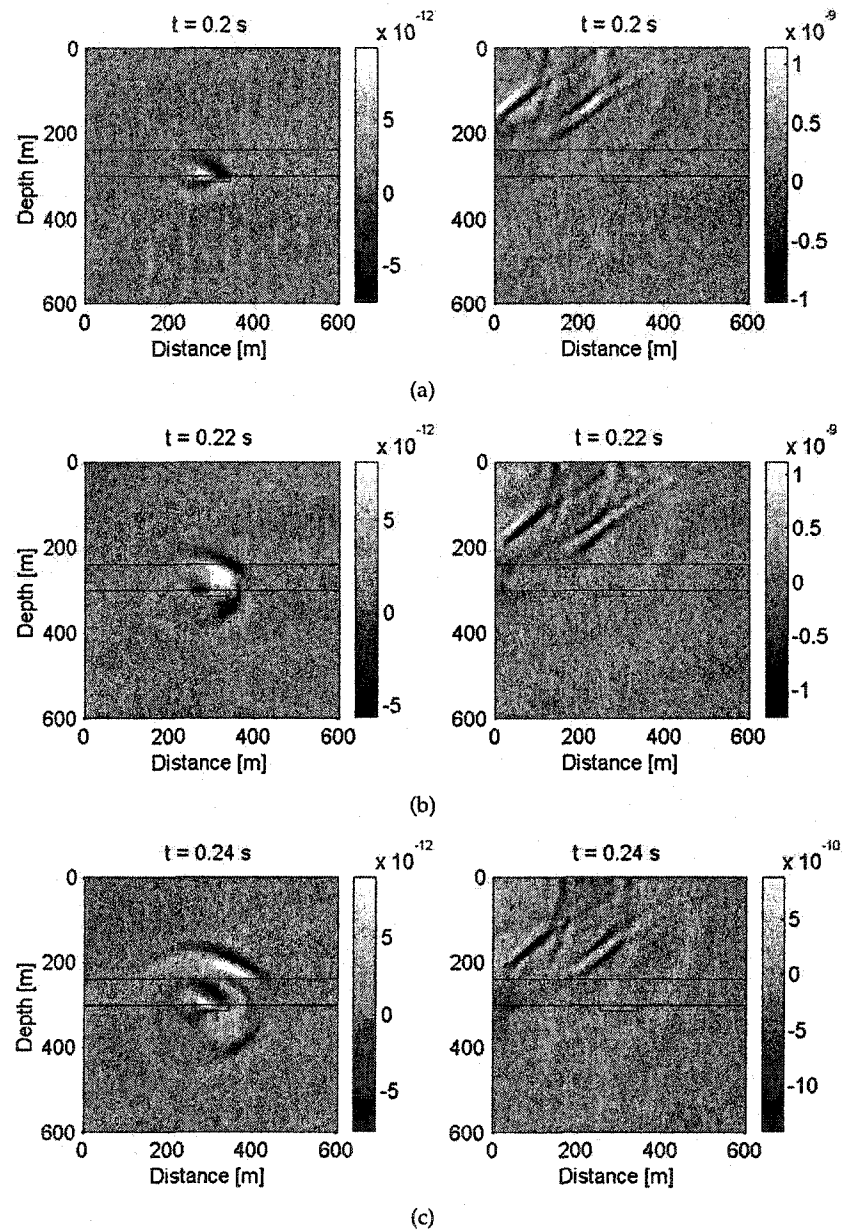
Figure 4.10: Left: Differential wavefields simulation B - simulation A. Right: Wavefield simulation A. The vertical displacements are shown here at three different times. Source location: 2.

159
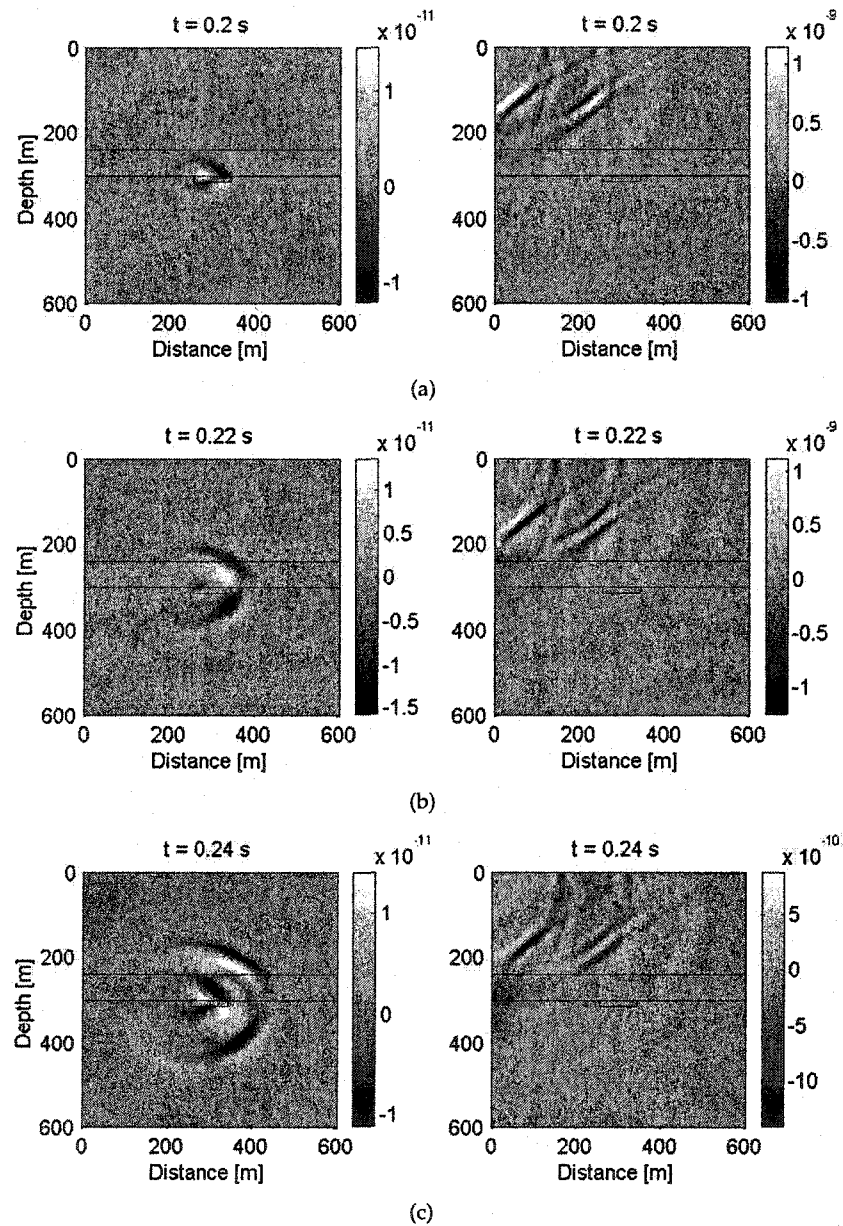
Figure 4.11: Left: Differential wavefields simulation C - simulation A. Right: Wavefield simulation A. The vertical displacements are shown here at three different times. Source location: 2.
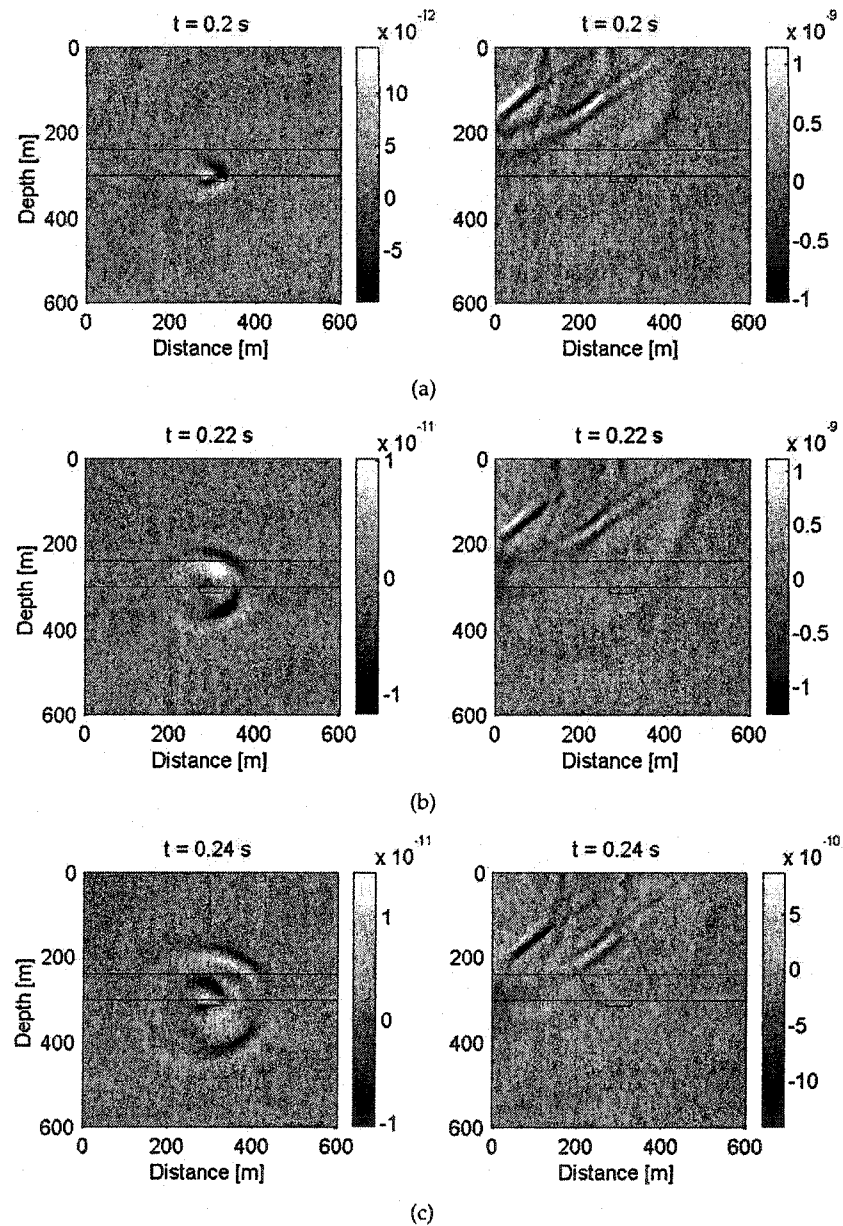
Figure 4.12: Left: Differential wavefields simulation D - simulation A. Right: Wavefield simulation A. The vertical displacements are shown here at three different times. Source location: 2.

161
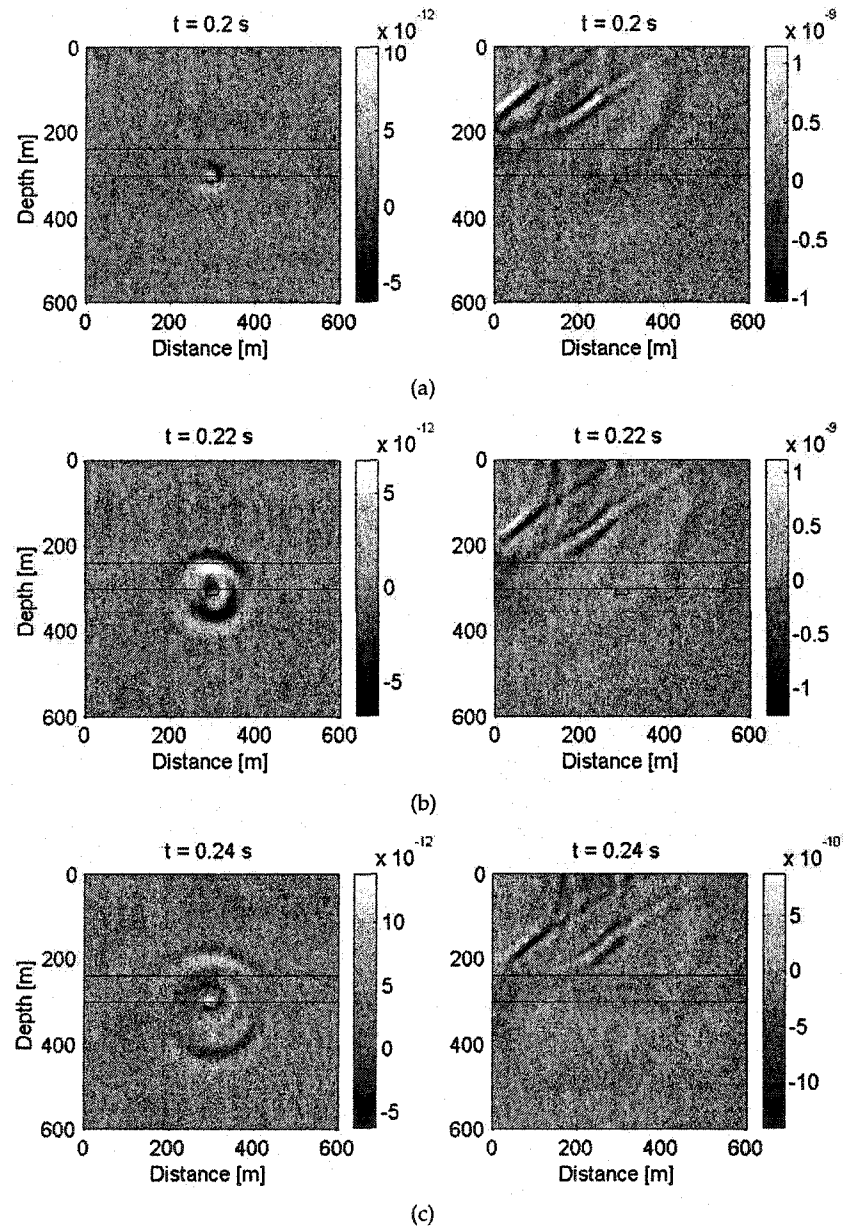
Figure 4.13: Left: Differential wavefields simulation E - simulation A. Right: Wavefield simulation A. The vertical displacements are shown here at three different times. Source location: 2.

162
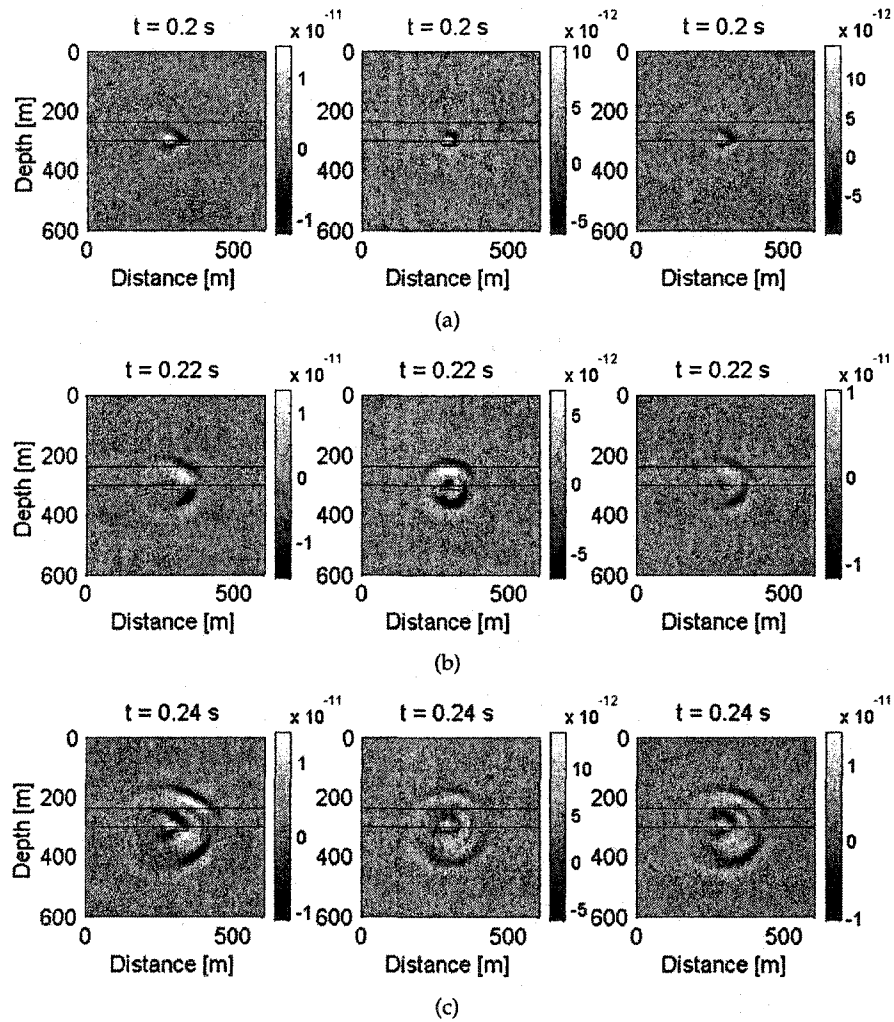
Figure 4.14: Comparison of the secondary wavefield for simulations C, D, and E at different times. Left panels: differential wavefield for simulation C; center: simulation E; right: simulation D. The vertical displacements are shown. Source location: 2.

was not possible to build a model that incorporates a more realstic shape of the steam chamber (for example, as attempted in Figure 4.1) there is no doubt that such models can be designed. With time and more experience in generating meshes and in choosing the best simulation parameter such simulations will be successful.

However, despite these problems the simulations showed that seismic monitoring for SAGD programs is possible if the steam chamber has grown to a sufficient size. Such a critical size can probably be estimated by the radius of the first Fresnel zone W. The simulations also showed that, in theory, seismic methods should be able to distinguish between subtle changes in the reservoir as it is the case in the simulations B and C. However, to fully analyse this issue entire seismic surveys should be modelled in the future.

Discussion and Conclusions

Exploiting the world's heavy oil and bitumen reservoirs will gain increasing significance in the future as light oil production reaches its peak. The physical properties of these hydrocarbons require that special and expensive recovery techniques be used in their production. For example, thermal oil recovery methods are most commonly applied to extract such resources from deeper reservoirs. Given the costs of many enhanced oil recovery methods, and in the case of heavy oil also those of the following upgrading process, comprehensive control of these programs *during* production is an essential step to ensure technically and economically successful reservoir exploitation. Monitoring subsurface processes *in-situ* and as close as possible in *real time* has become a major part in applied geophysics during the last decade.

At the moment, SAGD programs are dominantly applied in Western Canada to produce shallow heavy oil reservoirs. The high production rate and recovery of the original oil in place makes this method the most promising for heavy oil production. During a SAGD program two horizontal boreholes are drilled in a vertical plane close to the bottom of the reservoir (Figure 3). Through the top borehole hot steam is injected into the reservoir. Ideally, this steam then rises to through the oil bearing rock matrix to the top of the formation thus forming a steam chamber. The steam condenses at the boundaries of the chamber, where it heats the oil. The viscosity of the heavy oil reduces significantly and the oil becomes mobile. As the density of the oil is larger than that of the steam the oil flows along the chamber to the bottom borehole where it is produced.

Installing and running a SAGD program is technically challenging. Many problems such as well completion problems or asymmetric and anisotropic steam propagation are possible. Such complications will cause an uneven distribution of the steam with parts of the reservoir bypassed, thereby reducing the economical value of the reservoir. In order

to detect such problems at an early state of the reservoir life remote monitoring of SAGD program has the potential to be an important tool in the engineering decision process.

Detecting small changes in the reservoir with seismic methods may be difficult. In order to access the feasibility of seismic monitoring a *priori* modelling of the physical processes is necessary.

This thesis dealt with remotely seismic monitoring applied to SAGD programs for heavy oil reservoirs in the Western Canadian Sedimentary Basin. The main issues being investigated were:

- Are the changes of the fluid and consequently in the physical properties of the effective media large enough to monitor changes in the reservoir using time-lapse seismic surveys?

- Can the growth of the steam chamber be accurately resolved using seismic data?

To address these questions two modelling approaches have been used. The feasibility of seismic monitoring of SAGD programs has been investigated first using a rock physical modelling carried out to estimate the effective physical properties of the reservoir after steam injection. The second modelling technique employed in this project is the spectral finite element method to simulate the propagation of elastic waves in two dimensions.

In the past the feasibility of seismic monitoring of thermally enhanced oil recovery has been justified by the significant decrease of the P-velocity of a hydrocarbon saturated rock sample when heated (Figure 1.2, e.g., *Wang and Nur*, 1988, 1990; *Wang et al.*, 1990; *Eastwood*, 1993). However, such experimental data do not represent the physical processes of a SAGD program where oil is not only heated but also replaced by steam and water at elevated temperature. The rock physical modelling summarized in chapter 3 does incorporate the fluid replacement oil for a mixture of steam, water, and oil at *in situ* pressure and increased temperature. Therefore, this approach, carried out for the first time to simulate the rock physical impact by a SAGD program, does represent the real situation more accurately.

Identical modelling has been carried out for two different reservoirs: a bituminous reservoir near Fort MacMurray in Northern Alberta, which is part of the Athabasca complex, and a Lloydminster styled heavy oil reservoir in Saskatchewan. Successful seismic

monitoring for the Athabasca reservoir has been reported by *Schmitt* (1999), whereas the time-lapse seismic data acquired at the Lloydminster reservoir site do not show any changes in the seismic response (*Zhang and Schmitt*, 2003).

The rock physical simulations confirm the field observations in such that for the Athabasca reservoir the synthetic data predict a significant change in the reflected seismic amplitude from the top of the reservoir as well as in the travel time to the bottom of the reservoir after fluid substitution (Figure 3.16 and Table 3.9). On the contrary, the simulations for the Lloydminster reservoir indicate that there can be no substantial changes in the seismic response expected during the SAGD program. Neither the travel time delay to the bottom of the reservoir nor differences in the reflected amplitude at the top of the reservoir can be expected to be detectable in real time-lapse seismic data (Figure 3.15 and Table 3.9).

The difference in these seismic attributes for the two reservoirs can be explained through rock physics by the much stiffer rock matrix of the Lloydminster reservoir. The elastic frame moduli for this reservoir have been determined from well log data under *in situ* conditions; the frame bulk modulus is $K_d = 8.7 \pm 0.8$ GPa, and the shear frame modulus is $\mu_d = 4.2 \pm 0.2$ GPa. Compared to these values the rock matrix for the Athabasca reservoir is much weaker: the frame bulk and shear moduli are $K_d = 0.667$ GPa and $\mu_d = 0.308$ GPa, respectively. The determination of the frame moduli from well logs was not possible because (a) no shear sonic well log data are available from this reservoir, and (b) it is likely that the Athabasca bitumen has a finite shear rigidity. For the latter reason the determination of K_d and μ_d is not possible using the approach presented in chapter 3.1.2, which is based on the validity of *Gassmann's* (1951) equation. Instead, the values for the Athabasca reservoir have been measured by *Chalaturnyk* (1996) in quasi-static uniaxial bulk compressibility experiments. How well such data compare to the elastic frame moduli under *in situ* condition is unfortunately not known. However, experience shows that such static measurements present the lower bound for the dynamic (seismic) values (*Wang*, 2000a).

The much stiffer frame of the Lloydminster reservoir does not allow for a large change in the P-velocity. This best seen by analysing the P-wave modulus M (Table 3.10). The P-wave modulus can be split into two contributions: the frame modulus M_{frame}, which

167

does not depend on the fluid, and the pore modulus M_{pore}. For the Lloydminster reservoir the contribution of M_{frame} is 83 %, and only 17 % come from M_{pore}. As the fluid substitution affects only the pore modulus (in the particular steam injection modelling M_{pore} effectively vanishes) the effect on the P-velocity for the Athabasca reservoir is much stronger than for the stiff Lloydminster reservoir.

That seismic monitoring of enhanced oil recovery is challenging for reservoirs with stiff rock matrices is known (e.g., *Lumley et al.*, 1997; *Lumley and Behrens*, 1998). However, it is surprising that the monitoring program for the Lloydminster reservoir failed. This reservoir consists of a dominantly unconsolidated sand matrix, as such it can be expected to be an elastically weak reservoir. *Lumley et al.* (1997) and *Lumley and Behrens* (1998) did not clearly specify a lower limit for compressibility of the rock matrix. The results of the fluid substitution modelling and the field data suggest that even for unconsolidated reservoirs a successful monitoring program is not necessarily guaranteed.

To further investigate the dependance of the feasibility on the elastic frame properties and fluid composition, the changes in P-velocity, reflection coefficient, and two-way travel time have been calculated for a hypothetical reservoir. In this work, another interesting and important aspect for feasibility assessment of seismic monitoring was found (see Figure 3.17). The results of these calculations suggest that the effects of steam injection during a SAGD program are stronger at the low temperature and pressure conditions. Lower injection temperature is typically chosen for shallower reservoirs where the pore pressure is lower. Generally, it is likely that the elastic frames of shallower heavy oil reservoirs in the Western Canadian Sedimentary basin are weaker than those for deeper deposits. Therefore, there are two mechanisms in favour for successful seismic monitoring for the Athabasca reservoir: the reservoir rock has an extremely weak elastic frame and the low temperature regime create substantial changes in the seismic properties. Hot steam is injected into the relatively stiff Lloydminster reservoir; the analysis presented here shows that such conditions inhibit successful seismic monitoring.

The second focus of this project was the numerical simulation of elastic wave fields with the intention of modelling seismic surveys over heavy oil reservoirs. Numerical simulations can be helpful to address questions such as

168

- Are seismic methods able to image changes in the size of the steam chamber? In other words: is the seismic resolution sufficient to detect subtle changes in the reservoir?

- Is there an optimum survey design to monitor changes in the reservoir efficiently?

- Given an assumed growth rate of the steam chamber, how frequently do seismic surveys need to be repeated to see changes between two surveys?

The geometry of the models can be complicated due to significant variations of the surface and internal interfaces, and the shape of a steam chamber. As such, the simulation algorithm must be able to handle geometrically complex models. Furthermore, the program must perform the simulation accurately (that is, free of numerical artifacts) and sufficiently fast. At the beginning of chapter 2, several numerical techniques have been discussed that are currently used in numerical seismic modelling. Of these methods, the spectral finite element was chosen for the numerical simulations presented in this thesis. This technique, recently introduced into seismic modelling by e.g., *Faccioli et al.* (1997) and *Komatitsch and Tromp* (1999), combines the geometrical flexibility of the standard finite element method with the accuracy of spectral methods, and the simulations shown in section 2.4.3 demonstrate that this method is indeed able to simulate the propagation of elastic waves in geometrically complex models with significant topographical variations.

Limited computer memory resources requires the numerical model to be truncated, which implies the introduction of *artificial* boundaries. At the truncation boundaries, wave energy will be reflected and propagate back into the model. Such waves do not occur in reality and they must be inhibited from interfering with the "real" waves propagating inside the model. Eliminating these spurious waves requires that they are suppressed at the truncating boundaries of the model. To reduce reflections from the artificial boundary conditions, a *Raleigh* attenuation approach was implemented. An additional boundary layer several elements wide surrounds the outside of the model. Within this layer, wave energy is gradually reduced by a damping mechanism. The Rayleigh method is very suitable for finite element schemes as the damping mechanism is described by the two system matrices **M** and **K** (section 2.3.1, equation (2.43)). Therefore, no additional

169

memory needs to be reserved for a damping matrix, and this makes this method computationally economical. Rayleigh attenuation has been applied by *Sarma et al.* (1998) to suppress artificial reflections in finite element simulations. In their simulations, plane wave excitation was used, that is, an array or sources was employed at, for example, the surface. Such a situation does not realistically represent wave propagation in the earth. Consequently, in the numerical tests presented in this thesis a single point-like source in the center of the model was used. However, strong numerical artifacts appear (Figure 2.9). The waves do not any longer propagate symmetrically from the source. Instead, a significant antisymmetry occurs in the observed wave patterns in the central part of the model: the waves propagating to the right are significantly stronger than those moving to the left away from the source. The model is symmetric; therefore, such a propagation pattern cannot be "model-intrinsic" but must be caused by technique dependent numerical instabilities or artifacts. Therefore, this boundary condition could not be applied for the seismic simulations for this thesis. The *perfectly matched layer* technique (*Berenger*, 1994), recently tested by *Komatitsch and Tromp* (2003), seem to be a more promising technique for absorbing wave energy at artificial boundaries.

Further problems that occurred in some simulations are *apparent* or *mesh anisotropy* and numerical instabilities in simulations containing "rough" topography (section 2.4.4). The simulation shown in Figure 2.15 was carried out to test the potential of the spectral finite element method to model seismic wave propagation in rough terrains. The simulation results show two numerical artefacts:

- First, the wave fronts apparently propagate as if they were in an anisotropic medium; that is, the propagation speed in the vertical direction seems to be faster than for the horizontal direction. The mesh generated for this model contains elements in the central part that are elongated in the vertical direction. As the physical properties in this model are isotropic this wave propagation pattern must be due to the mesh design.

- The second numerical problem is due to the shape of the surface. When the surface wave reaches the "valley" to the right of the source numerical instabilities develop. The surface wave does not propagate further but increasingly gains amplitude. On

the other hand, the simulation for the model with smooth topographic variations shown in Figures 2.13 and 2.14 demonstrate that simulations of wave propagation are possible for such models. The difference between the two simulations is that for the smooth model the variation of the surface's topography are longer than the wavelength of the propagating wave. For the rough model the variations of the topography are at the same length scale of the wavelength, or even shorter. It can only speculated at the moment if there is a criterion between the wavelength and the a 'length scale' of the surface's topographic variation.

The simulation of seismic surveys over a reservoir subjected to SAGD oil recovery was the intention of the work presented in chapter 4. The focus of interest was the resolution potential of seismic surveys to detect (a) changes in the rock physical properties within the steam chamber and (b) the minimum change in the size of steam chambers required to be detectable in repeated seismic surveys. Unfortunately, severe computational problems occurred in these simulations which are related to mesh design and the lack of working absorbing boundary conditions. The meshes created for the simulations caused numerical instabilities which are likely related to

- distorted elements that cause local instabilities which then contaminate the calculated seismic wavefield. Even such a simplified model as shown in Figure 4.1 requires the use of unstructured meshes or perhaps triangular elements. However, the required mesh generation tools for unstructured quadrilateral element meshes were not available, and in order to modify the simulation program to incorporate triangular elements with the same spectral accuracy as the spectral finite element codes is non-trivial.

- 'Thin' layers in the model seem to cause numerical instabilities. Whether this problem is due to the layer being too thin with respect to the seismic wavelength or if the spectral finite element method requires a minimum number of elements and consequently collocation points per layer should be investigated in future studies.

The finite element models needed to be significantly simplified and the intended purpose of the simulation could unfortunately not be met. However, these simple simulations revealed that a steam chamber needs to be of minimum width to be resolved with

171

seismic methods which is described by the radius of the first Fresnel zone. Secondly, seismic methods are sensitive even to subtle changes in the rock physical parameters of the steam chamber. Whether such changes are detectable in real seismic surveys needs further investigation. An entire seismic survey should be simulated and then subjected to different random noise of realistic amplitudes to test whether the possibly weak response of a steam chamber is still recognizable in the synthetic data sets.

Future research directions

The analyses and results presented in this thesis could be extended to accommodate the following points. For the rock physical part these items are:

- A better control on the determination of the elastic frame properties from well log would be useful. Maybe, comparative measurements of these values in the laboratory could prove (or disprove) the values for the Lloydminster reservoir, which according to the sonic logs seem to be high. Also, measurements of these parameters for the Athabasca reservoir would be helpful, as the quasi-static values in *Chalaturnyk* (1996) are likely lower than is expected for seismic frequencies and strains.

- The estimation of the pressure dependence was based on published general trends of the *P*-velocity variation with pressure. Although the determination of the *in situ* pressure dependence it is especially difficult for unconsolidated sands, such measurements are important to estimate pressure effects on the seismic velocities. Secondly, a better understanding of the pressure variation during a SAGD program is necessary. Currently, it has been assumed that the pore pressure remains constant during the steam injection. Field data provided by the operating companies show that probably due to technical needs considerable pressure changes are possible.

- The model assumed in the analysis was rather simplistic. More physical processes possibly occur during a SAGD program. First of all, natural gas coming out of solution has not been considered in the analysis. Secondly, thermal effects on the solid material (for example thermal expansion and changes in the elastic properties and density) has not been included in the calculation. Additionally, the influences

172

of the processes happening in the reservoir on the layer above and below will need future consideration. For example, especially the layer overlying the reservoir will experience thermal stresses, which can change its elastic behaviour. This will then change the reflectivity at the top of the reservoir. Further, damage to the formation due to injection and sand production has not yet been considered.

The numerical modelling scheme would benefit from the following work:

- First of all, the non-reflecting boundary problem needs to be addressed. It is recommended that the work by *Komatitsch and Tromp* (2003) is followed.

- Some of the simulations presented in this thesis were problematic because of problems with the mesh. Particulary, apparent anisotropy and numerical instabilities at the surface with 'rough' topography are problems that reduce the quality of the simulations significantly. Such problems may be intrinsic to the numerical technique and further studies should investigate on how much these artifacts can be reduced by proper mesh design.

- The simulation of seismic surveys would benefit from including a dispersive constitutive relationship into the modelling algorithm. The theory of visco-elasticity is well developed. Unfortunately, a computer implementation of such a program was not possible due to current hardware limitation.

- Lastly, the extension of the current program to three dimensions is possible and would be useful. The design of three-dimensional meshes, however, is significantly more challenging than in two dimensions, especially with the limitation of current spectral element techniques to hexahedral elements. Also, one must be aware of that three dimensional simulations require significantly more hardware resources and computation time.

Bibliography

Aki, K., and P. G. Richards, 2002, *Quantitative seismology*, 2nd ed., W. H. Freeman and Company.

Alford, R. M., K. R. Kelly, and D. M. Boore, 1974, Accuracy of finite-difference modeling of the acoustic wave equation, *Geophysics, 39*, 834–842.

Alterman, Z. S., and F. C. Karal, 1968, Propagation of elastic waves in layered media by finite difference methods, *Bull. Seism. Soc. Am., 58*, 367–398.

Bathe, K. J., 1990, *Finite-Elemente Methoden*, Springer Verlag.

Batzle, M., and Z. Wang, 1992, Seismic properties of pore fluids, *Geophysics, 57*, 1396–1408.

Batzle, M., R. Hofmann, D. H. Han, and J. Castagna, 2001, Fluids and frequency dependent seismic velocity of rocks, *The Leading Edge*, pp. 168–171.

Becki, K. N., and R. A. McIntosh, Geology and resources of the Primrose crude bitumen deposits North-Eastern Alberta, in *Int. conf. on heavy crude and tar sands*, vol. 2, p. paper No. 71, UNITAR/UNDP, Edmonton, 1988.

Berenger, J. P., 1994, A perfectly matched layer for the absorption of electromagnetic waves, *J. Comput. Phys., 14*, 185–200.

Biot, M. A., 1956a, Theory of propagation of elastic waves in a fluid-saturated porous solid. I low-frequency range, *J. Acoust. Soc. Am., 28*, 168–178.

Biot, M. A., 1956b, Theory of propagation of elastic waves in a fluid-saturated porous solid. II higher-frequency range, *J. Acoust. Soc. Am., 28*, 179–191.

Biot, M. A., 1962, Mechanics of deformation and acoustic propagation in porous media, *J. Appl. Phys., 33*, 1482–1498.

Blackburn, H. M., and S. Schmidt, 2003, Spectral element filtering techniques for large eddy simulation with dynamic estimation, *J. Comput. Phys., 186*, 610–629.

Blanch, J. O., J. O. A. Robertson, and W. W. Symes, 1995, Modeling of a constant Q: Methology and algorithm for an efficient and optimally inexpensive viscoelastic technique, *Geophysics, 60*, 176–184.

Bland, D. R., 1960, *The theory of linear viscoelasticity*, vol. 10 of *International Series of monographs on Pure and Applied Mathematics*, Pergamon Press.

174

Boadu, F. K., 2000, Wave propagation in fluid-saturated media: waveform and spectral analysis, *Geophys. J. Int.*, *141*, 227–240.

Bohlen, T., Viskoelastische FD-modellierung seismischer Wellen zur Interpratation gemessener Seismogramme, Phd, Christian Albrechts Universität, Kiel, 1998.

Bohlen, T., C. Müller, and B. Milkereit, Elastic seismic wave scattering from massive sulfide orebodies: on the role of composition and shape, in *Hardrock Seismic Exploration*, edited by D. Eaton, B. Milkereit, and M. Salisbury, Geophysical developments, SEG, 2003.

Bolt, B. A., and W. D. Smith, 1976, Finite-element computation of seismic anomalies for bodies of arbritrary shape, *Geophysics*, *41*, 145–150.

Boltzmann, L., 1876, Zur Theorie der elastischen Nachwirkung, *Poggendorfs's Ann. Phys. Chem., Ergänzungsband 7*, 624–654.

Borcherdt, R. D., 1973, Energy and plane waves in linear viscoelastic media, *J. Geophys. Res.*, *78*, 2442–2453.

Bos, L., M. A. Taylor, and B. A. Wingate, 2000, Tensor product Gauss-Lobatto points are Fekete points for the cube, *Mathematics of Computation*, *20*, 1543–1547.

Bourbi, T., O. Coussy, and B. Zinszner, 1987, *Acoustics of porous media*, Gulf Publishing Company, Houston, Texas.

Bouzidi, Y., The acoustic reflectivity and transmissivity of liquid saturated porous media: experimental tests of theoretical concepts, Phd, University of Alberta, 2003.

Brudy, M., Determination of in-situ stress magnitude and orientation to 9 km depth at the KTB site, Phd, University of Karlsruhe, 1995.

Butler, R., 1994, Steam-assisited gravity drainage: Concept, development, performance, and future, *J. Can. Pet. Tech.*, *33*, 44–50.

Butler, R. M., 1991, *The Recovery of Oil and Bitumen*, Princten Hall.

Canuto, C., M. Y. Hussaini, A. Quarteroni, and T. A. Zang, 1988, *Spectral Methods in Fluid Dynamics*, Springer Series in Computaional Physics, Springer Verlag, New York.

Carcione, J. M., 1988, Viscoacoustic wave propagation simulation in the earth, *Geophysics*, *53*, 769–777.

Carcione, J. M., 1993, Seismic modeling in viscoelastic media, *Geophysics*, *59*, 110–120.

Carcione, J. M., 1994, The wave equation in generalized coordinates, *Geophysics*, *59*, 1911–1919.

Carcione, J. M., and G. Quiroga-Goode, 1995, Some aspects of the physics and numerical modeling of Biot compressional waves, *J. Comput. Acoust.*, *3*, 261–280.

Carcione, J. M., D. Kosloff, and R. Kosloff, 1988, Wave propagation simulation in a linear viscoelastic medium, *Geophysical Journal*, *95*, 597–611.

Castagna, J. P., Avo analysis - tutorial and review, in *Offset-dependent reflectivity - theory and practice of AVO analysis*, edited by J. P. Castagna and M. M. Mackus, vol. 8 of *Investigation in Geophysics*, pp. 3–36, SEG, 1993.

Caughey, T. K., 1960, Classical normal modes in damped linear dynamic systems, *J. Appl. Mechanics*, pp. 269–271.

Cerjan, C., D. Kosloff, R. Kosloff, and M. Reshef, 1985, A non-refelecting boundary condition for discrete acoustic and elastic wave equations, *Geophysics, 50*, 705–708.

Chakrabarty, C., J. P. Fossey, G. Renard, and C. Gadelle, SAGD process in the East Senlac field: from reservoir characterization to field application, in 7th *UNITAR conference on heavy crude and tar sands*, Beijing / China, 1998.

Chalaturnyk, R. J., Geomechanics of the steam assisted gravity drainage process in heavy oil reservoirs, Phd, University of Alberta, 1996.

Chaljub, E., Y. Capdeville, and J. P. Vilotte, 2003, Solving elastodynamics in a fluid-solid heterogeneous sphere: a parallel spectral element approximation on non-conforming grids, *J. Comput. Physics, 187*, 457–491.

Chapman, C. H., and J. A. Orcutt, 1985, The computation of body wave synthetic seismograms in laterally homogeneous media, *Review of Geophysics, 23*, 105–163.

Chew, W. C., and Q. H. Liu, 1996, Perfectly matched layers for elastodynamics: a new absorbing boundary condition, *J. Comput. Acoust., 4*, 341–359.

Christensen, N. I., Measurements of dynamic properties of rock at elevated temperatures and pressures, in *Measurement of Rock Properties at elevated pressures and temperatures*, edited by H. Pincus and E. Hoskins, vol. ASTM STP 869, pp. 93–107, ASTM, Philadelphia, 1985.

Christensen, N. I., and H. F. Wang, 1985, The influence of pore pressure and confining pressure on dynamic elastic properties of berea sandstone, *Geophysics, 50*, 207–213.

Christensen, R. M., 1971, *Theory of viscoelasticity - An introduction*, Academic Press, Inc.

Christopher, J. E., Evolution of the Lower Cretaceous Mannville Sedimentary Basin in Saskatchewan, in *Petroleum Geology of the Lower Cretaceous Mannville group, Western Canada*, edited by S. Pemberton and D. James, vol. 18, pp. 191–210, Canadian Society of Petroleum Geologists, 1997.

Clayton, R., and B. Enquist, 1977, Absorbing boundary conditions for acoustic and elastic wave equations, *Bull. Seis. Soc. Am., 67*, 1529–1540.

Collino, F., and C. Tsogka, 2001, Application of the perfectly matched absorbing layer model to the linear elastodynamic problem in anisotropic heterogeneous media, *Geophysics, 66*, 294–307.

Dablain, M. A., 1986, The application of high-order differencing to scalar wave equation, *Geophysics, 51*, 56–66.

Diallo, M. S., Acoustic waves attenuation and velocity dispersion in fluid-filled porous media: theoretical and experimental investigations, Phd, Eberhard-Karls Universität, 2000.

Diallo, M. S., and E. Appel, 2000, Acoustic wave propagation in saturated porous media: reformulation of the biot/squirt flow theory, *J. Appl. Geophysics*, *44*, 313–325.

Dilay, A., and J. Eastwood, 1995, Spectral analysis applied to seismic monitoring of thermal recovery, *The Leading Edge*, *14*, 1117–1122.

Domenico, S. N., 1977, Elastic properties of unconsolidated porous sand reservoirs, *Geophysics*, *42*, 1339–1368.

Dvorkin, J., and A. Nur, 1993, Dynamic poroelasticity: A unified model with the squirt and the Biot mechanisms, *Geophysics*, *58*, 524–533.

Dvorkin, J., R. Nolen-Hoeksema, and A. Nur, 1994, The squirt-flow mechanism: Macroscopic description, *Geophysics*, *59*, 428–438.

Dvorkin, J., G. Mavko, and A. Nur, 1995, Squirt flow in fully saturated rocks, *Geophysics*, *60*, 97–107.

Dvorkin, J., D. Moos, J. L. Packwood, and A. M. Nur, 1999, Identifying patchy saturation from well logs, *Geophysics*, *64*, 1756–1759.

Eastwood, J., 1993, Temperature-dependent propagation of P- and S-waves in Cold Lake oil sands: Comparison of theory and experiment, *Geophysics*, *58*, 863–872.

Eaton, D. W., 1999, Weak elastic-wave scattering from massive sulfide orebodies, *Geophysics*, *64*, 289–299.

Eberhart-Phillips, D., D. H. Han, and M. D. Zoback, 1989, Empirical relationships among seismic velocity, effective pressure, porosity, and clay content in sandstone, *Geophysics*, *54*, 82–89.

Emmerich, H., and M. Korn, 1987, Incorporation of attenuation into time-domain computations of seismic wave fields, *Geophysics*, *52*, 1252–1264.

Faccioli, E., F. Maggio, A. Quarteroni, and A. Taghan, 1996, Spectral-domain decomposition methods for the solution of acoustic and elastic wave equation, *Geophysics*, *61*, 1160–1174.

Faccioli, E., F. Maggio, R. Paolucci, and Q. A., 1997, 2d and 3d elstic wave propagation by a pseudo-spectral domain decomposition method, *J. Sesimology*, *1*, 237–251.

Fjær, E., R. Holt, P. Horsund, A. Raaen, and R. Risnes, 1992, *Petroleum Related Rock Mechanics*, vol. 33 of *Developements in petroleum science*, Elsevier, Amsterdam.

Fornberg, B., 1987, The pseudospectral method: Comparisons with finite differences for the elastic wave equation, *Geophysics*, *52*, 483–501.

Fuchs, K., and G. Müller, 1971, Computation of synthetic seismograms with the reflectivity method and comparison with observations, *Geophys. J. R. Astron. Soc.*, *23*, 417–433.

Furumura, T., and H. Takenaka, 1995, A wraparound elimination technique for the pseudo-spectral wave synthesis using an antiperodic extension of the wavefield, *Geophysics, 60*, 302–307.

Futtermann, W., 1962, Dispersive body waves, *J. Geophys. Res., 67*, 5279–5291.

Gallop, J., Asymptotic description of seismic waves, Phd, University of Alberta, 1999.

Gardner, G. H. F., M. R. J. Wyllie, and D. M. Droschak, 1965, Hysteresis in the velocity-pressure characteristics of rocks, *Geophysics, 30*, 111–116.

Garvin, W. W., 1956, Exact transient solution of the buried line source problem, *Proc. Royal Soc. London, Series A, 234*, 528–541.

Gassmann, F., 1951, Über die Elastizität poröser Medien, *Vierteljahresschrift d. Naturf. Ges. Zürich, 96*, 1–24.

Gazdag, J., 1981, Modeling of the acoustic wave equation with transform methods, *Geophysics, 46*, 854–859.

Geertsma, J., and D. C. Smit, 1961, Some aspects of elastic wave propagation in fluid-saturated porous solids, *Geophysics, 26*, 169–181.

Giraldo, F. X., 1998, The Lagrange-Galerkin spectral element method on unstructured quadrilateral grids, *J. Comput. Physics, 147*, 114–146.

Givoloi, D., 1991, Non-reflecting boundary conditions, *J. Comput. Physics, 94*, 1–29.

Gray, S. H., and M. A. Epton, *Multigrid migration: Reducing the migration aperture, but not migrated dips*, p. 1172, Soc. of Expl. Geophys., 1989.

Gray, S. H., and M. A. Epton, 1990, Multigrid migration: Reducing the migration aperture but not the migrated dips, *Geophysics, 55*, 856–862.

Greaves, R. J., and T. J. Fulp, 1987, Three-dimensional seismic monitoring of an enhanced oil recovery process, *Geophysics, 52*, 1175–1187.

Gunasekera, R. C., G. R. Foulger, and B. R. Julian, 2003, Reservoir depletion at The Geysers geothermal area, California, shown by four-dimensional seismic tomography, *J. Geophys. Res., 108*, 2134.

Han, D. H., A. Nur, and D. Morgan, 1986, Effets of porosity and clay content on wave velocities in sandstones, *Geophysics, 51*, 2093–2107.

Hare, J. L., J. F. Ferguson, C. L. V. Aiken, and J. L. Brady, 1999, The 4d microgravity method for waterflood surveillance: a model study for the Prudhoe By reservoir, alaska, *Geophysics, 64*, 78–87.

Henderson, R. D., and G. E. Karniadakis, 1995, Unstructured spectral element methods for simulation of turbulent flows, *J. Comput. Phys., 122*, 191–217.

Hesthaven, J. S., and C. H. Teng, 2000, Stable spectral methods on tetrahedral elements, *SIAM J. Sci. Comput., 21*, 2352–2380.

Hestholm, S., and B. Ruud, 1998, 3-d finite difference elastic wave modeling including surface topography, *Geophysics, 63,* 613–622.

Higdon, R. L., 1991, Absorbing boundary conditions for elastic waves, *Geophysics, 56,* 231–241.

Hornby, B. E., and W. F. I. Murphy, 1987, V_P/V_S in unconsolidated oil sands: Shear from Stoneley, *Geophysics, 52,* 502–513.

Huber, K., K. Fuchs, J. Palmer, F. Roth, B. N. Khakhaev, L. E. Van-Kin, L. A. Pevzner, S. Hickman, D. Moos, M. D. Zoback, and D. Schmitt, 1997, Analysis of borehole televiewer measurements in the Vorotilov drillhole, Russia - first results, *Tectonophysics, 275,* 261–272.

Ito, H., J. DeVilbiss, and A. Nur, 1979, Compressional and shear waves in saturated rock during water-steam transition, *J. Geophys. Res., 84,* 4731–4735.

Joel, B., 1977, Only the good die young, *The Stranger.*

Johnson, D. L., Recent developments in the acoustic properties of porous media, in *Frontiers in Physical Acoustics,* edited by D. Sette, vol. 93 of *Proceedings of the International School of Physics "Enrico Fermi",* pp. 255–290, North Holland Physics Publishing, 1984.

Johnston, D. H., and M. N. Toksöz, Definitions and terminology (chapter 1), in *Seismic wave attenuation,* edited by M. N. Toksöz and D. H. Johnston, vol. 2 of *Geophysics reprint series,* pp. 1–5, SEG, Tulsa, 1981.

Johnston, D. H., M. N. Toksöz, and A. Timur, 1979, Attenuation of seismic waves in dry and saturated rocks: II. mechanisms, *Geophysics, 44,* 691–711.

Jones, T. D., 1986, Pore fluids and frequency-dependent wave propagation in rocks, *Geophysics, 51,* 139–1953.

Karniadakis, G. E. M., and S. J. Sherwin, 1999, *Spectral/hp Element Methods for CFD,* Numerical Mathematics and scientific computation, 1st ed., Oxford University Press, Oxford.

Karrenbach, M., 1996, *Modeling physical systems: wave propagation by FD examples,* Institut für Geophysik, Universität Karlsruhe.

Kay, I., and E. S. Krebes, 1999, Applying finite element analysis to the memory variable formulation of wave propagation in anelastic media, *Geophysics, 64,* 300–307.

Kelly, K. R., R. W. Ward, S. Treitel, and R. M. Alford, 1976, Synthetic seismograms: a finite-difference approach, *Geophysics, 41,* 2–27.

Kieffer, S., 1977, Sound speed in liquid-gas mixtures: water-air and water-steam, *J. Geophys. Res., 82,* 2895–2904.

Kim, S., Multigrid domain decomposition techniques for the high-frequency numerical solution of scalar waves in heterogeneous media, in *International Exposition and 71st Annual Meeting,* pp. 1179–1182, SEG, San Antonio, 2001.

King, M. S., 1966, Wave velocities in rocks as a function of changes in overburden pressure and pore fluid saturants, *Geophysics, 31*, 50–73.

Kjartansson, E., 1979, Constant Q-wave propagation and attenuation, *J. Geophys. Res., 84*, 4737–4748.

Komatitsch, D., and J. Tromp, 1999, Introduction to the spectral element method for three-dimensional seismic wave propagation, *Geophys. J. Int., 139*, 806–822.

Komatitsch, D., and J. Tromp, 2002a, Spectral-element simulations of global seismic wave propagation - I. validation, *Geophys. J. Int., 149*, 390–412.

Komatitsch, D., and J. Tromp, 2002b, Spectral-element simulations of global seismic wave propagation - II: Three-dimensional models, oceans, rotation and self-gravitation, *Geophys. J. Int., 150*, 303–318.

Komatitsch, D., and J. Tromp, 2003, A perfectly matched layer absorbing boundary condition for the second-order seismic wave equation, *Geophys. J. Int., 154*, 146–153.

Komatitsch, D., and J. P. Vilotte, 1998, The spectral element method: an efficient tool to simulate the seismic response of 2d and 3d geological structures, *Bull. Seis. Soc. Am., 88*, 368–392.

Komatitsch, D., R. Martin, J. Tromp, M. A. Taylor, and B. A. Wingate, 2001, Wave propagation in 2-d elastic media using a spectral element method with triangles and quadrangles, *J. Comput. Acoustics, 9*, 703–718.

Komatitsch, D., J. Ritsema, and J. Tromp, 2002, The spectral-element method, Beowulf computing, and three-dimensional seismology, *Science, 298*, 1737–1742.

Kosloff, D., and H. Tal-Ezer, 1993, A modified Chebyshev pseudospectral method with an O(N-1) time step restriction, *J. Comput. Phys., 104*, 457–469.

Kosloff, D., D. Kessler, A. Q. Filho, E. Tessmer, A. Behle, and R. Strahilevitz, 1990, Solution of the equations of dynamic elasticity by a Chebychev spectral method, *Geophysics, 55*, 734–748.

Kosloff, D. D., and E. Baysal, 1982, Forward modeling by a Fourier method, *Geophysics, 47*, 1402–1412.

Kosloff, R., and D. Kosloff, 1986, Absorbing boundaries for wave propagation problems, *J. Comput. Phys., 63*, 363–376.

Lapidus, L., and G. F. Pinder, 1982, *Numerical solution of partial differential equations in science and engineering*, John Wiley & sons, New York.

Lay, T., and T. C. Wallace, 1995, *Modern global seismology*, vol. 58 of *International geophysics series*, Academic Press, New York.

Lemmon, E. W., M. O. McLinden, and D. G. Friend, Thermophysical properties of fluid systems, in *NIST chemestry webbook, NIST standard reference database number 69*, edited by P. Lindstrom and W. G. Mallard, National Institute of standards and technology (http://webbook.nist.gov), 2003.

Levander, A. R., 1988, Fourth-order finite difference P-S_V seismograms, *Geophysics*, 53, 1425–1436.

Li, G., G. Purdue, S. Weber, and R. Couzens, 2001, Effective processing of nonrepeatable 4-d seismic data to monitor heavy oil SAGD steam flood at East Senlac, Saskatchewan, Canada, *The Leading Edge*, 20, 54–62.

Li, Z., 2004, Key problems of seismic acquisition in a mountainous area in south China, *J. Geophys. Eng.*, 1, 160–167.

Liu, H. P., D. L. Anderson, and H. Kanamori, 1976, Velocity dispersion due to anelasticity: implications for seismology and mantle composition, *Geophys. J. R. astro. Soc.*, 47, 41–58.

Lumley, D. E., 2001, Time-lapse seismic reservoir monitoring, *Geophysics*, 66, 50–53.

Lumley, D. E., and R. A. Behrens, 1998, Pratical issues of 4d seismic reservoir monitoring: what an engineer needs to know, *SPE Reservoir Eval. & Eng.*, 1, 528–537.

Lumley, D. E., R. A. Behrens, and Z. Wang, 1997, Assessing the technical risk of a 4-d seismic project, *The Leading Edge*, 16.

Lysmer, J., and R. L. Kuhlemeyer, 1969, Finite dynamic model for infinite media, *J. Eng. Mech. Div., ASCE* 95, 859–877.

Madariaga, R., 1976, Dynamics of an expanding circular fault, *Bull. Seis. Soc. Am.*, 66, 639–666.

Makse, H. A., N. Gland, D. L. Johnson, and L. M. Schwartz, 1999, Why effective medium theory fails in granular materials, *Phys. Rev. Let.*, 83, 5070–5073.

Marfurt, K. J., 1984, Accuracy of finite-difference and finite-element modeling of the scalar and elastic wave equations, *Geophysics*, 49, 533–549.

Marion, D., and A. Nur, 1991, Pore-filling material and its effect on velocity in rocks, *Geophysics*, 56, 225–230.

Martínez, V. L., Seismic response of coal seams in the Western Canadian Basin, MSc, University of Alberta, 2002.

Mavko, G., and T. Mukerji, 1998, Bounds on low-frequency seismic velocities in partially saturated rocks, *Geophysics*, 63, 918–924.

Mavko, G., T. Mukerji, and J. Dvorkin, 1998, *The rock physics handbook*, Cambridge University Press.

Moucha, R., and R. C. Bailey, *Extending the Limits of Resistivity Modelling Using Multigrid Techniques*, p. P047, Eur. Assn. Geosci. Eng., 2001.

Murphy, W. F. I., 1984, Acoustic measures of partial gas saturation in tight sandstones, *J. Geophys. Res.*, 89, 11,549–11,559.

Murphy, W. F. I., K. W. Winkler, and R. L. Kleinberg, 1986, Acoustic relaxation in sedimentary rocks: Dependence on grain contacts and fluid saturation, *Geophysics*, 51, 757–766.

Murphy, W. F. I., A. Reischer, and K. Hsu, 1993, Modulus decomposition of compressional and shear velocities in sand bodies, *Geophysics, 58*, 227–239.

National Energy Board, Conventional heavy oil resources of the Western Canadian Sedimentary Basin, *Tech. rep.*, Webpage: www.neb-one.gc.ca, 2001.

Newmark, N. M., 1959, A method for computation for structual dynamics, *Journal of Engineering Mechanics Division, 85*, 67–94.

Nolen-Hoeksma, R. C., 1993, Porosity and consolidation limits of sediments and Gassmann's elastic wave equation, *Geophys. Res. Letters, 20*, 847–850.

Nur, A., 1989, Four-dimensional seismology and (true) direct detection of hydrocarbons: the petrophysical basis, *The Leading Edge, 8*, 572–578.

Nur, A., Critical porosity and the seismic velocities in rocks, vol. 73, p. 66, EOS, 1992.

Nur, A., G. Mavko, J. Dvorkin, and D. Glmudi, 1998, Critical porosity: a key to relating physical properties to porosity in rocks, *The Leading Edge, 17*, 357–362.

O'Connell, R. J., and B. Budiansky, 1977, Viscoelastic properties of fluid-saturated cracked solids, *J. Geophys. Res., 82*, 5719–5735.

Padovani, E., E. Priolo, and G. Seriani, 1994, Low and high order finite emenent method: experience in seismic modeling, *J. Comput. Acoust., 2*, 371–422.

Palmer, I. D., and M. L. Traviolia, 1980, Attenuation by squirt flow in undersaturated gas sands, *Geophysics, 45*, 1780–1792.

Parra, J. O., 1997, The transversely isotropic poroelastic wave equation including the Biot and squirt mechanisms: Theory and application, *Geophysics, 62*, 309–318.

Parra, J. O., 2000, Poroelastic model to relate seismic wave attenuation and dispersion to permeability anisotropy, *Geophysics, 65*, 202–210.

Parra, J. O., and P. Xu, 1994, Dispersion and attenuation of acoustic guided waves in layered fluid-filled porous media, *J. Acoust. Soc. Am., 95*, 91–98.

Patera, A. T., 1984, A spectral element method for fluid dynamics: Laminar flow in a channel expansion, *J. Comput. Phys., 54*, 468–488.

Press, W. H., S. A. Teukolsky, W. T. Vetterling, and B. P. Flannery, 1997, *Numerical recipes in C*, 2nd ed., Cambridge University Press, Cambridge.

Rasolofosaon, P. N. J., 1991, Plane acoustic waves in linear viscoelastic porous media: energy, particle displacement, and physical interpretation, *J. Acoust. Soc. Am., 89*, 1532–1550.

Reshelf, M., D. Kosloff, M. Edwards, and C. Hsiung, 1988, Three-dimensional elastic modeling by the Fourier method, *Geophysics, 53*, 1184–1193.

Reynolds, A. C., 1978, Boundary conditions for the numerical solution of wave propagation problems, *Geophysics, 43*, 1099–1100.

Rice, J. R., and M. P. Cleary, 1976, Some basic stress diffusion solutions for fluid-saturated elastic porous media with compressible constituents, *Rev. Geophys. Space Physics, 14,* 227–241.

Ricker, N., 1953, The form and laws of propagation of seismic wavelets, *Geophysics, 18,* 10–40.

Robertson, J. O. A., 1996, A numerical free-surface condition for elastic/viscoelastic finite-difference modeling in the presence of topography, *Geophysics, 61,* 1921–1934.

Robertson, J. O. A., J. O. Blanck, and W. W. Symes, 1994, Viscoelastic finite-difference modeling, *Geophysics, 59,* 1444–1456.

Rottenfusser, B. A., J. E. Palfreyman, and N. K. Alwast, Geology of the AOSTRA underground test facility site, in *Int. conf. on heavy crude and tar sands,* vol. 2, p. no 115, UNITAR/UNDP, Edmonton, 1988.

Saleck, F. M., C. Bunks, S. Zaleski, and G. Chavent, *Combining the multigrid and gradient methods to solve the seismic inversion problem,* pp. 688–691, Soc. of Expl. Geophys., 1993.

Sarma, G. S., K. Mallick, and V. R. Gadhinglajkar, 1998, Nonrefelcting boundary condition in finite element formulation for an elastic wave equation, *Geophysics, 63,* 1006–1016.

Savage, J. C., 1969, Comments on "Velocity and attenuation of seismic waves in imperfectly elastic rock", *J. Geophys. Res., 74,* 726–728.

Scales, J. A., and M. L. Smith, 1997, *Introductory geophysical inverse theory,* Samizdat Press, Colorado School of Mines, Golden, Colorado.

Schmitt, D. R., 1999, Seismic attributes for monitoring of a shallow heated heavy oil reservoir: A case study, *Geophysics, 64,* 368–377.

Serón, F. J., J. Badal, and F. J. Sabadell, 1996, A numerical laboratory for simulation and visualization of seismic wavefields, *Geophysical Prospecting, 44,* 603–642.

Seyer, F. A., and C. W. Gyte, Viscosity, in *AOSTRA technical handbook on oil sands, bitumens and heavy oils,* edited by L. G. Helper and C. Hsi, vol. 6, pp. 154–185, Alberta oil sands technology and research authority, Edmonton, 1989.

Shapiro, S. A., P. Audigane, and J. J. Royer, 1999, Large-scale in situ permeability tensor of rocks from induced microseismicity, *Geophys. J. Int., 137,* 207–213.

Sherwin, S. J., and G. E. Karniadakis, 1996, Tetrahedral hp finite elements: Algorithms and flow simulations, *J. Comput. Phys., 124,* 14–45.

Spencer, J. W., M. E. Cates, and D. D. Thompson, 1994, Frame moduli of unconsolidated sands and sandstones, *Geophysics, 59,* 1352–1361.

Taylor, M. A., B. A. Wingate, and R. E. Vincent, 2000, An algorithm for computing Fekete point in the triangle, *SIAM J. Numer. Anal., 38,* 1707–1720.

Timur, A., 1977, Temperature dependence of compressional and shear wave velocities in rocks, *Geophysics, 42,* 950–956.

Toksöz, M. N., D. . Johnston, and A. Timur, 1979, Attenuation of seismic waves in dry and saturated rocks: I. Laboratory measurements, *Geophysics, 44*, 681–690.

Valette, B., 1986, About the influence of pre-stress upon adiabatic perturbations of the earth, *Geophys. J. R. astr. Soc, 85*, 179–208.

Virieux, J., 1984, S_H-wave propagation in heterogenous media: velocity-stress finite-difference method, *Geophysics, 49*, 1933–1957.

Virieux, J., 1986, P-S_V wave propagation in heterogeneous media: velocity-stress finite-difference method, *Geophysics, 51*, 889–901.

Wang, Z., Dynamic versus static elastic properties of reservoir rocks, in *Seismic and acoustic velocities in reservoir rocks. Volume 3: Recent developments*, edited by Z. Wang and A. Nur, pp. 531–539, Soc. Expl. Geophys., 2000a.

Wang, Z., Velocity relationships in granular rocks, in *Seismic and acoustic velocities in reservoir rocks. Volume 3: Recent developments*, edited by Z. Wang and A. Nur, pp. 377–383, Soc. Expl. Geophys., 2000b.

Wang, Z., and A. Nur, Effect of temperature on wave velocities in sands and sandstones with heavy hydrocarbons, in *Seismic and Acoustic Velocities in Reservoir Rocks*, edited by A. Nur and Z. Wang, vol. 1 of *Geophysics reprint series*, pp. 188–194, Soc. of Expl. Geophys., 1988.

Wang, Z., and A. Nur, 1990, Wave velocities in hydrocarbon-saturated rocks: Experimental results, *Geophysics, 55*, 723–733.

Wang, Z., A. M. Nur, and M. L. Batzle, 1990, Acoustic velocities in petroleum oils, *Jour. Petr. Tech., 42*, 192–200.

Wang, Z., W. K. Hirsche, and G. Sedgwick, 1991, Seismic monitoring of water floods?-A petrophysical study, *Geophysics, 56*, 1614–1623.

Ward, S. H., and K. A. Clark, Determination of the viscosities and specific gravities of the oils in samples of Athabaska Bituminous Sand, *Tech. Rep. 57*, Province of Alberta, Research Council of Alberta, 1950.

Watson, I. A., L. R. Lines, and K. F. Brittle, 2002, Heavy-oil reservoir characterization using elastic wave properties, *The Leading Edge, 21*, 736–739.

Watt, J. P., G. F. Davies, and R. J. O'Connell, 1976, The elastic properties of composite materials, *Rev. of Geophys., 14*, 541–563.

Winkler, K. W., 1985, Dispersion analysis of velocity and attenuation in Berea sandstone, *J. Geophys. Res., 90*, 6793–6800.

Winkler, K. W., and A. Nur, 1982, Seismic attenuation: effects of pore fluids and frictional sliding, *Geophysics, 47*, 1–15.

Yilmaz, O., 1987, *Seismic data processing*, vol. 2 of *Investigations in Geophysics*, Soc. of Expl. Geophys.

Zhang, M., X. Li, and M. Wang, 2004, Finite-element implementation of reverse-time migration for anisotropic media, *J. Geophys. Eng.*, *1*, 103–108.

Zhang, Y., and D. Schmitt, Strategies for the acquisition and processing of high-fidelity time-lapse seismic data, in *CSPG/CSEG Convention*, CSPG/CSEG, Calgary, 2003.

Zienkiewsisz, O. C., 1971, *The finite element method in Engineering Science*, McGraw-Hill, London.

Ziolkowski, A., B. Hobbs, and D. Wright, 2002, First direct hydrocarbon detection and reservoir monitoring using transient electromagnetics, *First Break*, *20*, 224–225.

Appendix A

Numerical details and computational aspects of the finite element algorithm

In this appendix the diagonality of the mass matrix is shown first. The following sections then explain briefly numerical techniques employed in the finite element program. In particular, these are the Newmark time stepping technique (section A.2.1), the sparse matrix storage format (section A.2.2), and the iterative matrix solver technique of the conjugate gradients (section A.2.3). A detailed derivation and in-depth explanation of these techniques is beyond the scope of this work, and the reader is referred to the literature (e.g. *Zienkiewsisz*, 1971; *Lapidus and Pinder*, 1982; *Bathe*, 1990; *Scales and Smith*, 1997) for thorough discussions of these topics.

A.1 The diagonality of the mass matrix

Before evaluating the numerical approximation of the integral for the mass matrix the difference between *global* and *local* node numbering shall be discussed. After mapping of the element Ω_e to the reference square Λ a node labelled i in the global system is mapped to a index pair $[\alpha, \beta]$ (see Figure A.1). After mapping the element to the reference square the Gauss-Lobatto-Legendre quadrature rule (equation 2.38) is applied. The basis and weighting function $\phi_i(\xi, \eta)$ and $\phi_j(\xi, \eta)$, respectively, then become products of Lagrangian polynomials with the index transformation $i \rightarrow [\sigma, \tau]$ and $j \rightarrow [\mu, \nu]$. Evaluating the quadrature at the points $[\xi^\alpha, \eta^\beta]$ and applying the discrete orthogonality of

186

Global node numbering

Local node numbering
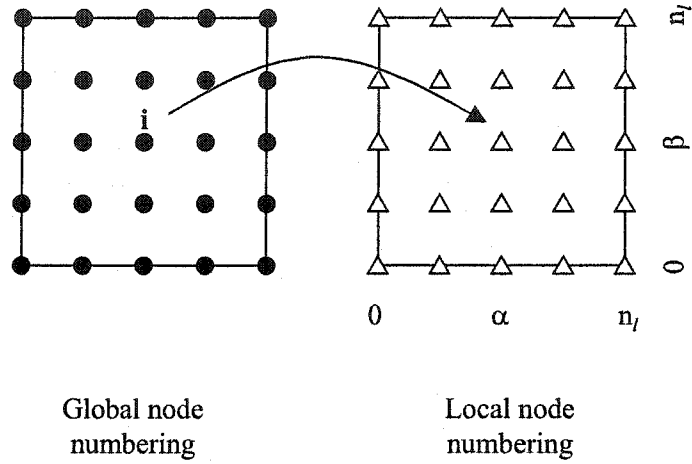
Figure A.1: The global nodes of an element are enumerated by arabic numbers on the left. The mapping to the reference square Λ also assigns the local coordinates $[\alpha, \beta]$ to the node i.

Lagrangian polynomials (equation 2.27) the product of the four Lagrangian polynomials in equation (2.41) reduces to

$$
\ell_\sigma^{n_l}(\xi^\alpha)\ell_\tau^{n_l}(\eta^\beta)\ell_\mu^{n_l}(\xi^\alpha)\ell_\nu^{n_l}(\eta^\beta) =
$$
$$
\delta_{\sigma\alpha}\delta_{\tau\beta}\delta_{\mu\alpha}\delta_{\nu\beta} = \tag{A.1}
$$
$$
\delta_{\sigma\mu}\delta_{\tau\nu}.
$$

First, each Lagrangian polynomial is replaced by a Kronecker-Delta symbol representing the orthogonality. Then, in a second step the first and third as well as a the second and fourth Delta function are combined resulting in the last line of equation (A.1). This shows that there are only non-zero terms in the summation if $\sigma = \mu$ and $\tau = \nu$. This also implies that only for $i = j$ the elements of the mass matrix M_{ij} are different from zero, but for $i \neq j$ the elements of this matrix are zero per definition. Therefore, the mass matrix has only entries in the main diagonal.

187

A.2 Numerical tools

A.2.1 The Newmark algorithm

The finite element equation (equation 2.42) requires a more advanced numerical solution scheme when the damping matrix can not be neglected. *Serón et al.* (1996) analysed several numerical integration scheme in terms of accuracy and computational efficiency. They found, that the *Newmark*-method excels the implicit and explicit central finite difference, Wilson, and Houbolt methods in terms of computational efficiency and numerical accuracy and therefore has been employed in the simulations presented in chapter 2.3.1.

To solve the finite element equation the displacement velocity $(\dot{U})$, and displacement (U) are approximated by (*Newmark*, 1959):

$$^{t+\Delta t}\dot{U} = {}^{t}\dot{U} + \left[(1-\delta)^{t}\ddot{U} + \delta\,{}^{t+\Delta t}\ddot{U}\right]\Delta t \tag{A.2a}$$

$$^{t+\Delta t}U = {}^{t}U + {}^{t}\dot{U}\Delta t + \left[(0.5-\alpha)^{t}\ddot{U} + \alpha\,{}^{t+\Delta t}\ddot{U}\right]\Delta t^2, \tag{A.2b}$$

where α and δ are parameters that control the accuracy and stability of the integration scheme. These parameters are typically chosen to be $\alpha = 0.25$ and $\delta = 0.5$ (*Bathe*, 1990).

To determine the displacements, displacement velocities, and displacement accelerations at time $t + \Delta t$ the algorithm summarized in Table A.1 is employed. If the equation of motion (2.42) is evaluated at time $t + \Delta t$, e.g.,

$$\mathbf{M}\,{}^{t+\Delta t}\ddot{\mathbf{U}} + \mathbf{C}\,{}^{t+\Delta t}\dot{\mathbf{U}} + \mathbf{K}\,{}^{t+\Delta t}\mathbf{U} = {}^{t+\Delta t}\mathbf{F}_s, \tag{A.3}$$

then equation (A.2b) can be solved for $^{t+\Delta t}\ddot{\mathbf{U}}$ in dependance of $^{t+\Delta t}\mathbf{U}$. After inserting $^{t+\Delta t}\ddot{\mathbf{U}}$ into equation (A.2a), two equations are obtained that contain only the unknown displacements $^{t+\Delta t}\mathbf{U}$. Using these equations in (A.3) allows the calculation of the displacements at time $t + \Delta t$ and subsequently the displacement acceleration and velocity vectors according to the scheme in Table A.1 (after *Bathe*, 1990).

A.2.2 The sparse matrix format

The system matrices of the finite element algorithm are very sparse; for example, in section A.1 it was shown that the mass matrix contains only non-zero elements in the main

Table A.1: Newmark time integration scheme

A. Before starting the actual time forward stepping

1. Determination of the integration constants

$$a_0 = \frac{1}{\alpha \Delta t^2} \qquad a_1 = \frac{\delta}{\alpha \Delta t} \qquad a_2 = \frac{1}{\alpha \Delta t} \qquad a_3 = \frac{1}{1\alpha} - 1$$

$$a_4 = \frac{\delta}{\alpha} - 1 \quad a_5 = \frac{\Delta t}{2} \left(\frac{\delta}{\alpha} - 2 \right) \quad a_6 = \Delta t (1 - \delta) \quad a_7 = \delta \Delta t.$$

2. Determination of the effective stiffness matrix $\hat{\mathbf{K}}$

$$\hat{\mathbf{K}} = \mathbf{K} + a_0 \mathbf{M} + a_1 \mathbf{C}.$$

B. For each time step

1. calculate the efficient source vector $\hat{\mathbf{F}}_s$

$$^{t+\Delta t}\hat{\mathbf{F}}_s = {}^{t+\Delta t}\mathbf{F}_s + \mathbf{M}(a_0\, {}^t\mathbf{U} + a_2\, {}^t\dot{\mathbf{U}} + a_3\, {}^t\ddot{\mathbf{U}}) + \mathbf{C}(a_1\, {}^t\mathbf{U} + a_4\, {}^t\dot{\mathbf{U}} + a_5\, {}^t\ddot{\mathbf{U}}),$$

2. determine the displacement vector $\mathbf{U}$

$$^{t+\Delta t}\mathbf{U} = \hat{\mathbf{K}}^{-1}\, {}^{t+\Delta t}\hat{\mathbf{F}}_s,$$

3. update the displacement velocities and accelerations

$$\begin{aligned} {}^{t+\Delta t}\ddot{\mathbf{U}} &= a_0({}^{t+\Delta t}\mathbf{U} - {}^t\mathbf{U}) - a_2\, {}^t\dot{\mathbf{U}} - a_3\, {}^t\ddot{\mathbf{U}} \\ {}^{t+\Delta t}\dot{\mathbf{U}} &= {}^t\dot{\mathbf{U}} + a_6\, {}^t\ddot{\mathbf{U}} + a_7\, {}^{t+\Delta t}\ddot{\mathbf{U}}. \end{aligned}$$

diagonal. The stiffness matrix contains non-zero entries outside the main diagonal but in general it is very sparse as well. If all elements of the matrices containing no information (that is, entries that are zero) are included in the matrices, enormous amounts of computer memory needs to be allocated. However, this is not very efficient and *sparse matrix storage formats* are preferable.

Consider the following matrix A that contains only a few non-zero entries (marked

189

Table A.2: Pseudo-code for a matrix-vector product in sparse data format

```
for i=1 to nrows   % Number of rows of A
    for j=1 to A_maxi[i]
        r[i]+=A_data[i][j]*u[A_colno[i][j]];
    end
end
```

by *)

$$A = \begin{array}{c} \begin{bmatrix} 1 & 2 & 3 & 4 & 5 & 6 \end{bmatrix} \\ \begin{bmatrix} * & * & 0 & 0 & 0 & 0 \\ * & * & * & 0 & 0 & 0 \\ 0 & * & * & * & 0 & 0 \\ 0 & 0 & * & * & * & 0 \\ 0 & 0 & 0 & * & * & * \\ 0 & 0 & 0 & 0 & * & * \end{bmatrix} \end{array}.$$

Instead storing the entire matrix A in the computer memory three matrices are created that contain a) the non-zero elements for each row (A_{data}), a matrix that contains the column numbers of the non-zero elements of A (A_{colno}), and finally a vector that saves the number of non-zero elements of each row in A (A_{maxi}). To store the matrix A the following three matrices are used:

$$A_{data} = \begin{bmatrix} * & * & - \\ * & * & * \\ * & * & * \\ * & * & * \\ * & * & * \\ * & * & - \end{bmatrix} \quad A_{colno} = \begin{bmatrix} 1 & 2 & - \\ 1 & 2 & 3 \\ 2 & 3 & 4 \\ 3 & 4 & 5 \\ 4 & 5 & 6 \\ 5 & 6 & - \end{bmatrix} \quad A_{maxi} = \begin{bmatrix} 2 \\ 3 \\ 3 \\ 3 \\ 3 \\ 2 \end{bmatrix}.$$

Although it is not obvious from this example, a significant reduction of computer memory results for large matrices when this storage system is applied.

Table A.2 provides a pseudo-code to calculate the product of a matrix A (in sparse matrix format) with a vector u, with the result written to the vector r; an operation occurring frequently in the finite element algorithm.

190

A.2.3 The Conjugate Gradient algorithm

In step B.2 of the Newmark algorithm the inverse of the effective stiffness matrix $\hat{K}$ is required. Generally, the finite element matrices are very sparse and they are therefore efficiently stored in a *sparse* matrix format in the computer memory (section A.2.2). The inverse of the effective stiffness matrix, on the other hand, would not be sparse anymore and the advantages of the sparse storage format would be lost. Therefore, it is computationally more efficient to solve the matrix $^{t+\Delta t}U = \hat{K}^{-1}\,{}^{t+\Delta t}\hat{F}_s$ in Table A.1 iteratively. For the current program, the *Conjugate Gradient Method* (e.g. *Scales and Smith*, 1997) has been used, which is known to converge fast for positive definite and symmetric matrices. Table A.3 summarizes the Conjugate Gradient algorithm (after *Scales and Smith*, 1997).

Closely related to the solution of the matrix equation $Ax = h$ is the minimization of the quadratic function f

$$f(x) = x^T \cdot A \cdot x - h \cdot x,$$

as the necessary condition for the minimum of f is

$$f'(x) = A \cdot x - h = 0. \tag{A.4}$$

Conjugate Gradients solve the matrix equation $Ax = h$ by iteratively searching for the solution vector x. After starting with an initial guess (which can be the zero vector, e.g. $x_0 = 0$). The algorithm then minimizes f along "search vectors" p_i and determines subsequently a residual r_i. The iteration continues until the difference between the the updated solution x_{i+1} and the previous approximation x_i is less than a certain criterion ϵ.

The Conjugate Gradient method is computationally simplistic, yet very efficient as it includes only one product of a matrix times a vector, an inner products of two vectors, and the sum of a vector plus a scalar times a vector per iteration step. It is therefore ideally for use on sparse matrix storage systems.

Table A.3: Conjugate Gradient algorithm

- **Step 1:** set $x_0 = 0$ and calculate $p_0 = r_0 = h - A \cdot x_0$.

- **Step 2:** then for each iteration $i = 0, 1\,2, \ldots$ step do the following:

  1. Calculate the coefficient α:

  $$\alpha_{i+1} = \frac{(r_i, r_i)}{(p_i, Ap_i)},$$

  2. Then update the solution

  $$x_{i+1} = x_i + \alpha_{i+1}\, p_i,$$

  3. Next calculate the new residual r_{i+1}

  $$r_{i+1} = r_i - \alpha_{i+1} Ap_i,$$

  4. Now determine β

  $$\beta_{i+1} = \frac{(r_{i+i}, r_{i+1})}{(r_i, r_i)},$$

  5. and finally update the 'search direction'

  $$p_{i+1} = r_{i+1} + \beta_{i+1}\, p_i,$$

A.3 Description of the finite difference operators and the pseudo-spectral algorithm

A.3.1 Finite difference operators

The *Finite Difference Method (FDM)* is the most widely used technique in numerical simulations. It is a rather simple yet efficient technique to solve a partial differential equation in a geometrical simple model. The idea of the FDM is to replace the differential operators in a differential equation by finite-difference operators.

To start the approximation of a derivative by a finite difference remember the definition of the derivative of a function f, df/dx, as the limit of $\Delta x \to 0$ when the secant line becomes the tangent to the curve of f (see also Figure A.2)

Figure A.2: On the definition of the derivative as an approximation by a finite difference.

$$\frac{df}{dx} = \lim_{\Delta x \to 0} \frac{f(x + \Delta x) - f(x)}{\Delta x}. \tag{A.5}$$

Instead of making Δx smaller and smaller the fundamental idea of the FDM is to stop the limit at a *sufficient small* step Δx. Then, the assumption is made that

$$\frac{df}{dx} \approx \frac{f(x + \Delta x) - f(x)}{\Delta x} \equiv \frac{\Delta f}{\Delta x}. \tag{A.6}$$

The last expression is the finite difference operator. From this derivations it becomes clear that in the FDM (and, in fact, in any other numerical method as well) the continuous model is split into discrete points separated by a distance Δx. The previously continuous function f is then only defined at these discrete points. Then, the differential operator is defined as the difference of two (or a combination of more) function values Δf over a certain distance Δx.

The finite difference operator can also be determined from a Taylor expansion of f

$$f(x + \Delta x) \approx f(x) + f'(x)\Delta x + \frac{1}{2}f''(x)\Delta x^2 + \dots \tag{A.7a}$$

$$f(x - \Delta x) \approx f(x) - f'(x)\Delta x + \frac{1}{2}f''(x)\Delta x^2 \mp \dots \tag{A.7b}$$

Now the discrete approximation of the first-order derivative results from subtracting

---

193

equation A.7b from A.7a and then dividing by $2\Delta x$:

$$f'(x) \approx \frac{f(x + \Delta x) - f(x - \Delta x)}{2\Delta x} \tag{A.8}$$

Adding A.7a and A.7b gives an approximation for the second derivative:

$$f''(x) \approx \frac{f(x + \Delta x) - 2f(x) + f(x - \Delta x)}{\Delta x^2} \tag{A.9}$$

Higher derivatives can be approximated in a similar way. However, for simulating the propagation of waves the second derivative is the highest order required.

A.3.2 The pseudo-spectral modelling algorithm

In section 2.1.2 the numerical solution of a partial differential equation using Chebychev polynomials $T_k(x_j)$ has been introduced. This section outlines briefly the modelling algorithm.

Chebychev polynomials are only defined on the interval $[-1, 1]$ by

$$T_k(x_j) = \cos\left(\frac{j\pi}{N}k\right), j = 1, \ldots, N.$$

A piecewise continuous function u(x) with $-1 < x < 1$ can be expanded in a truncated Chebychev series as follows

$$u(x_j) = \sum_{k=0}^{N} a_k T_k(x_j), \ j = 0, \ldots, N,$$

The coefficients a_k are calculated by the discrete transform

$$a_k = \frac{2}{N} \sum_{j=0}^{N} \alpha_j I_k u(x_j),$$

with

$$\alpha_j = \begin{cases} 1/2, & j = 0 \ or \ N \\ 1, & otherwise \end{cases}$$

$$I_k = \begin{cases} 1, & k \neq 0 \\ 1/2, & k = 0 \ or \ N \end{cases}$$

The derivative of the function u can be similarly calculated (*Canuto et al.*, 1988; *Kosloff et al.*, 1990)

$$u'(x_j) = \sum_{k=0}^{N} b_k T_k(x_j), \; j = 0, ..., N.$$

The coefficients b_k are related to the expansion factors a_k by a downward recursion relation (*Kosloff et al.*, 1990)

$$b_{k-1} = b_{k+1} + 2k a_k, \; k = N, ..., 2,$$

and

$$b_o = (2a_1 + b_2)/2.$$

The starting values for the recursion are $b_{N+1} = b_N = 0$. With this method determining the values of the function u and its first derivative are relatively straight forward. As the determination of the second derivative is computational expensive (*Kosloff et al.*, 1990) this method has only been applied to the first-order system to describe wave propagation (e.g. equations 1.18a and 1.18b).

A.4 Stability criterion

The von-Neumann stability analysis considers the evolution of an amplitude with time. In essence, it introduces an initial 'error' amplitudes that are represented by a finite Fourier series. These errors can be caused by numerical inaccuracy such as an inappropriate approximation of derivatives or computational errors like rounding errors. It is a 'local' stability criterion as it applies only to linear problems with constant parameters (e.g., spatially and temporal constant density and elastic properties). Furthermore, it applies theoretically only to unbounded computational domains as it completely neglects the influence of boundary conditions.

Such an erroneous amplitude $u(x, t)$ can be expressed by a harmonic decomposition at time $^n t$ and position x_j as

$$^n u_j = \xi^n(k) e^{i \, k j \delta x}, \; j=1,...,N, \tag{A.10}$$

where

k spatial wave number

$\xi = \xi(k)$ a complex number, which is sometimes called the amplification factor. It can be considered as the amplitude of the kth-mode (or harmonics) of the propagating wavelet.

The von-Neumann stability criterion requires that for a given numerical scheme the absolute value of the amplification factor ξ must not be larger than one. Otherwise, the erroneous amplitudes grow with time, thus making the scheme unstable:

$$|\xi(k)|^2 \begin{cases} > 1, & \text{unstable} \\ \leq 1, & \text{stable.} \end{cases}$$

To analyse a particular numerical scheme for stability the expression (A.10) is inserted into the numerical approximation and subsequently solved for $|\xi(k)|^2$. For example, for the implicit 2nd-order finite difference approximation of the acoustic wave equation,

$$\frac{\partial^2 u}{\partial t^2} - c^2 \frac{\partial^2 u}{\partial x^2} \approx$$
$$\frac{^{k+1}u_i - 2\,^k u_i + {}^{k-1}u_i}{\Delta t^2} - c^2 \frac{^k u_{i+1} - 2\,^k u_i + {}^k u_{i-1}}{\Delta x^2} = 0,$$

a von-Neumann stability analysis results in (*Karrenbach*, 1996; *Press et al.*, 1997)

$$\xi(k) = -i\frac{c\Delta t}{\Delta x}sin(k\Delta x) \pm \sqrt{1 - \left(\frac{c\Delta t}{\Delta x}sin(k\Delta x)\right)^2}.$$

The amplification factor is only less than one if the well-known *Courant condition* is met, e.g.

$$1 \leq c\frac{\Delta t}{\Delta x}.$$

Therefore, the implicit numerical approximation of the second order wave equation by finite difference operators is only conditionally stable.

In theory, a similar stability analysis is also possible for finite element schemes; however, the necessary numerical analysis is significantly more work extensive. In the following paragraphs, the main steps for the stability analysis are briefly outlined, a more detailed description can be found in *Lapidus and Pinder* (1982) and *Bathe* (1990), among others.

In general, the finite element approximation of the wave equation results in a matrix equation of the form

$$\mathbf{M} \cdot \ddot{\mathbf{U}} + \mathbf{C} \cdot \dot{\mathbf{U}} + \mathbf{K} \cdot \mathbf{U} = \mathbf{R}. \tag{A.11}$$

196

For the stability analysis it is of advantage to transform this equation to a principle axis system such that it becomes (*Bathe*, 1990)

$$\ddot{x} + \Delta \cdot \dot{x} + \Omega^2 \cdot x = \phi^T R,$$

where

- x is the solution vector in the new co-ordinate system,

- Ω^2 is a diagonal matrix containing the eigenvalues of (A.11),

- ϕ is a matrix built from the eigenvectors of (A.11), and

- Δ stands for the product $\phi^T C \phi$.

After this transformation the stability of a particular scheme can be assessed in a similar way as before by considering the solution at time $^n t$ as

$$^n x = A \cdot {}^n x + r.$$

In this equation the matrix A and the vector r depend on the numerical method to approximate the time derivatives. The numerical method is stable if the spectral radius of the matrix A, $\rho(A)$, is less than or equal to one. The spectral radius $\rho(A)$ is defined as the largest eigenvalue of A.

The required determination of the eigenvalues and eigenvectors of the finite element equation make the stability analysis rather cumbersome. Instead, numerical experiments by, for example, *Faccioli et al.* (1997) and *Komatitsch and Vilotte* (1998) have shown that the Courant condition also applies for the finite element method when the parameter Δx is replaced by the minimum spacing between two nodes in an element, h_{min}.

An important result of such analyses is the difference in the stability between *explicit* and *implicit* schemes. Explicit schemes such as the approximation of the time derivative by a finite difference operator are only conditionally stable, that is, the discrete time interval Δt must be chosen with respect to the velocity c and the spatial sampling interval Δx such that the Courant condition is met. On the other hand, implicit time schemes such as the Newmark algorithm (section A.2.1) are unconditionally stable. The solution will always be bounded regardless of the time step being used. Therefore, a much larger

discrete time interval can be used than for explicit schemes. However, implicit numerical schemes are computationally more expensive, and the costs of the required inversion of a matrix can counteract the advantage of the larger time step.

Appendix B

Description of the analysed well logs of the Lloydminster resrvoir

The rock physical characterisation for the Lloydminster reservoir presented in chapter 3 is based on the analysis of three well logs that were recorded in the vicinity of the Senlac SAGD site in Saskatchewan. These well logs are described in more detail in the following paragraphs.

Well A: CS SENLAC A13-7-40-35 This well was cored and is located in the South-East corner of the study area. The density and γ-ray curves clearly show the presence of the coal layer (low density) and shale layer (relatively high γ-ray values) above the reservoir. The reservoir layer itself is primarily filled with oil (high values in the resistivity curve), while water seems only to be present in the carbonate layer below the conformity (Figure B.1). As there are no shear sonic data available for this well the elastic properties of the frame can not be determined from this well log using the method as proposed in the theory part (chapter 3.1.2).

Well B: CS SENLAC SWD B4-18-40-25W3 As in the previous example the density and γ-ray curves clearly distinguish the relevant layers. However, the resistivity log indicates that there is a water saturated layer between the oil saturated sands and the underlying carbonates (see the resistivity log in Figure B.2). This well log does not contain shear sonic data so that we can not derive the elastic frame properties for this well.

199

Well C: PCP PCR SENLAC OBS DD 11C7-12-4C6-12-40   The location of this well within the Senlac site is not known. However, this well log contains the most curves. It must be noted that this is a deviated well, and no borehole deviation information are included in the file. Thus, a true vertical depth correction is not possible, but for the purpose of this study, such a correction is not necessarily required. As with the other well logs the reservoir layer can easily be distinguished from the overlying shale-coal layers and the carbonates below. The strong contrast in the resistivity data allow us to distinguish the oil-saturated section from the water saturated layer in the reservoir (Figure B.3). Furthermore, this is the only well log available that includes shear sonic data.
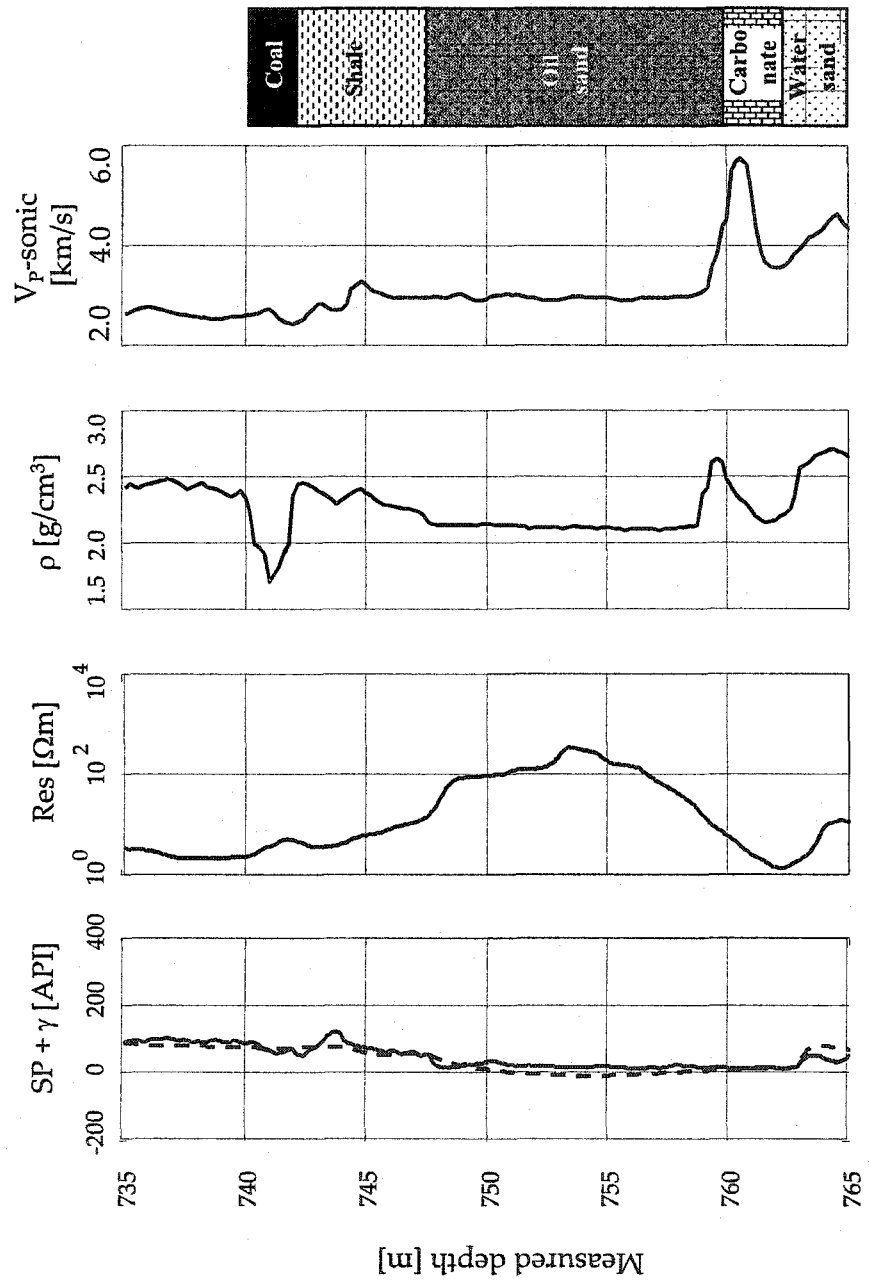
Figure B.1: Log data from Well A: CS SENLAC A13-7-40-35, Lloydminster reservoir.
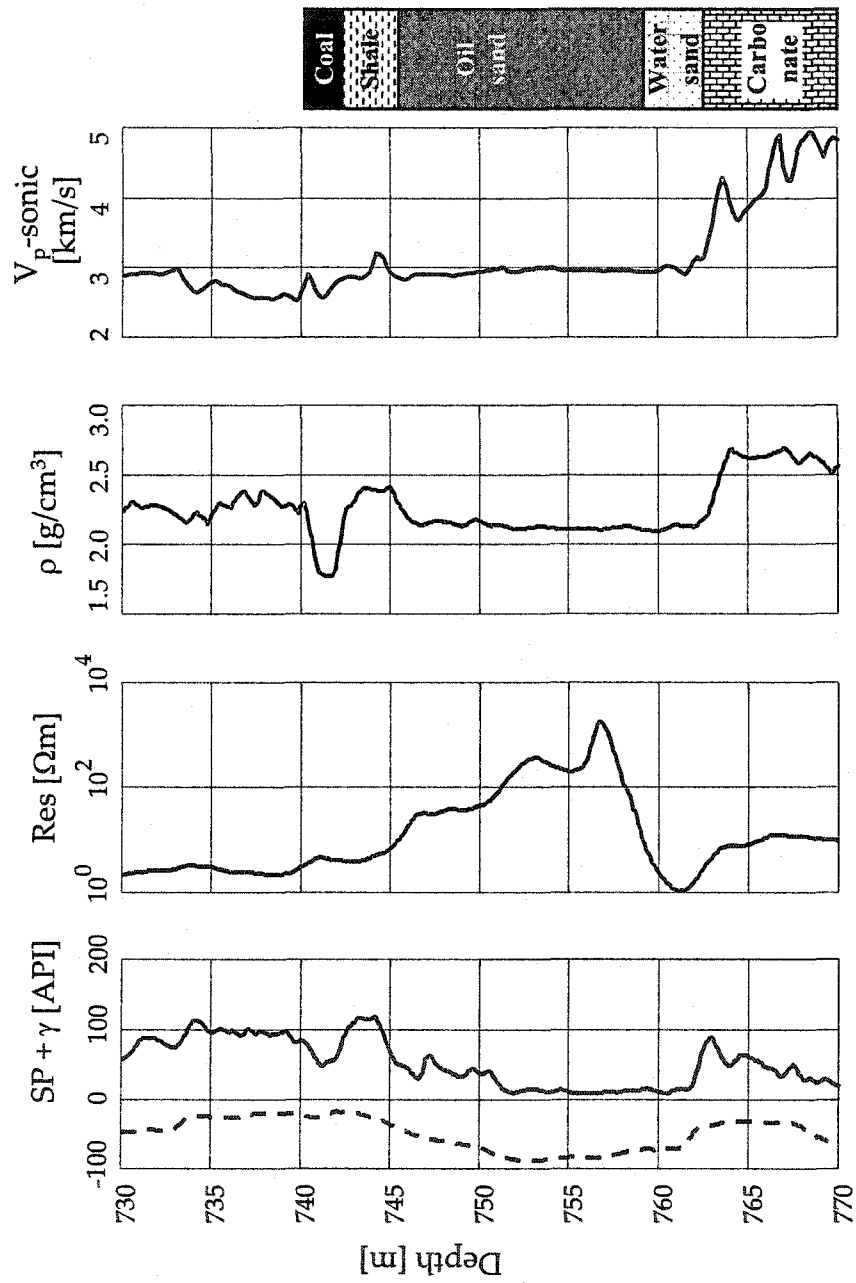
Figure B.2: Log data from Well B: CS SENLAC SWD B4-18-40-25W3, Lloydminster reservoir.
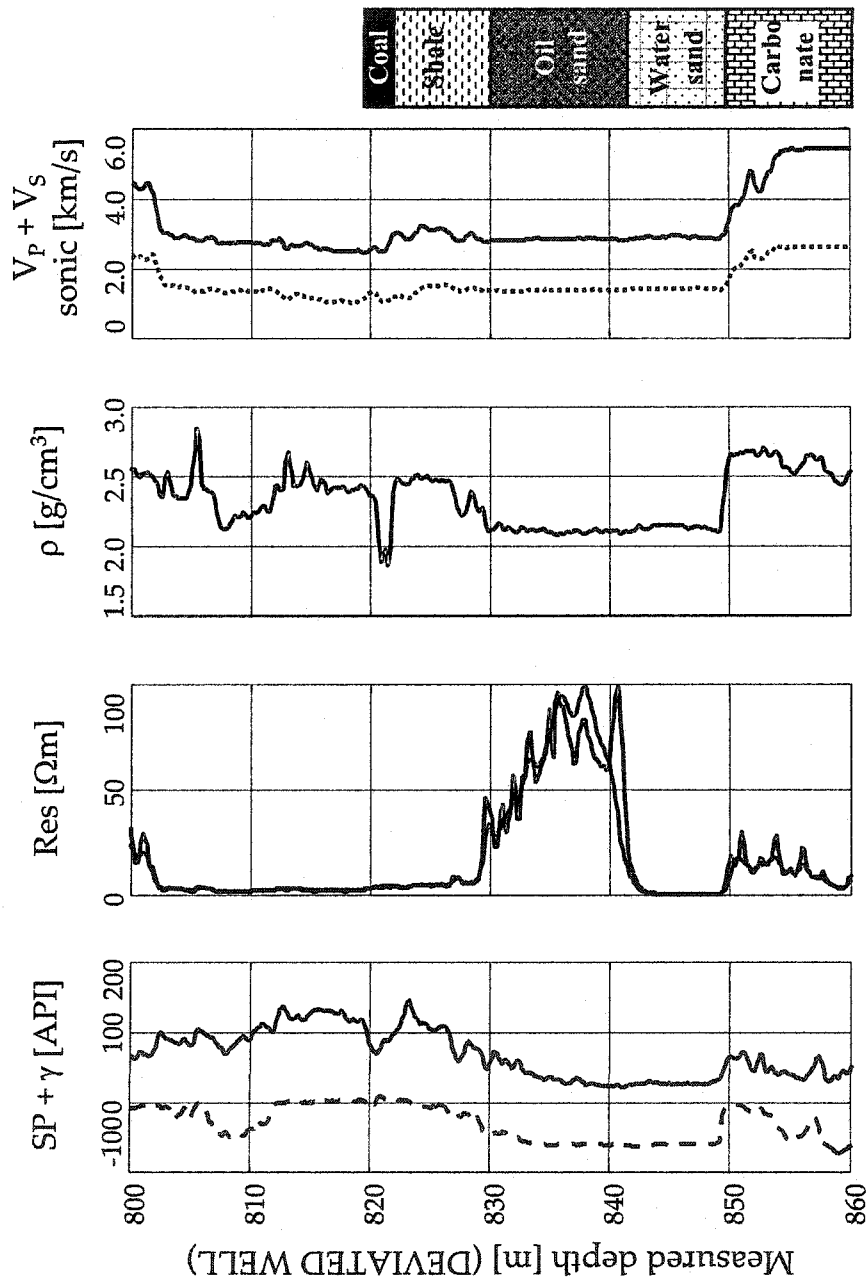
Figure B.3: Log data from Well C: PCP PCR SENLAC OBS DD 11C7-12-4C6-12-40, Lloydminster reservoir.

203

Appendix C

Empirical relationships for the properties of water

The properties of the saturating water in section 3.4 were calculated using the empirical relationships compiled by *Batzle and Wang* (1992), which are included in the following paragraphs.

The density of brine ρ_B is calculated in two steps. First, the density of pure water ρ_W is calculated as a function of temperature T (given in °C) and pressure P (measured in MPa). In a second step, the density of brine is calculated as a function of temperature T, pressure P, and salinity S (ppm/1000000). *Batzle and Wang* (1992) report only a relationship for sodium chloride as the dissolved substance. As the dependence of the brine density on the salinity is relative weak when compared to for example temperature, any variation of ρ_B with dissolved mineralogy is considered negligible here.

$$\rho_W = 1 + 1 \times 10^{-6}(-80T - 3.3T^2 + 0.00175T^3 +$$
$$+ 489P - 2TP + 0.016T^2P - 1.3 \times 10^{-5}T^3P-, \tag{C.1a}$$
$$- 0.002TP^2)$$
$$\rho_B = \rho_W + S\{0.668 + 0.44S + 1 \times 10^{-6}[300P-$$
$$- 2400PS + T(80 + 3T - 3300S - 13P + 47PS)]\}. \tag{C.1b}$$

The acoustic velocity is also found in two steps. After the velocity for clean water, V_W, has been calculated as a function of temperature and pressure, the brine's velocity (V_B) is determined depending on temperature, pressure, and salinity using the following

204

equations:

$$V_W = \sum_{i=0}^{4} \sum_{j=0}^{3} w_{ij} T^i P^j \tag{C.2}$$

$$\text{with} \quad w_{ij} = \begin{pmatrix} 1402.85 & 1.524 & 3.43 \times 10^{-3} & -1.2 \times 10^{-5} \\ 4.87 & -0.011 & 1.73 \times 10^{-4} & -1.63 \times 10^{-6} \\ -0.05 & 2.747 \times 10^{-4} & -2.14 \times 10^{-6} & 1.24 \times 10^{-8} \\ 1.49 \times 10^{-4} & -6.5 \times 10^{-7} & -1.46 \times 10^{-8} & 1.33 \times 10^{-10} \\ -2.19 \times 10^{-7} & 7.99 \times 10^{-10} & 5.23 \times 10^{-11} & -4.61 \times 10^{-13} \end{pmatrix},$$

and

$$V_B = V_W + S(1170 - 9.6T + 0.055T^2 - 8.5 \times 10^{-5}T^3$$
$$+ 2.6P - 0.0029TP - 0.0476P^2) + S^{1.5}(780 - 10P + 0.16P^2) - 820S^2. \tag{C.3}$$

Using these equations the bulk modulus of brine results as

$$K_B = \rho_B V_B^2. \tag{C.4}$$

205

Appendix D

Uncertainty calculation

The uncertainty δK_d of the frame bulk modulus (equation 3.4) is calculated using standard error propagation. It is assumed that all parameters occurring in this equation have some uncertainty. The uncertainty of values determined from well logs is the standard deviation of the data involved (e.g., K_{eff}, V_P, V_S, and ρ) or are assumed (e.g., ϕ, K_S, K_f). Then, the uncertainty δK_d is given by

$$\delta K_d = \left| \frac{\partial K_d}{\partial K_{eff}} \right| \delta K_{eff} + \left| \frac{\partial K_d}{\partial K_S} \right| \delta K_S + \left| \frac{\partial K_d}{\partial K_f} \right| \delta K_f + \left| \frac{\partial K_d}{\partial \phi} \right| \delta \phi, \qquad (D.1)$$

where the partial derivatives are given by

$$\frac{\partial K_d}{\partial K_{eff}} = \frac{[(\phi-1)/K_S]\,[(1-K_{eff}/K_s+\phi)/K_S-\phi/K_f]}{[(1-K_{eff}/K_S+\phi)/K_S-\phi/K_f]^2} +$$
$$+ \frac{[1+K_{eff}\,((\phi-1)/K_s-\phi/K_S^2)]/K_s^2}{[(1-K_{eff}/K_S+\phi)/K_S-\phi/K_f]^2} \quad , \qquad (D.2a)$$

$$\frac{\partial K_d}{\partial K_s} = \frac{[(1-K_{eff}/K_s+\phi)/K_s-\phi/K_s]\,[-K_{eff}(\phi-1)/K_s^2]}{[(1-K_{eff}/K_s+\phi)/K_s-\phi/K_f]^2} -$$
$$- \frac{[1+K_{eff}\,((\phi-1)/K_s-\phi/K_f)]\,(2K_{eff}/K_s^3-\phi/K_s^2)}{[(1-K_{eff}/K_s+\phi)/K_s-\phi/K_f]^2} \quad , \qquad (D.2b)$$

$$\frac{\partial K_d}{\partial K_f} = \frac{\phi K_{eff}/K_f^2\,[(1-K_{eff}/K_s+\phi)/K_s-\phi/K_s]}{[(1-K_{eff}/K_s+\phi)/K_s-\phi/K_f]^2} -$$
$$- \frac{\phi/K_f^2\,[1+K_{eff}\,((\phi-1)/K_s-\phi/K_f)]}{[(1-K_{eff}/K_s+\phi)/K_s-\phi/K_f]^2} \quad , \qquad (D.2c)$$

$$\frac{\partial K_d}{\partial \phi} = \frac{K_{eff}(1/K_s-1/K_f)\,[(1-K_{eff}/K_s+\phi)/K_s-\phi/K_s]}{[(1-K_{eff}/K_s+\phi)/K_s-\phi/K_s]^2} -$$
$$- \frac{(1/K_s-1/K_f)\,[1+K_{eff}\,((\phi-1)/K_s-\phi/K_f)]}{[(1-K_{eff}/K_s+\phi)/K_s-\phi/K_s]^2} \quad . \qquad (D.2d)$$

The uncertainty δK_{eff} is calculated from the statistical errors (that is, the standard deviations) of the well log data $\delta\rho$, δV_P, and δV_S according to

$$\delta K_{eff} = \left(V_P^2 - \frac{4}{3}V_S^2\right)\delta\rho + 2V_P\rho\,\delta V_P + \frac{8}{3}V_S\rho\,\delta V_S. \qquad (D.3)$$

After fluid substitution the effective velocity for the Gassmann model is calculated by equations 3.1 and 3.3, respectively, with the uncertainty of

$$\delta V_P = \frac{V_P}{2}\left(\frac{\delta K_{eff}+4/3\delta\mu_d}{K_{eff}+4/3\mu_d}+\frac{\delta\rho_{eff}}{\rho_{eff}}\right). \qquad (D.4)$$

In this equation the uncertainty of the effective density results from

$$\delta\rho_{eff} = \delta\phi(\rho_f+\rho_s)+\phi(\delta\rho_f+\delta\rho_s) \qquad (D.5)$$

and the uncertainty of the effective bulk modulus K_{eff} calculates according to

$$\delta K_{eff} = \left|\frac{\partial K_{eff}}{\partial K_d}\right|\delta K_d + \left|\frac{\partial K_{eff}}{\partial K_s}\right|\delta K_s + \left|\frac{\partial K_{eff}}{\partial K_f}\right|\delta K_f + \left|\frac{\partial K_{eff}}{\partial \phi}\right|\delta\phi \qquad (D.6)$$

with

$$\frac{\partial K_{eff}}{\partial K_d} = \frac{-2(1 - K_d/K_s)/K_s \left[(1 - \phi - K_d/K_s)/K_s + \phi/K_f\right]}{\left[(1 - \phi - K_d/K_s)/K_s + \phi/K_f\right]^2} +$$
$$+ \frac{(1 - K_d/K_s)^2/K_s^2}{\left[(1 - \phi - K_d/K_s)/K_s + \phi/K_f\right]^2} \qquad \text{(D.7a)}$$

$$\frac{\partial K_{eff}}{\partial K_s} = \frac{2(1 - K_d/K_s)K_d/K_s^2 \left[(1 - \phi - K_d/K_s)/K_s + \phi/K_f\right]}{\left[(1 - \phi - K_d/K_s)/K_s + \phi/K_f\right]^2} +$$
$$+ \frac{(1 - K_d/K_s)^2/K_s^2}{\left[(1 - \phi - K_d/K_s)/K_s + \phi/K_f\right]^2} \qquad \text{(D.7b)}$$

$$\frac{\partial K_{eff}}{\partial K_f} = \frac{(1 - K_d/K_s)^2(\phi/K_f^2)}{\left[(1 - \phi - K_d/K_s)/K_s + \phi/K_f\right]^2} \qquad \text{(D.7c)}$$

$$\frac{\partial K_{eff}}{\partial \phi} = \frac{(1 - K_d/K_s)^2(1/K_f - 1/K_s)}{\left[(1 - \phi - K_d/K_s)/K_s + \phi/K_f\right]^2}. \qquad \text{(D.7d)}$$

Finally, the uncertainty of the shear frame modulus is given by

$$\delta\mu_d = \delta\rho_{eff}V_S^2 + 2\rho_{eff}V_S\delta V_s. \qquad \text{(D.8)}$$

The uncertainty for the P-velocity according to the patchy saturation model is calculated according to

$$\delta V_P = \frac{V_P}{2}\left(\frac{\delta(K + 4/3\mu)_{patchy}}{(K + 4/3\mu)_{patchy}} + \frac{\delta\rho_{eff}}{\rho_{eff}}\right). \qquad \text{(D.9)}$$

The calculation of the uncertainty in the elastic modulus $(K + 4/3\mu)_{patchy}$ requires two steps:

$$\delta\left(\frac{1}{(K + 4/3\mu)_{patchy}}\right) = \left|\frac{\partial(K + 4/3\mu)_{patchy}^{-1}}{\partial\mu}\right|\delta\mu +$$
$$+ \sum_{i=1}^{3}\left(\left|\frac{\partial(K + 4/3\mu)_{patchy}^{-1}}{\partial S_i}\right|\delta S_i + \left|\frac{\partial(K + 4/3\mu)_{patchy}^{-1}}{\partial K_i}\right|\delta K_i\right) \qquad \text{(D.10a)}$$

with

$$\frac{\partial(K + 4/3\mu)_{patchy}^{-1}}{\partial\mu} = -\frac{4}{3}\sum_{i=1}^{3}\frac{S_i}{(K_i + 4/3\mu)^2} \qquad \text{(D.10b)}$$

$$\frac{\partial(K + 4/3\mu)_{patchy}^{-1}}{\partial S_i} = \frac{1}{K_i + 4/3\mu} \qquad \text{(D.10c)}$$

$$\frac{\partial(K + 4/3\mu)_{patchy}^{-1}}{\partial K_i} = \frac{-S_i}{(K_i + 4/3\mu)^2} \qquad \text{(D.10d)}$$

208

where S_i and K_i are, respectively, the saturation of steam, water, and oil, and the effective bulk modulus, when the pore space is completely saturated with either steam, oil, or water. The uncertainties δK_i are calculated via equation (D.1).

By using the empirical relationships for the calculation of the fluid properties the determination of the uncertainty in, for example, the bulk modulus of the brine is not possible because *Batzle and Wang* (1992) did not provide errors for the numerous fitting parameters. Therefore, the uncertainty of the effective fluid bulk moduli and density as well as the porosity and the bulk modulus of the solid material are assumed to be 10% of the actual value in the calculations of chapter 3.

So eine Arbeit kann niemals vollendet werden,

man muß sie für vollendet erklären,

wenn man nach Zeit *und* Umständen

das Möglichste getan hat.

(aus Johan Wolfgang v. Goethe:

"Die italienische Reise")